MODELLING AND EXPERIMENTAL STUDY OF THE SPRAY FORMING OF DISSIMILAR METALS

Tung Lik Lee
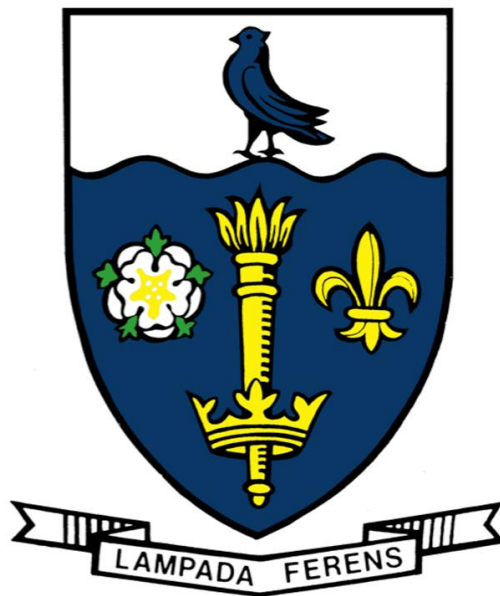
University of Hull

November 2015

THE UNIVERSITY OF HULL

MODELLING AND EXPERIMENTAL STUDY OF THE SPRAY FORMING OF DISSIMILAR METALS

being a Thesis submitted for the Degree of

Doctor of Philosophy in Engineering

in the University of Hull

by

Tung Lik Lee, BEng

School of Engineering

University of Hull

November 2015

Abstract

This research describes a systematic study to develop a strong interfacial bond in as-sprayed dissimilar metallic alloys. Non-destructive three-dimensional microstructure and residual stress characterisations via X-ray micro-computed tomography and neutron diffraction, respectively and numerical modelling of the preform shape evolution, transient heat flow and thermal residual stress developed were employed. The study revealed quantitatively the links between the key spray forming parameters, corresponding microstructures formed and the interfacial bonding characteristics in thick as-sprayed dissimilar metallic alloys.

The key novelties of this research include:

- The development of a preform shape and heat flow model that incorporates: (1) the use of a mesh deformation method with automated re-meshing algorithm to model the growing preforms and address the coupling of droplet mass/enthalpy input at the deposition surface and (2) a substrate induction preheating model.

- Validated against experimental measurements, the preform heat flow model was used to establish the correlations between the preform thermal history and microstructures formed. The correlations established based on the tomography and diffraction measurements showed their interrelationship and agreements with one another. The correlations also provided the crucial links to take into account the effects of the microstructure formed on the corresponding material properties and stresses developed in the preform after cooling.

- The combined use of thermal residual stress modelling and neutron diffraction in this research presents, for the first time, the non-destructive quantitative assessment of the interfacial bonding in thick as-sprayed dissimilar steels preforms. The effects of different substrate and spray temperatures on the microstructures, residual stress and interfacial bond developed were investigated systematically.

I

- The dynamics of the atomised droplets rapid microstructural change during deposition were revealed when subjected to rapid Joule heating ($\sim$500 K s^{-1}) to a range of isothermal temperatures in the vicinity of the precipitate solvus and alloy solidus temperatures with a short ($\sim$10 s) high temperature holding time. A finite element model of the transient heat flow in the powder compact was developed to provide more quantitative information of the specimen internal temperature distribution which was otherwise unavailable and the rapid microstructural change in the powders was rationalised in terms of the transient temperature conditions. These results can be useful in reconciling thermal histories and microstructures in the as-sprayed preforms, and may guide the optimisation of the spray forming process if desirable microstructural features are to be preserved into the bulk preform.

- The elastic and plastic deformation behaviours of the spray formed steels containing different levels of porosity and the integrity of the bonded interface of the spray formed dissimilar steels were studied *in situ* via three-point bend tests with neutron diffraction. The study revealed the role of the constituent phases in the as-sprayed high speed steel when subjected to stresses above the elastic limit and the characteristics of the interfacial bond formed in comparison to the non-destructive assessment carried out in this research.

Dedication

I dedicate the successful completion of this thesis to my ever supportive Mother (Siew Choo, Ching), ever inspiring Father (Siew Choy, Lee) and ever encouraging Brother (Tung Wai, Lee). Their relentless support and love have brought me to where I stand today.

Acknowledgements

Publications, conference presentation and beam times awarded

The published peer reviewed journal papers, conference presentations and neutron beam times awarded throughout this research are listed below:

Journal papers:

1. Tan, D., **Lee, T.L.**, Khong, J., Connolley, T., Fezzaa, K. & Mi, J. 2015. High-Speed Synchrotron X-ray Imaging Studies of the Ultrasound Shockwave and Enhanced Flow during Metal Solidification Processes. Metallurgical and Materials Transactions A, 46, 2851-2861.

2. **Lee, T. L.**, Mi, J., Zhao, S. L., Fan, J. F., Zhang, S. Y., Kabra, S. & Grant, P. S. 2015. Characterization of the residual stresses in spray-formed steels using neutron diffraction. Scripta Materialia, 100, 82-85.

3. Mi, J., Tan, D. & **Lee, T.L.** 2014. In Situ Synchrotron X-ray Study of Ultrasound Cavitation and Its Effect on Solidification Microstructures. Metallurgical and Materials Transactions B, 1-5.

4. Zheng, L., Zhang, G., **Lee, T. L.**, Gorley, M. J., Wang, Y., Xiao, C. & Li, Z. 2014. The effects of Ta on the stress rupture properties and microstructural stability of a novel Ni-base superalloy for land-based high temperature applications. Materials & Design, 61, 61-69.

5. Zheng, L., Zhang, G., Xiao, C., **Lee, T. L.**, Han, B., Li, Z., Daisenberger, D. & Mi, J. 2014. The interdendritic-melt solidification control (IMSC) and its effects on the porosity and phase change of a Ni-based superalloy. Scripta Materialia, 74, 84-87.

6. **Lee, T.L.**, Khong, J.C., Fezzaa, K., & Mi, J. Ultrafast X-ray Imaging and Modelling of Ultrasonic Cavitations in Liquid Metal, 6th International Light Metals Technology Conference, Windsor, Materials Science Forum 765 (2013) 190-194.

Manuscripts in preparation:

1. **Lee, T.L.**, Mi, J., Ren, S.B., Fan, J.F. & Grant, P.S. Modelling and 3-D characterisation of spray formed dissimilar steels: Part 1 - Shape and thermal models and experimental validation, Acta Materialia, *To be submitted.*

2. **Lee, T.L.**, Mi, J., Ren, S.B., Fan, J.F., Zhang, S.Y., Kabra, S., Panzner, T. & Grant, P.S. Modelling and 3-D characterisation of spray formed dissimilar steels: Part 2 - Thermal stress model and validation using neutron diffraction, Acta Materialia, *To be submitted.*

3. Zheng, L., **Lee, T.L.**, Liu, N., Li, Z., Zhang, G., Mi, J. & Grant, P.S. Numerical and physical simulation of rapid microstructural evolution of gas atomised Ni superalloy powders, Acta Materialia, *Submitted*.

Conference presentations:

1. Invited by the UK Science and Technology Facilities Council as a speaker to present "**3-Dimensional Characterisation of the Microstructures and Strains of Sprayed Steel using X-ray Tomography and Neutron Diffraction**" at the UK Neutron & Muon User Meeting 2015, 19-21st May 2015, Leicestershire, UK.

2. Poster with the title "***In situ* Neutron Diffraction Study of the Deformation of Dissimilar Materials**" was presented at the UK Neutron & Muon User Meeting 2014, 10-11th April 2014, Warwick, UK.

3. Conference presentation with the title "**Ultrafast X-Ray Imaging and Modelling of Ultrasonic Cavitations in Liquid Metal**" at the 6th International Light Metals Technology Conference 2013, 24-26th July 2013, Old Windsor, UK.

4. Poster with the title "**Mapping the Strains & Stresses across the Interface between Dissimilar Metallic Alloys**" was presented at the UK Neutron & Muon User Meeting 2013, 8-9th April 2013, Warwick, UK.

Beam times awarded:

1. Proposal titled "**Mapping the evolution of strains/stresses across the interface between dissimilar metallic alloys – Phase 2**" was awarded 3 days beam time (ID: RB1510231) by ENGIN-X of Rutherford Appleton Laboratory (UK).

2. Proposal titled "**Mapping the evolution of strains/stresses across the interface between dissimilar metallic alloys**" was awarded 3 days beam time (ID: RB1320313) by ENGIN-X of Rutherford Appleton Laboratory (UK).

3. Proposal titled "**Mapping the evolution of strains/stresses across the interface between dissimilar metallic alloys**" was awarded a 1 day beam time (ID: RB1310425) by ENGIN-X of Rutherford Appleton Laboratory (UK).

Contents

CHAPTER 1 : INTRODUCTION

1.1 Background

Spray forming was invented in the late 1970s in the UK [1], and has been commercialised and licensed worldwide since then by Osprey Metal Ltd (now Sandvik Osprey). It has developed into a successful and profitable manufacturing route for the production of high value added products of special alloy systems including novel Al, Si, Cu, Fe and Ni based alloy systems (alloys that often cannot be or very difficult to be processed by conventional casting or ingot metallurgy) in the forms of round billets, rings, clad rolls, composite tubes etc.

Spray forming [2] has also been exploited extensively for the manufacture of near-net shape components of either (1) monolithic material to reduce the overall materials cost and enhance process efficiency that could not be achieved by using conventional casting, ingot metallurgy or powder metallurgy; or (2) dissimilar materials to obtain optimal combinations of mechanical and functional properties provided by the constituent materials.

A composite product of dissimilar materials is basically a bimetallic component comprising of: (1) an inner core/substrate made of a low cost carbon or low alloy steel to provide high strength/toughness, and (2) an outer thin or thick shell to be made of high alloyed steel or other alloys e.g. stainless steel or tool steel, to provide high hardness and/or high resistance to wear/corrosion/oxidisation.

The industrial applications of these bimetallic products include: (1) hot and/or cold rolling mill work rolls for steel mills, and (2) corrosion resistant reinforced carbon steel bars/tubes for large civil engineering infrastructures e.g. buildings, bridges, municipal waste incinerators, etc. The bimetallic products can offer a significant performance-cost advantage in the market. This approach depends critically upon a robust, reproducible manufacturing process suitable for mass production, as well as new know-how and intellectual property that will prevent easy adoption by competitors. Spray forming has been identified as one of the most promising techniques to achieve this, and a number of investigations into using spray forming

technology to manufacture bimetallic composite tubes and clad rolls in the UK, Japan, Europe and the US [3-8] have been carried out in the past 15-20 years as highlighted below:

- In Japan

In the late 1980s, Osprey Metals Ltd collaborated with Sumitomo Heavy Industries Ltd, Japan, to spray form high carbon, high speed tool steel (Fe-6V-2.5C) rolls for rolling mill applications [3]. Spray forming resulted in refined microstructures of spherical MC type carbides of less than 10 μm and small grain size, leading to a reduced roll wear loss and double roll service life compared with the conventionally cast products [3] .

- In the UK

In the 1990s, Osprey Metals Ltd collaborated with Sheffield Forgemasters Rolls Ltd and Sheffield University to spray form clad rolls of dissimilar materials with a "metallurgical" bond at the interface [6, 7]. A spray forming plant (Fig. 1.1) that consisted of: (1) a 500 kg steel melting furnace, (2) a 600 kW induction heater for preheating the roll arbour, and (3) a twin gas atomiser system, was used to spray form thick layers (typically 25-100 mm) of standard cold mill roll steel, hot mill roll steel and high speed steel onto a preheated low-alloy steel arbour. For arbours of 250 mm in diameter or less, with optimised deposition and arbour pre-heating conditions, high-integrity metallurgical bonds could be produced at the interface between the low-alloy steel arbour and the roll alloy [6, 7]. The spray formed clad rolls showed uniformly distributed fine carbides of ~0.13 μm and much finer microstructures that increased thermal shock resistance and reduced wear loss (3-5 times less) when compared with those made by casting and forging [6, 7]. This equipment had the ability to produce rolls of up to 400 mm in diameter and 1 m in length. However, larger diameters proved more difficult due to mechanical limitations of the plant, inefficient preheating, and poor atmosphere control, leading to oxidation and bond degradation at the interface [9].
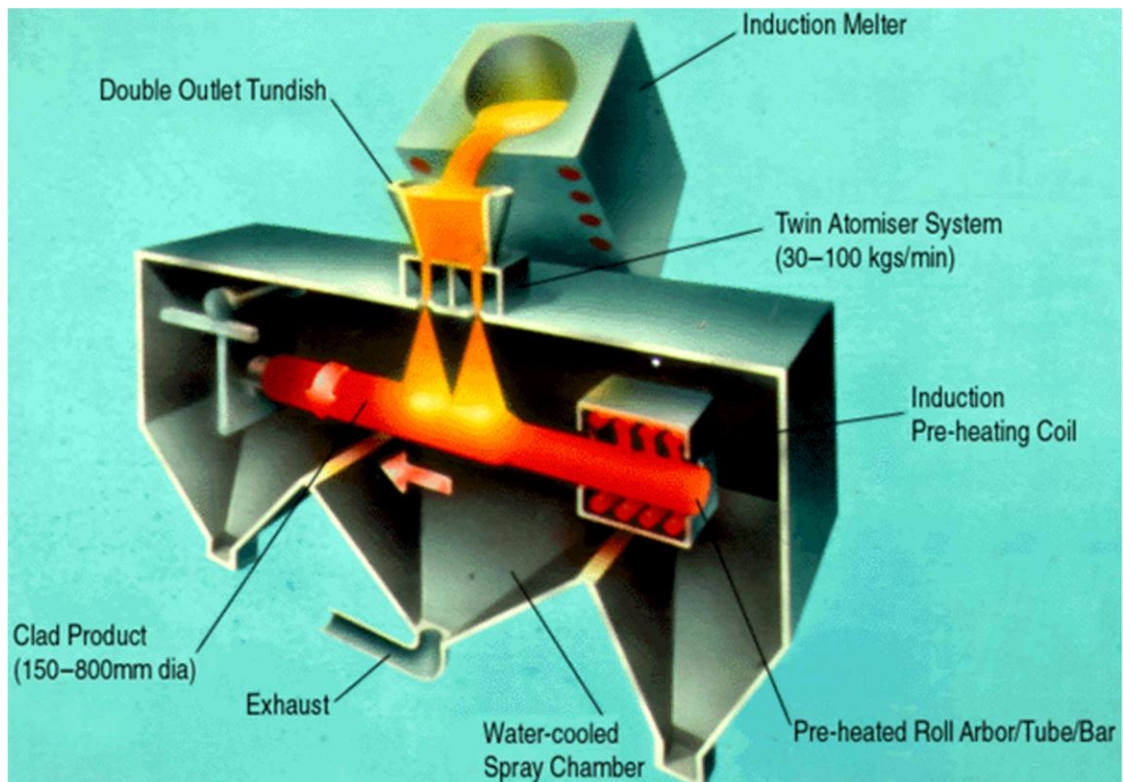
Fig. 1.1. A schematic showing the spray forming of a composite roll at Forgemasters Rolls Ltd, UK [9].

- In Europe

AB Sandvik Steel, Sweden installed a one-tonne spray forming plant in the 1990s to develop composite tubes (depositing a Ni-21%Cr-8.5%Mo-3.4%Nb-3%Fe alloy on top of a low-alloyed steel tube) for municipal waste incinerator applications [5]. A high quality metallurgical bond at the interface between the two materials was achieved by extrusion after spray forming [5]. The spray formed Ni alloy outer layer had a uniform composition and microstructure, significantly improving hot workability during extrusion and providing the high temperature corrosion resistance against flue gases. The inner C-steel tube provided the high strength, high load carrying capacity. The composite tubes had a typical life of ten years compared to two years for the monolithic low-alloy steel tubes, or refractory-protected or overlay-welded tubes [9].

▪ In the US

In 1996, a five-tonne melt capacity spray forming plant was installed at Babcock & Wilcox Nuclear Equipment Division, Barberton, Ohio, US and then moved to CMC Steel Group to manufacture: (1) bimetallic pipes for applications in boiler, incinerator and chemical plants; and (2) composite rolls for rolling mills [8]. Small scale feasibility studies showed that "metallurgical" bonding between C steel and stainless steel or IN625 could be achieved by optimised spray forming conditions [8]. Since late 2001, CMC Steel has scaled up the plant to achieve a continuous operation with a capability of 25,000 tonnes per year as shown in Fig. 1.2, to produce stainless steel clad C steel reinforced bars and other products for applications in civil constructions, such as bridges, highways, and etc. [10]. The stainless steel clad C steel reinforced products can last 70-100 years similar to the solid stainless steels but at a half price, while the C steel equivalents last only for 20 years even with careful maintenance [10]. This is the world's first plant to manufacture spray formed clad products on a commercial basis to provide the solution for the corrosion related damage to civil structures, which was estimated at a cost of $1 billion per year in the US only [10].
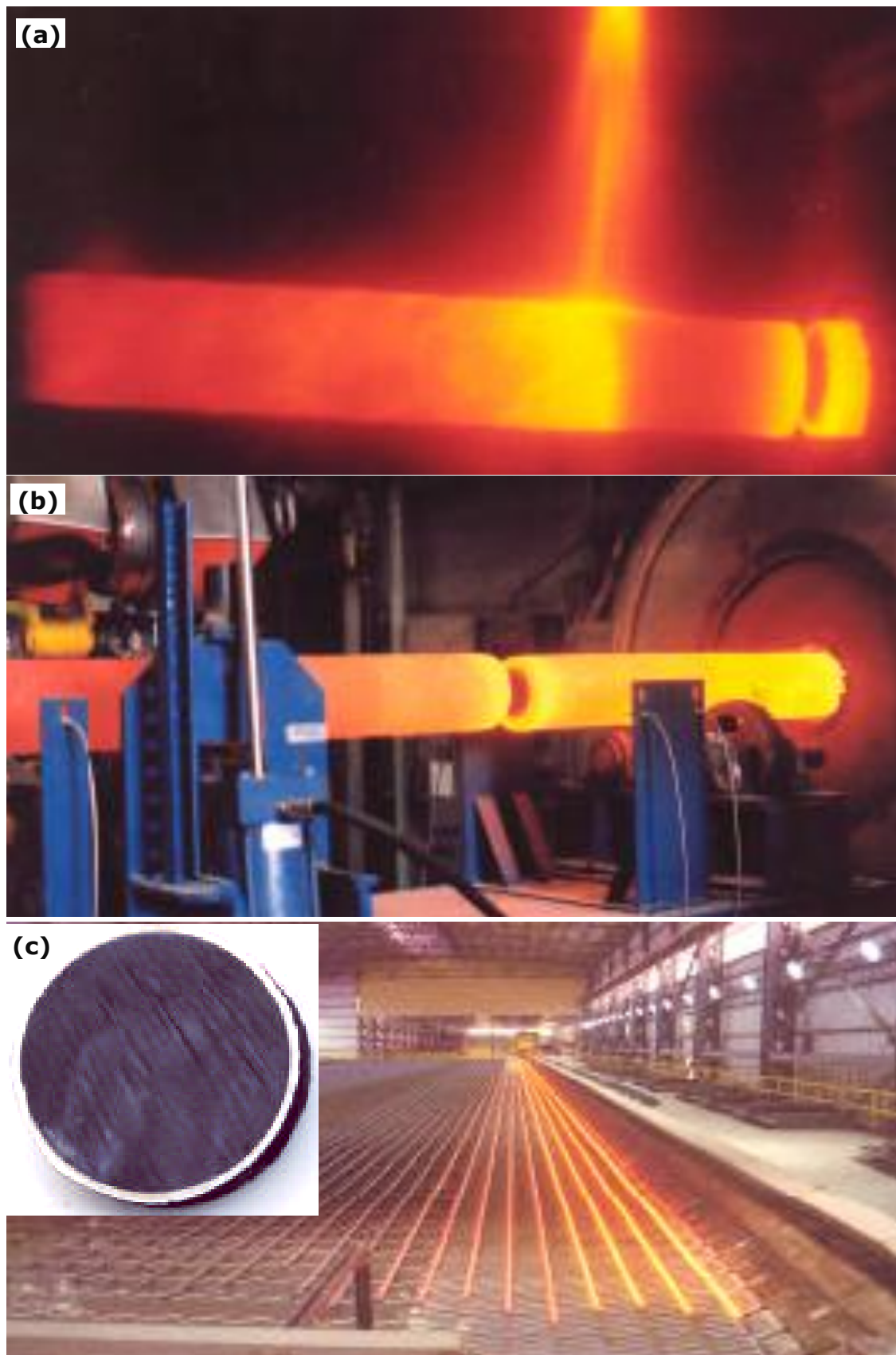
Fig. 1.2. (a-b) Spray forming of stainless steels onto C steel bars and (c) hot rolled stainless steel clad C steel reinforced bars, and an insert showing the good interfacial bonding between them [10].

1.2 The need for research

Although research and industrial development in the past 15-20 years concerning the spray forming of bimetallic products has been encouraging, these investigations have not made a sustained industrial impact. The technological reasons for this limited market penetration are suggested to be:

- Lack of basic understanding because studies have been focused on specific product development rather than generic understanding.

- Poor reproducibility of the process because of poorly instrumented equipment and again a lack of understanding on how to control the critical aspects of interfacial strength/toughness.

In order to gain a market share from the existing processing technologies e.g. casting, wrought and powder metallurgy, the underlying physics and the optimised conditions to achieve bimetallic metallurgical interfacial bonding by spray forming must be understood fully. For example, the effects of: (1) the deposition surface temperature; (2) the microscopic roughness of the substrate, and (3) the possible use of novel composition inter-layers need to be studied.

1.3 The objectives

The main research objectives are to study the fundamental physics associated with the spray forming of dissimilar materials (metallic alloys), especially the key factors in controlling the metallurgical bonding between dissimilar metal alloys, and the mechanical properties of the spray formed products.

The research tasks the author have undertaken are (1) the spray forming of dissimilar steels; (2) modelling of the key aspects of spray forming i.e. preform shape evolution, heat flow, thermal stresses and microstructural evolution; (3) microstructural characterisation and mechanical property investigations of the sprayed components.

1.4   The project and author's contribution

The project (*Development of high performance products comprising dissimilar materials by spray forming, £254 K; 01/05/2012 -30/09/2015*) is funded by the largest steel company in China, Baosteel Co. Ltd. Prof. Patrick Grant of the Department of Materials, University of Oxford is the principal investigator, and Dr. Jiawei Mi of School of Engineering, University of Hull is the co-investigator of the project. The experimental part of the research was predominantly carried out with Prof. Patrick Grant's group in the Department of Materials, University of Oxford, while the numerical modelling and X-ray and neutron characterisation of the spray formed materials were carried out in Dr. Jiawei Mi's group in the School of Engineering, University of Hull. The author was a PhD researcher in Dr. Mi's group and led the key research tasks of this project in the University of Hull and is responsible for, including participating the main spray forming experiments at University of Oxford, developing the comprehensive numerical model, leading the X-ray and neutron experiments and data analyses at ISIS Neutron Source, Diamond Light Source, and Swiss Light Source.

1.5 Thesis structure

This thesis consists of 8 chapters as described below:

Chapter 1 provides a brief introduction of the research background, project and objectives.

Chapter 2 reviews the literatures directly related to this research.

Chapter 3 describes the details of the systematic spray forming experimental study performed including the apparatus designs and experimental set-ups used, and the microstructure characterisations carried out.

Chapter 4 describes in detail the numerical modelling of the preform shape evolution, heat flow and thermal stress.

Chapter 5 presents the three-dimensional characterisations of the microstructures and residual stress distributions in the as-sprayed dissimilar metal preforms manufactured with different spray parameters and the complementary numerical modelling of the preform shape evolution, heat flow and thermal stress developed.

Chapter 6 describes a systematic study on using rapid Joule heating of atomised metallic powders to simulate the consolidation conditions during spray forming, and revealed the dynamics of the rapid dendritic-to-equiaxed microstructure transformation during spray deposition.

Chapter 7 describes the elastic and plastic deformation behaviours of the spray formed steels containing different levels of porosity and the integrity of the bonded interface of the spray formed dissimilar steels assessed *in situ* via three-point bend tests with neutron diffraction.

Chapter 8 summarises the key findings and contributions from this research. The future work that stems from this research is also described.

CHAPTER 2 : LITERATURE REVIEW

The literatures directly related to this research is critically analysed and reviewed in this chapter. The chapter is made up of 7 sections: (1) an overview of the spray forming process, (2) the melt atomisation process that generates the atomised metal droplets and spray, (3) the droplet spray dynamics detailing the droplets' behaviour in the gas flow field prior to deposition, (4) the deposition of the droplets and the associated dynamic preform shape evolution, heat flow, microstructural and residual stress development, (5) the typical residual stress measurement techniques used for sprayed components and their application in measuring the stresses in spray formed materials, (6) the underlying physics of neutron diffraction and the technique used to characterise the residual stresses and lattice strains in the as-sprayed preforms, and (7) the physics of X-ray micro-tomography and the technique used to perform 3D characterisation of the spray formed microstructures.

2.1   An overview of the spray forming process

Singer [1] pioneered the research on spray forming in the 1970s. The process was subsequently developed and first commercialised by the researchers in Singer's group [9, 11, 12] who established the company called Osprey Metals in Wales, UK. Hence, the spray forming process is also known as the Osprey process.

Spray forming is one of the thermal spray processes that combines melt atomisation and spraying deposition together, and can be used for the production of ingot preforms or near net shape products [2]. A typical schematic diagram of the spray forming process is illustrated in Fig. 2.1. In the spray forming process, molten metal from a furnace is poured into a nozzle via a tundish that directs the melt stream into the gas atomisation region where high velocity gas jets impinge onto the melt stream, disintegrating the molten metal stream into many discrete droplets, and collectively referred to as a metal spray. The metal spray is subsequently accelerated by the gas flow, projected and deposited on a substrate. Prior to deposition, the droplets experience high cooling rates (10^3 to 10^5 Ks^{-1} [13]) due to the large volume of high velocity gas used and thus a

substantial amount of heat is removed from the droplets before consolidating on the substrate surface.
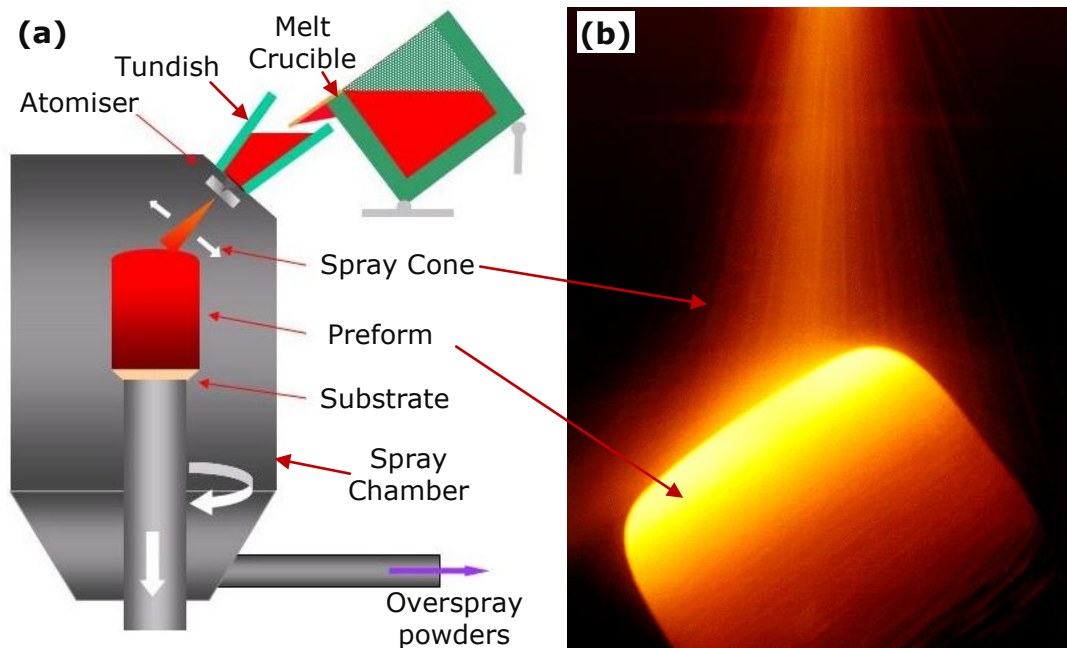
Fig. 2.1. (a) A schematic diagram [14] and (b) a photo, showing the typical spray forming process [15].

By manipulating and controlling the relative movement of the spray and substrate, products of axial symmetrical geometry can be produced, including:

(1) *Cylindrical billets* where the spray is directed towards the substrate at an angle (with optional scanning movement) and typically with an off-set distance from the central axis of the rotating substrate. During spraying, the substrate is retracted and withdrawn at a rate that maintains a constant spray distance between the preform surface and the atomiser. Twin atomisers were often used for large size preforms where higher deposition rate and better control of heat distribution in the preform during spray forming are needed [16-18].

(2) *Tubes or rings* that are produced by spraying onto cylindrical or tube substrates using a stationary or scanning spray configuration. The underlying substrate can be removed after spraying to produce a hollow tube. Clad products that consist of dissimilar alloys with metallurgical bonding at the interface can be also produced, for example high alloyed outer layer plus carbon steel inner layer composite tubes for waste

incinerators [5] and thick spray formed Ni superalloy rings for applications in aero-engines and gas turbines [9].

Since its inception, the spray forming process has sparked worldwide interest because it can produce fine equiaxed grain structures regardless of the alloy systems used when operated at the optimum conditions. This is especially the case for those heavy-alloyed materials where conventional casting methods often produce large dendritic structures with severe element segregation, for example, high speed steels (HSS) and high-chromium cast irons [19, 20]. Since the 1980s, Osprey Metals has licensed the spray forming technology to numerous universities, research institutions and companies worldwide to conduct research on spray forming of Ni superalloys [21], bulk metallic glasses [22], Cu alloys [23], Al alloys [24-28], steels or Fe alloys [29, 30], and composite materials or metal-matrix-composites [31]. At the same time, a large number of studies have focused on understanding and optimising the process through numerical modelling and establishing numerical or empirical correlations between the processing parameters, providing better understanding of the governing mechanisms in the different stages of the process, i.e. from melt atomisation to preform consolidation/solidification.

The commercial applications of spray forming technology are mainly due to the advantages of being able to produce equiaxed microstructures and the integrated melt atomisation and spray deposition process for large volume metal production. The high metal flow rates (up to ~55 kg min^{-1}) used in the spray forming process offer production times that are comparable to conventional metal casting methods [32], capable of manufacturing relatively large tool steel billets (2.4 m long $\times$ 400 mm diameter) in 50 minutes [9]. Fig. 2.2 shows the microstructures of tool steels manufactured by conventional ingot casting and spray forming. There is high degree of segregation in the conventionally cast materials in comparison to the relatively homogeneous microstructure in spray formed materials, especially for high alloyed materials. Manufacturing highly alloyed materials through conventional casting methods remains problematic as the high concentration of the alloying elements and the relatively slow cooling rate

give rise to severe macro-segregation and the formation of coarse eutectic carbide structures that leads to poor mechanical properties [19].
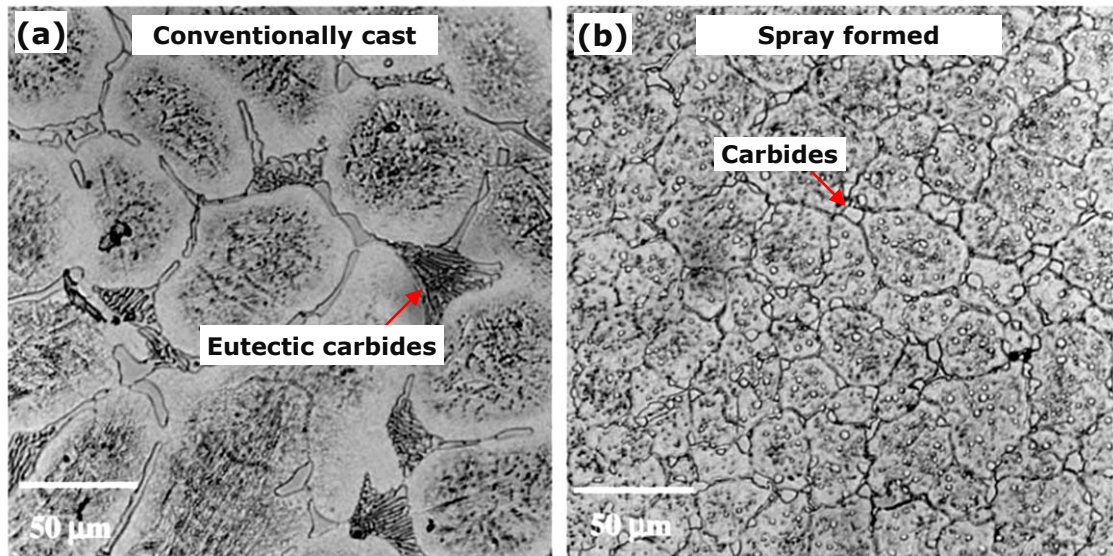
Fig. 2.2. Microstructures of tool steels manufactured by (a) conventional casting method and (b) spray forming showing the difference in segregation levels [33].
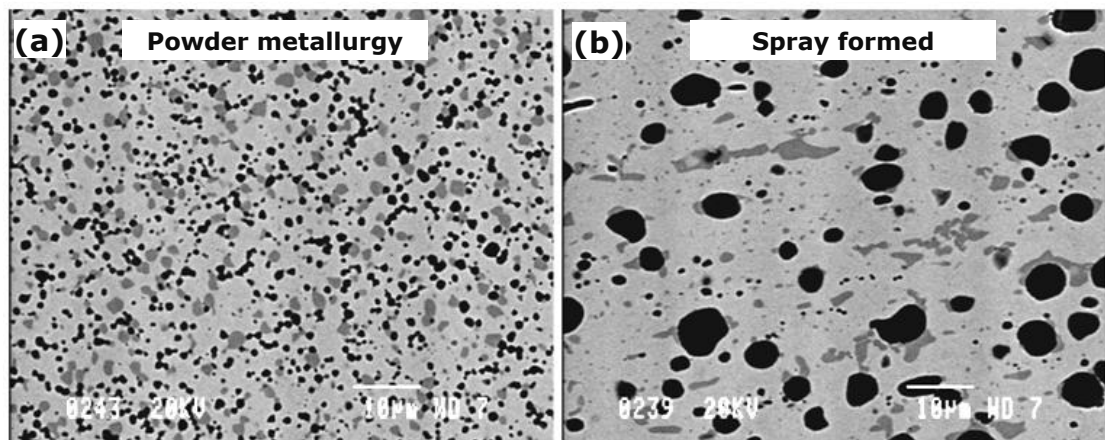
Fig. 2.3. Microstructures of high alloy steels manufactured by (a) powder metallurgy and (b) spray forming [32].

Powder Metallurgy	Electroslag Remelting	Spray Forming
Melting	Melting of Electrodes	Melting
Atomisation	Preparation of Electrodes	Spraying
Classification (grain size)	Remelting	Hot Forging, Rolling
Mixing	Diffusion Annealing	Heat Treatment
Capsulation	Hot Forging, Rolling	Grinding
Cold Isotatic Pressing	Heat Treatment	
Hot Isotatic Pressing	Grinding	
Hot Forging, Rolling		
De-capsulation		
Milling		
Heat Treatment		
Grinding		

Fig. 2.4. Comparison of the typical processing steps and manufacturing cycles between powder metallurgy, electroslag remelting (conventional ingot casting method) and spray forming [32].

Powder metallurgy (PM) provides a solution to the segregation problem by atomising the highly alloyed metal into tiny droplets that are subjected to solidification rates several orders of magnitude higher than conventional casting methods, resulting in fine and homogeneous microstructures [34] PM alloys can contain highly alloyed elements to significantly enhance material properties [35-37]. However, hot isostatic pressing (HIP) is typically required to consolidate the powders, which significantly increase production times and costs with a premium over conventionally produced alloys of up to 50%, and thus, PM products constitute only a small portion of the metal market [19, 37, 38].

Spray forming offers the advantages of comparable refined and macro-segregation free microstructures (Fig. 2.3) while reducing processing steps in comparison to the PM approach (Fig. 2.4). High alloy steel rolls produced by spray forming were reported to offer service lives up to 3 times longer than conventionally cast rolls [39]. Nevertheless, the typical problem of the spray formed products is the porosity in the as-sprayed preforms [40-42] and the relatively low production yields (typically 60~70% for a single atomiser system [19]).

Extensive research and developments have been made to optimise the spray forming process and enhance its economical advantage on producing ingots or shaped products with special alloys that cannot be made by conventional casting. Some of the commercially successful cases of novel alloy systems developed to exploit the unique solidification advantage of spray forming process are:

- Fe-6%Cr-3%Mo-6%V tool steels at Dan Spray A/S, Denmark

Dan Spray has developed a series of high speed steels and tool steels (typical composition: Fe-1.4~2.8%C-1.0%Si-4.5~7.0%Cr-2.3~3.2%Mo-3.7~9.0%V) using spray forming technology [32, 43]. The spray formed tool steels have a uniform microstructure and refined carbides of less than 10 μm, and the alloy composition can be tailored in a wide range to achieve a good combination of high strength, toughness and wear resistance. The spray formed tool steels consists of carbide content of up to 28% (hardness

of ~70 HRC) were used as crush cutting die in plastic component manufacturing with increased service life time of more than 100% compared to conventionally produced tool steel die [32].

Dan Spray uses a twin-atomiser spray forming plant linked to a four-tonne melt furnace, and can produce steel billets of up to 0.5 m (diameter) x 2.5 m (long) as shown in Fig. 2.5, with an annual production capacity of 6000 tonnes. Dan Spray is currently collaborating closely with Edelstahl Witten-Krefeld GmbH, Germany and Uddeholm Tooling AB, Denmark to develop a series of novel tool steels for applications in extremely demanding conditions.
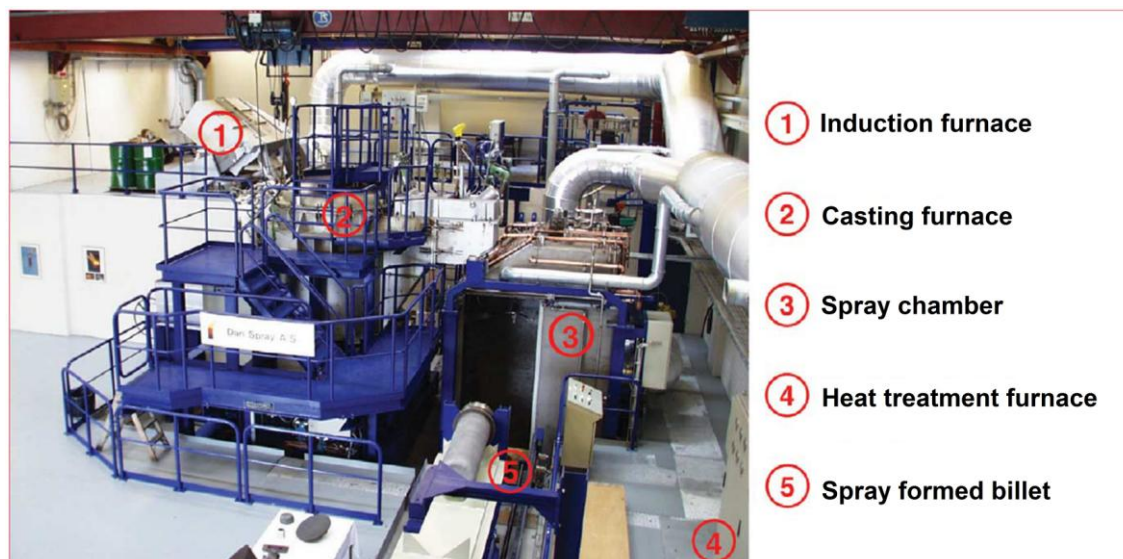
Fig. 2.5. Spray forming plant at Dan Spray A/S, Denmark.

- Al-25%Si alloy cylinder liner at PEAK Werkstoff GmbH, Germany

PEAK developed a range of alloys based on Al-25-30%Si alloys that were used as cylinder liners in engine blocks of many Mercedes (Daimler Chrysler) car engines in the automotive industry (Fig. 2.6a). These alloys typically contain 20-30wt%Si, and can only be manufactured by spray forming on a large industrial scale with the required uniform and refined microstructure (Fig. 2.6b). These materials offer excellent wear resistance, low thermal expansion and high thermal conductivity that helped to improve the engine fuel and power efficiency [9, 44]. PEAK now has three plants producing billets at a production scale of more than 3500 tonnes per year [9].
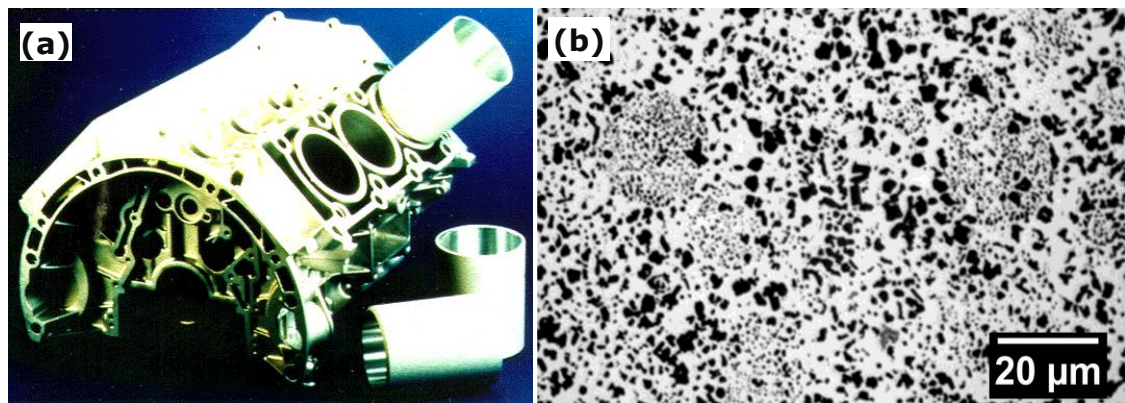
Fig. 2.6. (a) A car engine cylinder block and Al-25%Si cylinder liners produced by PEAK, Germany [9] and (b) the typical microstructure of spray formed Al-25%Si [45].

Nevertheless, the difficulty in spray forming dissimilar metal preforms lies in the formation of a high integrity bonding at the deposit-substrate interface. All past research in this aspect pointed out that the interfacial bonding strength between the sprayed dissimilar alloys is a critical parameter in determining the integrity, properties and functionalities of the sprayed components and the temperature of the depositing droplets and that of the layer below are the dominant factor in controlling the interfacial bonding behaviours [4, 7]. Droplet splats, trapped gas bubbles and excessive porosity are the common defects often found at the interface when non-optimal spray conditions are used [40], resulting in a weak bond across the interface. So far, spray forming of thick dissimilar metallic alloys to utilise the combined properties with high integrity metallurgical bonding across the interface remains a persisting and significant technical challenge.

The key concepts, experimental and characterisation methodologies, and numerical models concerning spray forming are described and reviewed in the following sections to provide the scientific and technological background for this research.

2.2   Melt atomisation

Atomisation is the process of disintegrating a bulk liquid into a collection of small droplets, which can be used for a wide range of materials from aqueous water solution (low temperature and surface tension) to molten metal (high temperature and surface tension).

Metal melt can be atomised using water, oil and gases [46]. In water and oil atomisation, the atomising fluid is generally accelerated using a fluid injector and released as discrete jets. Water atomisation involves the momentum transfer from the accelerated water droplets to the metal melt stream which is disintegrated under impact. Water atomised metal droplets are generally irregular in shape as compared to droplets produced from gas atomisation as the cooling rate is about one to two orders of magnitude higher than that of gas atomisation [46]. Oil atomisation is also generally used for high volume production of metallic powders where irregular particle shapes are acceptable [46].

In spray forming, the metal droplets are created mainly through gas atomisation in which high velocity inert gas jets are used to disrupt the molten metal stream. The atomising gas is accelerated to high velocity through expansion from the high pressure atomising gas plenum into the low pressure spray chamber. The kinetic energy transfer from the high velocity atomising gas to the relatively lower velocity liquid metal flow causes the flow to disintegrate into discrete droplets. Inert gas such as N_2 and Ar are often used to minimise the oxidation of the atomised metal. Gas velocity, flow rate and pressure are the most important parameters for gas atomisation.

2.2.1 Atomiser configuration

In a typical spray forming set-up, the melt flows vertically from a tundish via a nozzle under the effect of gravity and the atomising gas is directed onto the melt stream through a slit or discrete gas nozzles surrounding the melt flow. Depending on the gas nozzle design, the atomising gas can flow parallel or at an inclined angle to the melt stream. The two main atomiser configurations commonly used for metal melt atomisation are the close-coupled and the free-fall atomisers as illustrated in Fig. 2.7a and Fig. 2.7b, respectively.

(a) Close-coupled atomiser   **(b) Free-fall atomiser**
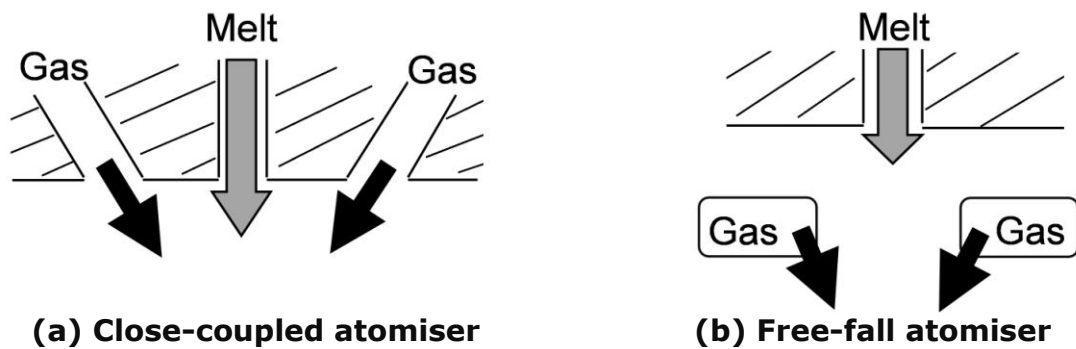
Fig. 2.7. Schematics of the (a) close-coupled and (b) free-fall atomiser configurations [47].

In the close-coupled atomiser configuration, the metal melt stream travels a short distance before it is disintegrated by the gas flow near to the nozzle. Therefore, this atomiser configuration offers higher atomisation efficiencies compared to the free-fall atomiser, and is often used for producing fine powders due to the efficient kinetic energy transfer from the gas flow onto the melt flow. However, the close-coupled atomiser setup is sensitive to melt flow freeze-up because of the significant cooling of the melt by the atomising gas flow near to the nozzle [48]. The problem usually occurs in the initial stage of the atomisation process when the melt nozzle is relatively cold and requires time to be heated up. Therefore, superheating of the melt before pouring into the tundish is typically performed. The close-coupled atomiser set-up is also subjected to pressure variations near to the nozzle that can generate either negative or positive pressures, resulting in an increased melt flow rate or blocked melt flow from the tundish, respectively [46].

The free-fall atomiser set-up generally is not subjected to melt freeze-up problems at the nozzle since the atomising gas flows into the spray chamber at a larger distance away from the nozzle. However, the increased distance between the atomising gas inlet and the melt flow causes lower atomisation efficiencies compared to the close-coupled atomiser set-up as the gas velocity is decreased significantly before impingement. Nevertheless, one of the key advantages of a free-fall atomiser is that it provides an extra degree of freedom to mechanically oscillate or scan the spray generated to spread the droplet mass over larger areas [49].

2.2.2 Gas flow field near melt nozzle outlet

It has become a standard industrial practice to use the free-fall atomiser configuration as it can be scaled up (more than one atomiser) to manufacture preforms in large volumes and offer better heat distribution control [18], hence, the characteristics of the gas flow field generated from this particular set-up near the melt nozzle and its effects on the spray is reviewed here.

At the atomiser gas inlet, the gas velocity is the highest and decreases at increasing distances along the spray axis due to the momentum transfer to the melt flow. The gas velocity profile along the spray axis from the atomisers were experimentally measured in previous studies [50, 51] and have been used typically in atomisation models [52-54]. The atomiser gas velocity (v_{gas}) profiles were shown to be approximated to an exponential profile [13],

$$v_{gas} = v_{gas0} \exp \left(-\frac{d_{gas}}{\lambda_{gas}} \right) \tag{2.1}$$

$$\lambda_{gas} = a_{gas} \, v_{gas0}^{n_{gas}} \tag{2.2}$$

where v_{gas0} is the initial gas velocity, d_{gas} is the axial distance from atomisation point, a_{gas} and n_{gas} are the experimental constants.

In a conventional free-fall atomiser, the angle of inclination of the atomiser gas jets and the open configuration of the atomiser may generate recirculating gas flow regions [49]. These recirculating regions in the atomiser can cause atomised metal droplets to be transported against the gas flow direction and point towards the tundish exit nozzle, resulting in a back-splashing phenomenon as shown in Fig. 2.8a. The back-splashed metal droplets may disrupt or completely block the melt flow. The key parameters that affect the recirculating gas in the vicinity of the atomiser nozzle were investigated via numerical modelling and experimental study with and without primary atomiser gas flow, while the secondary atomiser gas pressure was kept constant [55]. In the set-up without primary atomiser gas flow (Fig. 2.8a), a recirculating gas region was formed in gas

flow field near to the tundish nozzle outlet (marked as solid line in the vector plot) and can be observed from experiment with droplets back-splashed above the atomisation point. The recirculating gas region was suppressed when primary atomiser gas flow was used (Fig. 2.8b).

Primary atomiser gas nozzle exits

Secondary atomiser gas nozzle exit

Recirculating gas region

Back-splashing

Simulation   Experiment

(a) Without primary atomiser gas flow

Primary atomiser gas nozzle exits

Secondary atomiser gas nozzle exit

Simulation   Experiment

(b) With primary atomiser gas flow
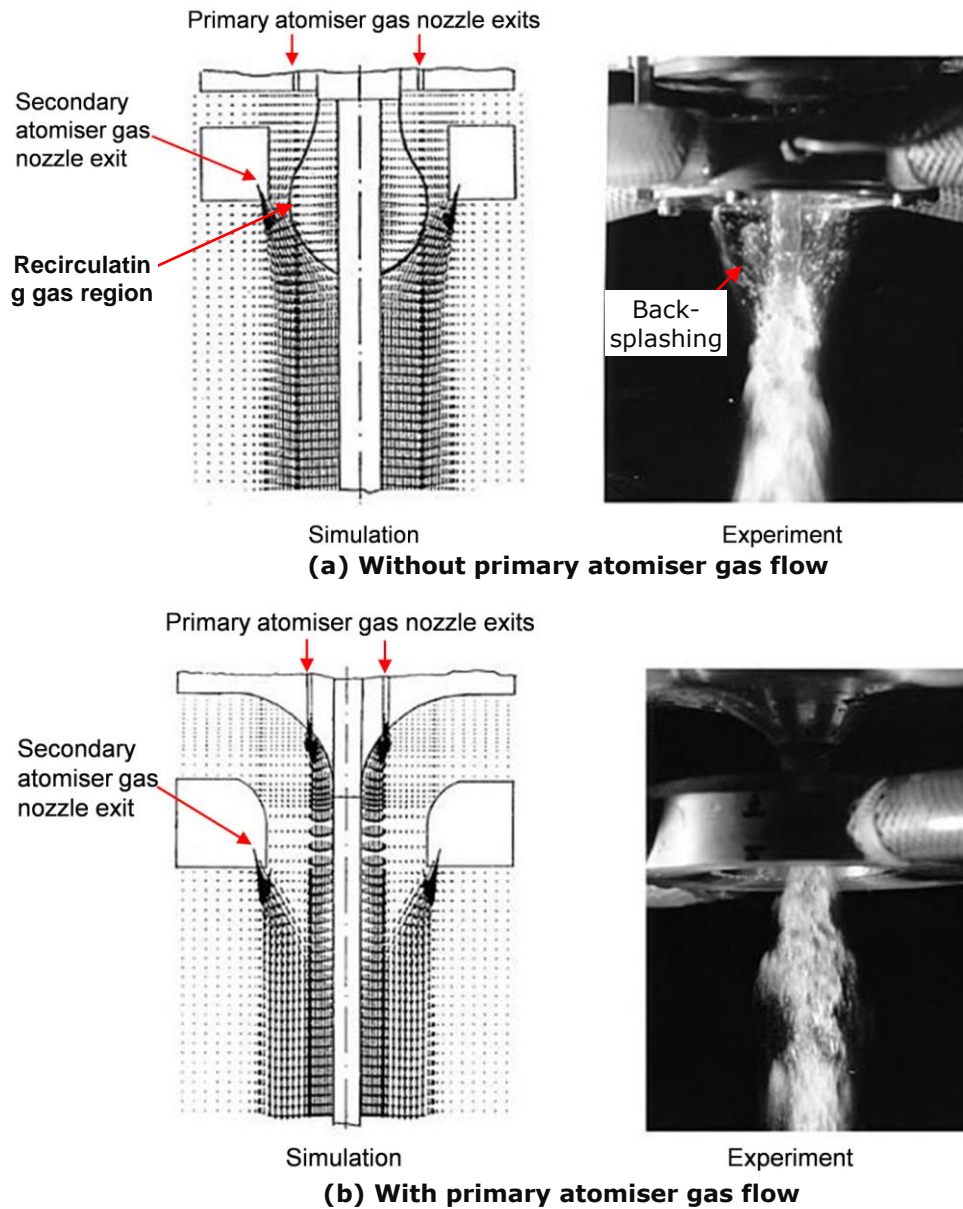
Fig. 2.8. The numerical simulation and experimental study of the gas flow field near to the melt nozzle outlet (a) with and (b) without primary atomiser gas flow [55].

Growing waves

Disintegration into ligaments

Ligaments break-up into droplets
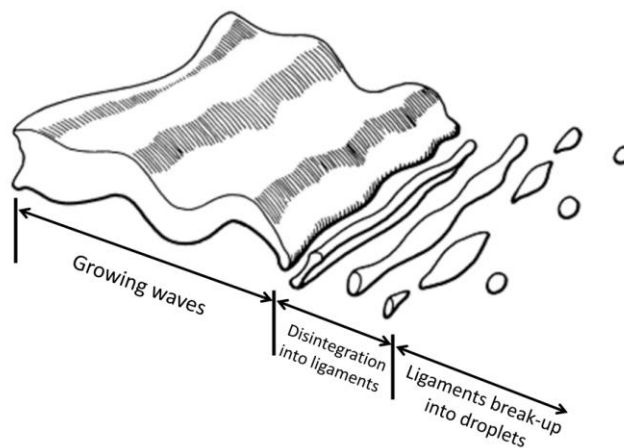
Fig. 2.9. Aerodynamic disintegration model of a plane liquid jet [56].

2.2.3 Atomised droplet size distribution

The relative velocity between the liquid and the atomising gas significantly affects the melt disintegration in the gas atomisation process as reported by a recent study on the breakup mechanism of coaxial air-assisted water jet under ultrafast synchrotron X-ray phase-contrast imaging which concluded that the breakup is strongly dependent on the competition between the aerodynamic forces and liquid surface tension [57]. The correlation for the resulting droplet size distribution from the breakup of a liquid flow was established using an aerodynamic disintegration model of a plane liquid jet emerging from a planar slit nozzle as illustrated in Fig. 2.9 [56]. The model shows that ligaments were separated from the jet with growing instability along the longitudinal direction which subsequently deformed into cylindrical ligaments. Due to capillary instabilities, the ligaments disintegrate into fragments which eventually form the droplet structures due to surface tension effects.

Under typical spray forming conditions, the droplet size distribution for gas atomised alloys was reported to follow a lognormal distribution [58-60],

$$P(d_d) = \frac{1}{\sigma_{std}\sqrt{2\pi}} \exp\left[-\frac{(\ln d_d - \ln d_m)^2}{2\,(\sigma_{std})^2}\right] \qquad (2.3)$$

where $P(d_d)$ is the probability density function, d_d is the droplet diameter, σ_{std} is the standard deviation and d_m is the mean droplet diameter.

The correlation of mean droplet diameter for metal atomisation takes into account the spray processing conditions was expressed as [59],

$$d_m = d_l\,K_{Lub} \left[\frac{v_l}{v_g}\,\frac{1}{We}\left(1 + \frac{\dot{m}_l}{\dot{m}_g}\right)\right]^{0.5} \qquad (2.4)$$

$$We = \frac{\rho_l\,v_{gas0}^2\,d_l}{\sigma_{ST}} \qquad (2.5)$$

where $\frac{v_l}{v_g}$ and $\frac{\dot{m}_l}{\dot{m}_g}$ is the melt-to-gas viscosity ratio and inverse of gas-to-melt flow rate ratio (GMR), respectively, d_l is the melt nozzle diameter, K_{Lub} is the atomiser-dependent empirical constant, ρ_l is the melt density, v_{gas0} is the maximum melt velocity, and σ_{ST} is the melt surface tension. The typical

lognormal droplet size distribution of carbon steel atomised using N_2 is shown in Fig. 2.10.
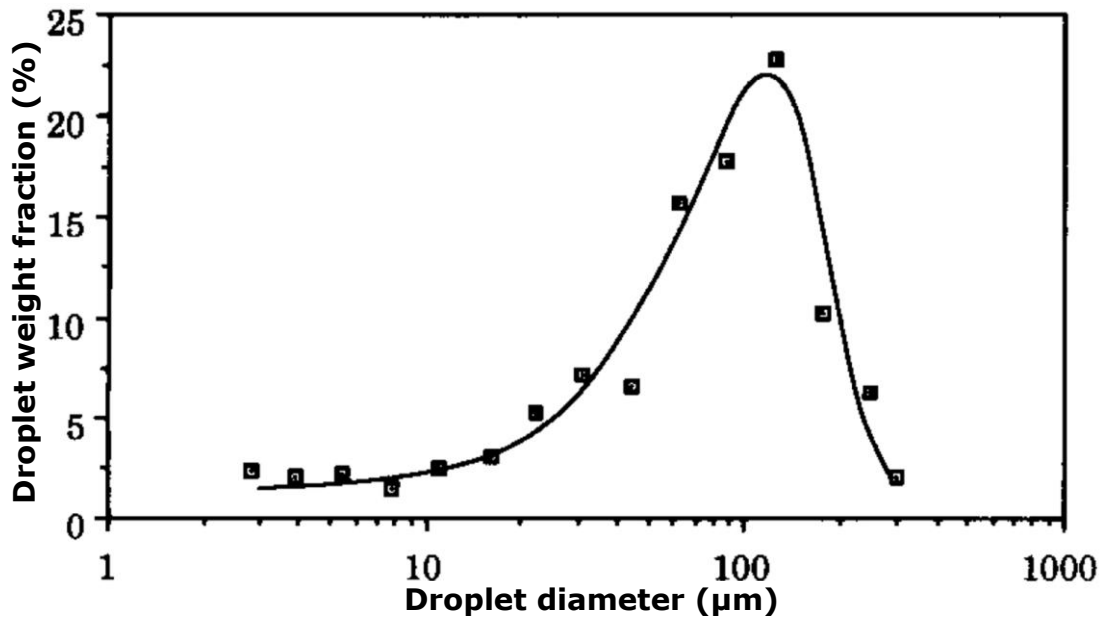
Fig. 2.10. The typical log-normal droplet-size distribution of atomised carbon steel using N_2 at a spray distance of 350 mm with average droplet diameter of ~100 µm [61].

2.3   Droplet spray dynamics

The dynamic thermal and kinetic evolutions of the droplet spray prior to deposition are of direct influence on the preform growth and solidification behaviours in spray forming. Numerous numerical modelling and experimental studies of the spray dynamics were conducted [13, 47, 62-65] and there is on-going research to study droplet kinetics at much smaller length scales (nanometer droplets) that are used in inkjet printing to manufacturing high-resolution conductive metallic lines [66]. The findings from these studies relevant to this research are described in this section.

2.3.1 Droplet kinetic evolution

At the point of atomisation, the droplets are accelerated under the action of drag force exerted by the higher velocity atomiser gas jets and the drag force (F_{drag}) can be expressed as [67],

$$F_{drag} = c_{drag} \, \pi \left(\frac{d_d}{2}\right)^2 \rho_{gas} \left(v_{gas} - v_d\right)^2 \qquad (2.6)$$

where c_{drag} is the drag coefficient, ρ_{gas} is the density of the atomiser gas and v_d is the droplet velocity. The drag coefficient is dependent on the droplet Reynolds number (Re_d) and can be approximated by [68],

$$c_{drag} = 0.28 + \frac{6\sqrt{Re_d} + 21}{Re_d} \tag{2.7}$$

$$Re_d = \frac{\rho_{gas}\left(v_{gas} - v_d\right)d_d}{\mu_{gas}} \tag{2.8}$$

where μ_{gas} is the gas viscosity. The simulated droplet velocities and droplet flight times along the spray axis with respect to different atomised droplet diameters with $v_{gas0} = 150$ m s^{-1} are shown in Fig. 2.11a and Fig. 2.11b, respectively. Due to the relatively lower inertia in smaller droplets, they accelerate faster and are relatively more sensitive to the changes in gas velocity along the spray axis. Therefore, the smaller droplets in a typical spray travel faster at distances near to the atomisation point but gradually slow down at increasing distances.

2.3.2 Droplet thermal evolution

Grant *et al.* [13] and Bergmann *et al.* [69] developed numerical models to calculate the thermal history of droplets with different sizes along the spray axis and showed that the droplet cooling and solidification behaviours were significantly influenced by the droplet size, and that maximum heat transfer occurred near to the atomisation point with higher heat transfer coefficients for smaller droplets. Therefore, the smaller droplets with lower enthalpy in a typical spray cools more rapidly and are generally solidified at relatively short distances from the atomisation point (Fig. 2.12).
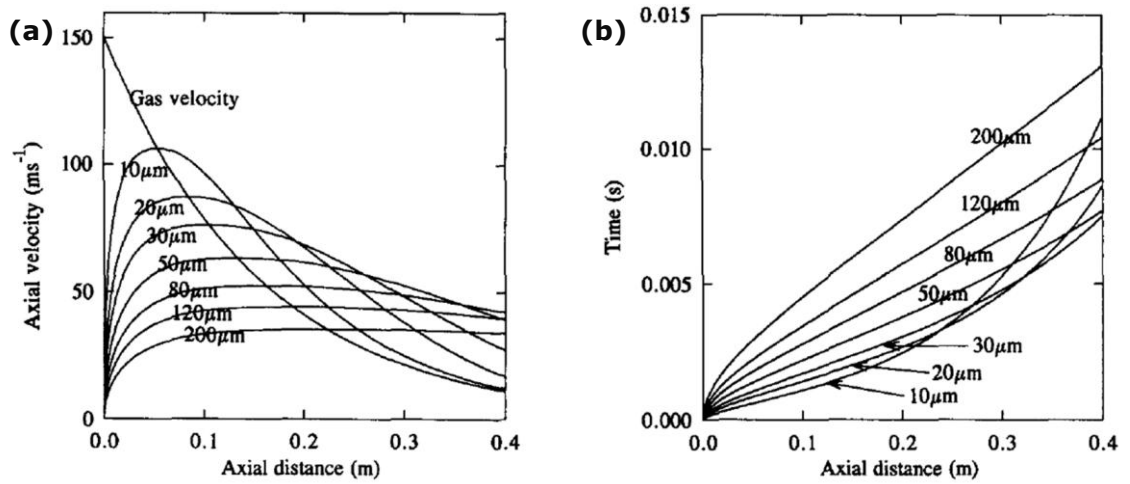
Fig. 2.11. The (a) droplet velocities and (b) droplet flight times along the spray axis with respect to different Al alloy droplet diameters atomised using N_2 and an initial gas velocity of 150 m s^{-1} [13].
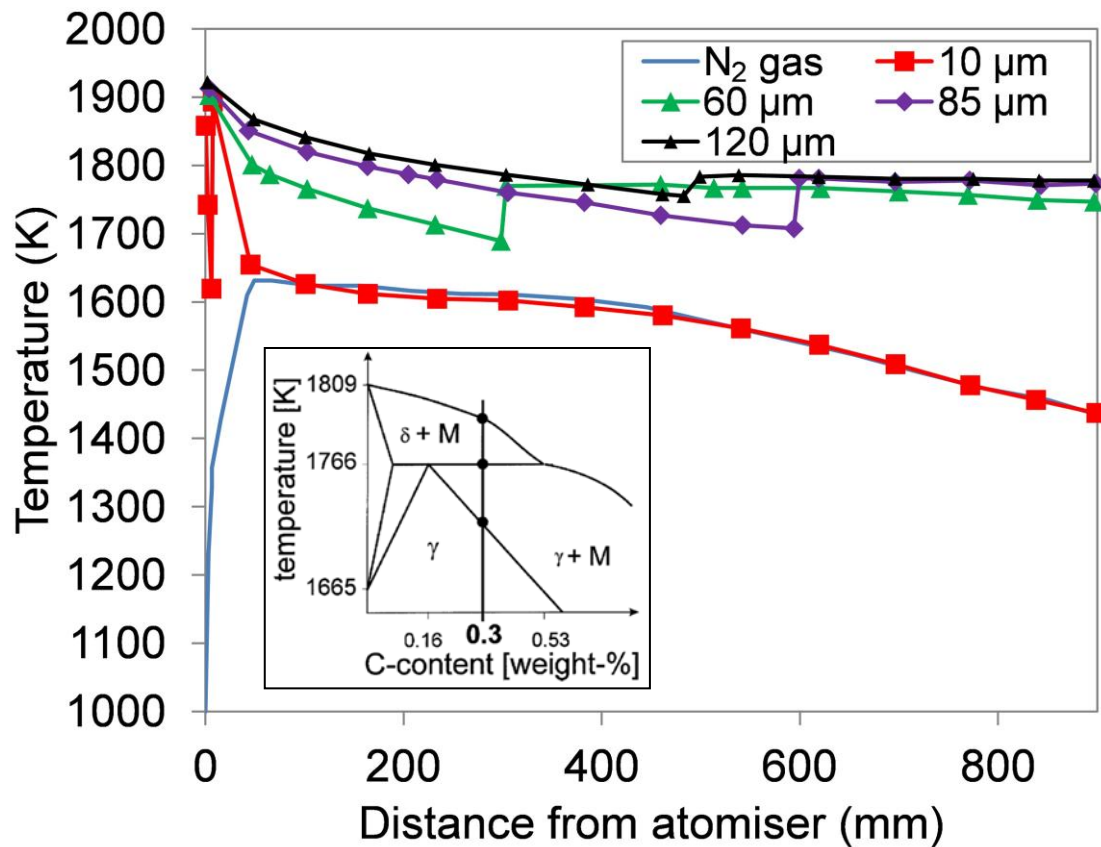
Fig. 2.12. The carbon steel droplets thermal history along the spray axis with respect to the different droplet sizes atomised using N_2 and a gas-to-melt flow ratio of 1.5 [69]. The phase diagram of the carbon steel atomised is shown in the figure inset.

Nevertheless, the collective solidification behaviour of the droplets with different sizes in the spray can be described by integrating the individual droplet solidification behaviours over the typical droplet size distribution [62]. The average solid fraction of the spray (f_s^{avg}) along the spray axis can be determined by averaging the individual droplet solid fractions, $f_S(d_d)$ and can be expressed as,

$$f_s^{avg} = \int_0^\infty P(d_d)\, f_S(d_d)\, \Delta \ln d_d \qquad (2.9)$$

The average enthalpy of the spray can be determined by averaging the individual droplet enthalpy per unit mass, $H(d_d)$ which can be calculated by:

$$H(d_d) = L_f\, [1 - f_S(d_d)] + C\, [T(d_d) - T_E] \qquad (2.10)$$

where L_f is the latent heat of fusion, C is the specific heat capacity, $T(d_d)$ is the droplet temperature and T_E is the alloy eutectic temperature. The average spray enthalpy (H_S^{avg}) can then be expressed as,

$$H_S^{avg} = \int_0^\infty P(d_d)\, H(d_d)\, \Delta \ln d_d \qquad (2.11)$$

2.4 Preform consolidation dynamics

2.4.1 Preform shape evolution

The preform growth due to the impinging droplets from the spray has been typically shown to follow a Gaussian shaped distribution due to the distribution of droplet mass in the spray [54, 63, 70-74]. Fig. 2.13a shows that the droplet mass flux distribution widens at increasing distances from the atomisation point along the spray axis due to the droplet kinetic dynamics in the spray under the action of the atomiser gas flow field as described previously. The typical simulated shape evolution of a tubular preform and the as-sprayed tube preform is shown in Fig. 2.13b and Fig. 2.13c, respectively [72].

During spraying, certain parts of the preform surface may be "hidden" from the spray cone (Fig. 2.14) due to the substrate movement and thus, the mass from the spray do not deposit on these surfaces throughout the

hidden duration. In order to consider the "visibility" of the preform surface to the impinging mass from the spray cone, several types of visibility algorithms were used by previous preform shape evolution numerical models. The two commonly used visibility algorithms were back face culling and the Z-buffer algorithm [16, 75, 76]. Back face culling conducts the evaluation if the deposition surface normal is pointing towards the direction of the incoming spray and removes any surface if they are invisible from the viewpoint which can be calculated using,

$$\vec{n} \times \vec{v} \geq 0 \tag{2.12}$$

where $\vec{n}$ is the deposition surface normal vector and $\vec{v}$ is the incoming spray vector. The algorithm is suitable for simple convex shaped geometries but is unable to conduct a full visibility evaluation for concave surfaces. The Z-buffer algorithm performs full visibility evaluations and is typically used for complex preform shapes. The algorithm is generally available in computer graphics software packages such as OpenGL [77].

The droplet deposition on the preform surface that contributes to the preform growth is termed as droplet primary deposition. However, there may be a fraction of the droplets that do not retain on the deposition surface as there is a possibility that these droplets that typically impinge at velocities of 50 - 100 m s^{-1} would bounce-off from the point of impact depending on spray conditions [78, 79]. These droplets may re-deposit onto parts of the preform surface that are within the scattering direction where re-deposition occurs and the droplets that do not land on the deposition surface or scattered away without re-deposition are referred to as overspray [80-82]. The amount of overspray also increases with increasing distance between the substrate and atomisation point since the spray cone coverage area is wider than the substrate as one could envisage from the schematic shown in Fig. 2.14.
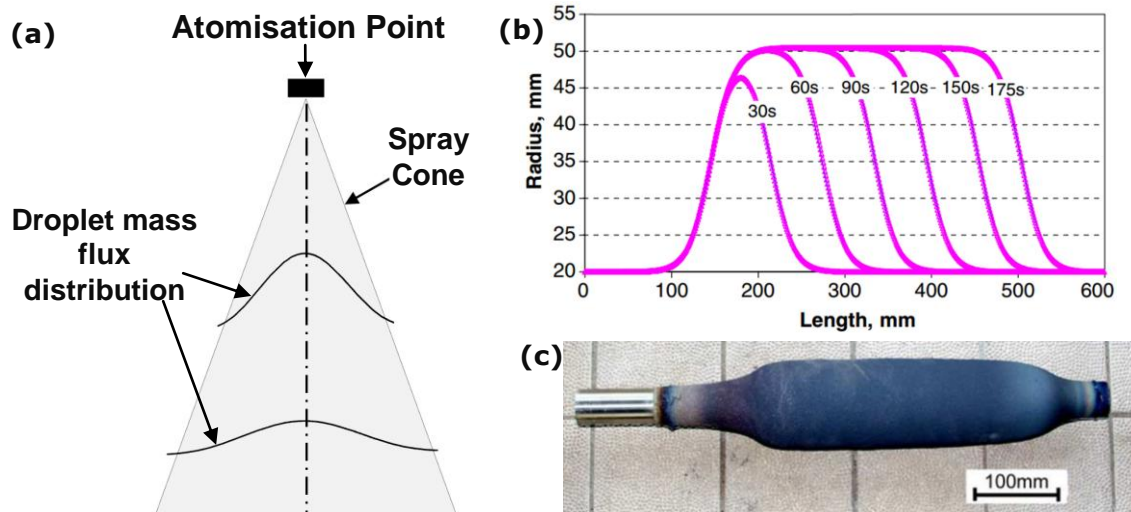
Fig. 2.13. (a) A schematic of the Gaussian droplet mass flux distributions along the spray axis at different distances away from the atomisation point, (b) the typical simulated shape evolution of a tubular preform and (c) the typical spray formed alloy steel tube preform [72].
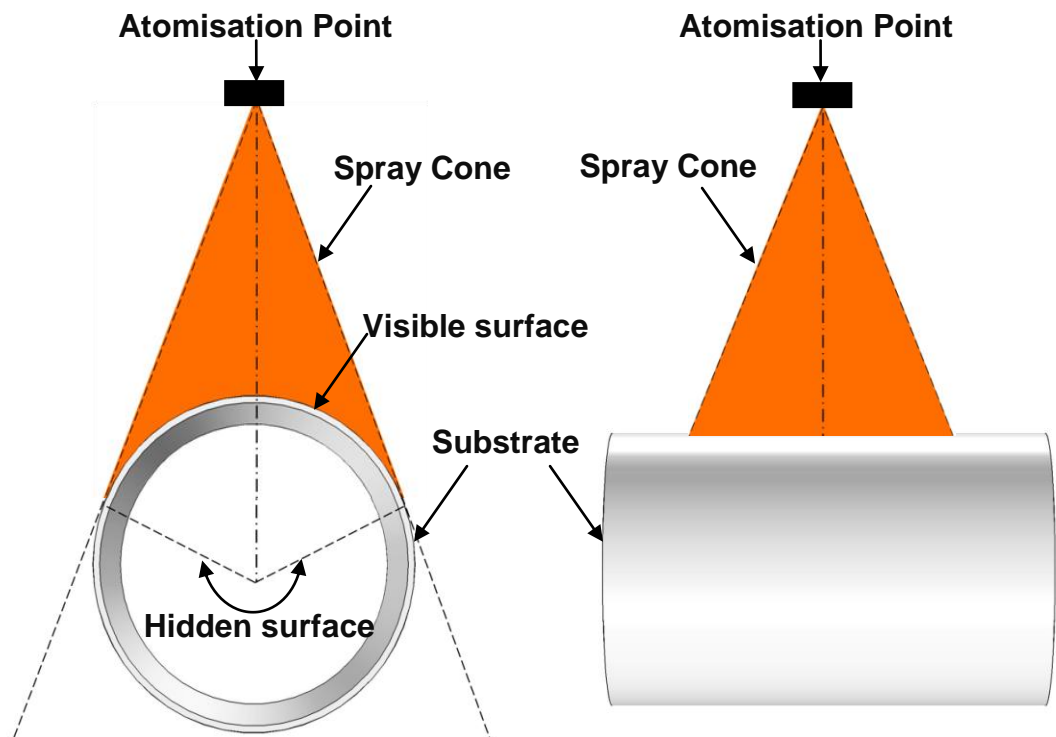
Fig. 2.14. A schematic of the typical spray forming of a tubular preform set-up showing the hidden and visible deposition surfaces with respect to the spray cone direction.

28

The thermal state of the droplet in the spray is also one of the key parameters that affect droplet deposition on the preform surface. Mathur *et al.* [83] studied the deposition conditions based on different depositing droplet and preform surface thermal states (Fig. 2.15) and established that only a portion of the droplets from the spray sticks to the preform surface during spraying, and the ratio of the deposited mass at the point of impact over the total impinging mass was termed as the sticking efficiency (SE) which governs the spray yield and preform shape. The SE was proposed to be dependent on the geometrical and thermal conditions between the deposition surface and the impinging droplets, and was expressed as [83],

$$SE = SE(\theta) \cdot SE(T) \tag{2.13}$$

where $SE(\theta)$ is the geometric component that depends on the angle of incidence between the impinging droplets and the deposition surface normal (θ_{SE}) and $SE(T)$ is the thermal component which is dependent on the liquid fractions (f_L) of the depositing droplets and the preform surface. The $SE(\theta)$ was expressed in the form of,

$$SE(\theta) = G_{max} \cdot \cos \theta_{SE} \tag{2.14}$$

where G_{max} is an experimentally determined constant [84]. Thus, $SE(\theta)$ increases from θ_{SE} = 90° (deposition surface is parallel to the spray direction) to a maximum when θ_{SE} = 0° (deposition surface perpendicular to spray direction). An empirical correlation of the $SE(T)$ was proposed by Mathur *et al.* [83] based on experimental measurements,

$$SE(T) = \left[\, f_S^{avg}\eta_S \;+\; (1\text{-}f_S^{avg})\eta_L \,\right] \times \varepsilon_{SE} \tag{2.15}$$

$$\eta_S \;\approx\; 1 - 0.75(\, 1 - f_L \,) \tag{2.16}$$

$$\eta_L \;\approx\; 0.98 \tag{2.17}$$

where η_S and η_L are the sticking coefficients of the solid and liquid from the droplet spray respectively, and ε_{SE} varies from 0 to 1 in correspondence to the viscosity variation based on f_L as described in [85].

	S	M	L
L	Surface **ejected** due to low viscosity	Surface **ejected** due to low viscosity	Surface **ejected** due to low viscosity
M	Partial **bounce-off** of the solid particles	**Good sticking**	
S	Total **bounce-off** of the solid particles	**Partial sticking**	**Layered structure**

Preform surface thermal state (vertical axis)

Impinging droplet thermal state

Fig. 2.15. A qualitative description of the deposition conditions based on the preform surface and impinging droplet state (S = solid, M = mushy and L = liquid) [83].

2.4.2 Preform heat flow

The mass deposited on the preform surface during spraying induces heat into the preform and the preform thermal history depends greatly on the droplet spray temperature which is in turn governed by the spray processing parameters. The dynamic temperature changes within the preform and heat transfer with the gas flow field in the spray chamber directly influence the microstructure and material properties of the sprayed component [40, 86-88]. However, acquiring accurate temperature information within the entire preform is a technical challenge due to the dynamic spray conditions and preform shape evolution, and thus, only the temperatures from certain points of the preform can be obtained [89]. Previous studies have typically measured the preform surface temperatures using pyrometers and/or by inserting thermocouples into the growing preform [90, 91] while the temperatures of the substrate and near to the

deposit-substrate interface regions were generally measured using thermocouples [54, 61, 88]. Due to the limitation in temperature measurements, a large number of experiments are usually needed to determine the key governing parameters in the spray forming process. Therefore, numerical modelling of the heat flow in the preforms were employed to provide an insight into the dynamic temperature changes within the preform throughout the spraying process and determine the effects of the spray processing parameters [89, 92-96]. The numerical model predicts the temperature distributions or liquid fractions and the thermal histories in different regions of the preform which can be validated by the experimental measurements from certain sections of the preform.

Nevertheless, a length scale problem exists in numerical modelling of the heat flow in the growing preform as the Gaussian mass or enthalpy flux distribution of the depositing layer involves the discretisation of the relatively thin layer (typically 10^{-5}-10^{-4} m in thickness) from the periphery of the spray cone at infinitesimal time steps on the surface of the bulk preform (typically 10^{-1}-10^{0} m in thickness or width) [96]. The length scale difference typically leads to limitations during the meshing operation in finite element (FE) based numerical modelling.

Previous studies have carried out the thermal simulation of the growing preform using a simplified approach that avoids the length scale problem by simulating one-dimensional preform growth [97] in its thickness direction (Fig. 2.16a) and assuming regular depositing layer geometries and thicknesses (Fig. 2.16b) at relatively larger time steps [93]. The preform temperature distributions and thermal histories simulated using such simplified approaches may not be accurate representation of the actual spray process and preform geometry especially in determining the temperatures in the regions deposited with droplets from the periphery of the spray cone.
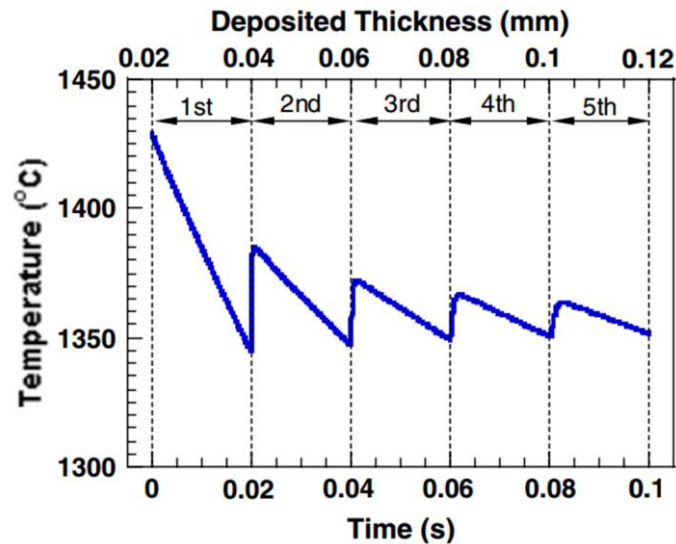
(a) One-dimensional preform growth
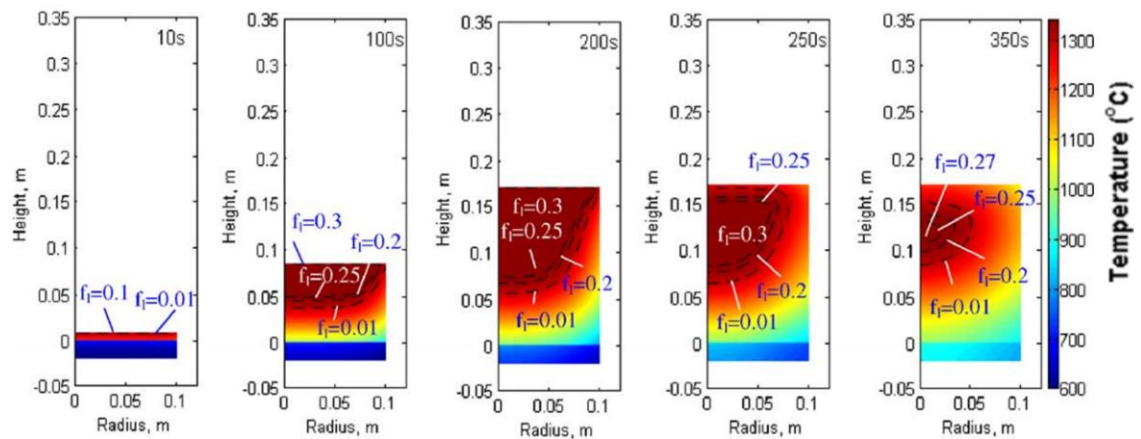
(b) Regular depositing layer geometry and thickness
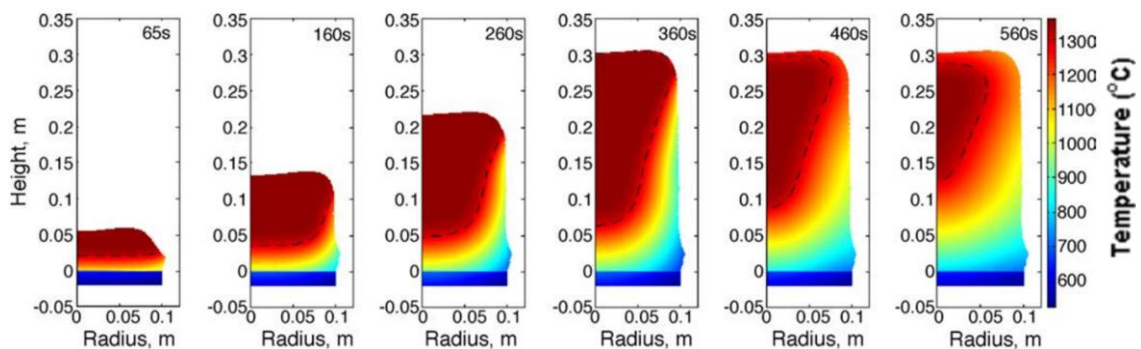
(c) Gaussian distribution mass or enthalpy flux deposit layer

Fig. 2.16. Thermal simulation of the growing preform considering (a) one-dimensional preform growth in the thickness direction, (b) regular depositing layer geometries and thicknesses, and (c) Gaussian shaped depositing mass or enthalpy flux distribution [93, 94, 97].

Numerical models that considered the Gaussian shaped depositing mass or enthalpy flux distribution showed more reliable simulated temperature distributions (Fig. 2.16c) that were verified by experimental measurements [94-96]. These studies have typically employed novel modelling methods supplemented with in-house algorithms developed to (1) couple the mass or enthalpy flux of the growing preform surface during spraying at a given infinitesimal time step and (2) perform the mesh refinement to bridge the length scale problem efficiently. The general modelling approach used typically involves generating new meshes at the deposition surface or stretching the preform domain mesh with respect to the incoming mass flux distribution. The mesh stretching can be limited to a certain layer under the the deposition surface boundary by defining a fixed curve to separate the deformable and fixed mesh in the computational domain (Fig. 2.17). The enthalpy input at the deposition surface was taken into account by solving the transient heat equation for the entire computational domain with the stretched mesh. Subsequently, the domain was re-meshed and the data from the nodes in the preceding mesh were interpolated to the nodes in the new fixed mesh. The meshing procedure was repeated to efficiently and accurately simulate the continuous preform growth and heat flow.
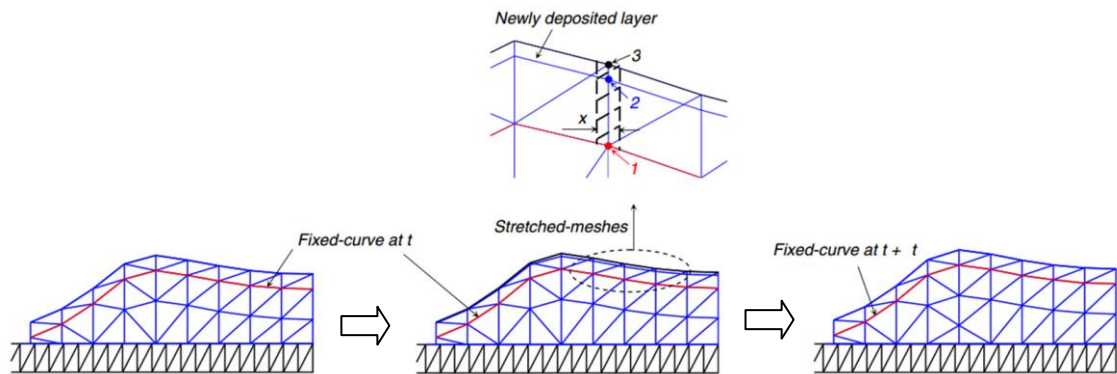
Fig. 2.17. The meshing and re-meshing procedure used to couple the mass or enthalpy flux at the deposition surface [96].

Hence, the deformed mesh method described in the aforementioned approach is ideal to track/simulate the preform shape/thermal evolution since it avoids discretising the micrometer-scale shape changes at every time step to effectively bridge the length-scale problem. The deformed mesh method is based on the moving mesh algorithm in FE modelling and the fundamentals of the algorithm will be introduced herein. A

comprehensive description of the mathematical formulation of the moving mesh algorithm is given in [98, 99].

The moving mesh algorithm has been used to solve partial differential equations (PDE) and improve the accuracy of the FE solutions to track features such as moving boundaries in fluid flow problems [99-103]. Fig. 2.18 shows the application of the moving mesh algorithm to track the fluid surface movement in a container due to the changing gravitational force vector direction. The moving fluid surface boundary is tracked as the mesh deforms/moves according to the fluid flow.
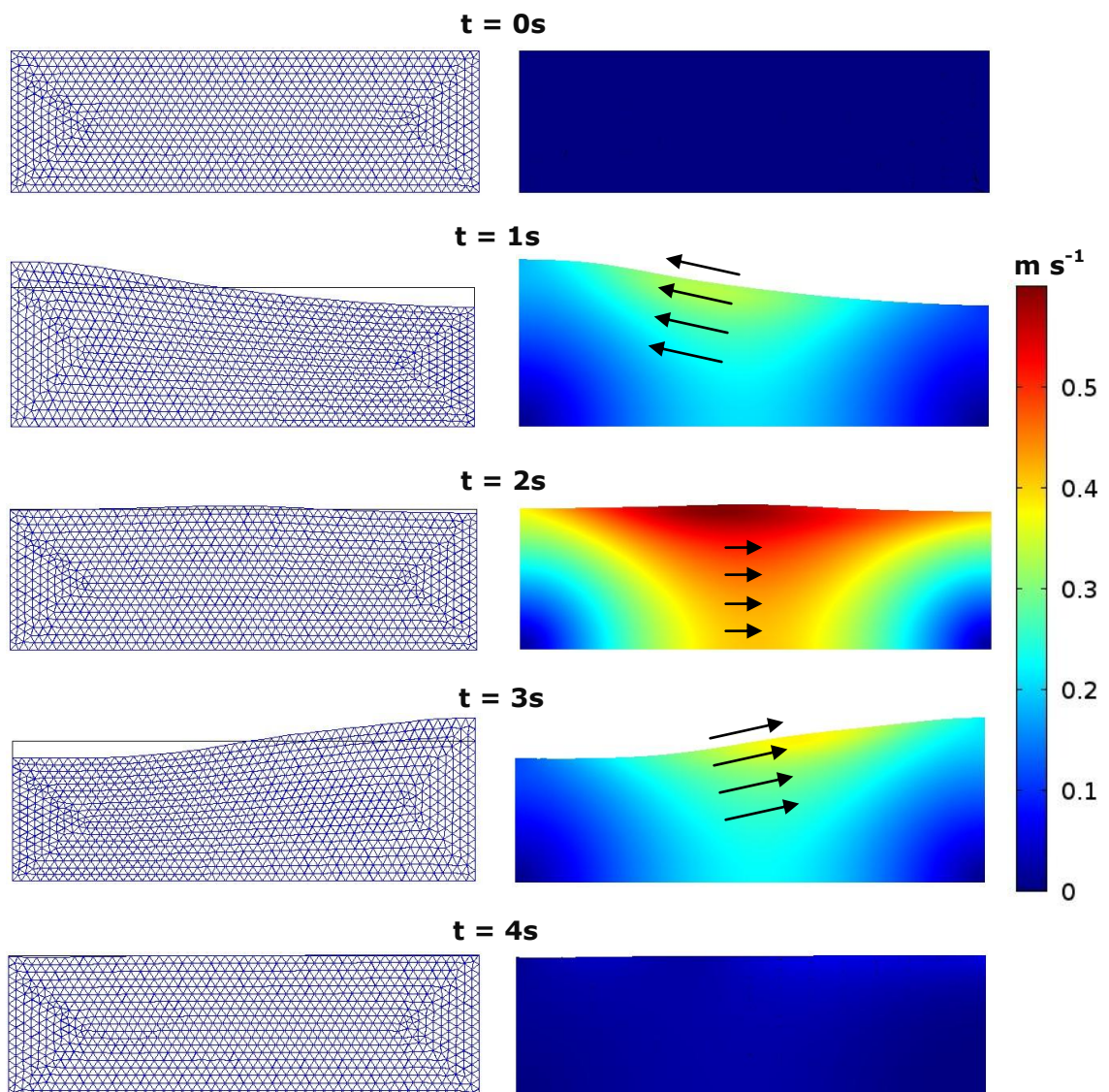
Fig. 2.18. The 2D fluid surface movement in a container showing the (a) moving/deforming mesh and (b) the fluid flow velocity due to the changing gravitational force vector direction [104].

The moving mesh method can be divided into: (1) velocity-based methods [99] and (2) mappings between a fixed mesh and physical space [103]. The velocity-based moving mesh method, which is based on geometric conservation law [105], is ideal to track the preform shape/thermal evolution as the growth rate of the deposition boundary can be defined based on the Gaussian shaped depositing layers. The velocity-based algorithm was devised to be in a general form and was successfully applied to a wide range of time-dependent nonlinear PDE problems [106] and a summary of the complete algorithm for a single time step is described in Fig. 2.19.

The solution values for a set of mesh nodes are determined at nodes where Dirichlet boundary conditions are not specified. The solution values in the remaining nodes are defined with the Dirichlet boundary condition.

The local velocity potential and rate of change in mass at each node are calculated using the solution values determined.

The node velocity for the whole set of mesh nodes is calculated using the determined velocity potential.

The corresponding mass at each node can be updated using the calculated node velocity of the moving mesh frame based on the Arbitrary Lagrangian-Eulerian (ALE) equation to determine the rate change of total mass of the whole set of mesh.

Fig. 2.19. A summary of the complete moving mesh algorithm for a single time step [106].

However, the limitation of the moving mesh method is that the quality of the mesh deteriorates significantly as the mesh deformation grows to larger scales, causing numerical errors and computational instability. Therefore, the deformed mesh has to be re-meshed to map the data from the deformed mesh to the new mesh points before the accuracy of the solution deteriorates.

The accuracy of the preform thermal simulation also depends greatly on the cooling boundary conditions specified along the preform surface throughout the spray process. Proper heat transfer coefficients must be defined to

calculate thermal histories that are representative of the actual process in order to study the spray processing parameters effects and their influence on the microstructures formed and stresses developed due to cooling. The preform is typically subjected to convective and radiative cooling along its surface (Fig. 2.20a) throughout the spraying process [95, 96].
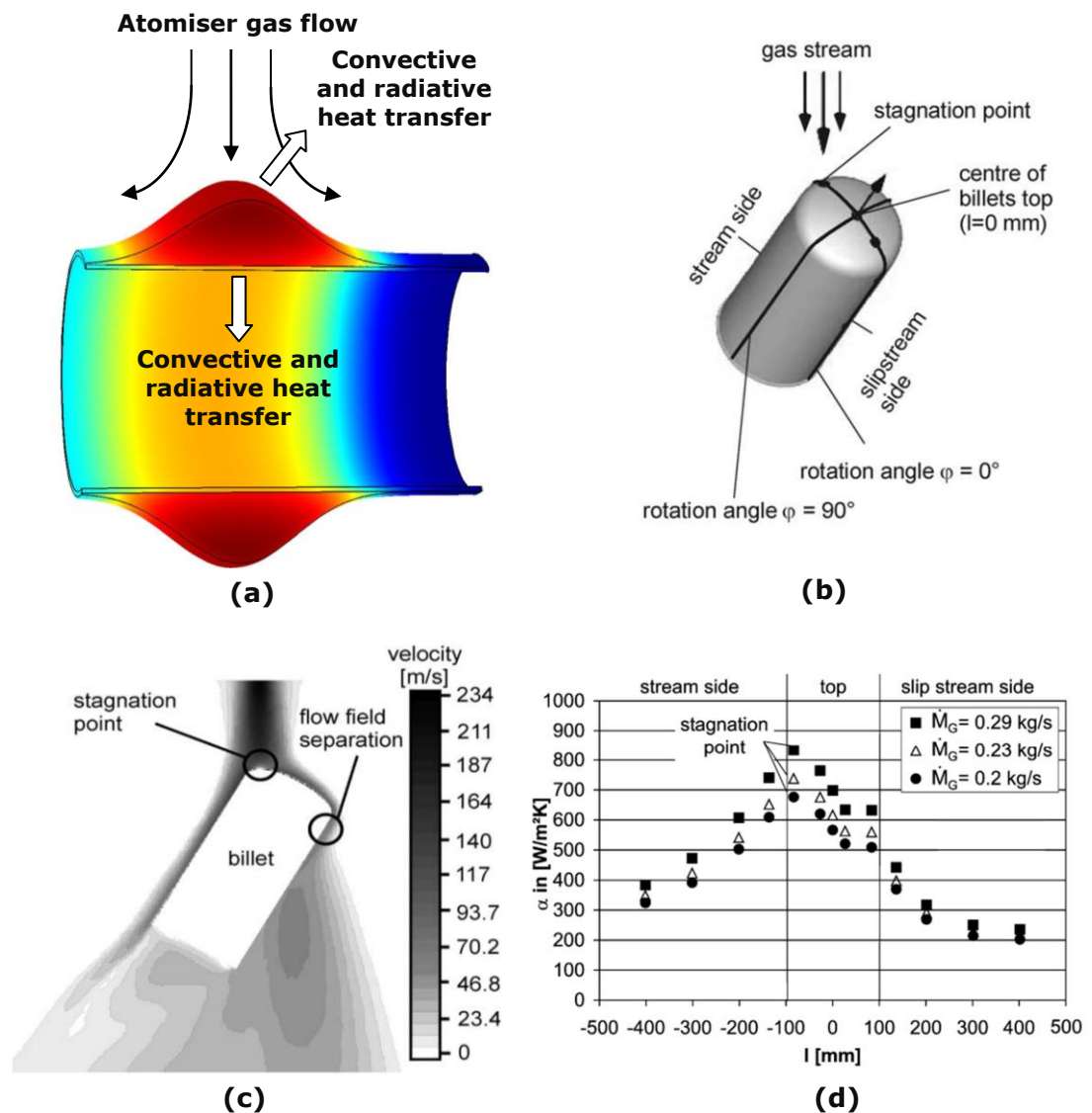
Fig. 2.20. (a) The typical preform cooling boundary conditions throughout the spraying process, (b) a schematic of a typical billet preform subjected to atomiser gas flow cooling showing the gas flow stagnation point, (c) the simulated gas flow field impinging the billet preform surface, and (d) the heat transfer coefficients along the preform surface at different gas flow rates [92].

Previous studies have investigated the relationship between the heat transfer coefficients and gas flow field as well as the preform geometry [92,

107, 108]. Their results indicated that the heat transfer coefficient increases at higher gas flow rates and at decreasing distance between the preform and the atomiser. In addition, Meyer *et al.* [92] showed that the heat transfer coefficient is maximum at the gas flow stagnation point on the preform surface and decreases exponentially at surfaces where the atomiser gas jet impinge obliquely (Fig. 2.20b - Fig. 2.20d).

2.4.3 Microstructure development

The microstructure formed in spray formed components is directly affected by the preform thermal history [109] and the as-sprayed microstructure typically consists of porosity formed as a result of the different thermal conditions between the impinging mass/gas flow and the preform surface [110-113]. Porosity affects the material properties [25, 41, 114, 115] and is typically formed in the deposit-substrate interface and preform surface regions with porosity of up to 20% [42, 95, 116, 117]. In general, the porosity in spray formed materials can be categorised into interstitial porosity and gas entrapment porosity [40, 109]. Interstitial porosity is formed when the droplets from the spray consist of low liquid fractions which lead to insufficient liquid metal available to fill the voids between the deposited droplets that are solidified. On the other hand, the gas entrapment porosity is formed due to gas bubbles being trapped when the droplets impinge regions where there are relatively high liquid fractions. Interstitial porosity typically has an irregular shape while gas entrapment porosity is more circular and their formation during spraying is illustrated in Fig. 2.21.

(a) Interstitial porosity   **(b) Gas entrapment porosity**
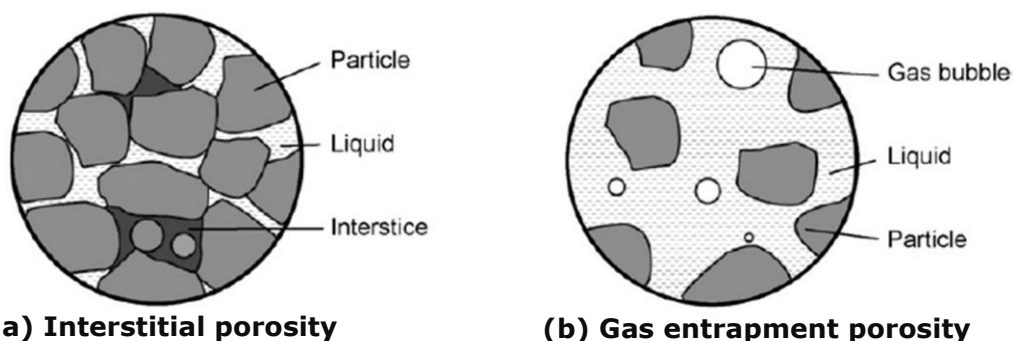
Fig. 2.21. An illustration of the formation of (a) interstitial and (b) gas entrapment porosity during the spray forming process [109].

Previous studies were done to establish the correlation between porosity formed and the spray processing parameters [118-121] as shown in Fig. 2.22. However, these correlations are generally valid for the particular experimental set-up and conditions. Cai *et al.* [40] developed a theoretical model to estimate the porosity formed in the as-sprayed deposit that assumed the calculated solid fractions in the spray to form sphere particles arranged in a packed structure and the remaining liquid fraction to fill the voids between the particles. The resulting porosity is determined from the difference between the volume of the voids and the remaining liquid fractions [86]. However, the model is only valid for colder spray conditions where the droplets are solidified since the droplets in a typical spray would deform during impingement. Recently, Meyer *et al.* [42] reported a systematic investigation on the effects of substrate preheating on the porosity formed in the deposit-substrate interface. Their study established the relationship between the porosity formed in the interface and the preform enthalpy. They concluded that the substrate temperature immediately before spraying governed the porosity formed in the interface region and that porosity was lower at higher substrate preheat temperatures. Nevertheless, the correlation established was shown to be dependent on the type of sprayed material and was unable to predict the absolute porosity level. Therefore, there is a persisting difficulty in predicting the porosity formation under the dynamic temperature changes in spray formed materials.

The dynamic events during preform consolidation also give rise to microstructure transformations in the sprayed alloys. In a typical spray forming process, the atomised droplets are often rapidly cooled before landing onto a cold deposition layer, and the subsequent layer of hot droplets deposits in less than a second [61, 97]. These cyclic rapid cooling/heating operations plus a short dwell time (in the 10^{-3} to 10^{0} s range) [96, 122] create highly transient and dynamic thermomechanical environments that drive the non-equilibrium evolution of the droplet/preform microstructure during the consolidation process. One of the important findings that had been reported by numerous researchers in the past is the transformation of dendritic/cellular microstructures in the

atomised metallic powders into equiaxed grains [123-130] after consolidation in the preform (Fig. 2.23).
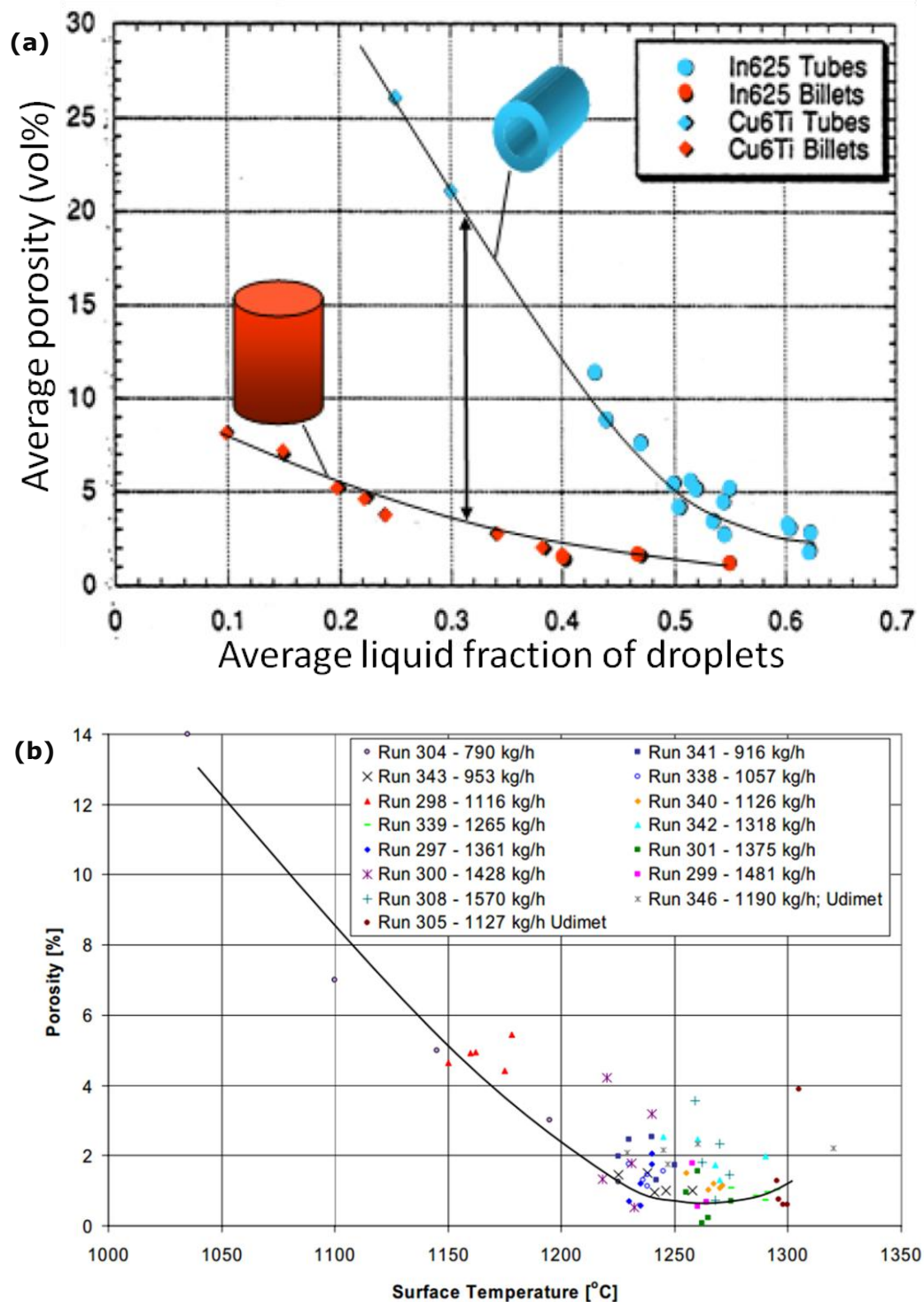
Fig. 2.22. (a) Correlation between average liquid fraction of the droplets and the average porosity formed in spray formed billets and tubes [120] and (b) the relationship between local porosity and preform surface temperature of spray formed Ni superalloy rings using different melt flow rates [121].
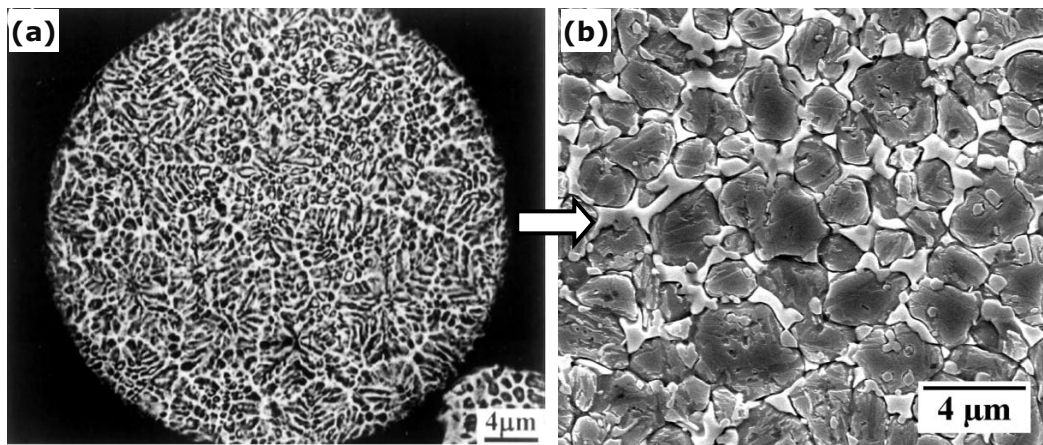
Fig. 2.23. (a) The dendritic microstructure formed in the atomised ASP30 HSS powder [126] and (b) the typical equiaxed microstructure formed when the droplets consolidate in the preform.

It was proposed that the large enthalpy input associated with the impinging large-sized droplets (higher liquid fractions) may be sufficient to partially remelt the solidified microstructures to induce fragmentation which provides the grain multiplication effect in the consolidating preform [123], while some other studies suggested that the mechanical deformation and fragmentation induced during deposition effectively refined the microstructures formed in the partially solidified droplets prior to deposition [131, 132]. Therefore, it is generally well perceived that the thermal and/or mechanical shock experienced by the consolidating metallic droplets caused the dendrite fragmentation that increased the nucleation sites to produce a grain multiplication effect for an equiaxed grain growth formation, and as a result, the as-sprayed microstructure often differs from the initial dendritic microstructure formed in the rapidly cooled atomised metallic powders [125-127, 133]. However, almost all previous studies were conducted using samples that already experienced many such cooling/heating cycles or were heat-treated for a relatively long period of time [125, 134-137] which certainly cannot represent the rapid cooling/heating operation, i.e. thermal shock at all. Hence, the dynamics of the dendritic-to-equiaxed microstructure transformation under rapid heating/cooling in a single cycle with short heat treat times (in a few seconds range) remain unclear.

Recently, J. Mi and his collaborators have developed an experimental approach that used a Gleeble thermomechanical simulator to rapidly heat atomised Ni superalloy and high speed steel powders to semisolid conditions

and held isothermally for a relatively short period of time (~10 s) before rapidly cooling the samples to room temperature [138]. In this way, the single cycle of rapid heating/cooling or more precisely thermal shock can be realised in order to study the microstructure evolution in a single thermal shock operation.

The different cooling rates throughout the preform can also give rise to varying grain sizes within the preform. Hu *et al.* [113] showed that the as-sprayed tool steel preform consists of relatively larger grains towards the central region of the preform where the heat concentration is higher. Fig. 2.24 shows the typical scanning electron microscopy (SEM) images of the as-sprayed microstructures formed in the preform central and surface regions acquired from the ASP30 HSS preforms sprayed in this research. Mingard *et al.* [91] established the relationship between the final grain size and solid fraction in the growing preform surface measured by plunging thermocouples into the preform surface during spraying which indicated that larger grain sizes were formed when the preform maintained lower solid fractions during spraying. The equiaxed grain growths in spray formed microstructures were reported to follow typical diffusion-controlled growth kinetics [123],

$$ d_g^3 - d_{g0}^3 = K_g \cdot t \qquad (2.18) $$

where d_g is the grain diameter, d_{g0} is the initial grain size, K_g is the coarsening constant and t is time. The grain growth kinetics were shown to be valid at liquid fractions down to ~0.3 and that the coarsening constants were typically in the range of K_g = 150 to 200 $\times$ 10^{-18} m^3 s^{-1} for Ni-based superalloys [139, 140].

(a) Preform central region   **(b) Preform surface region**
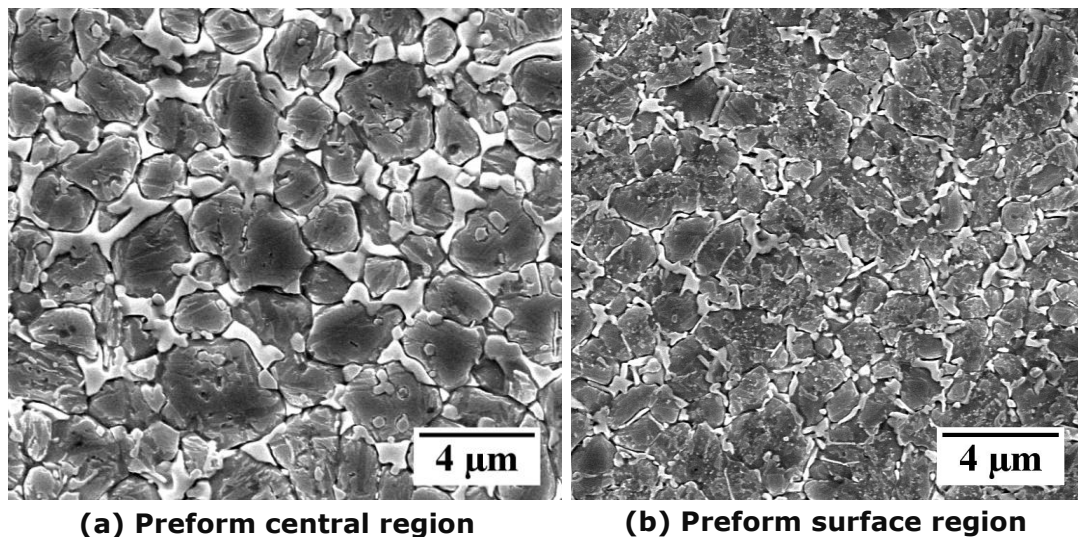
Fig. 2.24. The SEM images of the microstructures formed in the (a) central and (b) surface regions of the as-sprayed ASP30 HSS preform sprayed in this research showing the difference in grain sizes.

In addition, the carbides in the as-sprayed microstructures were typically shown to be generally much larger in the preform central region as compared to the carbides formed towards the edge of the preform [141, 142]. Kjeldsteen *et al.* [141] proposed that the carbide size distribution can be related to the thermal gradient in the preform that showed higher heat concentration in the preform central region during spraying. The argument is further supported by the accelerated metastable carbide decomposition and coarsening behaviours in spray formed microstructures at higher temperatures as shown by Lee *et al.* [126].

2.4.4 Residual stress development

Spray forming dissimilar alloys that have different material properties, such as the Young's modulus (E) and coefficient of thermal expansion (CTE) can lead to significant thermal and residual stresses development across the interface [143, 144], and the residual stresses have been reported to be one of the primary causes of premature failure as-sprayed dissimilar alloy components [145]. The residual stress developed in as-sprayed materials was first investigated by Ho and Lavernia [146-148] and Hu *et al.* [149]. Their studies typically employed laboratory X-ray diffraction (XRD) to measure the residual stress developed along the preform thickness. In addition, they compared the measured stress with simulated stress

distribution calculated using FE numerical modelling by assuming a linear temperature distribution that increases towards the top surface of the Gaussian shaped preform. Nevertheless, the simplified numerical modelling approach that assumed linear temperature distribution is not representative of the dynamic temperature variations throughout the preform during spraying especially for larger preforms and other preform geometries. Furthermore, the residual stress measured using laboratory XRD was generally subjected to significant stress relaxation due to short penetration depth of X-ray especially in steels that limited the measurements to near surface regions.

Ristau *et al.* [71] have used FE modelling to study the residual stress development in sprayed tubes by considering the thermal history during spray forming and the post-processing heat treatments, but the stresses were not validated. Actually, most previous studies concerning the spray forming of dissimilar materials [62, 82, 95, 96, 150] did not investigate quantitatively the bonding characteristics across the interface, such as the bonding strength or residual stress distribution across the interface. This is mainly due to the experimental complexity in measuring the stresses developed during spraying. Furthermore, it is difficult to determine accurately the interfacial bond strength using typical mechanical testing methods especially when the as-sprayed specimen is porous that can cause failure to initiate at regions far from the interface [7]. This suggests that the typical destructive mechanical testing of as-sprayed specimen lacks consistency as the measured strength may not be an accurate representation of the bond strength. In addition, there is a physical limitation in cutting tensile test specimens from the preforms especially when the substrate used is relatively thin.

Neutron diffraction (ND) is currently a standard technique to measure the residual stress in thick metallic/engineering components. Lee *et al.* [151] used ND and X-ray micro-tomography (µCT) to characterize the 3D microstructures of spray formed HSS and established the correlation between microstructures and residual stresses in the as-sprayed preform (Fig. 2.25) due to different deposition temperatures. Kupperman *et al.* [152] used ND to characterise the residual stress in high temperature ceramic

superconducting composites bonded to a Ag substrate induced by differential thermal contractions during fabrication and showed that the interfacial bonding can be assessed based on the residual stress developed. ND is more suited to the stress measurements in metallic materials than X-ray based diffraction techniques because neutrons can penetrate up to a few centimeters into most metallic materials and thus, the measurements are not limited to the surface regions that are subjected to stress relaxation [153]. Unfortunately, there has been no report on the use of ND diffraction to characterise the residual stress across the bonded interface of thick spray formed dissimilar metallic alloys as a non-destructive means to assess the interfacial bonding and to provide the quantitative links between the key spray forming parameters and the interfacial bonding strength for dissimilar metallic alloys.

...
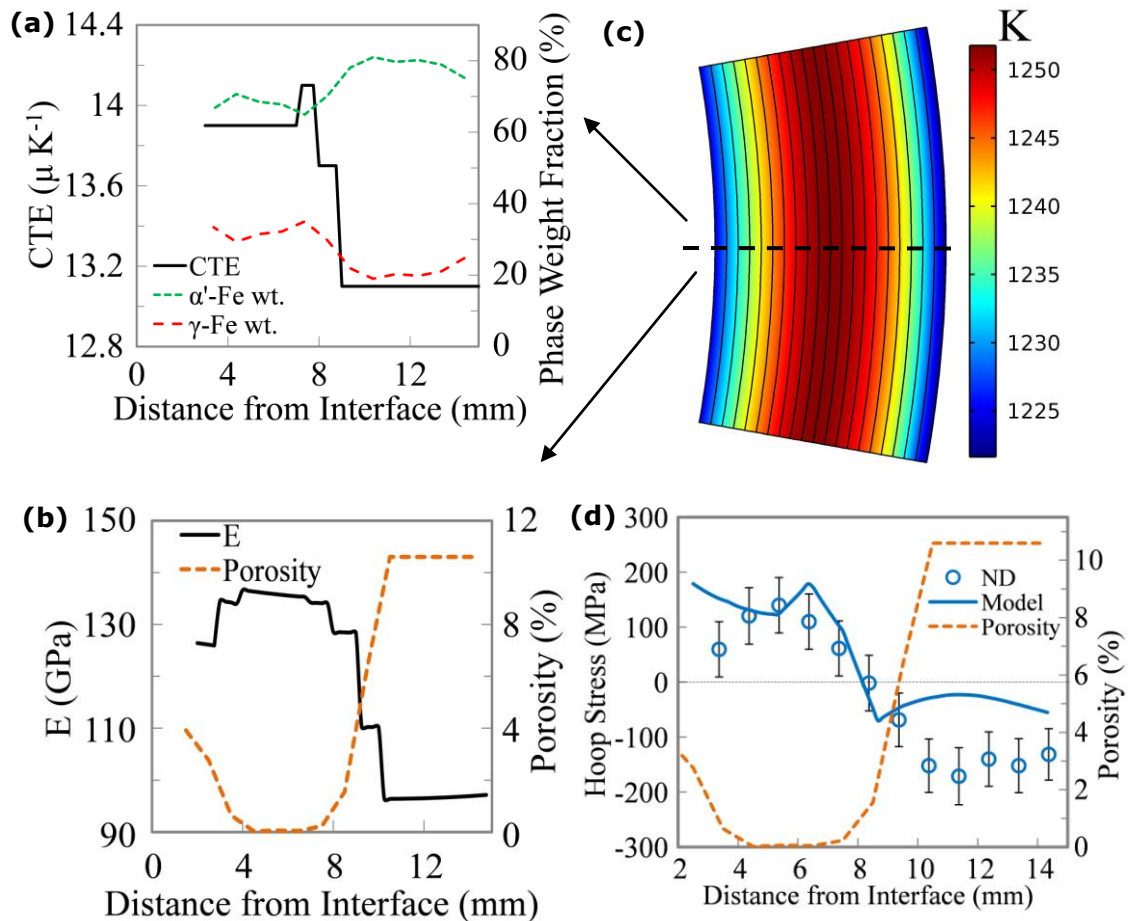
Fig. 2.25. The effects of microstructure variations in the (a) local CTE and (b) Young's modulus of the as-sprayed high speed steel, (c) simulated preform cross-sectional temperature distribution along the preform thickness (ring-shaped deposit layers) immediately after spray ended, and (d) the simulated and ND measured residual stress distribution across the dense-to-porous transition region along the preform thickness showing the correlation between the residual stress and microstructure formed [151].

2.5   Residual stress measurement methods

Residual stresses in most engineering components typically originate from thermal or elastic mismatch that may be induced during manufacturing or service and can be categorised into different length scales (L_0). Macro-stress, commonly referred to as type I stress, varies over large distances in comparison to the inter-granular stresses (type II stress) that change over the grain scale and the type III stress that varies within an individual crystallite on the atomic scale.

In the context of spray forming, residual macro-stresses are typically induced as a result of the temperature gradients and thermal property differences in the preform throughout the spray process. The thermal expansion mismatch coupled with dynamic temperature changes in the preform can generate significant residual macro-stresses in the as-sprayed preforms [71, 148, 149, 151]. Type II stresses typically exist in polycrystalline materials due to the variation in thermo-mechanical properties of the neighbouring grains in different orientations and the stresses are more significant if the microstructure consists of multiple phases since the lattice parameters, thermal and elastic properties of the phases can be significantly different [154]. Type III stresses are generally induced by voids or defects in the crystal lattice [155].

Depending on the residual stress measurement sampling length scale and method, different stress types in the component can be determined. The respective type of stress averages to zero if the measurement gauge volume is greater than the characteristic volume, V_0 ($\approx L_0^3$ [156]) and therefore, will not be recorded. Typical material removal stress measurement techniques such as hole drilling remove macroscopic regions from the material from which type II and III stresses average to zero. In diffraction methods, the gauge volume used may also be larger than the V_0 of type II and III stresses but the wavelength and diffraction conditions used allow the stress measurements of a particular phase or crystallographic plane within the gauge volume that provide both inter-phase and inter-granular stress information in addition to the macro-stress recorded.

A wide range of residual stress measurement methods are available which include destructive and non-destructive methods that offer distinctive measurement applications and accuracies [154]. An overview of the commonly used methods to measure residual stresses in sprayed materials [157] will be described and their applications to measure the stress in spray formed components are reviewed and discussed in this section.

2.5.1 Curvature measurement

The curvature measurement method is commonly used to determine the macro-stresses in sprayed components since the difference in thermal expansion between the deposit and substrate induces curvature and the change in stress is reflected by the variation in curvatures throughout the deposition process [158]. The curvature can be measured using a contact (e.g. strain gauges) and non-contact (e.g. laser scanning) approach with typical curvature resolutions of down to 0.1 mm^{-1} [154, 157]. The relationship between the curvatures and the stress developed along the component can be determined using the Stoney equation as described in [159, 160]. However, the method is commonly limited to planar geometries with narrow widths (width-to-length ratio <0.2) in order to avoid multi-axial curvatures that would lead to complex data interpretation of the stresses and the stress distribution from the curvature measurements are commonly derived with assumptions of the boundary conditions [157]. Therefore, the curvature method will not be ideal for measuring the residual stress developed in relatively thick and wide components manufactured by spray forming especially in the billet or tube form.

2.5.2 Material removal

The macro-stresses in the sprayed component can be determined by measuring the relaxation induced when material is removed from the stressed component. The material removal operation typically involves drilling a hole in the component with the local strain change measured using a rosette of strain gauges that are commonly attached to the uncoated side of the substrate [161, 162]. However, the physical problems pertaining to the material removal operation significantly increased the complexity of the stress measurements. The hole drilling can damage the component,

especially for brittle materials, and give rise to significant errors in the stresses measured [157] and the stress distribution along the depth of the hole drilled is typically limited to its diameter size beyond which may give rise to inaccurate stress measurements [154]. The measurement limitations associated with the damage induced during material removal can induce significant errors in the stress measured from spray formed materials since the typical as-sprayed components consists of relatively severe porosity at the preform surface which can cause significant crack propagation in the component when drilled. Thus, the material removal method is not suited for stress measurements in spray formed components, especially in the as-sprayed form.

2.5.3 Diffraction

The residual stresses in sprayed components can be determined non-destructively via diffraction methods that essentially use the lattice planes in polycrystalline materials as atomic strain gauges. The lattice strain is determined from the shift in the lattice parameter when compared to the corresponding reference unstressed state. The corresponding stress can be derived from the deduced lattice strain using the material elastic stiffness.

The diffraction method offers higher utility than other stress measurement methods since it can be used to provide the stress measurements of individual phases separately [163]. Diffraction reveals information of the different phases and grains in the material necessary to derive the bulk macro-stresses, inter-granular stresses and the stresses within the crystallites. Nevertheless, the limitations of the method are typically associated with its probing (penetration) depth. The commonly used for diffraction sources for sprayed metallic components are X-ray and neutron. However, their interaction with the material is different; i.e. X-rays are scattered from the electron clouds (electromagnetic interaction) while neutrons are scattered from the nucleus of the material (short-range nuclear reaction). The electromagnetic interaction is typically much stronger and thus, X-ray beams generally do not penetrate deep into a material as compared to neutrons (Fig. 2.26a) and X-ray penetration depth decreases with heavier atoms (more electrons) while neutron has a random scattering length (Fig. 2.26b).

(a)

(b)
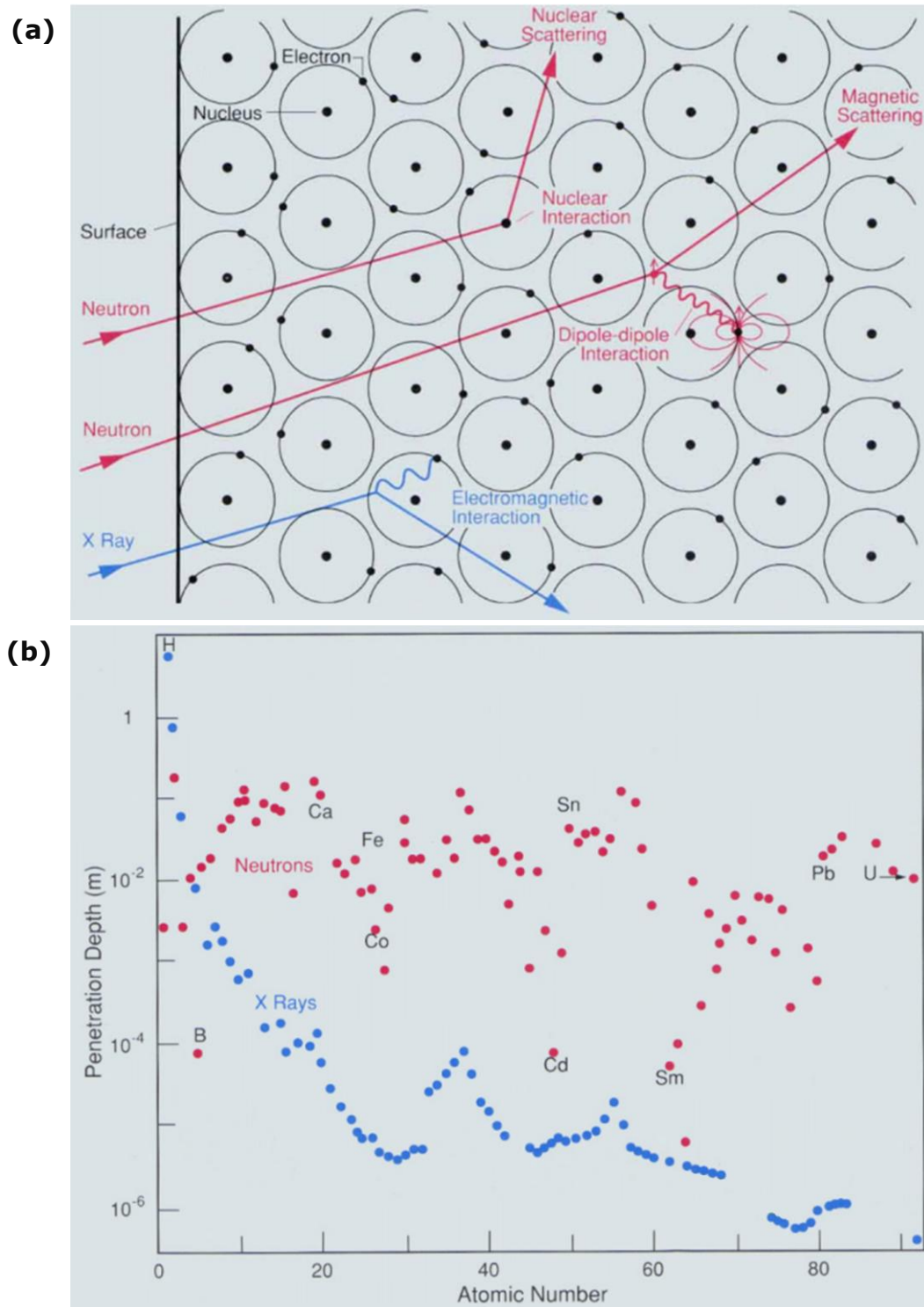
Fig. 2.26. (a) Illustration of the neutron and X-ray interactions with the material showing that the X-ray beam penetration is much shorter than that of the neutron beam and (b) the penetration depths (beam intensity reduced to ~37 % of incident intensity) of X-rays and neutrons (wavelength of 1.4 Å) [164].

Typical laboratory XRD measurements are limited to the surface regions due to the relatively small penetration depths (~0.01 mm) and a plane stress condition was commonly assumed to derive the stresses from the thin probed region [154, 165]. X-rays from synchrotron sources that are of up to a million times more intense than laboratory X-rays provide short data acquisition times (< 1s) and their energies of up to 300 keV allow much higher penetration depths (a few mm in steel) [166-172]. Neutrons, on the other hand, offer more utility to probe the stress deep within thick components due to larger penetration depths in most metallic materials (up to a few cm in steel [172]) in comparison to synchrotron X-rays. However, the flux from the typical neutron sources currently available is lower than that of synchrotron X-ray sources which leads to relatively longer data acquisition times. Nonetheless, the non-destructive nature and the capability to measure multiple stress types have clearly shown that the diffraction method, especially neutron diffraction, is highly suited for characterising the stress distributions in thick as-sprayed metallic preforms.

2.6   Neutron diffraction

In ND experiments, elastic scattering condition is typically assumed, i.e. no energy is transferred to or from the sample (Fig. 2.27). The scattering of neutrons by nuclei is a quantum mechanical process and neutron wavevectors $\left(\vec{k} \right)$ are commonly used to refer to the neutron's trajectory and can be expressed as:

$$\vec{k} = \frac{2\pi\, m_n\, v_n}{h_P} \qquad (2.19)$$

where h_P is Planck's constant, m_n is neutron mass and v_n is the neutron velocity. The neutrons scattered from a free nucleus are expressed in terms of a cross section (σ_n) measured in barns (1 barn = 10^{-28} m^2). If a neutron enters an effective area represented by the nucleus σ_n it is scattered isotropically in all directions since the wavelength of the neutron is much larger compared to the nucleus and thus, the nucleus acts as a point scatterer. The incident neutron beam travelling in the positive x-axis direction towards a nucleus can be described by a plane wave with wavefunction $e^{i k_{in} x}$ and the isotropically scattered wave (represented by the

circular waves in Fig. 2.27) from the scattering centre at the origin ($r = 0$) can be described by the wavefunction $\frac{-b}{r}e^{ik_f r}$ [173]. The factor $\frac{1}{r}$ in the scattered wavefunction takes into account the intensity decay with increasing distance from the scattering centre while b is the scattering length of the nucleus (the strength of the interaction between the neutron and the nucleus) and has a positive value in the case of repulsive interaction [173]. In elastic scattering, the assumptions are that the nucleus is fixed and the neutrons do not possess sufficient energy to change the internal state of the nucleus so the energy lost by the neutrons (E) is equals to zero. Therefore, the incident wavevector (k_{in}) and the final wavevector (k_f) are equal.

The neutron scattering from each nucleus in a matter is added and the scattering process may change in momentum and energy. The scattering may not necessarily be elastic as the atoms in the matter can move during collision with a neutron and impart energy to the neutron. The total energy and momentum are conserved in the collisions, and the momentum transfer from the neutron is given as:

$$m_n\, v_n = \frac{h_P\,(k_{in} - k_f)}{2\pi} = \frac{h_P\,\vec{Q}}{2\pi} \tag{2.20}$$

where $\vec{Q}$ is the scattering vector and the scattering vector triangle in Fig. 2.28 illustrates the scattering vector relationships.
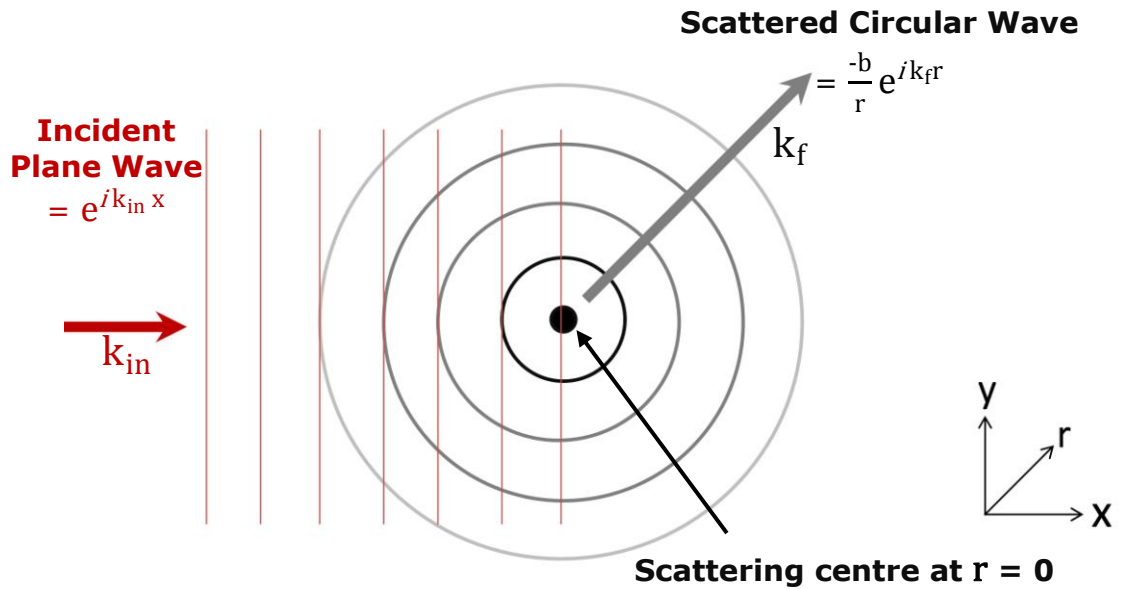
Fig. 2.27. Isotropic scattering of neutrons from a fixed nucleus (point scatterer).

$$\sin\theta = \frac{Q}{2k_{in}}$$

$$Q = 2k_{in}\sin\theta = \frac{4\pi\sin\theta}{\lambda}$$
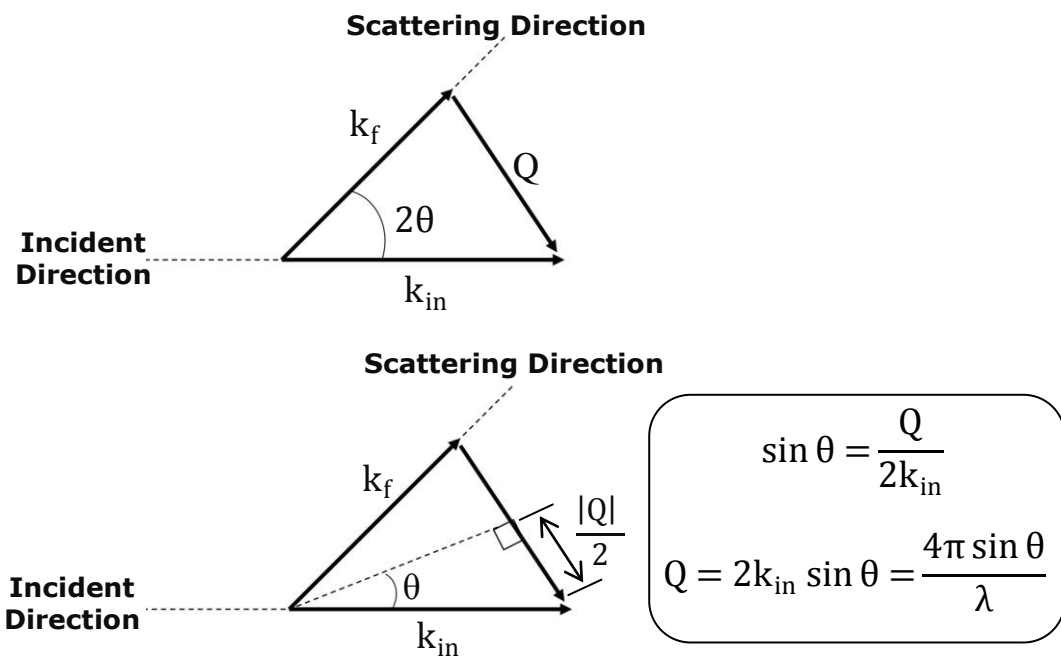
Fig. 2.28. Scattering vector triangles for an elastic scattering event showing the scattering vector, $\vec{Q}$ where the neutron is scattered through the scattering angle, 2θ and $k_{in} = k_f$.

The scattering angle (2θ) is the angle through which the neutron is deflected. During elastic scattering, $k_{in} = k_f$ and thus, the scattering vector triangle shows that,

$$Q = \frac{4\pi \sin\theta}{\lambda} \tag{2.21}$$

where λ is the wavelength. The intensity of the neutrons scattered by matter, $I(\vec{Q}, E)$ are measured as a function of Q and E, and is expressed as:

$$I(\vec{Q}, E) = \frac{1}{h_P} \frac{k_f}{k_{in}} \sum_{i,j} b_i b_j \int_{-\infty}^{\infty} \langle e^{-i\vec{Q}\cdot\vec{r_i}(0)} \, e^{-i\vec{Q}\cdot\vec{r_j}(t)} \rangle \, e^{i\cdot\frac{E}{\hbar}t} \, dt \tag{2.22}$$

where the nucleus labelled "i" is at position r_i at the initial time (t = 0), while the nucleus labelled j is at position r_j at time, t. The equation is a double sum over all of the positions of the nuclei in the sample with the angular brackets $\langle ... \rangle$ indicating a thermodynamic average over all the possible configurations in that sample [173, 174]. However, the scattering lengths in a sample will not be equal due to the interaction between the neutron and nucleus depends on the nuclear spin and there is no correlation between the spin of a nucleus and its position in a sample [173]. Therefore, the scattering lengths can be averaged to:

$$\sum_{i,j} \langle b_i b_j \rangle A_{ij} = \sum_{i,j} \langle b \rangle^2 A_{ij} + \sum_{i} (\langle b^2 \rangle - \langle b \rangle^2) A_{ii} \tag{2.23}$$

where A_{ij} is shorthand for the integral in Eqn. (2.22) and the first term is a sum over all pairs of nuclei [173]. The first term in Eqn. (2.23) is referred to as the coherent scattering in which neutrons scattered from different nuclei interfere with one another and depends on the distances between atoms (A_{ij}) and $\vec{Q}$ to give information about the structure of a material. The second term represents the incoherent scattering in which there is no interference between the neutrons scattered by the different nuclei and the scattered neutron intensities from each nucleus are added independently.

Coherent scattering occurs in diffraction when the incident neutrons scattered from each atomic site constructively interfere with each other in certain directions depending on the symmetry and spacing of the scattering

sites (Fig. 2.29). The governing law for diffraction to occur is known as Bragg's law which depends on the $\vec{Q}$ to be perpendicular to a set of atomic planes [175],

$$n\lambda = 2d \sin\theta \qquad (2.24)$$

where d is the lattice parameter and n is an integer. Thus, constructive interference of the scattered waves occurs when the path length difference between waves scattered from adjacent atomic planes is a multiple of λ.
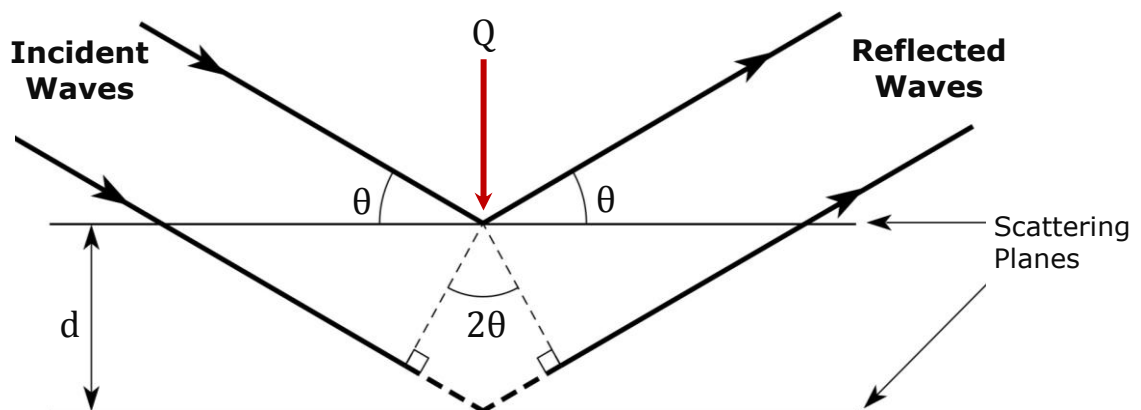
Fig. 2.29. Constructive interference of scattered waves when the path length difference between waves scattered from adjacent scattering planes is a multiple of λ.

In a typical diffraction experiment, the use of single wavelength incident neutrons requires that the crystal lattice structure to be rotated so that $\vec{Q}$ is perpendicular to the scattering planes and the signal from the crystal recorded by a detector is termed as a Bragg peak. The intensity of the scattered neutrons is proportional to the square of the density of atoms in the atomic planes (scattering planes) [173].

2.6.1 Neutron source

Neutrons produced from a neutron source possess high energies (~1 MeV) and wavelengths of ~3 $\times 10^{-4}$ Å. The neutron speeds are moderated to produce thermal neutrons (~25 meV) with wavelengths of 1.8 Å that are in the same order of magnitude of atomic spacings for diffraction experiments. The two main types of neutron sources are reactors and spallation sources. Generally, a reactor source emits continuous neutron beam from a fission

process while a spallation source produces a pulsed beam as it uses a particle accelerator to generate pulsed proton beams to emit neutrons through a spallation process from a target. Each source caters for specific science, for example, powder diffraction studies that can fully exploit the peak neutron flux from a pulsed source while irradiation-based and isotope production studies that depend on the time-averaged flux from a continuous source.

A typical neutron source operates on the basis of emitting excess neutrons in a neutron rich nuclei from a target material such as W, Pb, U, Be or Ta. The neutron flux (Φ_{flux}) represents the total path length covered by all neutrons emitted from the target travelling in different directions passing through a certain arbitrary cross-sectional unit area per unit time and can be expressed as,

$$\Phi_{flux} = n_n \, v_n \qquad (2.25)$$

where n_n is the neutron density (neutrons cm^{-3}). On the other hand, the neutron intensity (I_n) is the amount of neutrons travelling in a particular direction passing through a certain arbitrary cross-sectional unit area per unit time and therefore, considers the average neutron velocity in a certain direction. The difference in neutron intensity in a typical continuous flux reactor (57 MW Reactor Source at Institute Laue-Langevin, France) and a pulsed spallation source (160 kW Pulsed Spallation Source at ISIS neutron source, United Kingdom) is shown in Fig. 2.30 and the comparable peak neutron intensities shows that a spallation source is more energy efficient in generating neutrons. Further increments in intensity from a reactor source are not expected due to the limitation in heat extraction while significant enhancement can be expected from a spallation source of up to 30 times the intensity of the current sources in the next generation spallation source (European Spallation Source, Sweden) [176].
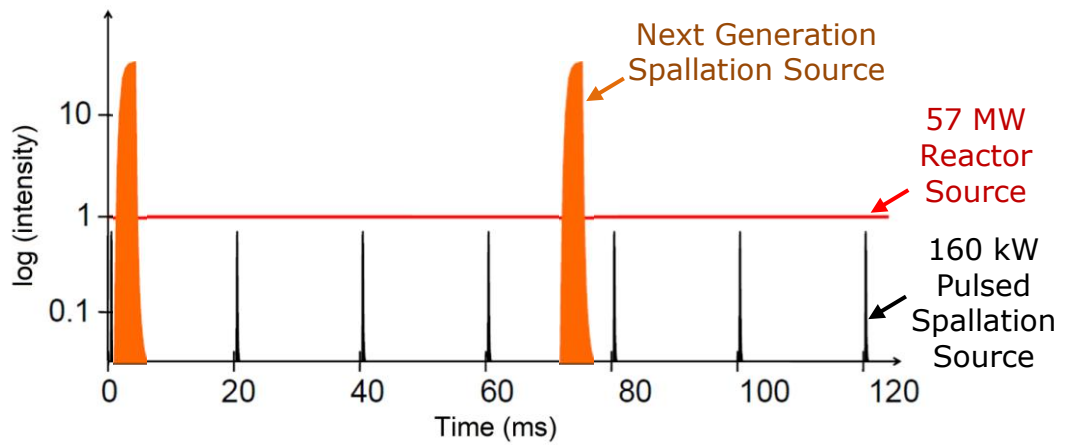
Fig. 2.30. The neutron intensity in a reactor (Institute Laue-Langevin), spallation source (ISIS at 50 Hz) and the next generation spallation source (European Spallation Source) [176].

(a) Nuclear Fission Process

(b) Nuclear Spallation Process
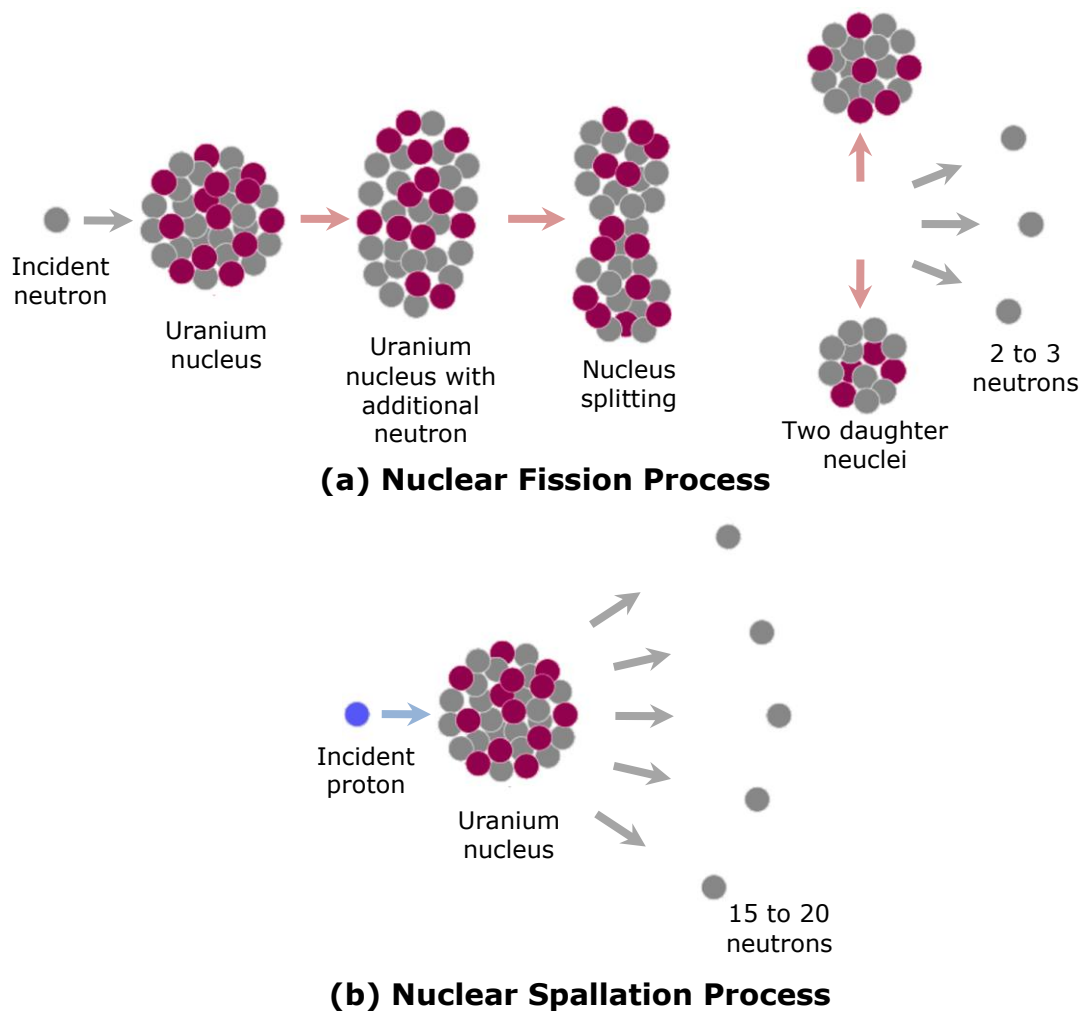
Fig. 2.31. Illustration of the nuclear (a) fission and (b) spallation processes.

The difference in neutron generation efficiency from the sources is due to the neutron emission process involved. In a typical reactor source, the fission chain reaction (Fig. 2.31a) is initiated by bombarding a U nucleus with a low speed neutron and to induce excitation energy. The excited nucleus then splits into lighter elements while releasing large amounts of energy and emits 2 to 3 free neutrons that travel at high velocity. These neutrons can then be absorbed by other U nucleus to produce a cascaded effect and thus, a nuclear chain reaction. On the other hand, high energy protons driven by accelerators are used to collide with the U nucleus to excite the nucleus in a spallation process (Fig. 2.31b). The collision then emits neutrons, protons and pions with energy sufficiently high enough to collide with other nuclei and produce the chain reaction. The excited nuclei in the target then shed their energy by evaporating particles that are predominantly neutrons. Each proton generates about 15-20 neutrons from a typical spallation process. The free neutrons emitted by either fission or spallation possess high kinetic energies and must be reduced in order for their wavelengths to be useful for diffraction and scattering experiments. The neutron energy moderation is performed through inelastic collision with light atoms in a moderator (typically water).

2.6.2 Time-of-flight neutron diffraction

In addition, the neutrons emitted from a spallation source in a pulsed nature provide additional advantages and one of which is the ability to acquire a complete diffractogram at any scattering angle. This is achieved by measuring the time taken for the neutrons to travel over a fixed path to determine their wavelength and the method is referred to as the time-of-flight (TOF) method. The wavelengths of the detected neutrons can be determined using de Broglie equation,

$$\lambda = \frac{h_P\, t_n}{m_n\, L_n} \tag{2.26}$$

where L_n is the total neutron flight path from the moderator to the detector through the sample and t_n is the recorded neutron TOF. In a typical TOF powder diffraction experiment, the corresponding lattice parameter can be determined according to Bragg's law and Eqn. (2.26),

$$d = \frac{h_P \, t_n}{2 \, m_n \, L_n \cdot \sin(\theta)} \qquad (2.27)$$

Therefore, a complete diffractogram can be acquired by restricting the scattering angle and counting the arrival time of the scattered neutrons from the sample.

2.7 Non-destructive 3D microstructure characterisation

The microstructures in spray formed materials were typically characterised using two-dimensional (2D) image analysis [119] which may provide a limited representation of the actual microstructure in comparison to three-dimensional (3D) characterisation techniques such as X-ray tomography.

X-ray micro-tomography, often referred to as X-ray μCT, is a radiographic imaging technique used to generate 3D images of the internal structure of a scanned material typically at spatial resolutions better than 1 μm. In general, minimal sample preparation is required and the technique is non-destructive which allows the same specimen to be scanned under different conditions. X-ray μCT was derived from computerised axial tomography (CAT) scans used in medical imaging [177] to produce 2D images of an object's internal structure and the internal features can be identified based on the variations in X-ray absorption within the object. However, the features are limited to a 2D plane of the image and other features located out of the plane of the image can be missed completely. CT scan provides the solution by combining and stacking information from a series of 2D X-ray absorption images acquired from an object rotated around an axis. These acquired projection images of the object at different rotation angles can be mathematically reconstructed to produce a 3D image of the scanned object where each 3D pixel (voxel) represents the X-ray absorption at that particular point [178] and the 3D images are displayed as a series of 2D "slices" of the object referred to as tomograms. The X-ray CT data acquisition and reconstruction process is illustrated in Fig. 2.32.
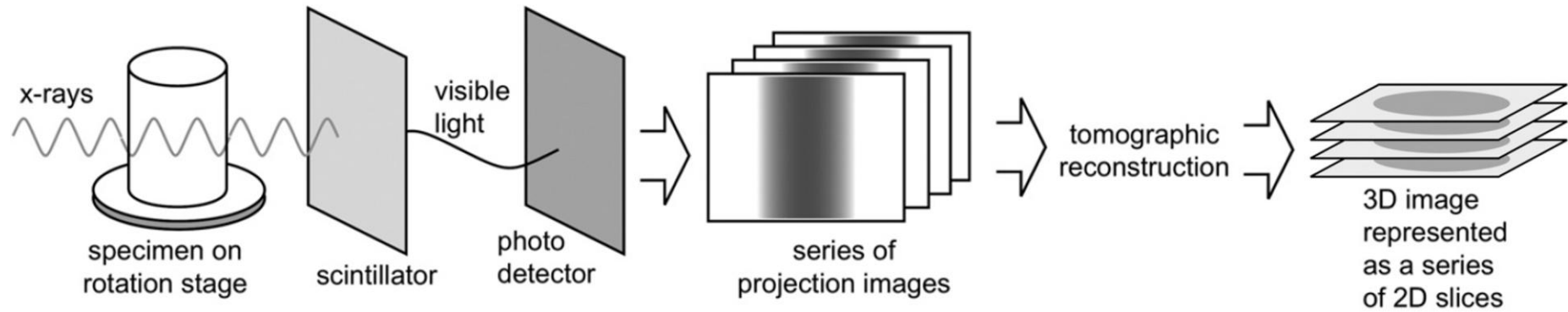
Fig. 2.32. An illustration of the X-ray CT data acquisition and reconstruction process [179].

(a) Fan beam **(b) Cone beam** **(c) Parallel beam**
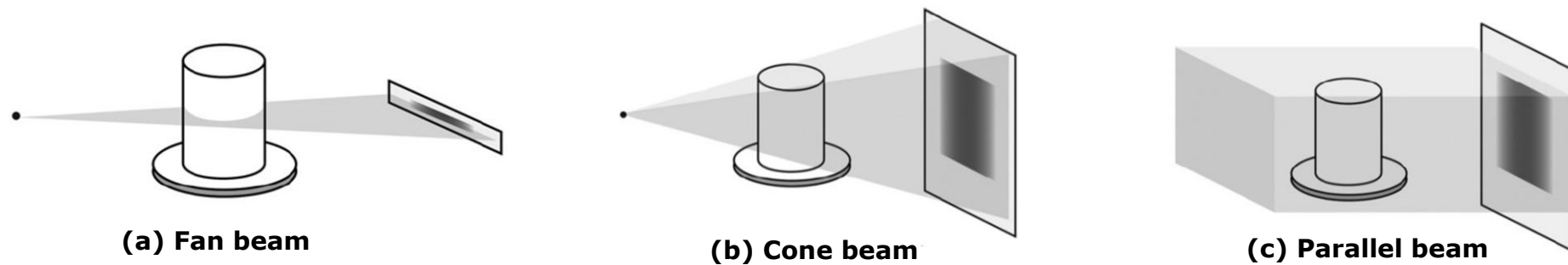
Fig. 2.33. Illustration of the different types of X-ray CT acquisition configurations using a (a) fan beam, (b) cone beam and (c) parallel beam [179].

2.7.1 Lab-based X-ray CT scanners

Conventional lab-based X-ray CT scanner typically operates using X-ray tube source that accelerates electrons to strike a heavy metal target to produce X-ray photons (Bremsstrahlung radiation). Scanning times were relatively long in the earlier CT scanners as they feature the use of a linear array of photodetectors (fan beam) that acquired and reconstructed tomographic slice images in a plane by plane manner as shown in Fig. 2.33a. Shorter scanning times were achieved with the use of 2D detectors (cone beam) that acquired complete 2D projections in a single step (Fig. 2.33b). The spatial resolution is typically limited by the X-ray beam geometry and the detector used.

2.7.2 Synchrotron X-ray CT

The use of synchrotron radiation as the X-ray source in CT scanning has significantly enhanced the imaging capabilities of the technique [180]. The emitted radiation in the synchrotron is of several orders of magnitude higher than the brightness emitted by conventional X-ray sources and this high flux characteristic offers the capability to delineate X-ray absorption contrast variations in the specimen at higher resolutions. In addition, the synchrotron radiation source offers X-ray beam collimation producing parallel X-ray beam (Fig. 2.33c) that simplifies the tomographic reconstruction algorithm. The X-ray monochromatic beam from the synchrotron source also improves the accuracy of the tomograms since there would be no energy dependence on X-ray absorption.

2.7.3 Physics of X-ray μCT

In CT, the 2D projections imaging is based on X-ray absorption physics while the conversion of the projection image series to a 3D volume representation is carried out using tomographic reconstruction mathematics.

The absorption of X-ray as it travels through a material is a logarithmic function of the material's absorptivity and the distance that the X-ray has to travel through the material. The absorptivity is dependent on the material density and type of atoms along the X-ray path and the absorption

decreases as the X-ray energy increases except near to the X-ray absorption "edges" of the element. Generally, the elements with lower atomic number have lower X-ray absorptions. Therefore, the X-ray intensity (I_X) at a particular point through the specimen can be determined using,

$$I_X = I_{0,X} \, e^{-\mu_a \, t_x} \tag{2.28}$$

where $I_{0,X}$ is the incident X-ray intensity, μ_a is the linear attenuation coefficient of the material, and t_x is the thickness of the specimen along the X-ray beam path as indicated in Fig. 2.34a. I_X can be determined experimentally by acquiring a raw projection image of the specimen such as shown in Fig. 2.34b and the incident X-ray intensity profile can be determined by capturing an image without the specimen in the field of view of the detector and is referred to as the dark field image (Fig. 2.34c). In the dark field image, the spatial variations in the incident X-ray beam and the detector can be determined. Therefore, such variations can be corrected by subtracting the dark field image from the raw projection image and the typical corrected radiograph is shown in Fig. 2.34d. In a typical CT scan, up to a few thousands of radiographs can be generated and each of them represents a projection of the specimen at the different specimen rotation angles.

The projection radiograph is a 2D map collection of a set line integrals of absorption profiles (L_Z) along the specimen rotation axis (z-axis). These absorption profiles are generated when X-rays pass through the specimen, represented by a function f (x, y), at a specific rotation angle (Fig. 2.35a). The series of these profiles acquired over an angular range can be mapped into a 2D grayscale image using Radon transform [181] to represent the raw data as a function of the angular range for image reconstruction and is referred to as the sinogram as shown in Fig. 2.35b. In the sinogram, the horizontal axis represents the detector channels while the vertical axis shows the projection angle.
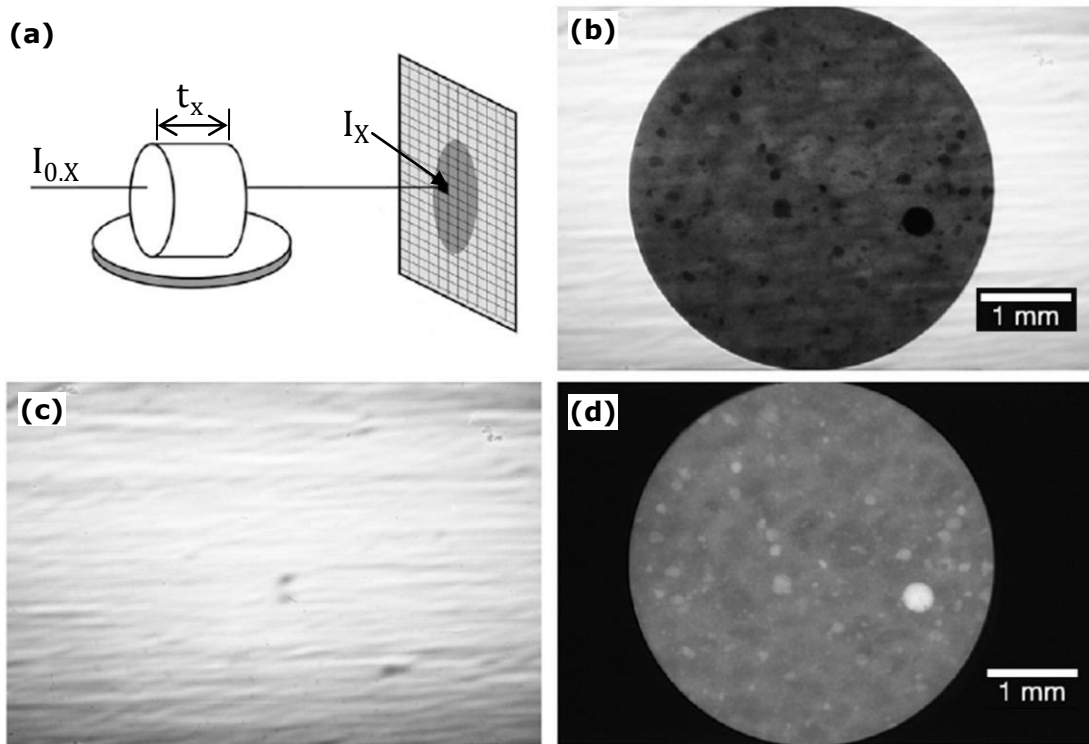
Fig. 2.34. (a) An illustration of the incident and acquired X-ray intensities through the specimen, (b) a typical I_X map, (c) the dark field map of $I_{0,X}$, and (d) the corrected radiograph [179].
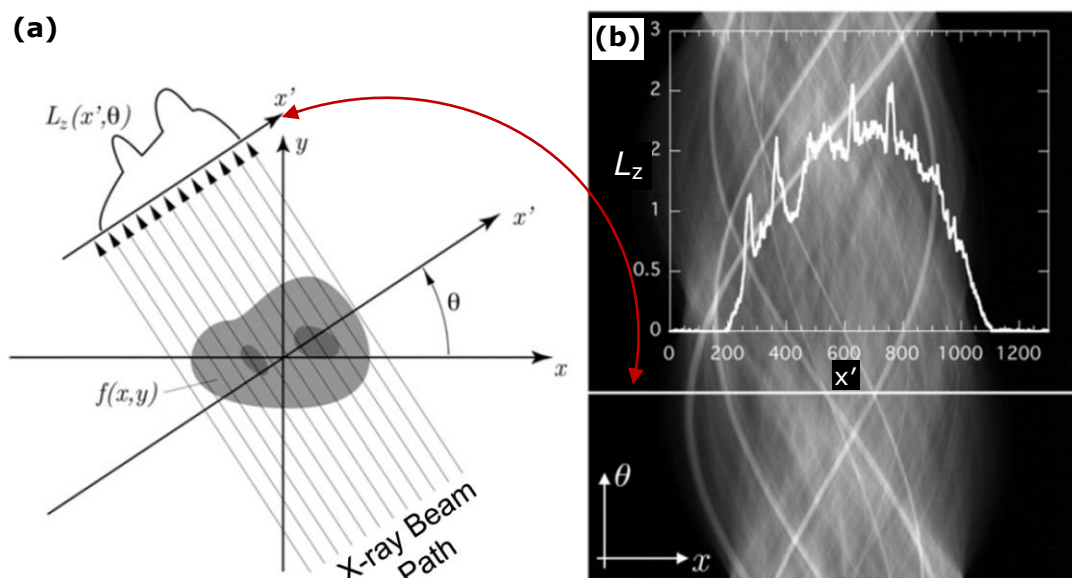
Fig. 2.35. (a) An illustration of the absorption profile generated when the X-ray beam passes through the specimen represented by a spatial function of X-ray absorption, f (x, y) at a specific specimen rotation angle and (b) the collected profiles over an angular range represented as a sinogram with a single line profile of the absorption profile superimposed [179].

The purpose of the tomographic reconstruction is to recalculate the specimen absorption function $f(x, y)$ from the projection radiographs in the sinogram. The acquired data in the projection space has to be transformed (inverse Radon transform) to the specimen space and the procedure is termed as back-projection. Several tomographic reconstruction techniques have been developed such as the filtered back-projection and direct Fourier inversion. Therefore, the Radon transform and its inverse transform operation provide the fundamental mathematics in tomographic reconstructions and details of the mathematics are described in [177].

2.8 Summary

In summary, the literature review conducted suggests that:

- The free-fall atomiser set-up offers significant advantages in terms of maintaining a relatively constant melt flow from the nozzle and the extra degree of freedom to mechanically scan the spray over a larger area.

- In order to accurately simulate the preform heat flow, the length scale problem associated with the discretisation of the Gaussian shaped depositing layer has to be addressed. The deformed mesh method described in the literature is ideal to simulate the preform shape/thermal evolution since it effectively avoids discretising the micrometer-scale shape growth at every time step.

- However, the limitation of the deformed mesh method is that the quality of the mesh deteriorates significantly as the mesh deformation grows to larger scales and thus, the deformed mesh has to be re-meshed before the accuracy of the solution deteriorates.

- There is a persisting difficulty in predicting the porosity distribution throughout the as-sprayed performs.

- In addition, most previous studies have developed numerical models for the atomisation process and preform heat flow. However, none of

them integrated a thermal stress model that simulates the preform stress distribution across the deposit-substrate interface to quantitatively assess the interfacial bonding formed.

- Neutron diffraction, a non-destructive stress measurement technique that is capable of probing at relatively large depths and measuring multiple stress types, is highly suited for characterising the stress distributions in thick as-sprayed metallic performs.

- The quantitative links between the key spray forming parameters and the interfacial bonding strength for thick as-sprayed dissimilar metallic alloys have yet to be seen reported in the literature.

- The refined equiaxed microstructures of the sprayed layer are typically developed from the fine dendritic structures of the rapidly cooled droplets due to a rapid microstructural transformation upon deposition. However, most of the understanding of this rapid microstructural change was obtained from materials that have undergone several heating/cooling cycles or heat treatment for a relatively long period. The dynamics of the microstructural change are important because increasingly in these powder-based processes, conditions are manipulated to try and minimise microstructural change or coarsening since the powders often have attractive features (refined grains and secondary phases, metastable phases, low levels of elemental segregation, etc.) that are beneficial if retained into the bulk component.

The research methodology used to address the aforementioned technical challenges in the spray forming of dissimilar metals and the key findings from this research are detailed in the subsequent chapters.

CHAPTER 3 : NEUTRON DIFFRACTION AND X-RAY EXPERIMENTS

This chapter describes the neutron diffraction experiments conducted at the ENGIN-X beamline of ISIS spallation neutron source, Rutherford Appleton Laboratory, UK. In addition, the microstructure characterisations carried out using lab-based and synchrotron X-rays are detailed in this chapter. The information in this chapter is directly relevant to the numerical model development in chapter 4 and the results described in chapter 5, 6 and 7.

3.1   Fundings and the neutron beam times awarded

The experimental studies conducted were part of the key research agenda defined in two collaborative projects funded by (1) the largest steel company in China, Baosteel Co. Ltd, and (2) the Chinese Ministry of Science and Technology:

- Baoshan Iron & Steel Co. Ltd. ("Baosteel") project – *Development of high performance products comprising dissimilar materials by spray forming"* (£254 k, 01/04/2012 – 31/03/2015). This project was led by Oxford University (OU) with Hull University (HU) as the project partner.

- Chinese Ministry of Science and Technology project – *"The atomisation and spray deposition of novel Ni-based superalloys"* (Grant No. 2012DFA50240, £700 k, 01/05/2012 – 30/04/2015). This project was led by Beijing Institute of Aeronautical Materials (BIAM) in collaboration with the UK partners, OU and HU with £150 k allocated to OU and HU.

The author's PhD supervisor, Dr. Jiawei Mi, was the UK investigator for the aforementioned projects and was awarded 3 neutron diffraction beam times from ISIS neutron source throughout the project duration. The author played the leading role in conducting those experiments and analysing the collected data accordingly. In order to carry out synchrotron X-ray microstructure characterisations, the author participated in the synchrotron X-ray beam time experiments at the TOMCAT beamline of Swiss Light Source (SLS), PSI, Switzerland and I12, I13 and I15 beamline of Diamond

Light Source (DLS), UK awarded to Dr. Mi in 2014 - 2015. In addition, the author participated and contributed to numerous other synchrotron X-ray experiments awarded to Dr. Mi throughout the course of the author's PhD study, including beam times at the sector 32-ID of Advanced Photon Source (APS), Argonne national laboratory, USA. The details of the aforementioned synchrotron X-ray and neutron beam beam times are described in Table 3.1.

ENGIN-X offered the capabilities of non-destructive strain mapping deep within thick metallic materials using the TOF diffraction technique. This diffractometer is the key instrument used to measure the residual stresses and lattice strains evolution in the sprayed metallic materials described herein. TOMCAT and I13 beamlines provided the synchrotron X-ray μCT 3D characterisation of the porosity and carbides formed in the as-sprayed materials with resolutions of up to an order of magnitude higher than lab-based X-ray μCT scanners. I12 and I15 beamlines facilitated the specimen texture analysis and carbide phase characterisation carried out in this research, respectively. The functionalities of the neutron source and beamlines used are described in this chapter followed by descriptions of the sample preparations and the experimental set-ups.

Table 3.1. The experiment proposal titles and synchrotron X-ray and neutron beam times awarded.

Experiment Dates	Proposal Title	Proposal ID	Beamline
29/02-03/03/2012 & 01-05/03/2013	Ultrafast synchrotron X-ray phase-contrast imaging study of ultrasound cavitation and its effect on nucleation and dendritic grain evolution: Phase 2 - investigation of metallic alloys	GUP 26170	32-ID-B (APS)
21/02/2013	Mapping the evolution of strains/stresses across the interface between dissimilar metallic alloys	RB1310425	ENGIN-X (ISIS)
20-25/06/2013	In situ study of optimal processing conditions to deliver embryonic nuclei for grain self-refinement in clean metals under ultrasound cavitation	EE8542-1	I12 (DLS)
22-25/02/2014	Mapping the evolution of strains/stresses across the interface between dissimilar metallic alloys	RB1320313	ENGIN-X (ISIS)
18-21/04/2014	In-situ study of the evolution of atomic structure of metallic glasses under extreme pressure	EE9902-1	I15 (DLS)
9-13/10/2014	Tomography study of 3-D dendritic crystalline microstructure in bulk metallic glass matrix composites	MT9974-2	I13 (DLS)
04-07/02/2015	Time-resolved X-ray diffraction in-situ studies of the atomic structure evolution of metallic glass and composites during solidification	EE10440	I12 (DLS)
04-07/06/2015	Mapping the evolution of strains/stresses across the interface between dissimilar metallic alloys – Phase 2	RB1510231	ENGIN-X (ISIS)
10-13/06/2015	In situ tomography study of the evolution of solidification microstructures under magnetic pulses	20141167	TOMCAT (SLS)

3.2 Spallation neutron source

3.2.1 ISIS neutron source

The ISIS spallation neutron source is currently Europe's brightest spallation source with a neutron flux of 4×10^{16} neutrons cm^{-3} s^{-1}. The schematic of the neutron source (Fig. 3.1a) shows that the linear accelerator employed to accelerate protons generated in 50 Hz up to 70 MeV. The protons are transferred into a synchrotron to be further accelerated up to 84% the speed of light. The synchrotron produces a pulsed proton beam at 800 MeV and 230 µA which is then fired at a heavy metal target housed in the target station that consists of Ta coated W target plates. The neutrons emitted from the irradiated target are moderated using water as shown in the cross-sectional schematic of the target (Fig. 3.1b). These moderated neutrons are then extracted from the moderator to the respective beamlines.

3.3 Time-of-flight neutron diffractometers

The two different types of TOF diffractometers currently in use are:

(i) Conventional TOF diffractometers that operate with separate pulses, i.e. the time between successive pulses must be sufficiently long so that the fastest neutrons cannot catch up with the slowest ones of the previous pulse. The wavelength of each neutron detected is determined from its TOF from the chopper to the detector.

(ii) Reverse TOF or Fourier diffractometers employ the use of a chopper with a comb-like structure to intermittently block the beam. In this configuration, the detected neutron may have originated from several hundreds of different pulses. The diffraction pattern is determined by a combination of different spectra measured at different chopper frequencies.

(a)

(b)
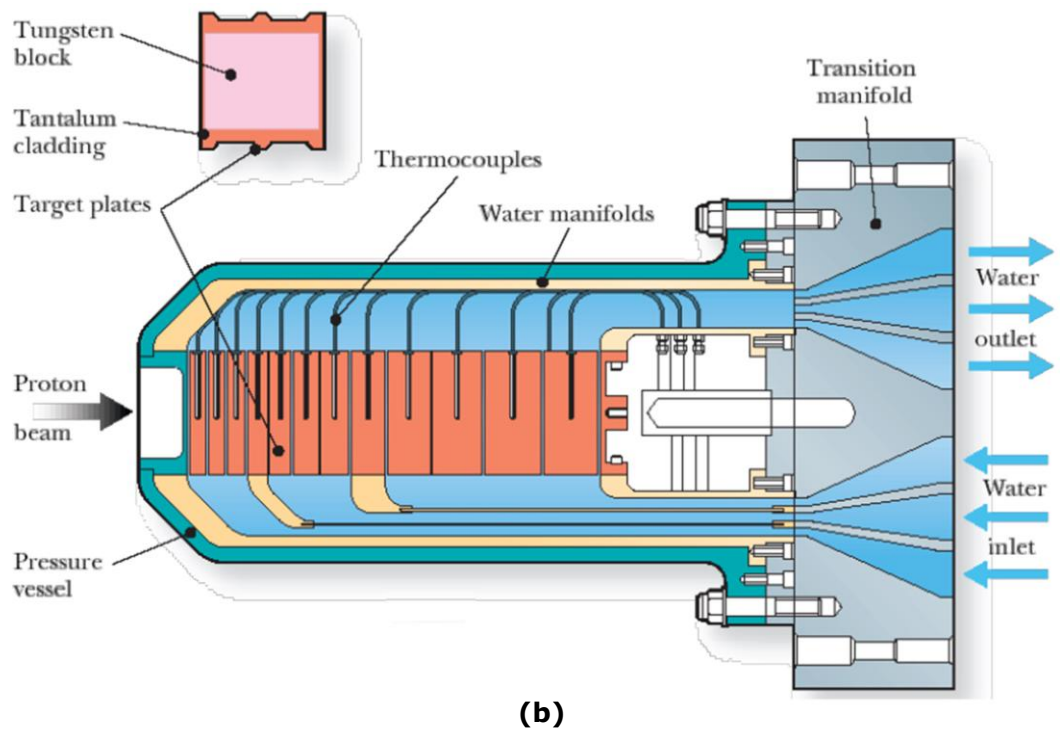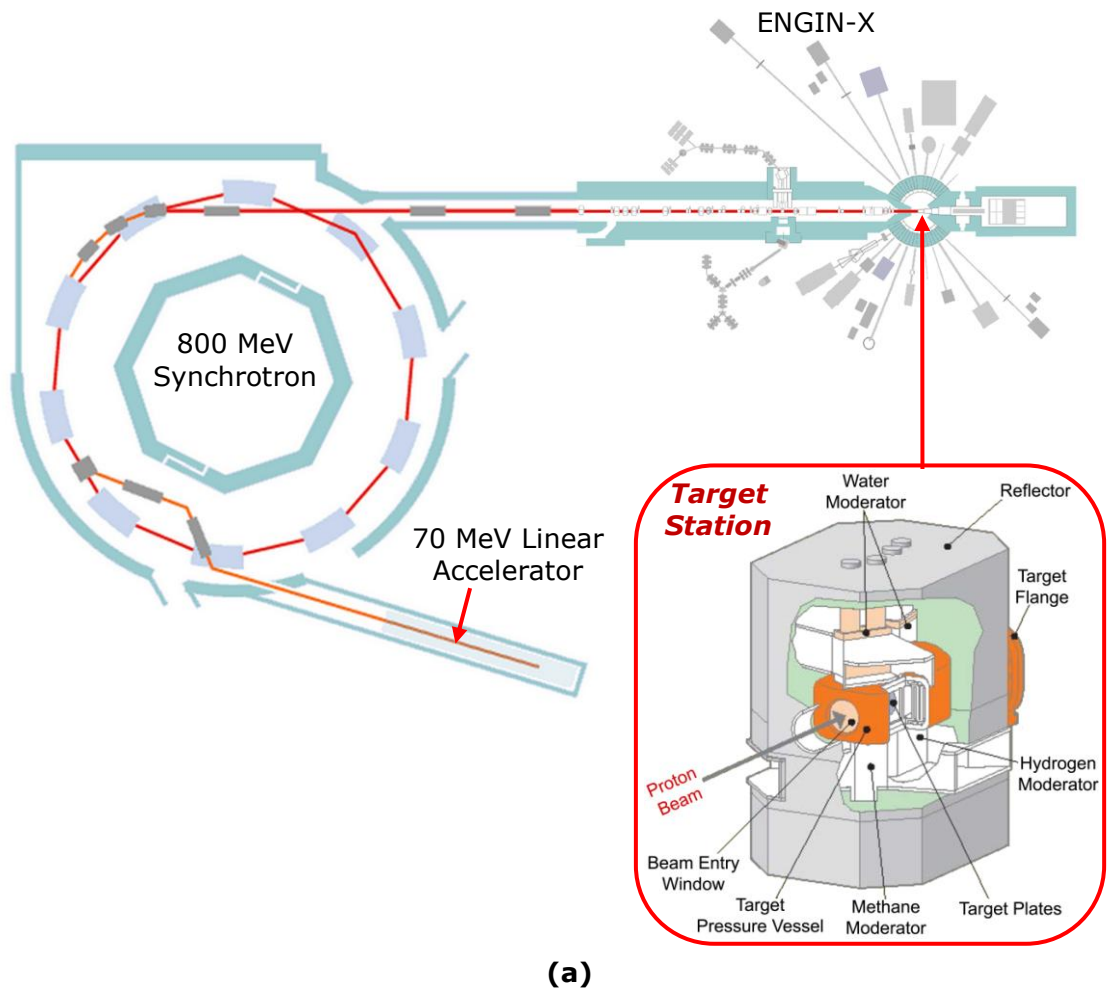
Fig. 3.1. (a) An overview schematic of the ISIS spallation neutron source [182] and (b) a cross-sectional schematic view of the target station [183].

3.3.1 ENGIN-X of ISIS

The ENGIN-X TOF diffractometer [153] housed at ISIS is a conventional type that directly determines the wavelength of the detected neutrons based on their TOF and a schematic of the instrument is shown in Fig. 3.2. The ENGIN-X beamline position in the neutron source is indicated in Fig. 3.1a. The neutron flight path from the moderator to the sample stage (positioner) is 50 m and the secondary flight path (from sample to detector) is 1.5 m.

The diffractometer uses a pulsed polychromatic beam and is optimised for strain measurements with a unique set-up of two detectors aligned at fixed scattering angles of $2\theta = \pm90°$ that allows simultaneous measurement of two strain directions. The detectors are made of 1200 ZnS/^{6}Li scintillators and each detector covers a horizontal angular range of $\pm14°$ and vertical angular range of $\pm21°$. The neutrons detected are scattered from a gauge volume (GV) defined in the sample using the incident beam slits and the outgoing beam radial collimator, and Table 3.2 shows the collimation size range.

Table 3.2. Gauge volume collimation size range at ENGIN-X. The X, Y and Z axis directions are indicated in Fig. 3.2.

Horizontal Collimating Slit X	Vertical Collimating Slit Y	Radial Collimator Z
0.2 - 10 mm	0.2 - 20 mm	0.5, 1, 2, 3 or 4 mm
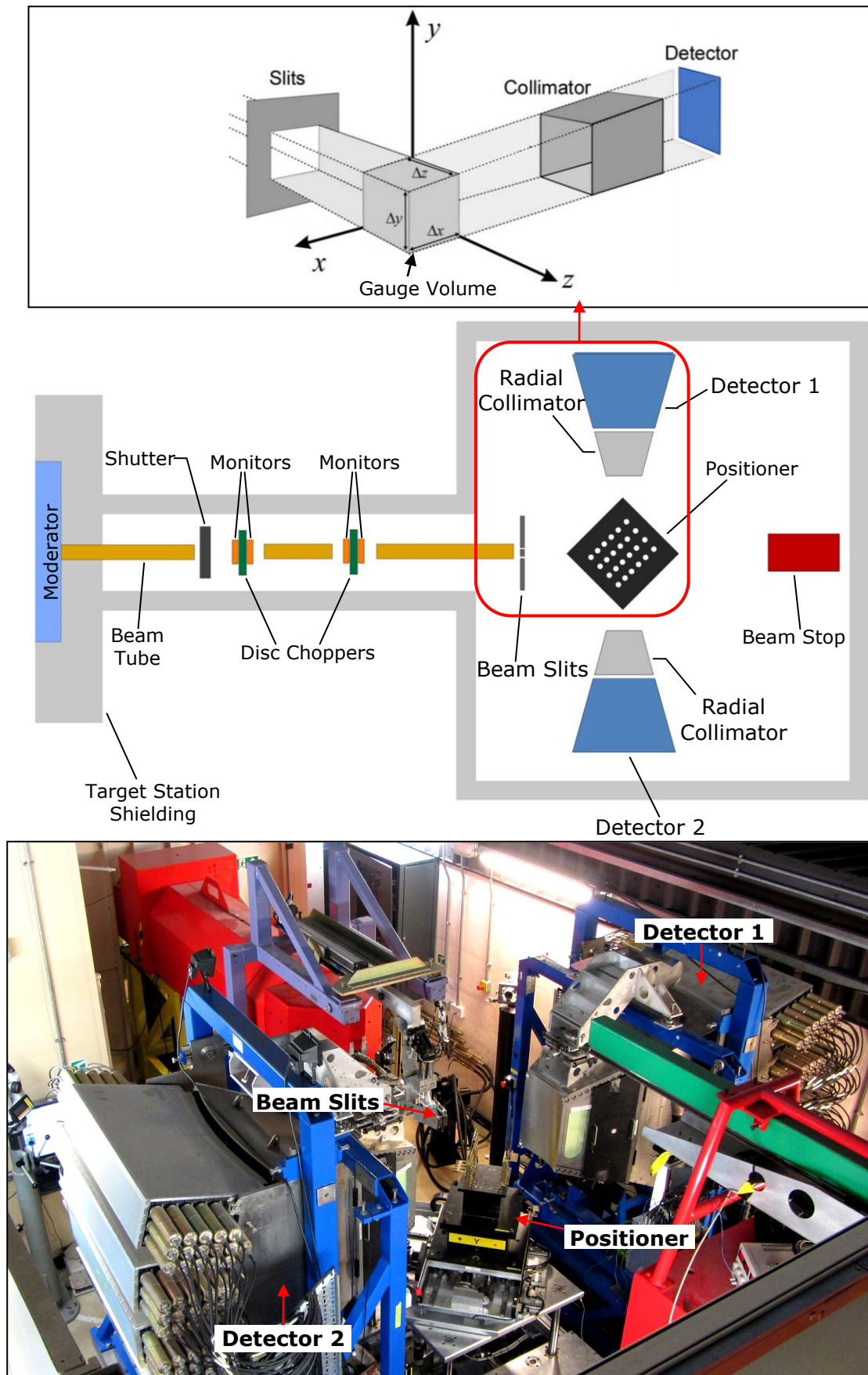
Fig. 3.2. Schematic diagram of the ENGIN-X TOF diffractometer with insets showing the gauge volume defined by the beam slits and radial collimator [153], and an overview of the experiment hutch .

3.4 The experimental apparatus

The spray forming of the preforms were carried out mainly at OU led by the researchers from Baosteel. During the course of the project duration, the author have participated in some of the key spray forming experiments as a junior academic visitor at OU for the period of 02 - 27/09/2013 to better understand the spray process and acquire the necessary parameters for the analysis and numerical modelling carried out in this research. In addition, the author have played the leading role to carry out the ND experiments to assess the quality of the interfacial bonding formed in the as-sprayed dissimilar steel preforms.

3.4.1 Sample preparation

HSS (AISI M2 and ASP30) were sprayed onto rotating and retracting mild steel tube substrates to form HSS-mild steel tube preforms using a free-fall atomiser with N_2 as the atomisation gas using the Osprey spray forming plant at OU (Fig. 3.3). The alloy droplet spray was mechanically scanned using a sinusoidal scan pattern with a fixed frequency of 16.6 Hz. Details of the key spray forming parameters used are described in Table 3.3. AISI M2 was used as the sprayed alloy in the non-preheated set-up mainly for spray process optimisation purposes due to its lower cost as compared to ASP30. Nevertheless, the key alloying elements and their composition between the two alloys are relatively similar. Thus, any effects on the interfacial bonding due to the compositional differences were expected to be minimal.

The preheating of the substrates was performed using a custom-made induction heater (Ekoheat, Ambrell Ltd. UK) operated at 37.7 kHz. The induction heater coils were installed inside the tube substrate, and a schematic of the arrangement is shown in Fig. 3.4. The initial deposition position in the preheated preform set-up was at the midpoint of the induction heater coil length where the highest preheated substrate surface temperature is achieved. The temperatures at the preform interface and surface were measured using thermocouples (TC) embedded on the substrate surface and a two-colour pyrometer (Land Instruments International Ltd.), respectively. In order to improve interfacial bonding, the substrate surface was grit blasted before spray forming.
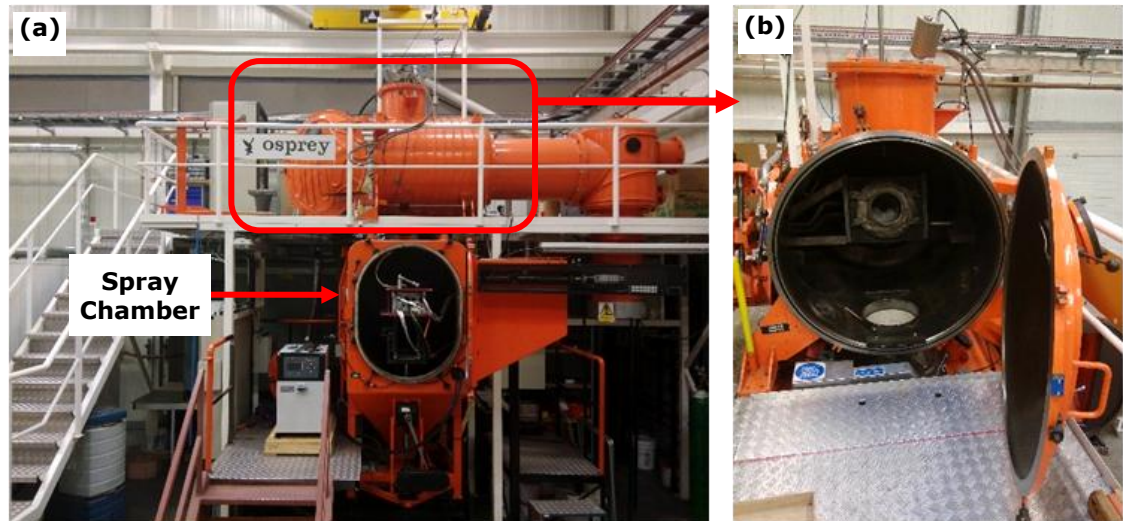
Fig. 3.3. (a) Overview of the spray forming plant at OU and (b) the melt chamber.
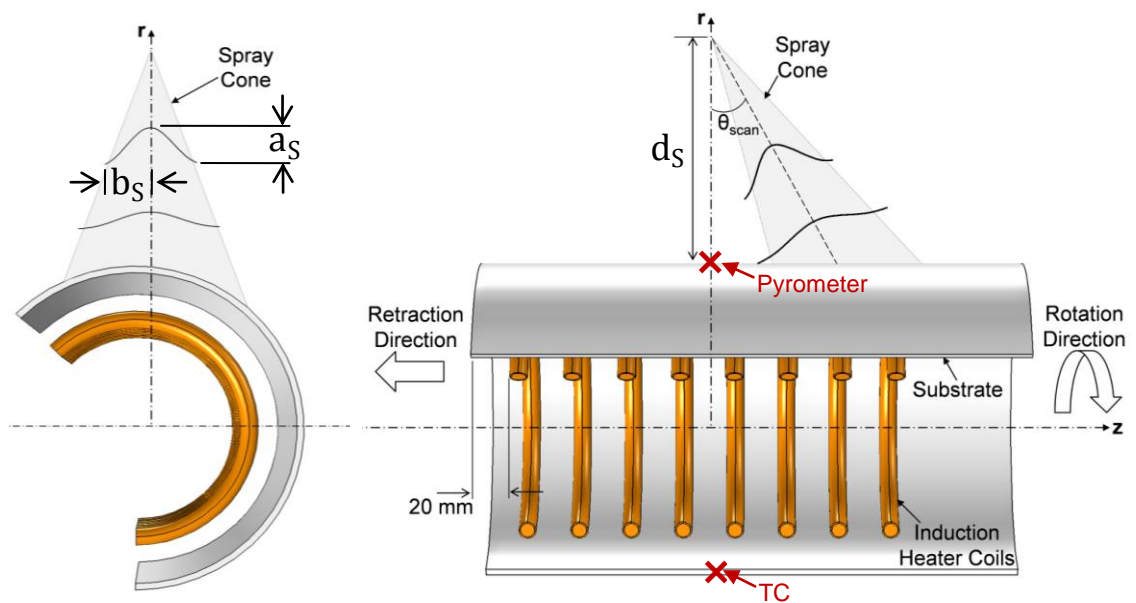
Fig. 3.4. Cross-sectional schematic views of the spray forming set-up showing the induction heater coils inside the tube substrate and the initial deposition position at the midpoint of the induction heater coil length (the maximum preheated substrate surface temperature). The pyrometer and thermocouple (TC) measurement positions are marked using red ×.

Table 3.3. Spray forming experiment parameters used at OU.

	Non-preheated		Preheated	
Preform	NP1	NP2	P1	P2
Sprayed alloy	M2	M2	ASP30	ASP30
Substrate inner diameter (mm)	104	99	144	144
Substrate thickness (mm)	3.00	1.50	3.00	3.00
Substrate rotation speed (rps)	2.00	2.20	1.70	1.70
Substrate retraction speed (mm s^{-1})	2.40	1.60	0.57	0.83
Induction heater input voltage (V)	N/A	N/A	400	450
Spray distance (mm)	500	550	600	600
Primary atomiser pressure (MPa)	0.30	0.25	0.25	0.25
Secondary atomiser pressure (MPa)	0.85	0.65	0.65	0.65
Atomiser scan angle (°)	0.00	± 2.00	± 2.50	± 2.50
Average melt flow rate (kg s^{-1})	0.65	0.32	0.29	0.32
Average gas flow rate (kg s^{-1})	0.38	0.18	0.18	0.18
Gas-to-melt flow ratio	0.52	0.56	0.61	0.56
Spray nozzle diameter (mm)	7.00	5.50	5.50	5.50
Mean sticking efficiency	0.65	0.71	0.73	0.68

Table 3.4. Spray forming experiment parameters used at Baosteel.

Preform	Multi-pass
Sprayed alloy	ASP30
Substrate inner diameter (mm)	160
Substrate thickness (mm)	10
Substrate rotation speed (rps)	1.1
Substrate retraction speed (mm s^{-1})	5.0
Induction heater input voltage (V)	N/A
Spray distance (mm)	460
Primary atomiser pressure (MPa)	1.3
Secondary atomiser pressure (MPa)	N/A
Atomiser scan angle (°)	0
Average melt flow rate (kg s^{-1})	0.5
Average gas flow rate (kg s^{-1})	N/A
Gas-to-melt flow ratio	N/A
Spray nozzle diameter (mm)	N/A
Mean sticking efficiency	0.60
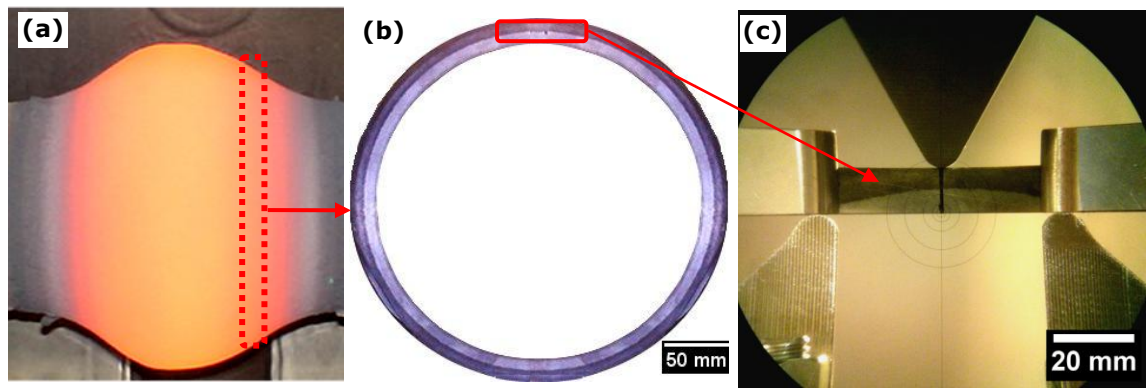
Fig. 3.5. (a) The as-sprayed multi-pass preform, (b) the etched preform cross-sectional ring slice from the deposit region showing the dense-to-porous transition region and (c) the bend test specimen sectioned from the ring slice.

After spraying, the typical cross-sectional ring shaped samples (10 mm width) were selected and cut from the as-sprayed dissimilar steel tube performs for the ND analysis. Additional cross-sectional samples were cut and polished down to 6000 grit surface finish for scanning electron microscopy (SEM) analysis of the microstructure formed at the interface.

In addition, a tube-shaped dissimilar steel prefom (Fig. 3.5a) was sprayed at Baosteel using a closed-coupled gas atomiser and N_2. ASP30 HSS was sprayed onto a 10 mm thick and 200 mm long T91 steel (nominal composition wt.% is Fe-0.1C-0.3Si-9Cr-1Mo-0.2V-0.1Nb-0.5Mn) tube substrate preheated to ~773 K with multiple spray passes under the atomised metal spray. The spray parameters used are given in Table 3.4.

A 10 mm wide and 20 mm thick ring-shaped cross-sectional sample was sectioned from one end of the multi-pass preform (Fig. 3.5a) for the ND analysis. The cross-sectional sample (deposit layer only) showed that no interfacial bonding was achieved and the preform had two distinct layers (Fig. 3.5b); a high density (dense) inner layer and a lower density (porous) outer layer. The dense layer was formed in the first few passes of the initial "hotter" spray, while the porous layer was developed in subsequent passes under a "colder" spray due to the depleting melt that reduces the melt flow rate.

Fig. 3.6 shows the SEM images of the interface region in the non-preheated and preheated preforms acquired using Cambridge Instruments Stereoscan S-360. Based on the SEM analysis of the interface region at higher magnification (Fig. 3.6e to Fig. 3.6h), interfacial bonding was seemingly formed in preform NP1 and P2. However, it is noteworthy that the bonding in preform NP1 was not continuous along the interface and length of the preform. An apparent crack was formed along the interface of preform NP2 (Fig. 3.6f) which suggests a relatively poor bond and that the deposit layer may be just attached to the substrate due to a mechanical interlock mechanism caused by the substrate surface roughness. The deposit layer in preform P1 was completely detached from the substrate surface (Fig. 3.6g). Therefore, the interfacial bond formed in the cross-sectional samples cut from preform NP1 and preform P2 were further analysed using ND.
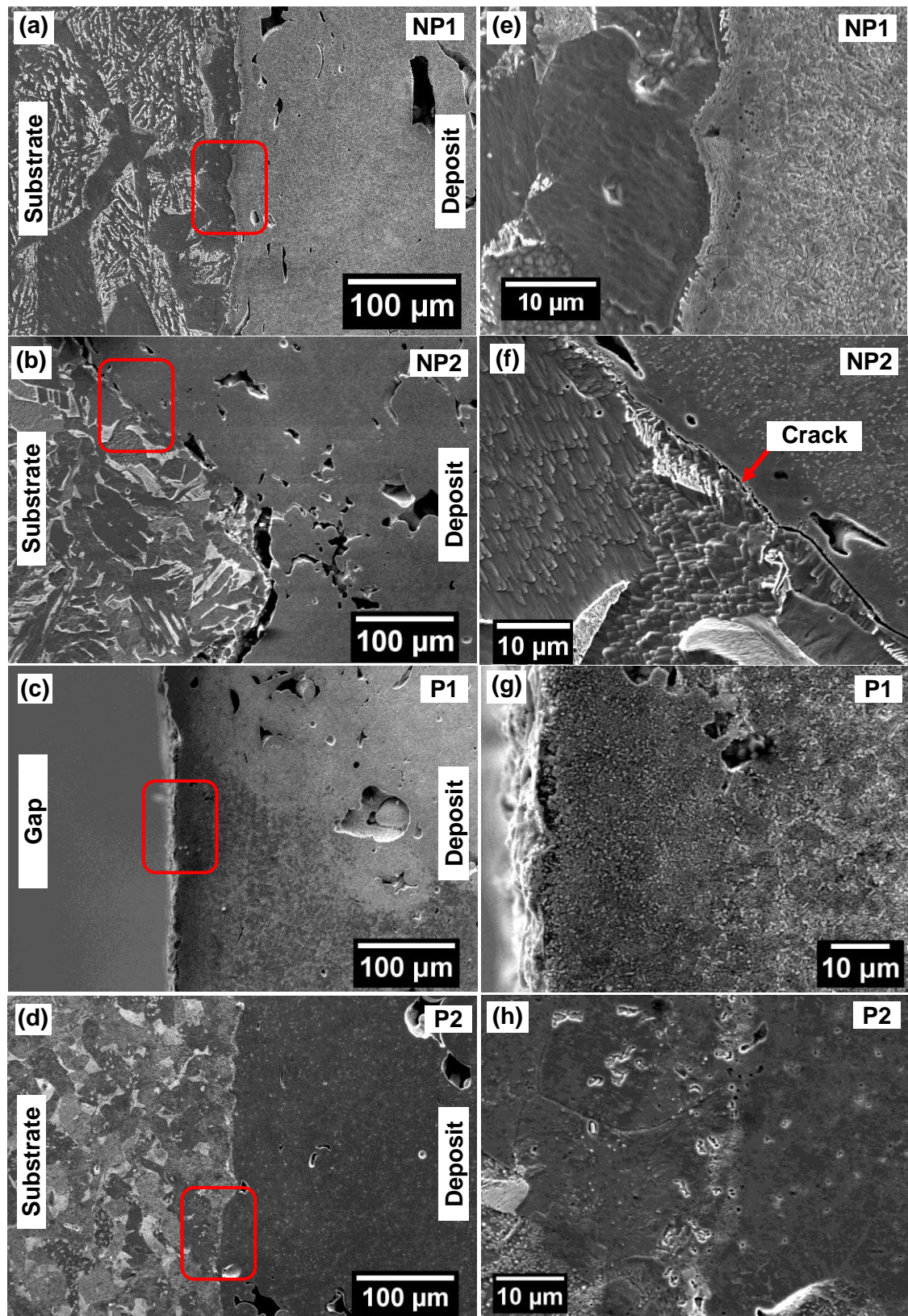
Fig. 3.6. SEM images of the interface region in preform (a) NP1, (b) NP2, (c) P1 and (d) P2 and (e-h) the corresponding images acquired at higher magnification (from the red bounding box region indicated).

3.4.2 Three point bend test rig for *in situ* ND experiments

Specimens were cut from the as-sprayed preforms in the HSS deposit and the bonded interface regions to study their deformation behaviours. The HSS specimens were cut from the as-sprayed multi-pass preform in the dense-to-porous transition region using EDM (Fig. 3.5c). In addition, specimens were cut from the bonded interface region along the tube length (Fig. 3.14a) of preform P2. The surfaces of the specimens were grinded down to 2500 grit surface finish and the final dimensions of the specimens are given in Table 3.5. Note that the specimen thickness corresponds to the preform thickness in the radial direction and is parallel with the loading axis.

The three point bend test experiments were carried out at ambient conditions in general accordance with ASTM E290 standards [184] using a bend test rig that was CNC machined in-house from EN24T steel (30 HRC) and features a pyramid-shaped (8 mm long half-round apex) crosshead (Fig. 3.7). The bend test rig schematics are shown in Appendix 1. The span between the supports (L_{Span}) was set according to ASTM E290 standards [184],

$$L_{Span} = 2r_{Crosshead} + 3t_{specimen} \pm \frac{t_{specimen}}{2} \qquad (3.1)$$

where $r_{Crosshead}$ = 5 mm is the crosshead radius as shown in Fig. 3.7c.

The bend test rig was designed to be capable of conducting *in situ* ND and *ex situ* (without ND) bending tests using adapters to suit the Instron load frames (Illinois Tool Works Inc.) at ENGIN-X and the Lloyd EZ50 load frame (AMETEK. Inc.) housed at HU, respectively. The shape and dimensions of the crosshead were optimised for strength and specifically designed to accommodate the incident and diffracted neutron beam paths from the specimen in order to maximise the neutron count rate. The modelled incident and diffracted neutron beam paths (ENGIN-X detector coverage angles) in the vertical and horizontal load axis bend test set-up are shown in Fig. 3.8a and Fig. 3.8b, respectively.
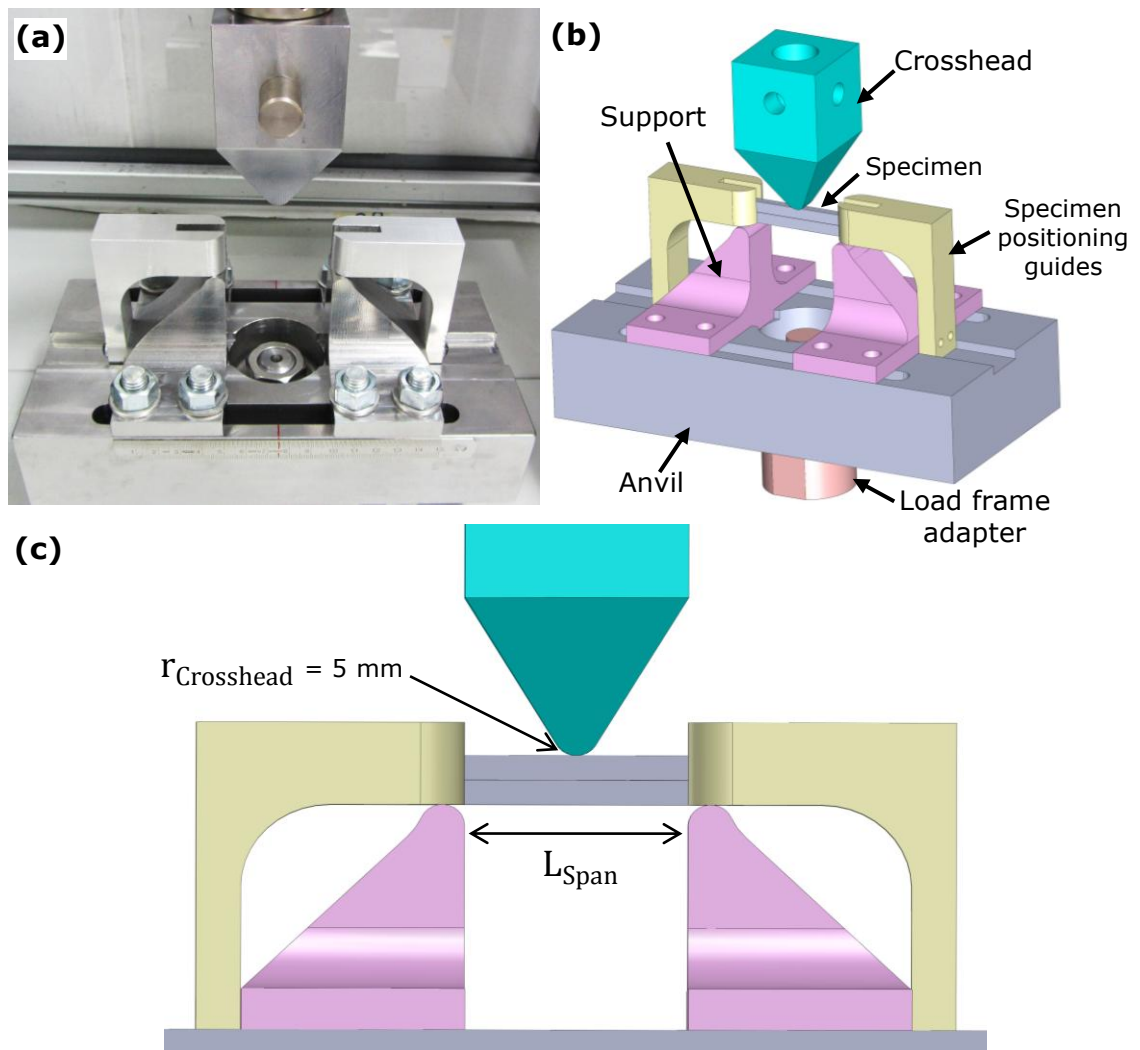
Fig. 3.7. (a) The in-house CNC machined bend test rig, (b) the 3D diagram of the rig and (c) front view of the rig showing the span between the supports and the crosshead radius.

Table 3.5. Bend test specimen cut from the as-sprayed preforms.

Preform	Region	Specimen dimensions (thickness × width × length)
Multi-pass	Deposit (dense-to-porous transition region)	11.5 × 5.0 × 75.0 mm
P2	Interface	6.2 × 7.7 × 50.0 mm
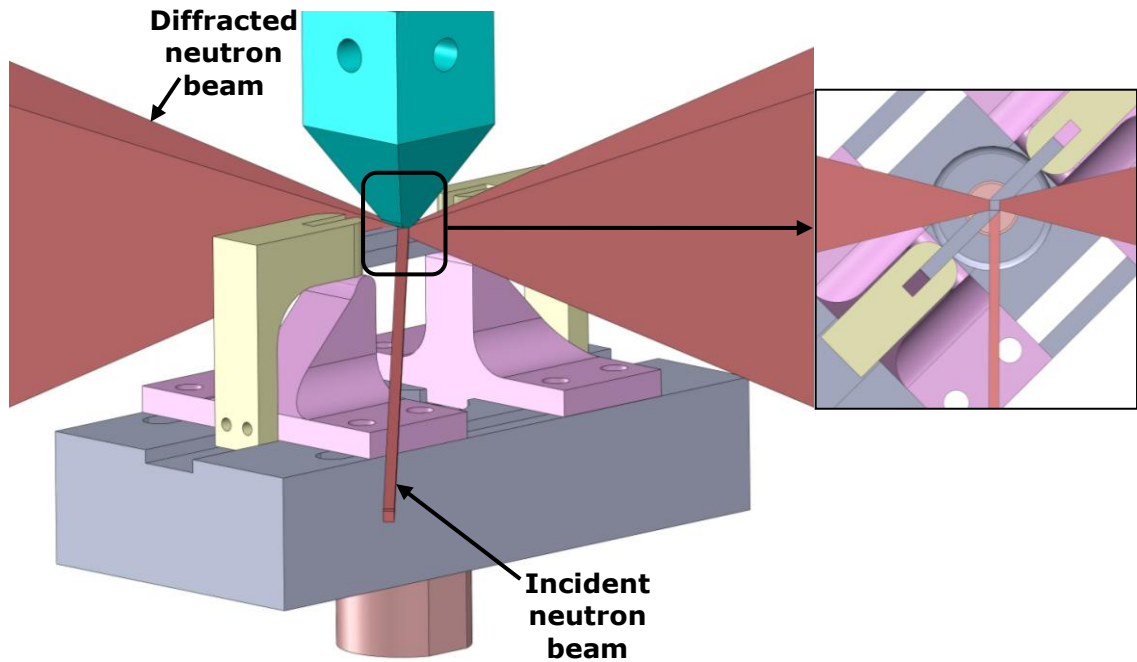
(a) Vertical Load Axis
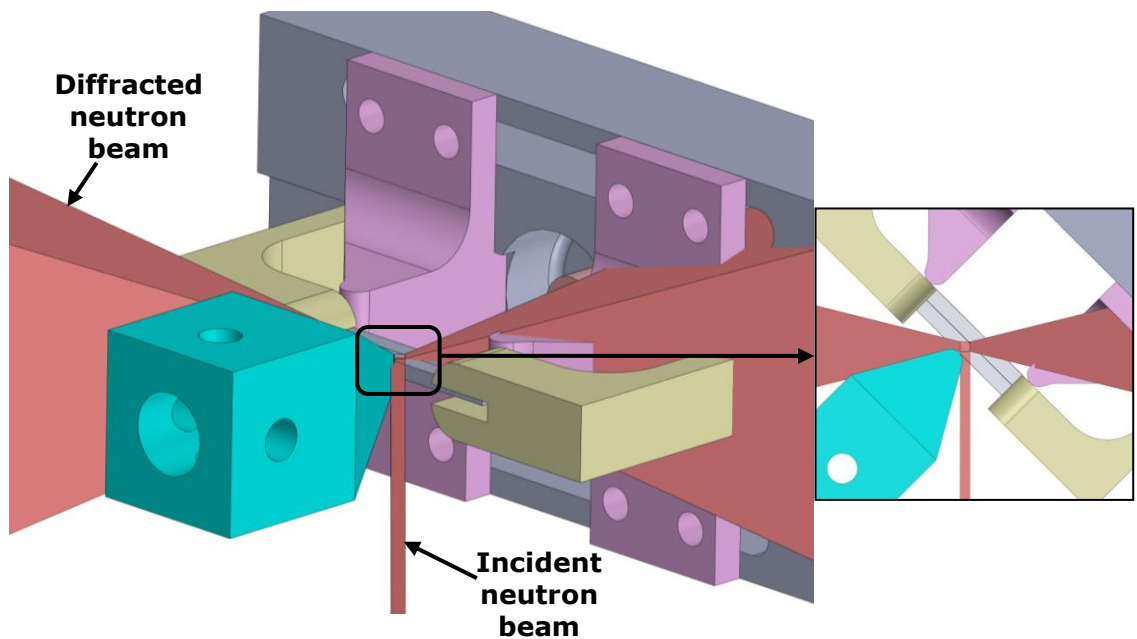
(b) Horizontal Load Axis

Fig. 3.8. The neutron beam paths in the (a) vertical and (b) horizontal load axis bend test set-up with figure insets showing the diffracted beam paths from the GV (4 x 4 x 4 mm) defined in the sample.

The bend test rig specimen positioning guides offers the flexibility of bend testing in vertical and horizontal loading orientations to acquire different principal strain direction measurements from the *in situ* ND experiment. It is noteworthy that the specimen positioning guides used do not constrain the specimen deformations and served as a safety feature to prevent the specimen from being ejected from the rig upon fracture.

3.5   Neutron diffraction residual stress experiments

3.5.1 Experimental set-up

In order to assess the interfacial bonding strength, the residual stress distributions across the interface of the selected samples were characterised using the TOF neutron diffractometer at ENGIN-X with a GV size of 2 x 2 x 2 mm. Such GV was selected for the optimal balance between the spatial resolution (especially near to the interface region) and the neutron counting times. The stress-free (d_0) samples used were 5×5 mm cross-sectional strip samples (Fig. 3.9) cut from the same ring shaped cross-sectional sample to ensure the same microstructures and phases formed along the preform thickness.
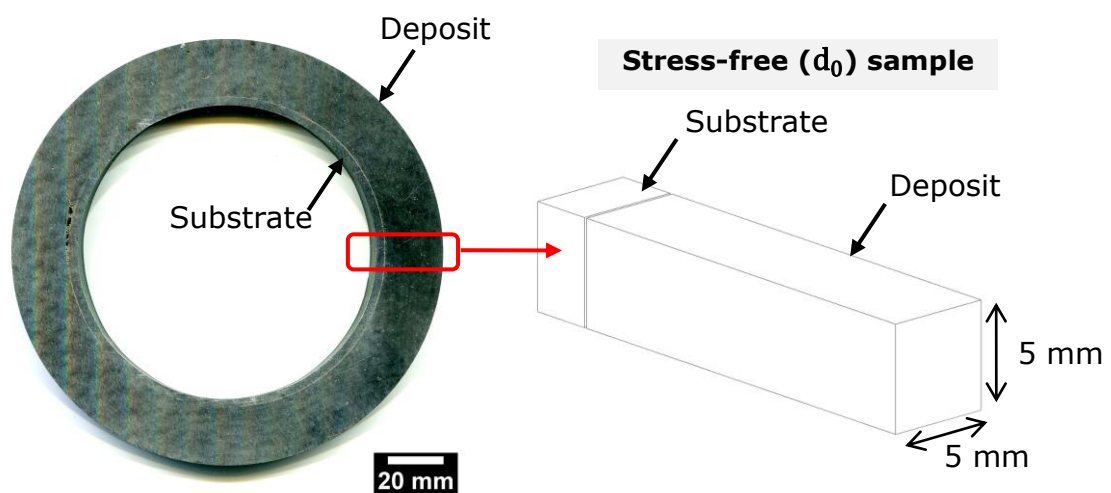
Fig. 3.9. The 5×5 mm cross-sectional sample used as the stress-free sample.
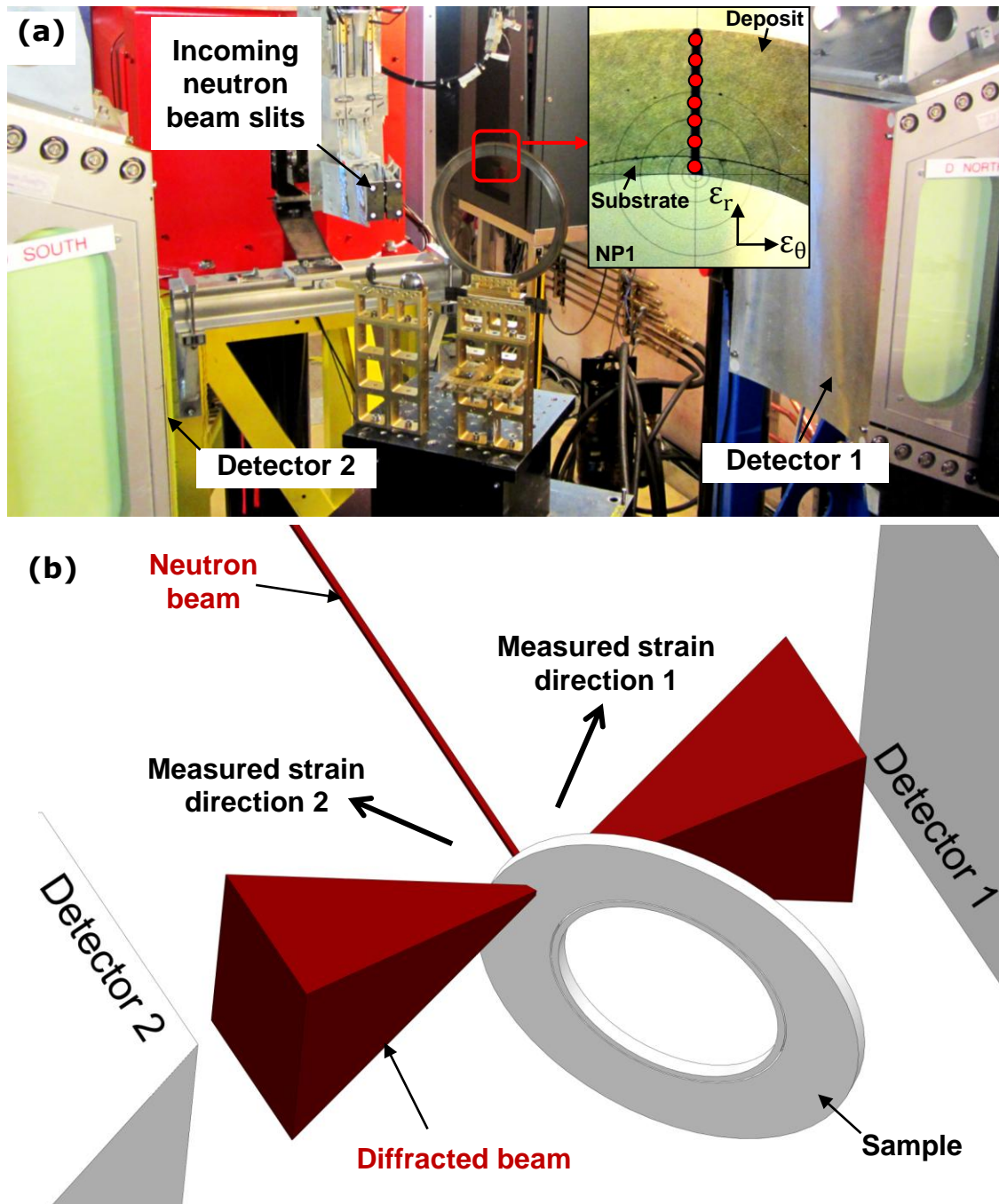
Fig. 3.10. (a) The ND experimental set-up at ENGIN-X, showing the cross-sectional sample (preform NP1) and the figure inset showing the 7 measurement points (marked as red points) taken along the preform thickness (ε_z is the out-of-plane strain direction) and (b) the schematic of the ND set-up.

A typical view and schematic of the ND experimental set-up at ENGIN-X is shown in Fig. 3.10a and Fig. 3.10b, respectively. Seven measurement points (marked as red points) were taken along the preform thickness and the hoop (ε_θ), axial (ε_z) and radial (ε_r) strains were measured. Due to the GV size and substrate thickness (3 mm), the substrate was limited to one measurement point to ensure a completely filled GV of the respective material in the dissimilar steel sample.

On the other hand, a larger GV was used to measure the residual stress distribution in the cross-sectional sample cut from the multi-pass preform that comprised of the dense-to-porous transition region with scan steps of 1 mm. A GV of 1 × 4 × 4 mm (1 mm in the ε_r direction) was used for ε_θ and ε_z measurements while 4 × 4 × 4 mm was defined for ε_r. The different GV was used to maintain a symmetrical GV shape. The stress-free sample used was a 5 × 20 × 30 mm (20 mm in the ε_r direction) coupon cut from the cross-sectional sample.

The diffractograms acquired showed that the dominant phases in the as-sprayed HSS were martensite (α'-Fe) and retained austenite (γ-Fe) and that the porous region consists of more α'-Fe (Fig. 3.11a). The microstructural change along the preform thickness will be discussed in relation to the preform thermal history and the residual stress development later in Chapter 5.
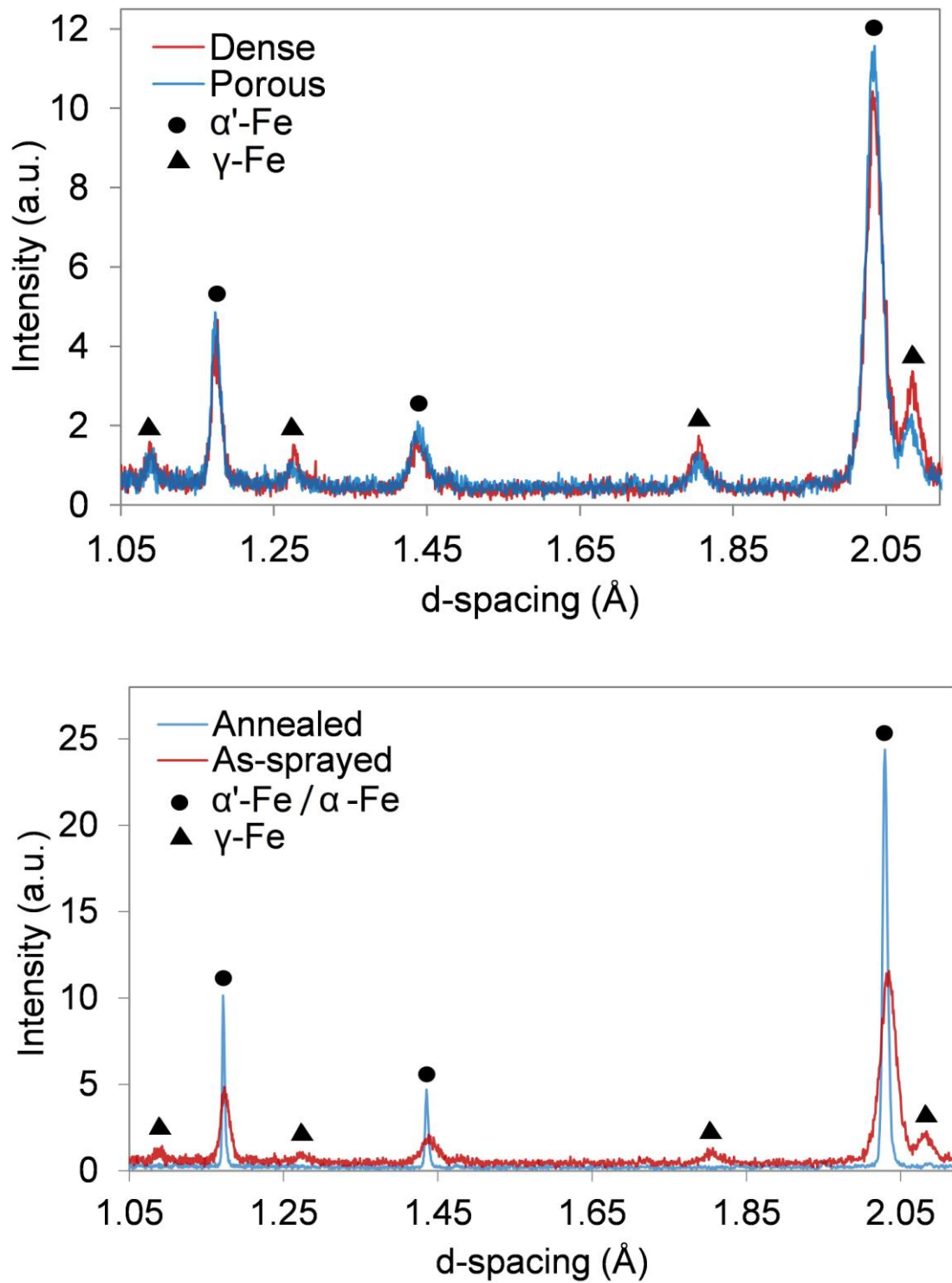
Fig. 3.11. (a) The TOF diffractograms acquired from the as-sprayed HSS in the dense and porous regions and (b) the diffractogram obtained from an annealed stress-free sample showing the microstructural change.

3.5.2 Determination of the stress-free lattice spacing

The accuracy of the strains/stresses determined from the ND experiments depends on the d_0 lattice spacing measured with the same experimental configuration used. Generally, the stress-free lattice spacing can be determined from (1) fillings or powders of the sample, (2) measurement from an unstressed region of the component, and (3) small coupons cut from the sample to relieve the macro-stress [185].

In this study, the d_0 lattice spacing was determined from small coupons cut from the preform. The typical d_0 samples used were cut with 5 x 5 mm cross-sections in order to accommodate the size of the GV used at the respective beamlines. Some of the d_0 samples were annealed (1173 K and then cooled at 10 K hr^{-1} to 973 K and natural cooling to room temperature) to obtain stress-free lattice parameter measurement. However, the heat treatment changed the as-sprayed microstructure and caused the decomposition of γ-Fe (Fig. 3.11b). Therefore, as-sprayed d_0 samples were used in the experiments and Fig. 3.12 shows the phase weight fraction (PWF) distributions in the ring-shaped cross-sectional and d_0 samples. The samples were measured using the same scan configurations and the PWF showed that there were consistent microstructure variations along the preform thickness between the the ring-shaped cross-sectional and d_0 samples.
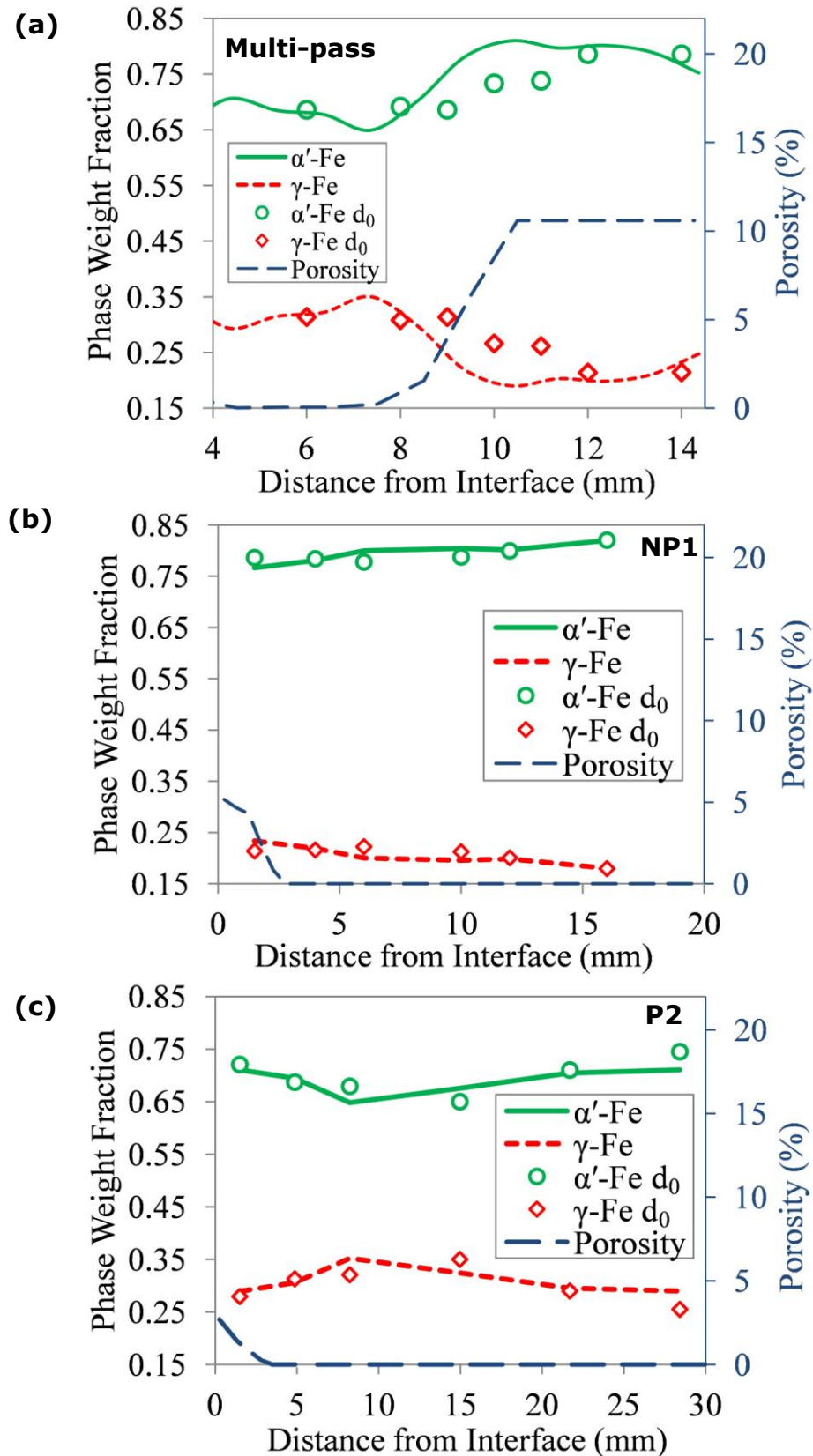
Fig. 3.12. The phase weight fraction distributions along the preform thickness from the ring and d_0 samples cut from the as-sprayed (a) multi-pass, (b) NP1 and (c) P2 preforms with the corresponding porosity distributions superimposed.

3.6 *In situ* neutron diffraction bend test experiments

3.6.1 Dense-to-porous transition region specimen

The in-house machined bend test rig was mounted onto the Instron uniaxial hydraulic load frame at ENGIN-X using both horizontal and vertical load frame orientations to measure three orthogonal principal strain directions (ε_I, ε_J and ε_K) *in situ* across the dense-to-porous transition region in the HSS specimen cut from the multi-pass preform (Fig. 3.13a) during the bend test. The strain directions are indicated in Fig. 3.13b with ε_K assigned as the out-of-plane strain direction. In both load frame orientations, the specimen position guides were used to align the specimen directly below the crosshead. GV of 1 × 4 × 4 mm (1 mm along the specimen thickness) was used for ε_I and ε_K, while 4 × 4 × 4 mm was defined for ε_J. Due to the ε_J scan orientation, the larger GV was necessary to maintain a symmetrical GV shape.

The ε_I and ε_K were measured from the vertically oriented 50 kN Instron load frame set-up that was aligned 45° to the incident beam (Fig. 3.13d). A 100 kN Instron load frame was used for the ε_J measurements and the loading axis was oriented horizontally and at 45° to the incident beam (Fig. 3.13e). In the horizontal load frame orientation, ε_I measurements were not recorded as the thick bend test rig anvil completely blocked the diffracted beam from the detector. A crosshead speed of 0.1 mm min^{-1} (16 N s^{-1}) was used and a preload of 35 N was applied to hold the specimens in place to acquire the d_0 measurements.
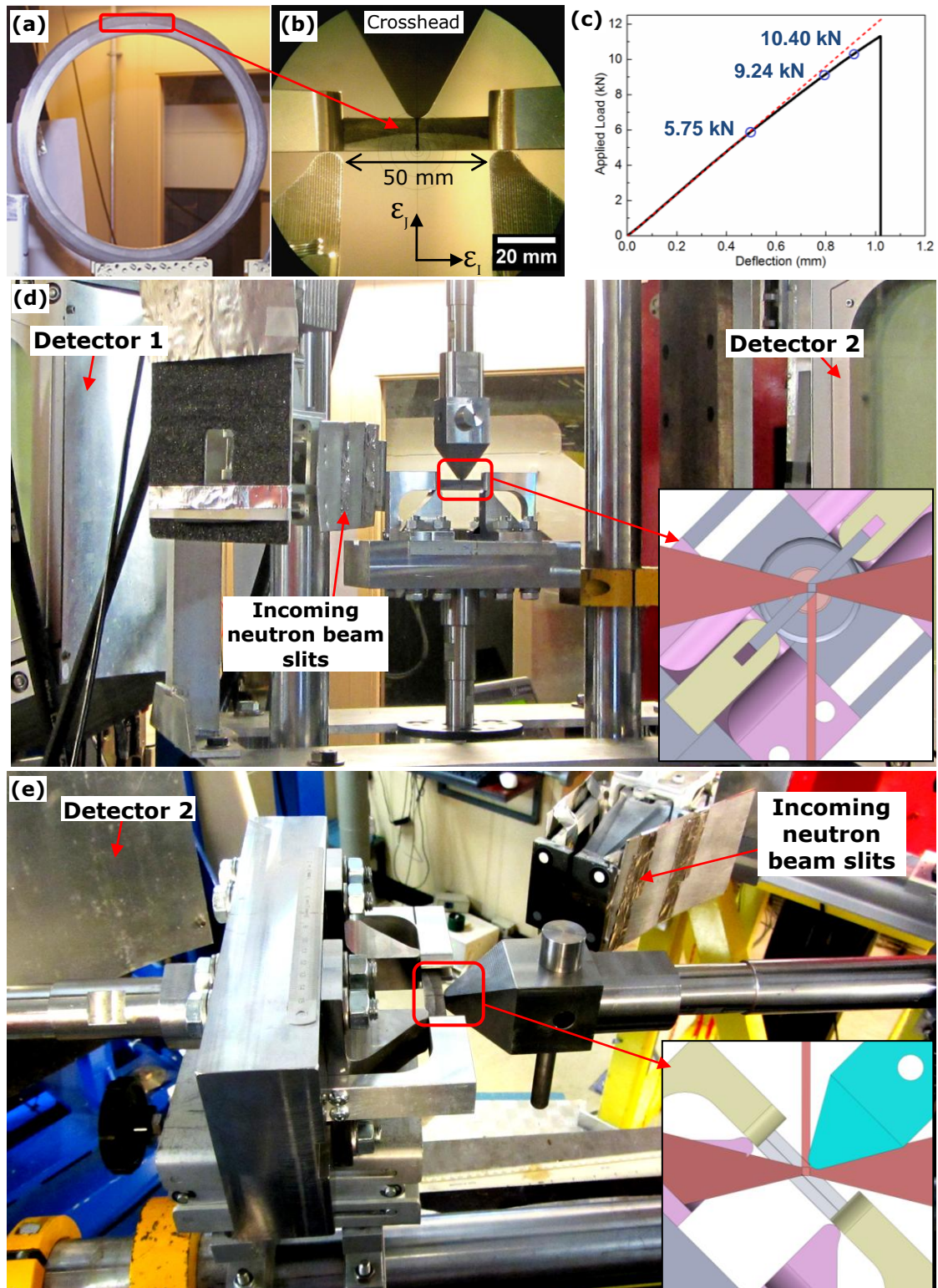
Fig. 3.13. (a) The cross-sectional sample cut from the multi-pass preform showing where the specimen was extracted, (b) the specimen positioned on the rig prior to bending, (c) load-deflection curve from the *ex situ* bend test, (d) the *in situ* ND bend test experimental set-up in vertical orientation for ε_I and ε_K measurements and (e) horizontal orientation for ε_J measurement. The figure insets show the modelled incident and diffracted neutron beam clearance from the bend test rig on the beam line.

The ND measurements were acquired at loads (5.75, 9.24 and 10.40 kN) that were representative of the material's behaviours at the onset of elastoplastic and plastic deformation according to the load-deflection curve (Fig. 3.13c) obtained from the *ex situ* three-point bend test results carried out using the 50 kN Lloyd Instruments uniaxial load frame with a crosshead speed of 1 mm min^{-1} and preload of 50 N. The applied load was held constant during the ND measurement intervals before the subsequent loads. A total scan time of ~4.5 h was required to complete each scan point along the specimen thickness at each load and the scan step size used was 1 mm. During the bend test, the preset scan point positions will shift progressively as the specimen deforms at increasing loads. In order to ensure the measurement point positions were comparable at the different loads, the rig set-up was displaced according to the loading rig crosshead travel distance from the previous load level before the subsequent set of measurements were taken.

3.6.2 Bonded interface region specimen

The specimens with a bonded interface cut from preform P2 along the preform length (Fig. 3.14a) were bend tested using the 50 kN Lloyd Instruments uniaxial load frame with a span between the support set at 30 mm and the crosshead speed used was 0.1 mm min^{-1} with a preload of 35 N (Fig. 3.14b). The specimen was loaded from the deposit side to investigate the function and strength of the sprayed HSS to act as the protective coating to the underlying mild steel substrate. The load-deflection curve (Fig. 3.14c) showed that the elastic limit of the as-sprayed dissimilar steel specimen was at ~2 kN and the HSS layer failed at ~4.565 kN and a deflection of ~0.9 mm. The specimen did not fracture completely after the HSS layer failed due to the more ductile mild steel substrate.
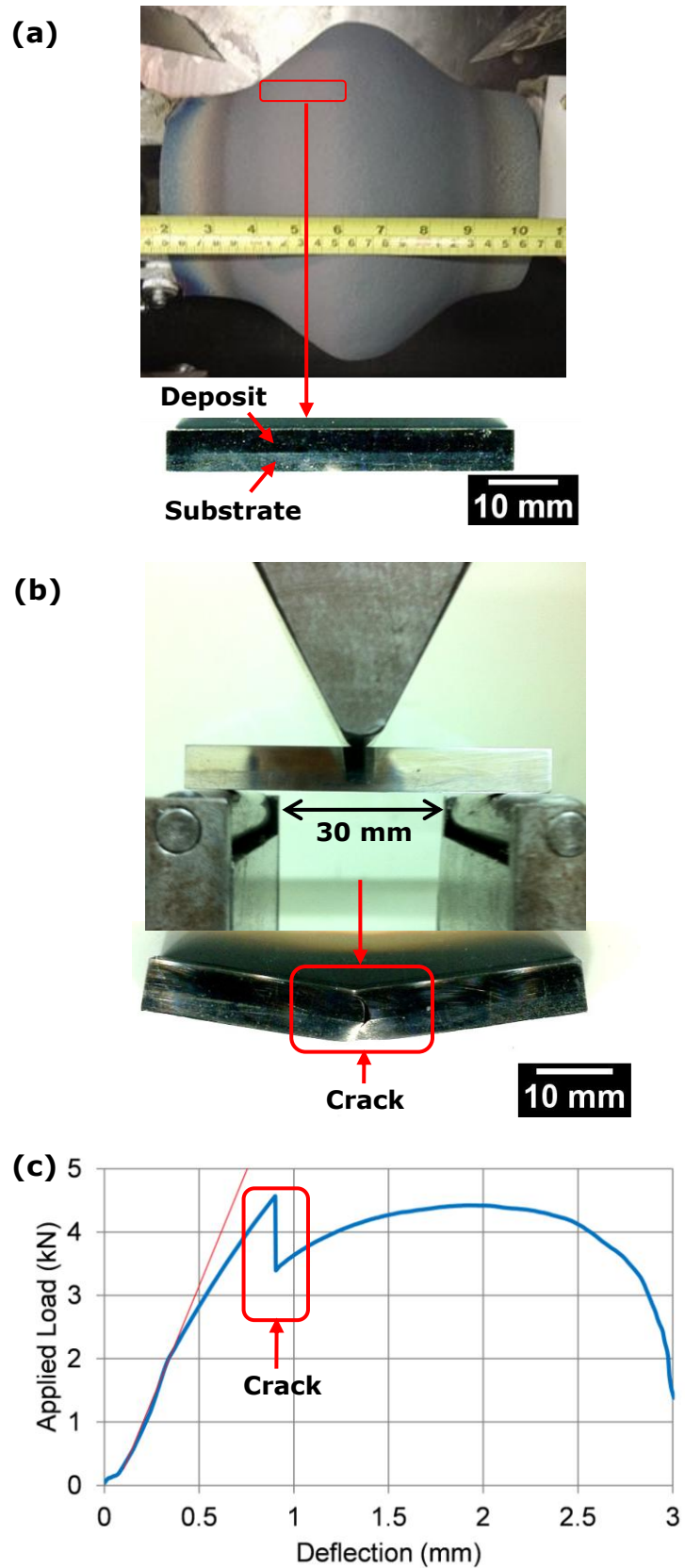
Fig. 3.14. (a) The typical specimen with a bonded interface cut along preform P2 length, (b) the *ex situ* bend test set-up showing the loading direction and the crack in the HSS layer after the bend test and (c) the load-deflection curve from *ex situ* bending test.

The *in situ* ND deformation study was carried out at loads from the elastic (0.5 and 1.5 kN) and plastic (2, 3 and 4 kN) regions based on the load-deflection curve shown in Fig. 3.14c. The *in situ* ND strain measurements were carried out at ENGIN-X using a GV size of 1 x 4 x 4 mm (1 mm along the specimen thickness) with a total of five scan points along the specimen thickness at each load; two scan points were acquired from the 3 mm thick substrate. The in-house machined bend test rig was mounted onto the vertically oriented 50 kN Instron load frame set-up that was aligned 45° to the incident beam in ENGIN-X (Fig. 3.15); and the ε_I and ε_K (out-of-plane strain direction) were measured in this orientation. A crosshead speed of ~0.1 mm min^{-1} (16 N s^{-1}) was used and a preload of 100 N was applied to hold the sample in place for the strain measurements. The applied load was held constant during the strain measurement intervals before the subsequent loads. A total scan time of ~3 h was required to measure the five scan points along the specimen thickness at each load. During the bend test, the rig set-up was displaced according to the loading rig crosshead travel distance from the previous load level before the subsequent set of measurements were taken to ensure comparable measurement point positions at the different loads.
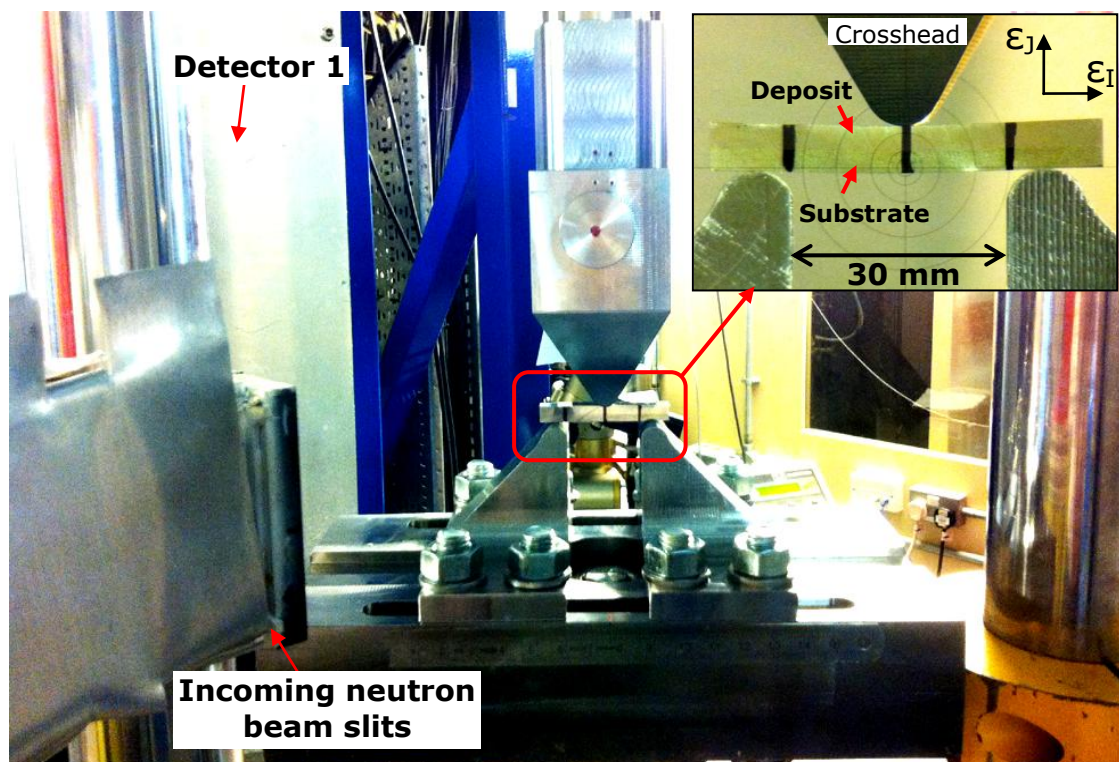
Fig. 3.15. The ND set-up at ENGIN-X used to bend test the specimen with a bonded interface cut from preform P2.

3.6.3 Stress-free lattice parameters

When subjected to the bending stress, the crystal lattice deforms with respect to the stress induced at different regions in the specimen. Therefore, the elastic lattice strains at different regions of the specimen along the scan path were calculated relative to the corresponding d_0 lattice parameters measured at the preload condition. Any residual stresses or strains that may exist in the specimen were neglected.

3.7   Neutron diffraction data analysis

TOF diffractograms are most commonly fitted using the Rietveld refinement method [186] to derive the lattice spacing by performing a whole-pattern fitting algorithm. This method has been shown both experimentally and theoretically to provide excellent representation of the bulk elastic response of the material [187]. Therefore, the peaks in the diffractograms acquired from ENGIN-X were fitted (Fig. 3.16) using Rietveld refinement with general structure analysis system (GSAS) [188] to obtain the lattice parameters and PWF. Phase analysis via ND yields reliable results since the relatively large GV defined deep within the measured sample provide diffraction patterns more representative of the bulk sample [189]. In addition, the whole-pattern fitting method averages and minimises the effects of preferred orientations. Detailed information regarding the PWF analysis using Rietveld refinement is available from [189].
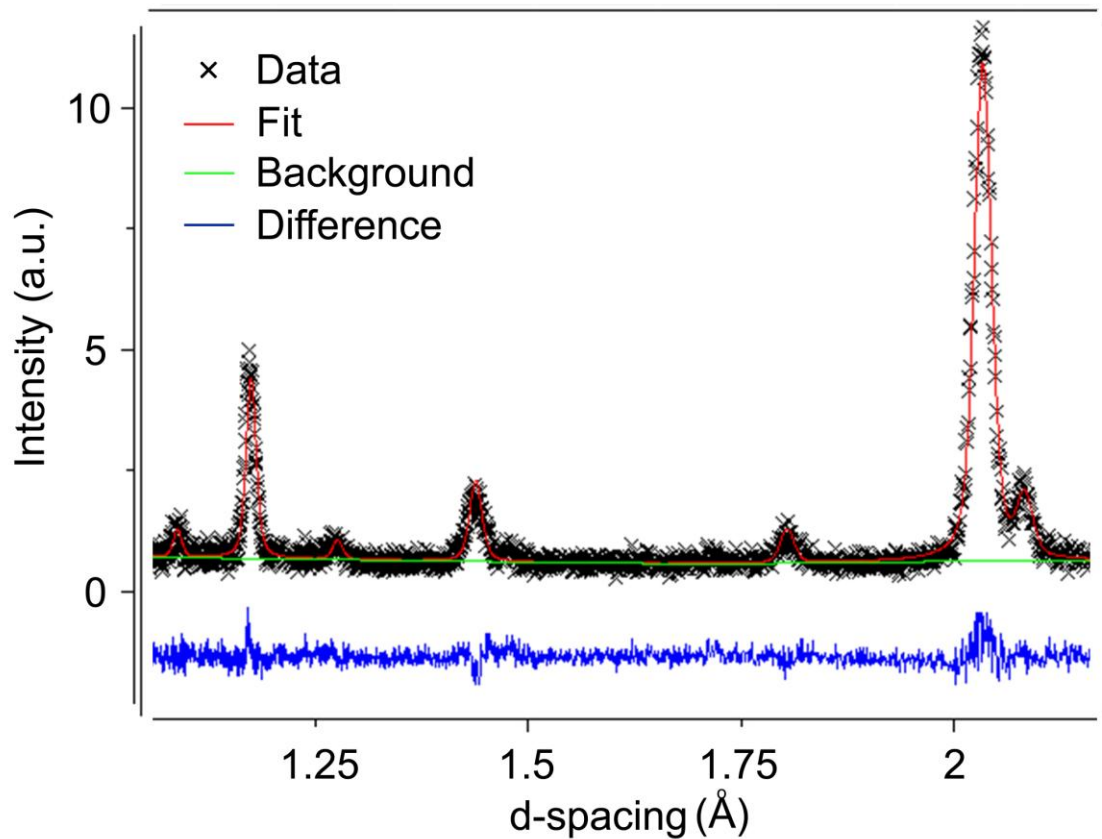
Fig. 3.16. The typical fitted neutron TOF diffractogram using Rietveld refinement.

In order to determine the stress or strain tensor at the GV, strain measurements in six different directions are typically required [190, 191]. Nevertheless, the principal stress directions can be derived and in most cases three strain directions are sufficient to calculate the principal stresses due to symmetry [154]. In the residual stress measurement ND set-up used, the ε_θ, ε_z and ε_r strains were measured from each scan point along the as-sprayed preform thickness. The residual strains in the samples were derived using,

$$\varepsilon = \frac{d - d_0}{d_0} \qquad (3.2)$$

The corresponding residual stresses, σ_P can be calculated from the measured strains using Hooke's law:

$$\sigma_P = \frac{E}{1 + \nu}\left[\varepsilon_P + \frac{\nu}{1 - 2\nu}(\varepsilon_r + \varepsilon_\theta + \varepsilon_z)\right] \qquad (3.3)$$

where the subscript "P" denotes the respective principal stresses, E is the Young's modulus and $\nu = 0.3$ is the Poisson's ratio of steel. The uncertainties in the stresses derived, $\Delta\sigma_P$ were calculating using [155],

$$(\Delta\sigma_P)^2 = \left(\frac{A_{err}}{d_0}\right)^2 \left[\begin{array}{l} B_{err}(\Delta d_P)^2 + C_{err}^2(\Delta d_0)^2 + \\ D_{err}^2((\Delta d_r)^2 + (\Delta d_\theta)^2 + (\Delta d_z)^2) \end{array} \right]$$

$$A_{err} = \frac{E}{1+\nu}, B_{err} = \frac{1}{1-2\nu}, C_{err} = \frac{1+\nu}{1-2\nu}, D_{err} = \frac{\nu}{1-2\nu}$$

(3.4)

ɑ'-Fe and γ-Fe are the typical dominant phases in as-sprayed HSS alloys [151, 192] and the bulk residual stress ($\sigma_{\alpha'+\gamma}$) can be determined from the phase-specific residual stress using a rule-of-mixture [193]:

$$\sigma_{\alpha'+\gamma} = f_{\alpha'}\sigma_{\alpha'} + f_\gamma\sigma_\gamma$$

(3.5)

where $f_{\alpha'}$, f_γ, $\sigma_{\alpha'}$ and σ_γ are the phase weight fraction and stress of the ɑ'-Fe and γ-Fe phase, respectively. The phase-specific stresses were calculated using Eqn. (3.3) with the Young's modulus of each phase estimated from the corresponding steel i.e. 200 GPa for ɑ'-Fe and 193 GPa for γ-Fe [194]. Fig. 3.17a shows the typical bulk residual stress in the hoop direction determined based on the PWF distribution. A similar approach was used to determine the lattice strains, phase-specific stress, bulk stress and their respective measurement uncertainties from the *in situ* ND bend test study. The lattice strains of the individual *hkl* planes from the bend test were derived through single peak analysis using GSAS.

Based on the ND derived PWF distributions, the local CTE (ɑ'-Fe + γ-Fe) along the preform thickness can be calculated using rule-of-mixture similar to Eqn. (3.5) with the CTE of ɑ'-Fe (= 11.6 µ K^{-1}) and γ-Fe (= 18.7 µ K^{-1}) [194]. The derived local CTE distributions (Fig. 3.17b) in the as-sprayed preforms were mapped and incorporated in the numerical model described in Chapter 5 to take into account their effects on the residual stress development during cooling.
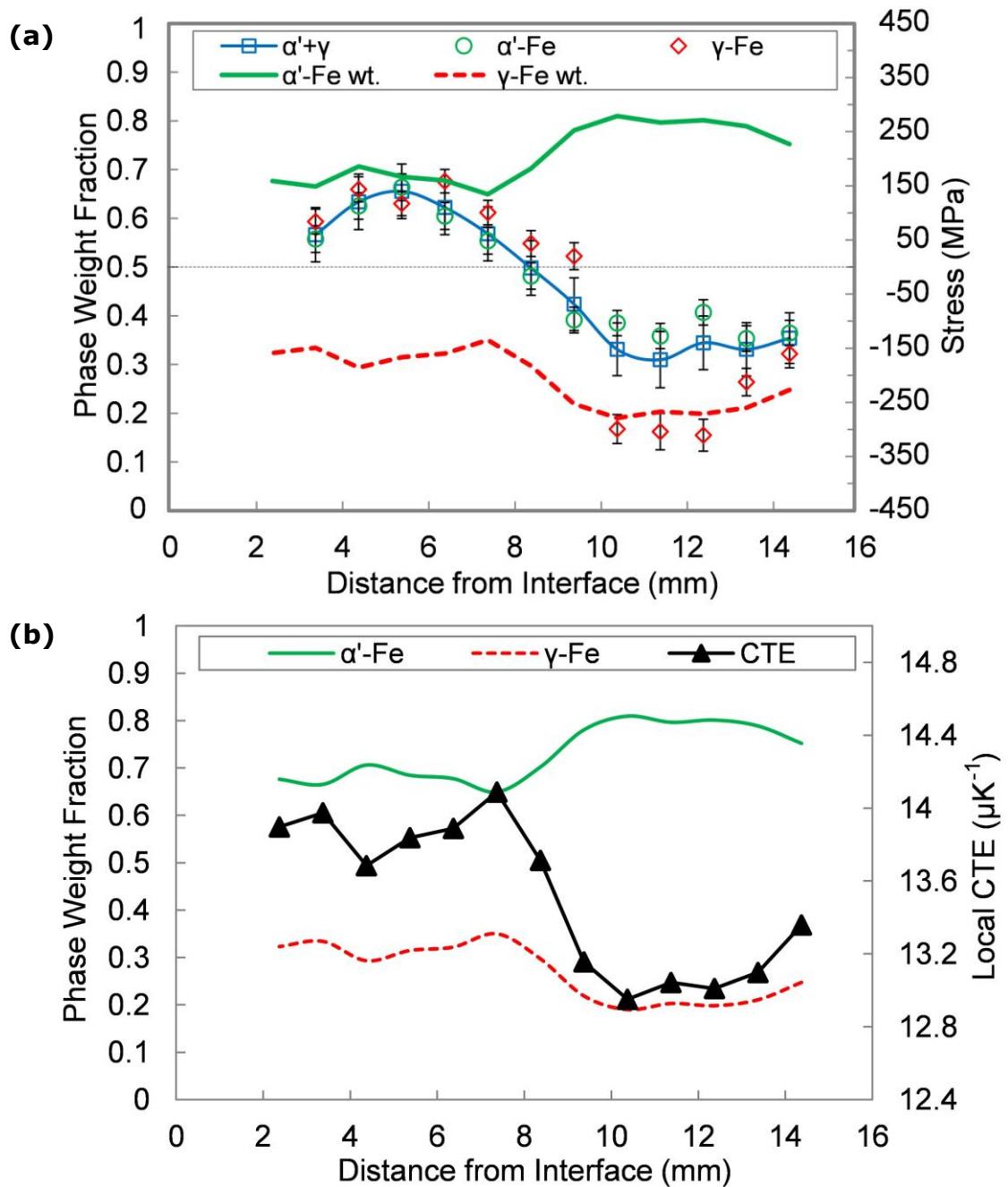
Fig. 3.17. The typical phase weight fraction distribution along the as-sprayed HSS preform thickness used to derive the (a) bulk residual stress and (b) local coefficient of thermal expansion.

3.8   Pseudo-strains

3.8.1 Effects of porosity distributions on ND strain measurements

The porosity in the as-sprayed preforms could cause the shift in the neutron-weighted centre of gravity (ncog) from the GV geometric centre of gravity (gcog) due to the difference in diffracting material in the defined GV. The shift directly causes artificial Bragg peak shift and consequently, pseudo-strains [195, 196]. Therefore, the effects of porosity on the residual strain and stress measurements were investigated from the ND experiments conducted using the dense-to-porous transition region in the cross-sectional sample cut from the multi-pass preform [151].

Along the preform thickness (Fig. 3.18a), the effects of porosity distribution in the GV (4 x 4 x 4 mm) on the shift in ncog was determined across the dense-to-porous transition region (Fig. 3.18b) by calculating the centre-of-mass of the material in the GV. The pseudo-strains (ε_{Ps}) caused by the ncog shift were determined with respect to the angular position of the detector at $2\theta = 90°$ (Fig. 3.18c) using [195]:

$$\varepsilon_{Ps} = \frac{\Delta L_D}{L_D} + \cot\frac{2\theta}{2} \cdot \frac{\Delta 2\theta}{2} \tag{3.6}$$

where 2θ and L_D are the diffraction angle and neutron flight path length from gcog to the detector, respectively, and $\Delta 2\theta$ and ΔL_D are their corresponding changes due to ncog shift. The measured strains ($\varepsilon_{Measured}$) can then be corrected using,

$$\varepsilon_{Measured} = \varepsilon_{True} + \varepsilon_{Ps} \tag{3.7}$$

where ε_{True} is the corrected strain value.
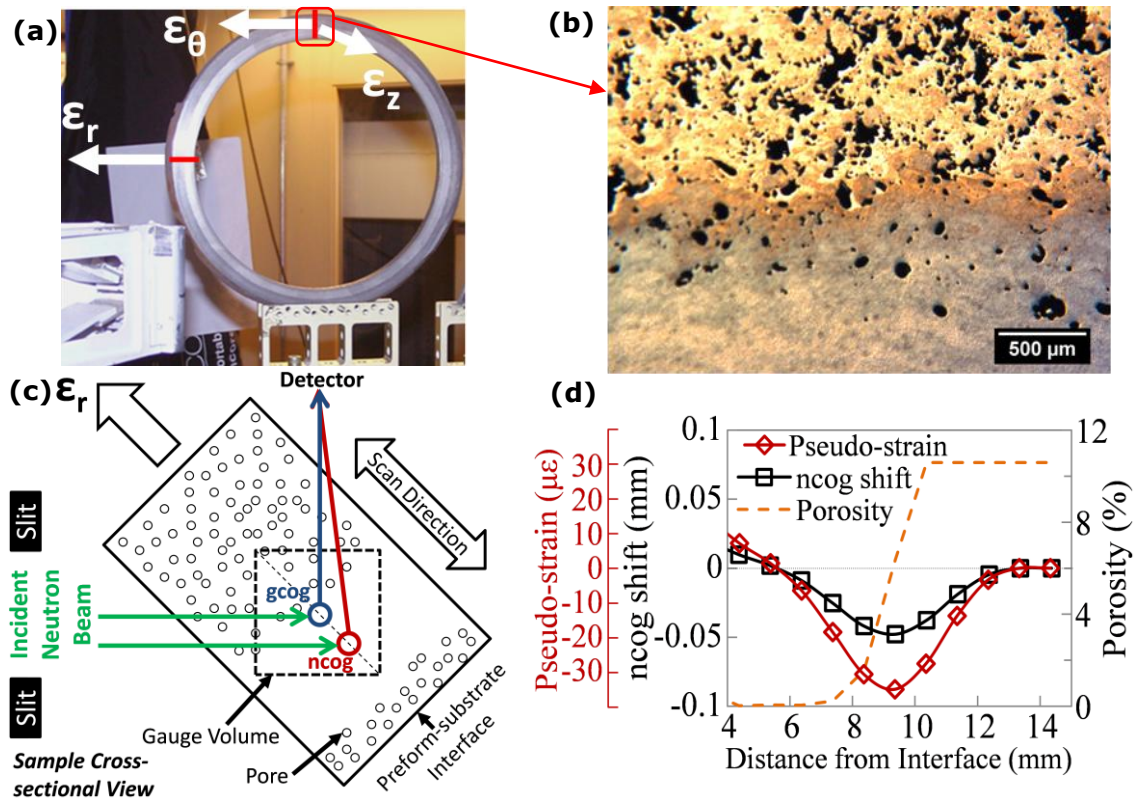
Fig. 3.18. (a) The ND experimental set-up at ENGIN-X showing the cross-sectional sample sectioned from the multi-pass preform, (b) an optical micrograph showing the dense-to-porous transition region, (c) a schematic diagram of the neutron beam path scattered from the gcog and ncog, and (d) the calculated ncog shift and pseudo-strains.

Fig. 3.18d shows that a maximum ncog shift was found when the GV was defined in a region with a relatively large change in porosity and there was no significant ncog shift in regions without porosity changes. The small shift in ncog at 4 - 6 mm from the interface was due to the porosity in the interface region. The calculated maximum pseudo-strain from the ~11 % change in porosity was relatively small (<40 µε) in comparison to the average ND measurement statistical uncertainty (up to ~200 µε). The pseudo-strains from the ε_θ and ε_z measurements were insignificant due to ncog shifts in the vertical directions are much smaller compared to lateral shifts [195]. Therefore, it was assumed that porosity-induced pseudo-strains do not affect the stress distributions characterised via ND significantly and the residual stress distribution measured across the dense-to-porous transition region of the multi-pass preform is shown in Fig. 2.25d.

3.8.2 Incomplete filling of gauge volume

The measurements near to the extreme edge of the specimens (where the strains are the highest) carried out in the *in situ* ND bend test experiments would typically include measurements from incompletely filled GVs. The relatively larger ncog shifts from the incompletely filled GV give rise to significant pseudo-strains especially in the horizontal loading axis orientation where the vertex of the GV would be protruding out from the specimen near the specimen edges. Using the aforementioned centre of mass calculation, the pseudo-strains caused by the porosity distribution and the incompletely filled GV (4 x 4 x 4 mm) near to the extreme edges of the HSS bend test specimen cut from the multi-pass preform were determined.

Fig. 3.19 shows that pseudo-strains associated to incomplete GV filling were significantly larger in comparison to porosity-induced pseudo-strains near to the bottom edge of the specimen (-5.26 mm from neutral axis) with a maximum pseudo-strain calculated to be ~640 $\mu\varepsilon$. The pseudo-strain corrections were applied to the measured ε_J. Pseudo-strains towards the top of the specimen (directly next to crosshead) were not calculated since the GV incorporated materials from the crosshead in addition to being incompletely filled. The measured ε_J from this scan point was therefore inaccurate and disregarded since the diffraction peaks from the steel crosshead are indiscernible as they directly overlapped the peaks measured from the HSS specimen.
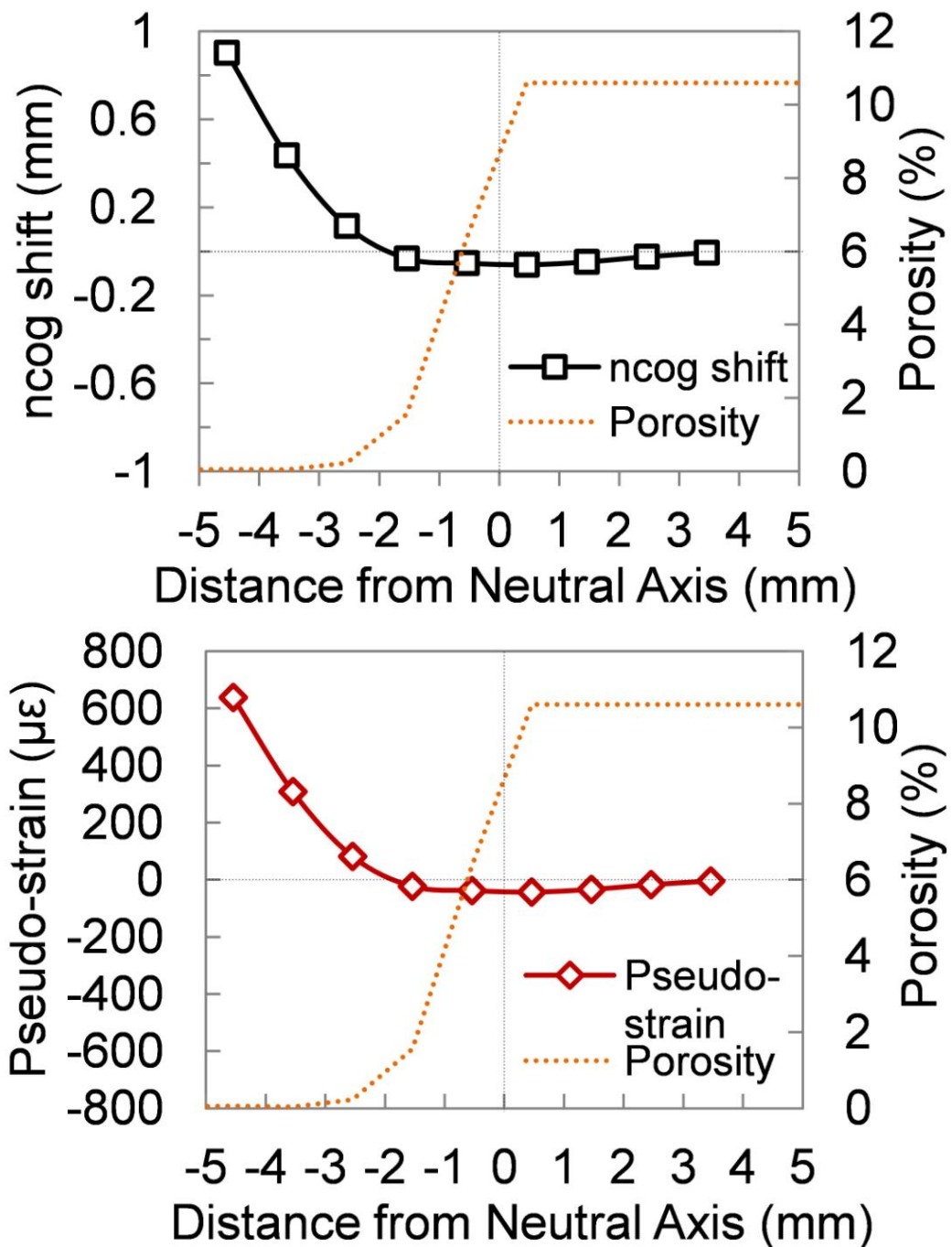
Fig. 3.19. The calculated ncog shift and the corresponding pseudo-strains due to GV (4 x 4 x 4 mm) incomplete filling and porosity distribution across the dense-to-porous transition region in the HSS specimen cut from the multi-pass preform. The bottom edge of the specimen is at -5.26 mm from the neutral axis.

3.9   Microstructure characterisation using X-ray

3.9.1 Synchrotron X-ray diffraction

The preferred orientation (texture) of polycrystalline materials can cause anisotropic mechanical properties such as the stress-strain relationship, yield surface and crack propagation. Texture in engineering components is generally induced by plastic deformation during the manufacturing process and is important for predicting component performance. The texture in the porous and dense regions of the as-sprayed preform was determined using synchrotron XRD conducted at beamline I12 of DLS with Ø1 mm diameter and 20 mm long cylindrical specimen EDM cut from the multi-pass preform along the thickness direction. A monochromatic synchrotron X-ray beam at 70 keV and a beam size of 0.3×0.3 mm was used to scan the as-sprayed specimen in the dense and porous regions. The schematic of the experimental setup is shown in Fig. 3.20a. The specimen was mounted parallel with Y-axis and perpendicular to the incident X-ray beam (Z-direction). The specimen was rotated around the Y-axis by an angle, ω in 10° increments from 0° to 180° and the transmission diffraction patterns were recorded after each rotation (generating 18 diffraction patterns from each scanned region) using a Thales Pixium RF4343 2D detector with a pixel size of 148×148 µm and a sample-to-detector distance of 618 mm. A CeO_2 standard was scanned to determine the instrument parameters (e.g. sample-to-detector distance) for the calibration of the subsequent diffraction pattern analyses.

The typical 2D transmission diffraction pattern obtained from the dense and porous regions of the as-sprayed specimen are shown in Fig. 3.20b and Fig. 3.20c, respectively. Intensity variations within each Debye-scherrer rings shown in 2D X-ray transmission diffraction patterns are indicative of strong texture effects. Preferred orientations were not apparent in the dense and porous regions of the as-sprayed HSS based on the relatively consistent and homogeneous Debye-scherrer ring intensities shown in the acquired X-ray transmission diffraction patterns.

(a)
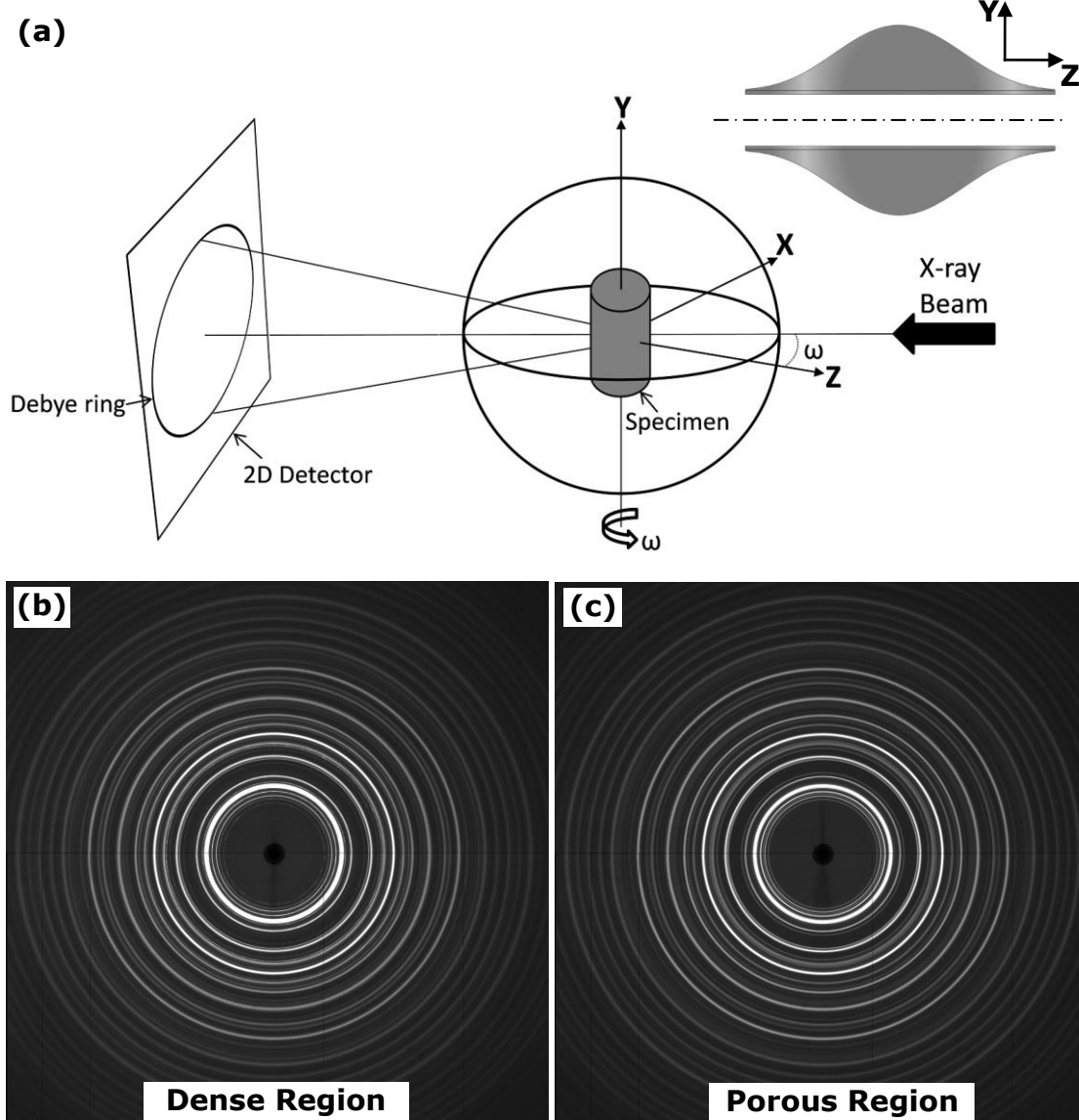
Fig. 3.20. (a) A schematic diagram of the synchrotron XRD set-up at I12 and the typical 2-D transmission diffraction pattern acquired from the (b) dense and (c) porous region of the as-sprayed HSS.

The diffraction patterns were analysed using the Rietveld refinement programme MAUD (Material Analysis using Diffraction) [197] and the patterns were integrated over 10° sectors from 0 to 180° producing 18 spectrums. Detailed description of the procedure to import and integrate the diffraction patterns directly in MAUD can be found in [198]. In this case, a total of 18 × 18 = 324 spectrums were analysed for each scanned region that was rotated by 180°. Since the specimen was prepared in a cylindrical shape, the X-ray absorption was constant across its cross-section when rotated around the Y-axis. Therefore, corrections for sample volume and absorption variations were not performed.

(a) Dense Region
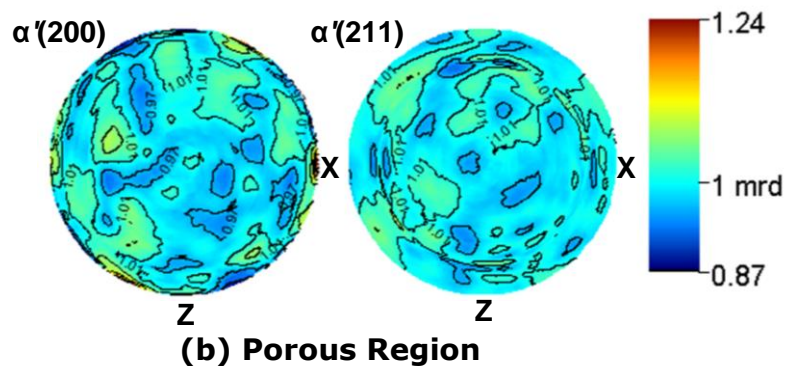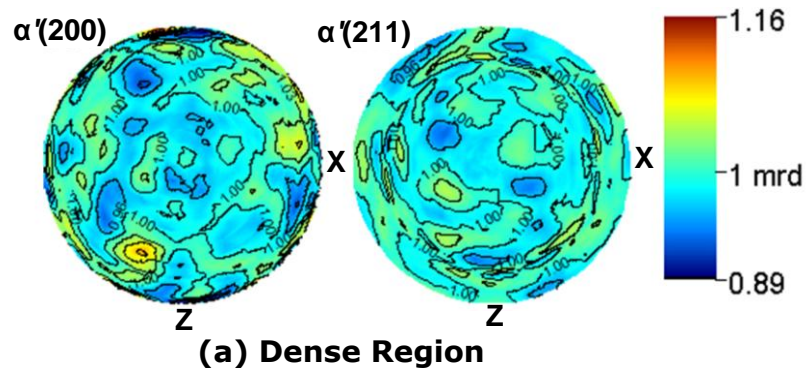
(b) Porous Region

Fig. 3.21. Pole figures for ɑ'(200) and ɑ'(211) planes in the (a) dense and (b) porous regions of the as-sprayed HSS.

(a) Dense Region
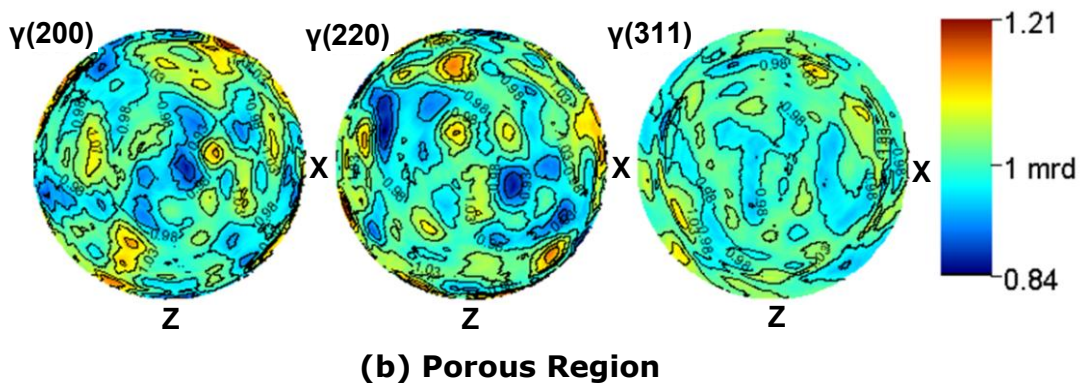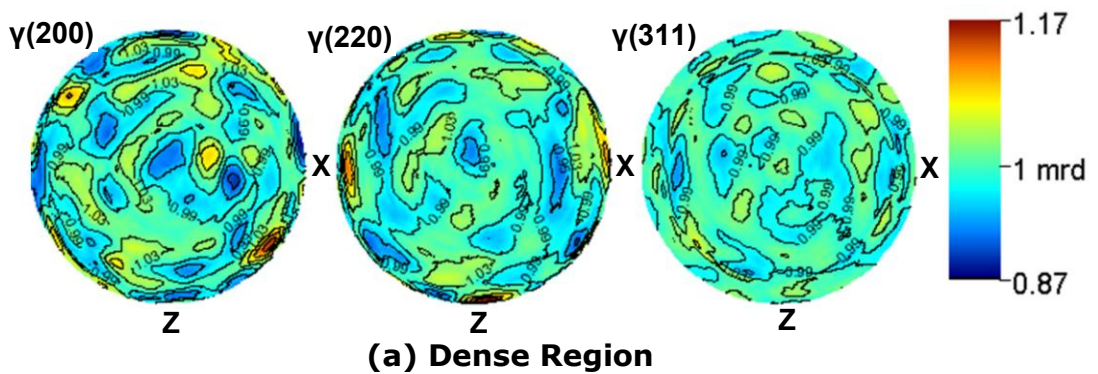
(b) Porous Region

Fig. 3.22. Pole figures for γ(200), γ(220) and γ(311) planes in the (a) dense and (b) porous regions of the as-sprayed HSS.

The Extended Williams-Imhof-Matthies-Vinel (E-WIMV) method [199-201] integrated in MAUD was used to compute the orientation distribution functions (ODF). The reconstructed pole figures (Fig. 3.21 and Fig. 3.22) from the computed ODF showed that the ODF maximum and minimum are 1.24 and 0.84 multiples of a random distribution (mrd), respectively. These values that are ~1 mrd indicate that the α'-Fe and γ−Fe crystallites in the dense and porous regions of the as-sprayed steel have a random texture essentially. Therefore, the deformation behaviours and material properties of the as-sprayed HSS can be assumed to be free from texture effects and are isotropic, respectively.

The carbides and phases formed in the interface and dense region of the as-sprayed HSS were also characterised using synchrotron XRD (transmission mode) at beamline I15 of DLS with a monochromatic X-ray beam at 75 keV collimated with a Ø70 µm pin hole. The cross-sectional sample used was ~1 mm thick and the Debye-Scherrer rings were collected on a 2D area detector (Perkin Elmer 1621 AN) with a sample-to-detector distance of 327.65 mm and CeO_2 was used as the calibrant sample. The XRD set-up is shown in Fig. 3.23a. The acquired diffractograms (Fig. 3.23b) were analysed and the peaks were fitted using Rietveld refinement with MAUD (Fig. 3.23c). The diffractograms from the interface region (1.5 mm from interface) and dense region (6 mm from interface) showed that the dominant phases formed in the as-sprayed HSS were α'-Fe and γ-Fe with minor M_2C (Mo_2C), M_6C (Fe_3W_3C) and MC (VC) carbide phases. The findings are consistent with the microstructures formed in typical as-sprayed HSS [202]. Table 3.6 shows the constituent phase volume fractions which indicated increasing α'-Fe content towards the preform surface consistent with the ND measurements (Fig. 3.12).
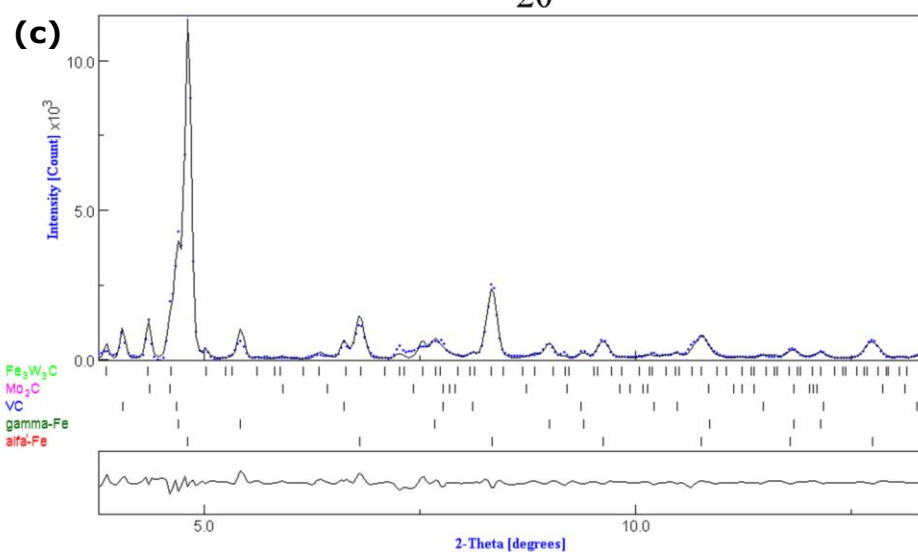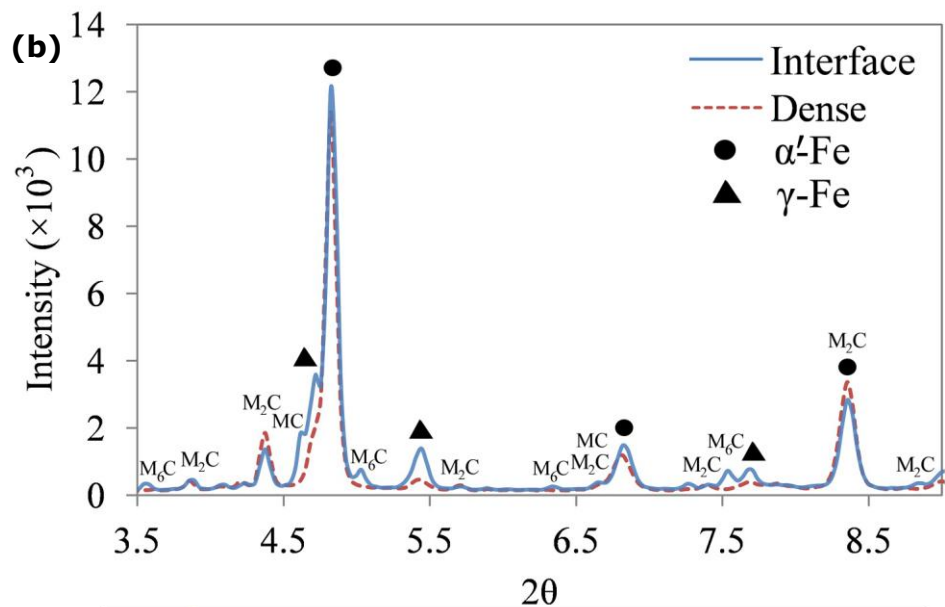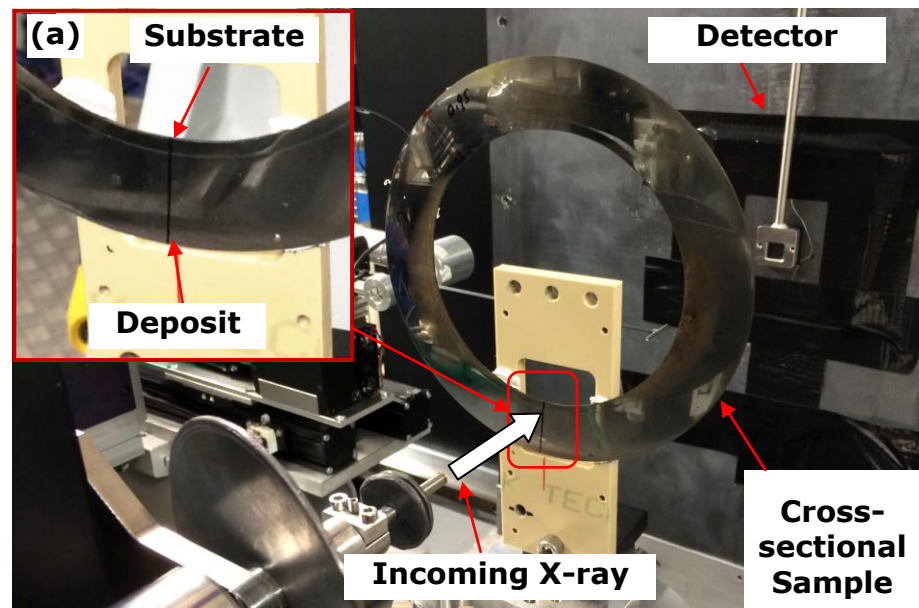
Fig. 3.23. (a) Synchrotron XRD set-up at I15, (b) the raw diffractograms acquired from the interface and dense regions in preform NP1 and (c) the typical fitted diffractogram.

Table 3.6. Constituent phase volume fractions of the interface and dense regions in preform NP1.

	Volume Fractions (%)				
	α'-Fe	γ-Fe	M_2C	M_6C	MC
Interface	70	21	1	3	5
Dense	77	13	3	0	7

Elemental mapping in the interface region done using JEOL JXA-8800 also revealed that the carbides formed were rich in W, Mo and V (Fig. 3.24) which confirmed the validity of the identified carbide phases from the XRD diffractograms.
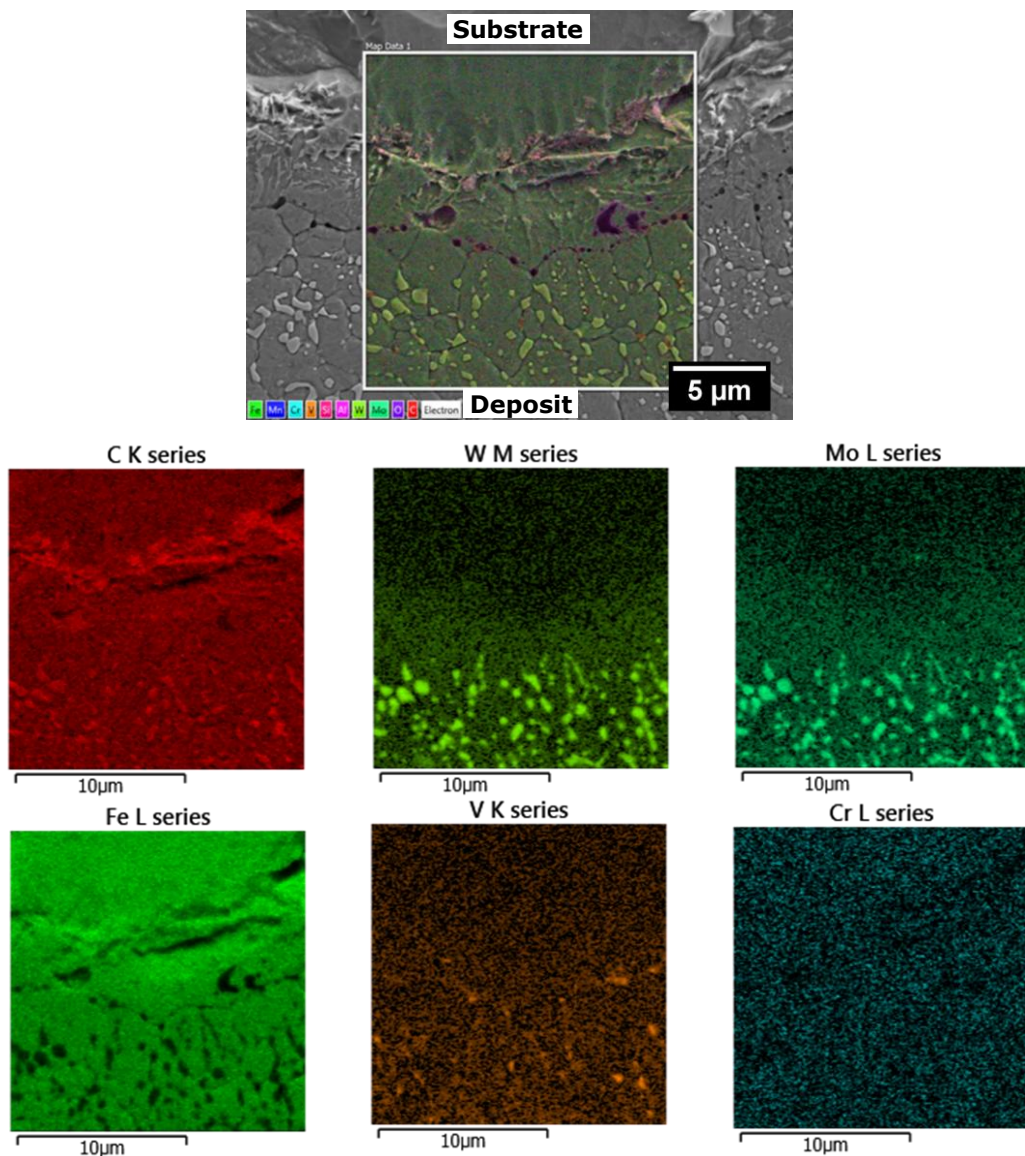
Fig. 3.24. Elemental mapping of the interface region in preform NP1.

3.9.2 Lab-based X-ray µCT scanner

The porosity distributions along the thickness of the as-sprayed preforms were characterised using the X-ray µCT scanner (HMX160, X-Tek Systems) at HU with resolutions of ~3 µm per pixel. The experiments were carried out using X-ray tube voltage of 100 kV and a W target. Optimisation of the X-ray µCT set-up and sample cross-sectional size/shape was carried out to achieve the best possible tomogram quality obtained from the steel specimens. The cross-sectional strip samples were grinded to smaller cross-sections with a 2500 grit surface finish in order to reduce the X-ray absorption through the steel samples. Typical tomograms acquired from the strip samples with a cross-sectional size of ~2 × 2 mm are shown Fig. 3.25. Generally, the tomograms showed that the porosity is discernible from the steel sample based on the difference in contrast difference (porosity is darker). However, the features in the sample are blurred (Fig. 3.25a) if the sample is not secured properly during the scan. In order to avoid the sample from vibrating or moving during the scan, the sample was clamped using a pin chuck which was secured onto the sample table in the X-ray µCT scanner. The set-up produced tomograms with more resolved features (Fig. 3.25b). Nevertheless, the sharp edges of the square-shaped cross-section blurred the features near to the edge regions (Fig. 3.25c).

Therefore, the samples were grinded into cylindrical rods with diameters of ~1 mm with a 2500 grit surface finish and were scanned using the aforementioned X-ray settings and set-up. The typical tomograms acquired from the rod samples were relatively well resolved showing the porosity in the denser region (Fig. 3.26a) and could reveal the boundaries of solidified droplets that deposited in the porous region (Fig. 3.26b). Hence, the porosity distribution characterisations were typically conducted using the ~1 mm diameter cross-sectional rod samples. The 3D tomography data-sets were segmented using Avizo® and porosity was quantified over 1 mm segments along the preform thickness.
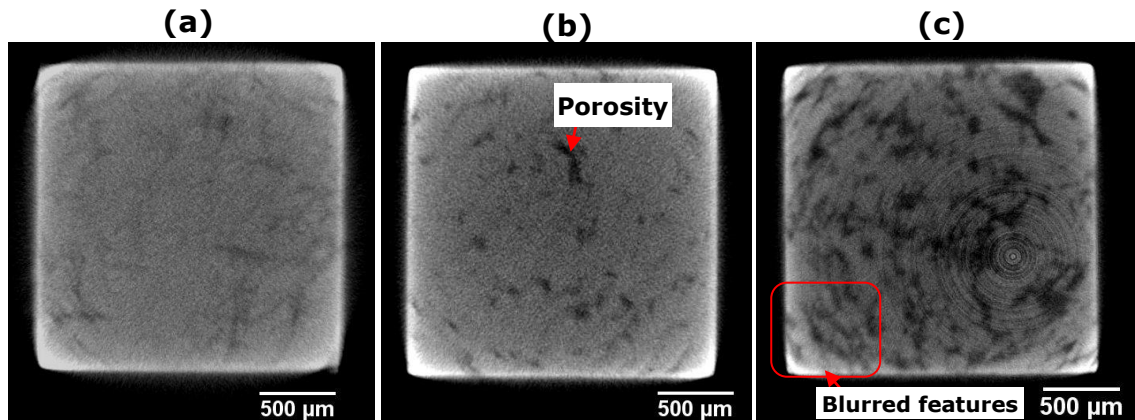
Fig. 3.25. The X-ray µCT tomograms acquired from a 2 × 2 mm cross-sectional strip sample showing the (a) blurred and smeared features in the sample due to the unsecured sample holder, (b) features in the sample were more resolved using a secured sample holder and (c) sharp edges of the sample blurred the features near to these edges.
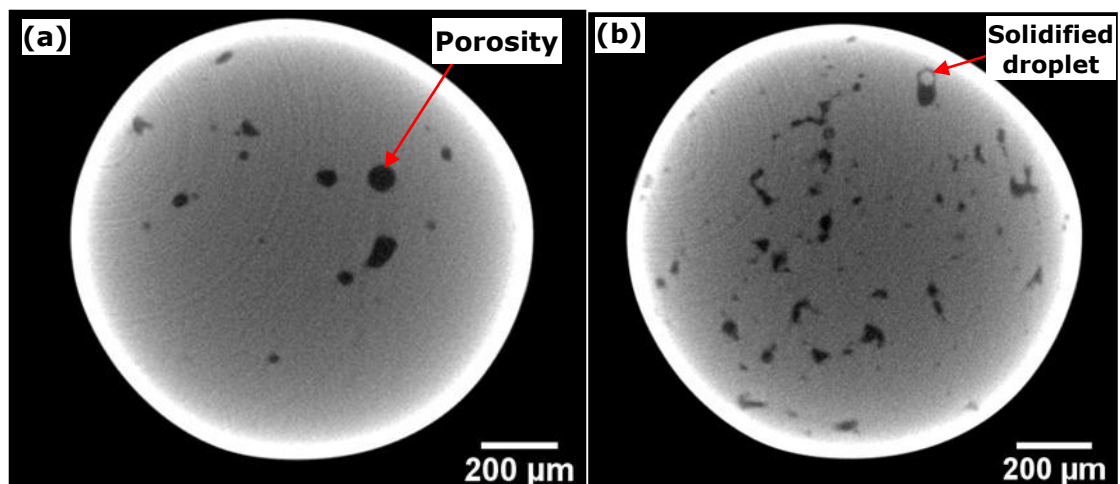
Fig. 3.26. The X-ray µCT tomograms acquired from a ~1 mm diameter cross-sectional sample showing the porosity in the relatively (a) dense and (b) porous regions.

3.9.3 Synchrotron X-ray µCT

In order to reveal the characteristics of the interface, synchrotron X-ray µCT at TOMCAT with monochromatic X-ray at 42 keV was used to characterise the interface region of the cross-sectional samples cut from preform P2 that were machined into cylindrical rods with diameters of ~1 mm with a 2500 grit surface finish, and a typical view of the experimental set-up is shown in Fig. 3.27a. The synchrotron X-ray beam transmitted through the sample was detected using a 20 µm thick LAG:Ce scintillator and high resolution imaging detector (Pco.edge 5.5). The sample was rotated at steps of 0.12° over a 180° rotation and each scan comprised of 1501 projections with an exposure time of 1.9 s per projection and resolution of 0.65 µm per pixel.

The boundary between the HSS deposit and mild steel substrate can be delineated due the difference in Fe content between the materials and thus, producing the variation in the X-ray absorption contrast (higher Fe content = darker contrast) as shown in the tomogram acquired from the interface region (Fig. 3.27b). Fig. 3.27c and Fig. 3.27d shows the typical SEM image of the preheated preform-substrate interface and the 3D rendering of the porosity (in blue) segmented from the tomograms acquired at the interface region, respectively. Comparing between the 2D SEM images and 3D rendering of the porosity at the interface, it is apparent that the 3D X-ray µCT characterisation provides a more reliable representation of the porosity in the preform.
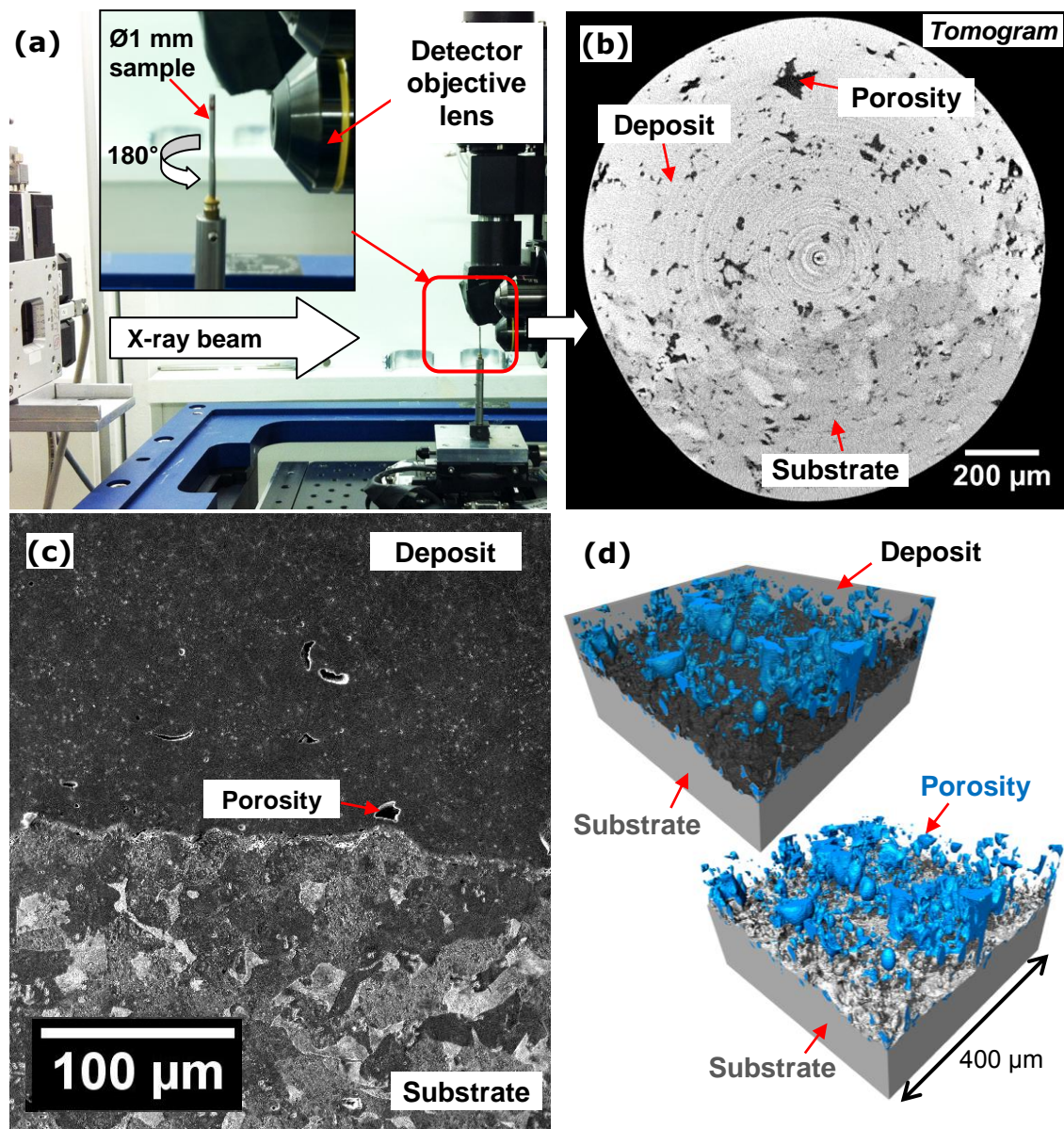
Fig. 3.27. (a) The synchrotron X-ray µCT set-up at TOMCAT, (b) the tomogram acquired at the preform-substrate interface, (c) a typical SEM image of the bonded interface, and (d) the typical 3D rendering of the porosity (in blue) segmented from the tomograms acquired in the interface region.
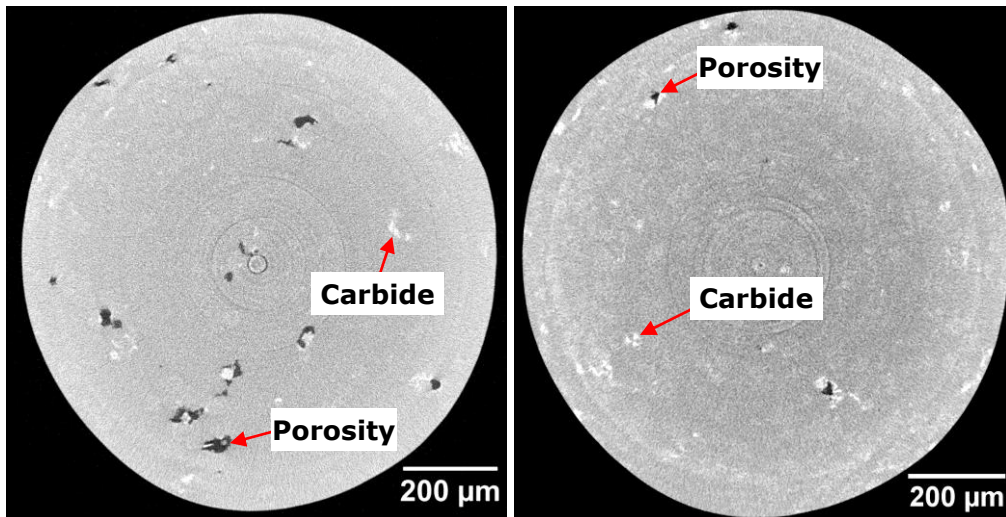
Fig. 3.28. The typical synchrotron X-ray µCT tomograms acquired at TOMCAT from the interface region in preform P2 showing the carbides (bright phase) and porosity (dark phase).
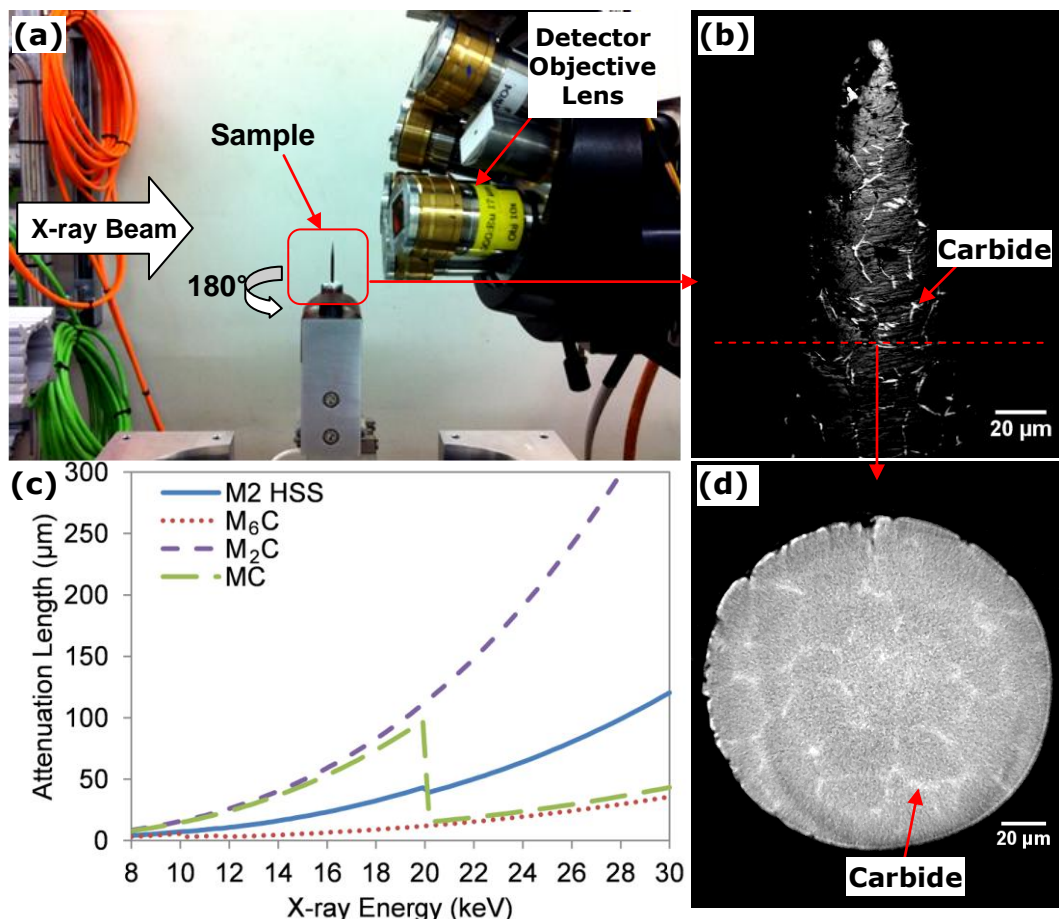
Fig. 3.29. (a) The X-ray µCT set-up at beamline I13, (b) backscatter electron image of the needle-like cross-sectional sample showing the carbide network (bright phase), (c) the X-ray attenuation length of the respective phases in the HSS and (d) the typical tomogram acquired from the dense region of preform NP1 showing the carbide network (bright phase) formed.

Thus, the morphology of the different carbide networks formed in the as-sprayed HSS was also investigated using synchrotron X-ray µCT. The typical tomograms acquired from TOMCAT (Fig. 3.28) near to the interface of the preform P2 also revealed the fine carbides (bright phase) and porosity (dark phase) in this region. The 3D morphology of the carbide network formed in preform NP1 was investigated at I13 beamline of DLS using a monochromatic X-ray beam at 22 keV and the experimental set-up is shown in Fig. 3.29a. An exposure time of 1.9 s per radiograph was used with the sample-to-detector distance set at 30 mm. X-ray beam transmitted through the sample was detected using a high resolution imaging detector (Pco.edge 5.5) and the sample was rotated at a step size of 0.045° over a 180° rotation generating 4001 projections in each scan with a resolution of 0.33 µm per pixel.

The cross-sectional sample extracted from the as-sprayed HSS preform was machined into a needle-like shape (Fig. 3.29b) with a 2500 grit surface finish to provide the optimum sample cross-sectional area and thickness with respect to the X-ray attenuation length (Fig. 3.29c). Fig. 3.29d shows the typical tomogram acquired from the needle-like shape cross-sectional sample showing the carbide network (bright phase) formed. The major carbides formed in the HSS are rich in heavy alloying elements that have different absorption compared to the iron matrix that provided the absorption contrast.

3.10 Summary

The neutron diffraction experiment set-ups and the features of the neutron TOF diffractometer used in this study were detailed in this chapter. The spray forming experiments and parameters used to manufacture the dissimilar steels preforms were also described. The effects of porosity in the as-sprayed preforms on the stress measurements acquired via neutron diffraction were taken into account. In addition, both lab-based and synchrotron X-ray experiments and the procedures used to characterise the microstructures in the as-sprayed steels were described in detail.

CHAPTER 4 : PREFORM SHAPE EVOLUTION, THERMAL HISTORY AND THERMAL STRESS MODEL DEVELOPMENT

This chapter describes the preform shape evolution, thermal history and thermal stress numerical model development using the commercial FE software, COMSOL Multiphysics®, to provide the links between the spray processing parameters, corresponding microstructures formed and the interfacial bonding developed in the as-sprayed dissimilar steel preforms. The main innovations of this model in comparison with previous work include:

(1) the development of an integrated preform shape and heat flow model that employs the mesh deformation method with automated re-meshing algorithm to address the coupling of the droplet mass/enthalpy input at the deposition surface,

(2) the integrated substrate preheating model to simulate the complete preform thermal history, and

(3) the incorporation of the porosity and local CTE distributions mapped from X-ray μCT and ND measurements, respectively in the modelled preform to take into account their effects on the material properties and the corresponding stress developed in the preforms during cooling.

The simulated results from this model are directly relevant to the experimental measurements and characterisations described in Chapter 5.

4.1   Droplet spray mass flux distribution and preform shape model

Many previous spray forming studies demonstrated that the mass flux along the spray cone axis can be approximated to a Gaussian distribution and the ability to retain the incoming mass on the substrate surface is described by the sticking efficiency (SE) [83]. The mass flux, $\dot{\mathrm{M}}$ of the spray cone at an arbitrary distance from the atomisation point can be expressed as [72],

$$\dot{\mathrm{M}} = \mathrm{SE} \cdot \mathrm{a}_S \cdot \exp\left(-\mathrm{b}_S \times \mathrm{R}^2\right) \qquad (4.1)$$

where a_S is the maximum deposition rate, b_S is the radial spray distribution coefficient and R is the distance from the spray axis. Many previous numerical shape models have assumed a constant mass flow rate/mass flux throughout the spraying process that may give rise to differences in the simulated and measured preform shapes especially towards the end of the spraying process [72]. This is caused by the progressively reducing melt hydrostatic pressure in the tundish towards the spray end time (t_{end}) due to the depleting melt that reduces the mass flow rate and thus, lower $\dot{M}$. The reduced deposition rate is associated with lower enthalpy input and has to be taken into account to accurately simulate the heat flow throughout the preform. Hence, the typical time taken to completely drain the melt in the tundish (t_{drain}) was estimated using Torricelli's law [203],

$$t_{drain} = \sqrt{\frac{2\, h_{metal}}{g}} \left(\frac{r_1}{r_2}\right)^2 \qquad (4.2)$$

where h_{metal} = 300 mm is the height of molten steel in the tundish, g is gravity, r_1 = 59 mm and and r_2 = 3.5 mm is the radius of the tundish (in an equivalent cylindrical shape) and outlet nozzle, respectively. Based on Bernoulli's equation, the melt flow rate or velocity of the liquid flow (v_{flow}) from the tundish follows the relationship [203],

$$v_{flow} = \sqrt{2\, g\, h_{metal}} \qquad (4.3)$$

Therefore, the $\dot{M}$ reduction factor (f_{reduce}) towards the end of the spraying phase (t_{end}-t_{drain} to t_{end}) was estimated (Fig. 4.1) using the relationship described in Eqn. (4.3).

The time-dependent mass flux, $\dot{M}(t)$ can thus be expressed as,

$$\dot{M}(t) = f_{reduce} \cdot SE \cdot a_S \cdot \exp\left(-b_S \times R^2\right) \qquad (4.4)$$

The mean SE was estimated from the spray experiments using [72],

$$SE = \frac{W_d}{W_s - W_o} \qquad (4.5)$$

where W_d, W_s and W_o is the weight of the preform deposit, melted alloy ingot and the overspray droplets, respectively. Both a_S and b_S varies with

the spray distance (d_S) and can be derived using the following relationship [70, 73]:

$$\frac{a_{ref}}{a_S} = \frac{b_{ref}}{b_S} = \left(\frac{d_S}{d_{ref}}\right)^2 \tag{4.6}$$

where the subscript "ref" refers to the known values determined from experimental measurements. In this study, a_{ref} (= 5.7 kg m^{-2} s^{-1}) and b_{ref} (= 0.6 × 10^{-3}) were experimentally determined by spraying onto a rotating but non-retracting substrate at d_{ref} = 600 mm using an atomiser scan angle (θ_{scan}) of ± 2.50°. To take into account the effect of the scanning atomiser, the time-averaged deposition rate over the θ_{scan} range was used to simulate the deposition growth profile as adopted in previous study [82, 204]. The deposition rate ($\dot{G}$) of the incoming mass flux can be determined using [82],

$$\dot{G} = \frac{\dot{M}(t)}{\rho} \tag{4.7}$$

where ρ is the density of the sprayed alloy. The typical time-averaged deposition rate profiles with θ_{scan}= ±2° (d_S = 550 mm) and θ_{scan}= ±2.5° (d_S = 600 mm) are shown in Fig. 4.2. The MATLAB code used to determine the typical deposition profile at θ_{scan}= ±2.5° (d_S = 600 mm) is given in Appendix 2. The tube preform shape evolution was simulated in a 2D axisymmetric configuration and any droplet re-deposition effects were ignored due to the simplicity of the tube-shaped preforms.
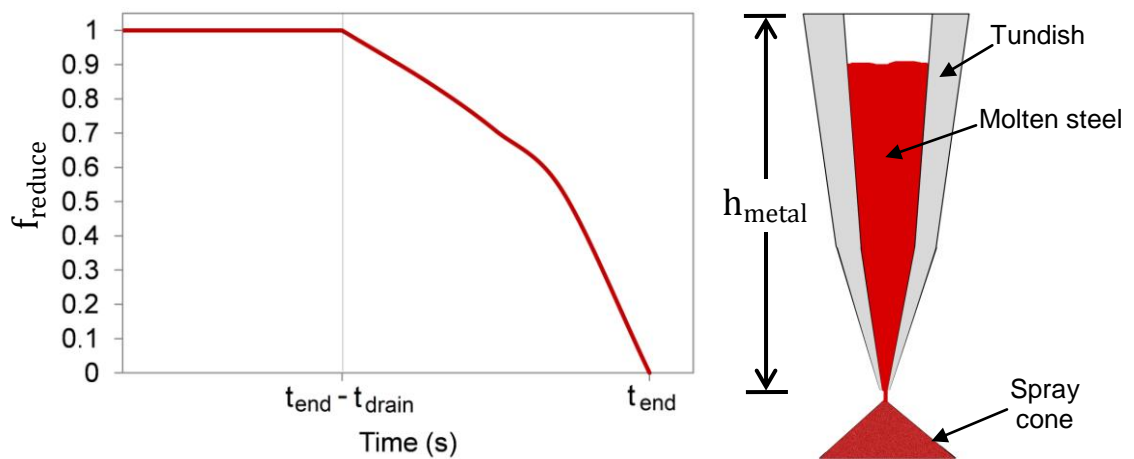
Fig. 4.1. The estimated $\dot{M}$ reduction factor (f_{reduce}) towards the end of the spraying process (t_{end}-t_{drain} to t_{end}).
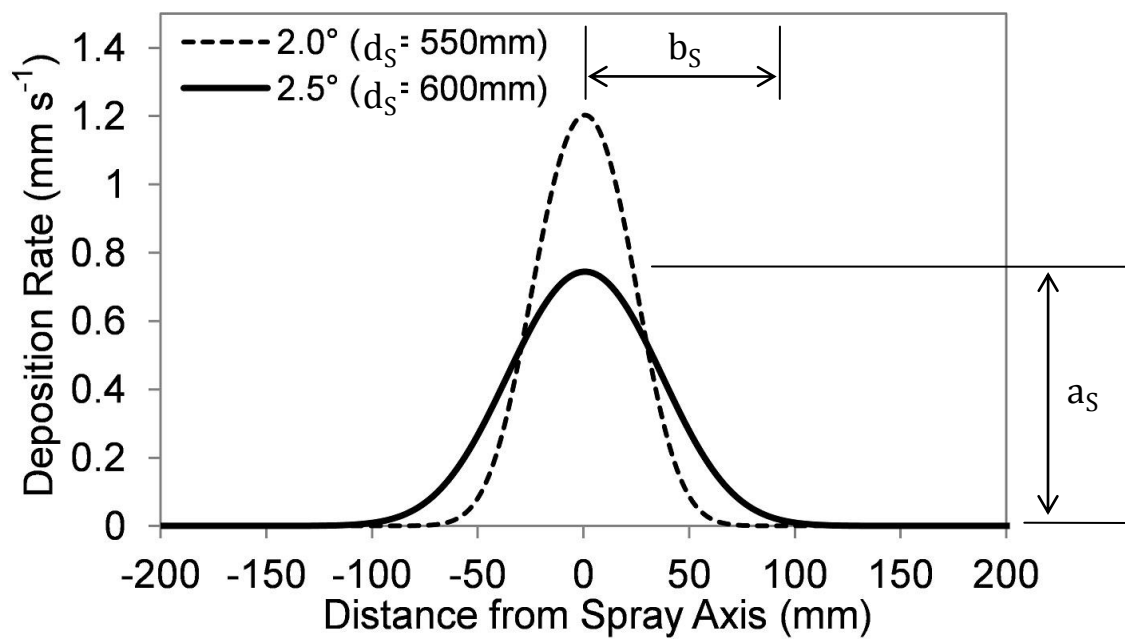
Fig. 4.2. The simulated time-averaged deposition rate profiles with $\theta_{scan}=\pm 2.0°$ ($d_S = 550$ mm) and $\pm 2.5°$ ($d_S = 600$ mm).

4.2 Heat flow and solidification model

The heat flow in the preform during spray forming is transient and non-linear with the release of latent heat as the materials undergo solidification. The governing heat equation in 2D cylindrical polar coordinates (z, r) is [96]:

$$\rho C \frac{\partial T}{\partial t} = \frac{1}{r}\left[\frac{\partial}{\partial z}\left(K{\cdot}r\frac{\partial T}{\partial z}\right) + \frac{1}{r}{\cdot}\frac{\partial}{\partial r}\left(K\frac{\partial T}{\partial r}\right)\right] + \rho L_f\left(\frac{\partial f_S}{\partial T}{\cdot}\frac{\partial T}{\partial t}\right) \quad (4.8)$$

where C is specific heat capacity, T is temperature, t is time, z is axial coordinate, r is radial coordinate, K is thermal conductivity, L_f is the latent heat and f_S is the alloy solid fraction. To take into account the melting/solidification effects, an alloy effective heat capacity C_{eff} was defined as [96]:

$$C_{eff} = C - L_f\left(\frac{\partial f_S}{\partial T}\right) \quad (4.9)$$

and Eqn. (4.8) can be expressed as:

$$\rho C_{eff}\frac{\partial T}{\partial t} = \rho\left[C + L_f\left(\frac{\partial f_L}{\partial T}\right)\right]\frac{\partial T}{\partial t} = \frac{1}{r}\left[\frac{\partial}{\partial z}\left(K{\cdot}r\frac{\partial T}{\partial z}\right) + \frac{1}{r}{\cdot}\frac{\partial}{\partial r}\left(K\frac{\partial T}{\partial r}\right)\right] \quad (4.10)$$

The volume fractions of the alloy liquid and solid phases during solidification are temperature dependent and can be determined using the Scheil function,

$$(1{-}f_S) = \left(\frac{T - T_S}{T_L - T_S}\right)^{\left(\frac{1}{1{-}k_p}\right)} \quad (4.11)$$

where T_S and T_L are the solidus and liquids temperature of the alloy, respectively and k_p is a partition coefficient. Fig. 4.3a shows the M2 HSS liquid fraction as a function of temperature and and the fit to the data from [205] using $k_p = 0.4$. A similar k_p value was assumed for ASP30 HSS.
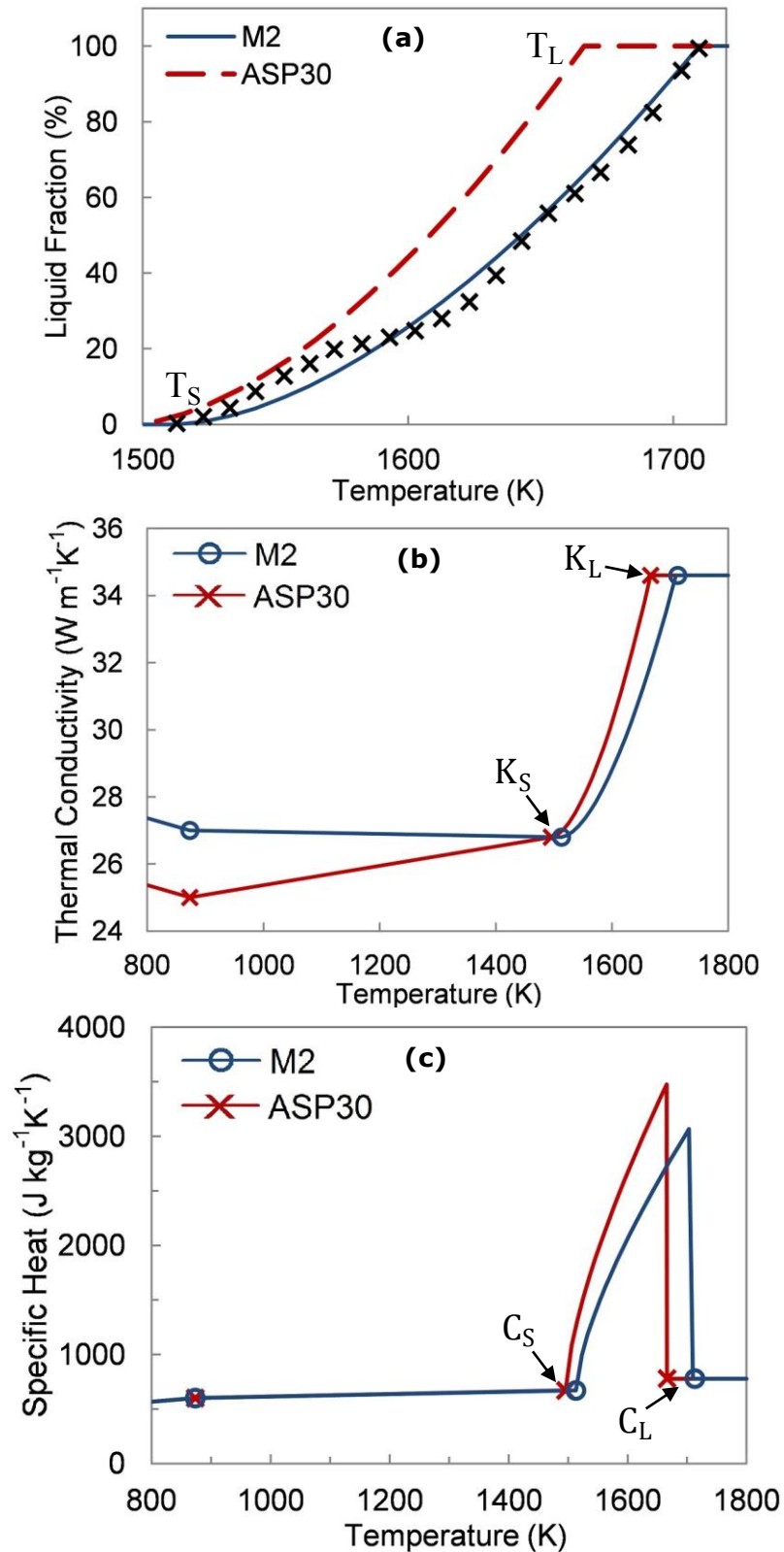
Fig. 4.3. The (a) alloy liquid fraction with a Scheil correlation, (b) thermal conductivity and (c) effective heat capacity as a function of temperature for M2 and ASP30 HSS. The measured data from [194, 205-207] are marked using o and ×.

Table 4.1. Thermophysical properties of M2 [194, 205, 207] and ASP30 [194, 206, 207] HSS.

Steel	M2	ASP30
ρ (kg m^{-3})	$-6.35 \times 10^{-5} \times T^2 - 0.20 \times T + 8224.61$	$2.27 \times 10^{-6} \times T^2 - 0.28 \times T + 8121.45$
E_D (Pa)	$-58983.7 \times T^2 - 8811250 \times T + 2.33 \times 10^{11}$	$-71687.8 \times T^2 + 850907 \times T + 2.46 \times 10^{11}$
ν	$1.05 \times 10^{-8} \times T^2 + 4.57 \times 10^5 \times T + 0.28$	
C_{eff} (J kg^{-1} K^{-1})		
293 K < T < 873 K	$3.68 \times 10^{-4} \times T^2 - 0.12 \times T + 423.09$	
873 K < T < T_S	$3.03 \times T - 1150.20$	$3.02 \times T - 1143.60$
$T_S < T < T_L$	$C + L_f \left(\dfrac{\partial f_L}{\partial T} \right)$	
$T \geq T_L$	778.74	
K (W m^{-1} K^{-1})		
293 K < T < T_S	$-6.59 \times 10^{-6} \times T^2 + 0.01 \times T + 20.72$	$-4.18 \times 10^{-6} \times T^2 + 0.01 \times T + 19.33$
T_S	26.80	
$T_S < T < T_L$	$f_S K_S + f_L K_L$	
$T > T_L$	34.60	
L_f (kJ kg^{-1})	277.17	

Table 4.2. Thermophysical and electromagnetic properties of mild steel substrate [194, 208-210] and copper induction coils [209].

ρ_{sub} (kg m^{-3})	$-5.15 \times 10^{-5} \times T^2 - 0.36 \times T + 8021.08$
ρ_{coil} (kg m^{-3})	8700
E_{sub} (Pa)	$-2.10 \times 10^4 \times T^2 - 4.28 \times 10^7 \times T + 2.16 \times 10^{11}$
ν_{sub}	$3.81 \times 10^{-8} \times T^2 - 3.24 \times 10^7 \times T + 0.30$
C_{sub} (J kg^{-1} K^{-1})	
293 K < T < 873 K	$2.22 \times 10^{-6} \times T^3 - 3.51 \times 10^{-3} \times T^2 + 2.19 \times T + 42.85$
873 K < T < 1008 K	$666 + 13002 \, (738 - T)^{-1}$
1008 K < T < 1173 K	$545 + 17820 \, (T - 731)^{-1}$
1073 K < T < T$_S$	650
C_{coil} (J kg^{-1} K^{-1})	385
K_{sub} (W m^{-1} K^{-1})	
293 K < T < 1073 K	$-3.11 \times 10^{-5} \times T^2 + 1.24 \times 10^{-2} \times T + 46.13$
1073 K < T < T$_S$	27.3
K_{coil} (W m^{-1} K^{-1})	400
α_{sub} (μ K^{-1})	14.4[a]
$\mu_{r \, sub}$	
293 K < T < 873 K	800
873 K < T < 1033 K	$0.03 \times T^2 - 70.03 \times T + 37402.90$
1033 K < T < T$_S$	1
$\mu_{r \, coil}$	1
$\rho_{r \, sub}$ ($\mu\Omega$m)	
293 K < T < 1033 K	$9.62 \times 10^{-7} \times T^2 - 1.52 \times 10^{-4} \times T + 0.15$
1033 K < T < T$_S$	$-4.11 \times 10^{-7} \times T^2 + 1.42 \times 10^{-3} \times T + 0.03$
$\rho_{r \, coil}$ ($\mu\Omega$m)	$0.01754 \times [\, 1 + 0.0039 \, (T - 293) \,]$

[a]Mean CTE value from 293 - 873 K

The thermophysical properties of the alloys used in the model were temperature dependent. The thermal conductivity and heat capacity of the alloy during solidification were determined using rule-of-mixture [96],

$$K = f_S K_S + f_L K_L \tag{4.12}$$

$$C = f_S C_S + f_L C_L \tag{4.13}$$

$$C_{eff} = C + L_f \left(\frac{\partial f_L}{\partial T} \right) = C + \left[\left(\frac{1}{(1-k_p)(T_L - T_S)} \right) \left(\frac{T - T_S}{T_L - T_S} \right)^{\frac{k_p}{1-k_p}} \right] L_f \tag{4.14}$$

where subscripts "S" and "L" refer to the solid and liquid, respectively. Fig. 4.3b and Fig. 4.3c shows the calculated thermal conductivity and the effective heat capacity for M2 and ASP30 HSS over the temperature range of 800 - 1800 K determined using Eqns. (4.11), (4.12) and (4.14). For M2, T_S = 1513 K and T_L = 1713 K; and for ASP30, T_S = 1495.5 K and T_L = 1666.3 K which are referenced from [205, 206] and the other thermophysical properties used are shown in Table 4.1.

The heat flow in the substrate involves transient heat conduction without solidification and is governed by:

$$\rho_{sub} C_{sub} \frac{\partial T}{\partial t} = \frac{1}{r} \left[\frac{\partial}{\partial z} \left(K_{sub} \cdot r \frac{\partial T}{\partial z} \right) + \frac{1}{r} \cdot \frac{\partial}{\partial r} \left(K_{sub} \frac{\partial T}{\partial r} \right) \right] \tag{4.15}$$

where the coefficients bear the same meaning as those specified in Eqn. (4.8) but refer to the substrate material using the subscript "sub" and Table 4.2 shows the thermophysical properties for the mild steel substrate used in the model.

Convective ($\dot{Q}_{con}$) and radiation ($\dot{Q}_{rad}$) heat flux boundary conditions were applied along the deposition surface and can be expressed as:

$$\dot{Q}_{con} = h \left(T - T_{gas} \right) \tag{4.16}$$

$$\dot{Q}_{rad} = \sigma_{SB} \cdot \varepsilon_e \left(T^4 - T_{chamber}^4 \right) \tag{4.17}$$

where h is convective heat transfer coefficient, T_{gas} is the temperature of the atomiser gas flow, σ_{SB} is Stefan-Boltzmann constant (5.6697×10⁻⁸ W m⁻² K⁻⁴), ε_e is emissivity (0.65 for steel [211]) and $T_{chamber}$ is the spray

chamber temperature. Bergmann *et al.* [212] have reported that the atomising gas temperature typically increases towards the atomiser during spraying. Therefore, experimentally measured T_{gas} and $T_{chamber}$ used in the model were assumed to increase linearly towards the atomiser (Fig. 4.4a) where the hot melt flow was atomised. Both T_{gas} and $T_{chamber}$ in the model were assumed to reduce to room temperature after the spray ended.

The convective cooling profiles assumed took into account the preform shape as shown in Fig. 4.4b. As the preform grows, the effective distance between the surface and the atomiser will progressively decrease and the surface will be subjected to a gas flow of increasing normal velocity and thus, the convective heat transfer coefficient is expected to be the highest at the thickest section of the preform surface, $t_{preform}$ [96]. The convective heat transfer coefficients at the preform surfaces where the gas flow impinged obliquely (for e.g. 0 - 125 mm in Fig. 4.4b) were assumed to reduced exponentially as typically adopted by previous studies [96]. Based on experimental measurements, the convective heat transfer coefficient with respect to the spray distances used are shown in Fig. 4.4a. A constant $h = 65$ W m^{-2} K^{-1} was assumed along the preform surface after the atomiser gas flow stopped. In the preheated preform, the convective heat transfer coefficient assumed along substrate inner surface was increased to 125 W m^{-2} K^{-1} as a small nitrogen gas flow was directed into the tube to ensure that the substrate do not deform excessively and collide with the induction coil that may cause the cooling water flow inside the coil to leak into the spray chamber during spraying at elevated temperatures and the accuracy of this assumed value was assessed.

Along the preform-substrate interface, heat flux between the deposited material and substrate, $\dot{Q}_{int}$ can be described as:

$$\dot{Q}_{int} = h_{int} \left(T - T_{sub} \right) \qquad (4.18)$$

where h_{int} is the heat transfer coefficient between the deposit and the substrate and T_{sub} is the substrate surface temperature. The typical value of $h_{int} = 1000$ W m^{-2} K^{-1} [95] was assumed at the interface.

Enthalpy/heat input in the growing preform model was taken into account by determining the heat flux (Q_{in}) into the preform domain,

$$Q_{in} = \dot{M}(t)\, C_d \left(T_d - T_p\right) \qquad (4.19)$$

where C_d, T_d and T_p are the effective heat capacity of the incoming droplets calculated using Eqn. (4.14), maximum impinging droplet and preform/substrate surface temperature, respectively. T_d was assumed using a rule-of-mixture based on the alloy liquid fraction:

$$T_d = (1 - f_L)\, T_S + f_L T_L \qquad (4.20)$$

and f_L was estimated from the relationship between average solid fraction as a function of spray distance and gas-to-melt ratio (GMR) established for alloy steel [63] as shown in Fig. 4.4c.
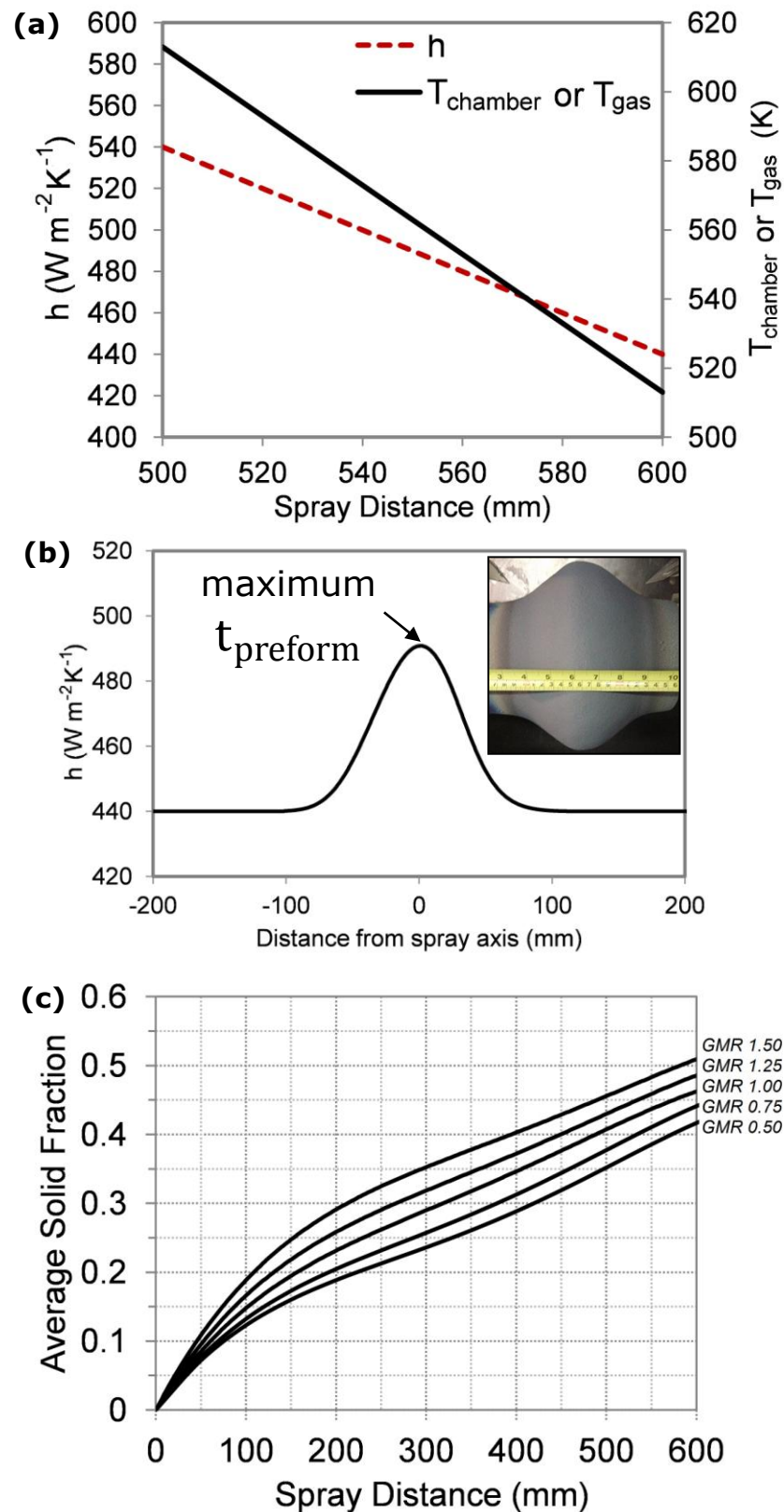
Fig. 4.4. (a) The convective heat transfer coefficient, and the spray chamber temperature as a function of the spray distance, (b) the typical convective heat transfer coefficient at the preform surface with respect to the preform shape, and (c) the average solid fraction of the spray as a function of spray distance and GMR [63].

The tube substrate was preheated via induction heating (ohmic heating) and the electromagnetic field generated by the induction coils was governed by Maxwell-Ampere's law with a magneto-quasi-static approximation [213],

$$\nabla \times \left(\frac{1}{\mu} \nabla \times A \right) + \frac{E_I}{\rho_r} = 0 \tag{4.21}$$

$$E_I = i\, A\, f_I \tag{4.22}$$

where μ is the magnetic permeability of the material, A is the magnetic vector potential, ρ_r is resistivity, f_I is induction heater frequency and E_I is the electric field. The substrate inductive heating is governed by,

$$\rho_{sub} C_{sub} \frac{\partial T}{\partial t} = \frac{1}{r} \left[\frac{\partial}{\partial z} \left(K_{sub} \cdot r \frac{\partial T}{\partial z} \right) + \frac{1}{r} \cdot \frac{\partial}{\partial r} \left(K_{sub} \frac{\partial T}{\partial r} \right) \right] + Q_I \tag{4.23}$$

$$Q_I = \frac{E_I^2}{\rho_r} \tag{4.24}$$

where Q_I is the heat source term due to ohmic heating. Throughout the preheating process, $\dot{Q}_{con}$ (h = 65 W m^{-2} K^{-1}) and $\dot{Q}_{rad}$ was defined along the tube surface. The electromagnetic properties of the mild steel substrate and copper coils are described in Table 4.2.

The copper induction coils were cooled via the water flow in the internal cooling channel of the coils. Therefore, the copper induction coils in the model were assumed to be subjected to a convective cooling ($\dot{Q}_{coil}$) [214],

$$\dot{Q}_{coil} = \frac{\dot{m}_w C_w \left(T_w - T_{coil} \right)}{2\, \pi\, r_{coil}\, A_{coil}} \tag{4.25}$$

where $\dot{m}_w$ = 0.16 kg s^{-1} is the water mass flow rate, C_w is the heat capacity of water, T_{coil} is the temperature of the copper coils, T_w = 293 K is the inlet temperature of the cooling water, r_{coil} = 52.2 mm and A_{coil} = 5.16 × 10^{-5} m^2 are the radial coordinate and internal cooling channel cross-sectional area of the coil, respectively.

The induction heating and spray forming modelling were carried out independently, i.e. the preheating of the tube substrate was simulated first and the resulting temperature distribution on the substrate was used as the initial substrate temperature in the subsequent spray forming simulation.

This approach is justified because the induction heating was turned off before the spray started. In this way, the simulation is more tractable and computationally less expensive, especially when re-meshing is used.

4.3   Mass and enthalpy coupling using mesh deformation algorithm

The coupling of the mass and enthalpy flux during the deposition process is critical to accurately simulate the shape and thermal evolutions for the growing preform. The preform shape growth and the enthalpy input in the FE model were coupled and simulated by employing the mesh deformation method available from the commercial FE package, COMSOL Multiphysics$^{®}$. The mesh deformation method governs the preform shape growth by stretching the deposition surface boundary with respect to the specified time-averaged deposition profile causing the mesh to be deformed at micrometer scales at an arbitrary time step from t to $t + \Delta t$ (Fig. 4.5a) and the enthalpy input was computed with respect to the incoming mass incorporated in the preform computational domain to provide the integrated coupling.

The computational mesh deformations throughout the preform domain were computed using a Laplace smoothing method,

$$\frac{\partial^2 \dot{r}}{\partial r^2} + \frac{\partial^2 \dot{z}}{\partial z^2} = 0 \qquad\qquad (4.26)$$

where $\dot{r}$ and $\dot{z}$ are the radial and axial displacement velocity, respectively.

The Laplace smoothing method is computationally inexpensive as it is linear and uses uncoupled single equation for each coordinate direction [215]. However, the mesh quality deteriorates as the preform grows since the mesh is deformed as shown in (Fig. 4.5a). Therefore, the limitation in the Laplace smoothing method is that there is no mechanism that prevents mesh element inversions especially when the deformation grows to larger scales and significantly deteriorates the quality of the mesh, causing numerical errors and computational instability. In order to avoid inverted mesh elements and maintain a high mesh quality, an automated re-meshing algorithm was employed to map the data from the deforming mesh to the new mesh points before the accuracy of the solution deteriorates. The solution value for each Lagrange point (node) on the new mesh was

interpolated from the solution on the preceding time step mesh and the re-meshing algorithm was automated by specifying a condition based on the maximum element distortion (MED) value allowable; where the MED value is zero for a mesh that is identical to the original mesh and increases with increasing mesh element distortion, and elements with MED value of ≥2 are considered to be severely distorted [215]. Therefore, the simulated preform growths were re-meshed when the MED value reached 1 and maintained an average mesh element quality of ≥0.87 (Fig. 4.5b).
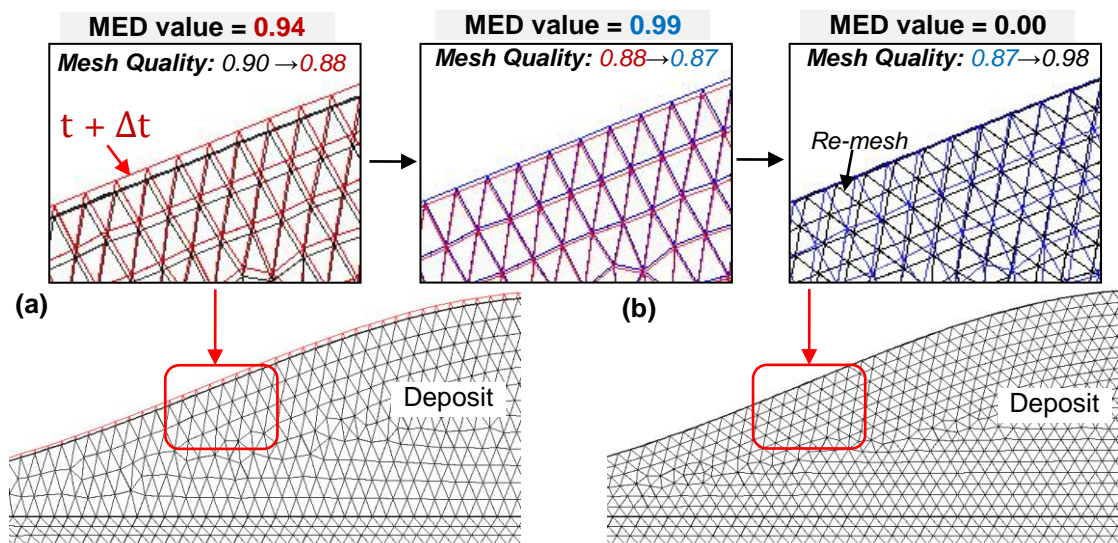
Fig. 4.5. (a) The deformed mesh at an arbitrary time step from t to $t + \Delta t$ (mesh shown in red color) due to the stretched deposition surface boundary and (b) the re-meshing of the deformed mesh when the maximum element distortion (MED) exceeded the specified threshold value of 1. The figure insets show the superimposed mesh from the preceding time steps that were masked out in the main figures for clarity.

Hence, the significance of the mesh deformation and automated re-meshing approach to simulate the preform shape and thermal evolutions is that it effectively solves the length-scale problem associated with depositing micrometer thick layers onto the surface of a preform/substrate of hundreds of centimeters by avoiding the need to generate ultrafine mesh to discretise the extremely thin regions, and allowing the shape growth to extend to relatively larger scales and also maintain sufficient simulation accuracy. Although this approach was conducted in 2D, it can be applied to any 3D spray deposition shape/enthalpy coupling.

4.4   Residual stress model

The stress, σ in the FE model was calculated using:

$$\sigma = C_{el} : (\varepsilon - \varepsilon_{TH} - \varepsilon_P) \qquad (4.27)$$

where C_{el} is the fourth order elasticity, and ε is the total strain tensor, ε_{TH} is the thermal strain component and ε_P is the plasticity strain component. In general, thermal residual stresses are developed when mismatch in strain arises due to CTE variations between the constituent materials in the preform [148] and the differences in thermal history along the preform thickness. Based on the ND derived PWF distributions, the local CTE distributions in the as-sprayed HSS were determined (Fig. 3.17b).

In general, the PWF distributions (Fig. 3.12) showed lower α'-Fe content in the central region of the preform where a dense region was formed due to the higher temperature in this region during spraying. In a typical spray, the atomised metal droplets are subjected to high cooling rates ($\sim10^2$ to 10^4 K s^{-1} [123]) that give rise to the formation of α'-Fe and γ-Fe microstructures in the sprayed HSS. These droplets are reheated rapidly during consolidation in the growing preform and higher temperatures would lead to a lower martensite starting temperature (M_s) since γ-Fe is more enriched with carbon and alloying elements, and thus retaining more γ-Fe content after cooling [19]. The simulated preform temperature (T) along the preform thickness after spraying (described in Chapter 5) showed that the ND measured f_γ in the as-sprayed HSS increases with T (Fig. 4.6a and Fig. 4.6b). Therefore, a correlation between the T and the volume fractions of the phases formed in the as-sprayed preform was established using the ND measured PWF distribution along the preform thickness to determine the local CTE distribution throughout the preform. The local M_s in the sprayed HSS estimated (Fig. 4.6a and Fig. 4.6b) using the classical Koistinen and Marburger equation [216],

$$f_\gamma = \exp\left[- k_{KM} \left(M_s - T_{amb} \right) \right] \qquad (4.28)$$

where k_{KM} = 0.0128 for tool steels [217] and T_{amb} = 293 K is the ambient temperature, were assumed with a linear relationship as a function of T for the as-sprayed HSS in preform NP1 (Fig. 4.6c) and P2 (Fig. 4.6d).

Table 4.3. The established correlations between local M_S and T for the as-sprayed HSS.

Preform	Sprayed alloy	Correlation
NP1	M2	M_S = -0.496 × T + 1153.83
P2	ASP30	M_S = -0.433 × T + 1008.175

The local volume fractions of the phases formed throughout preform were simulated using the established correlations between M_S and T as described in Table 4.3 and the typical simulated local CTE throughout the preform (P2) is shown in Fig. 4.7a. The mild steel substrate was assumed with a mean CTE of 14.4 μ K^{-1} [194]. The simulated local CTE distribution showed good agreements with the ND measured CTE along the preform thickness (Fig. 4.7b) in the preform central region. The simulated porosity distribution in preform P2 (described in Chapter 5) was shown (Fig. 4.7c) to show the links between porosity distribution and microstructures formed in the as-sprayed preform characterised using X-ray μCT and ND, respectively. In regions where porosity is relatively high (towards the preform surface and edges), the corresponding local CTE is low. This is due to the solidified/colder droplets deposited in the porous region typically undergo higher cooling rates that gave rise to more α'-Fe and thus, a decreased local CTE.

Therefore, the correlations established based on the X-ray μCT and ND measurements showed good agreements with one another and provided the crucial links to take into account the effects of the microstructure formed on the corresponding material properties and the stress developed during cooling.
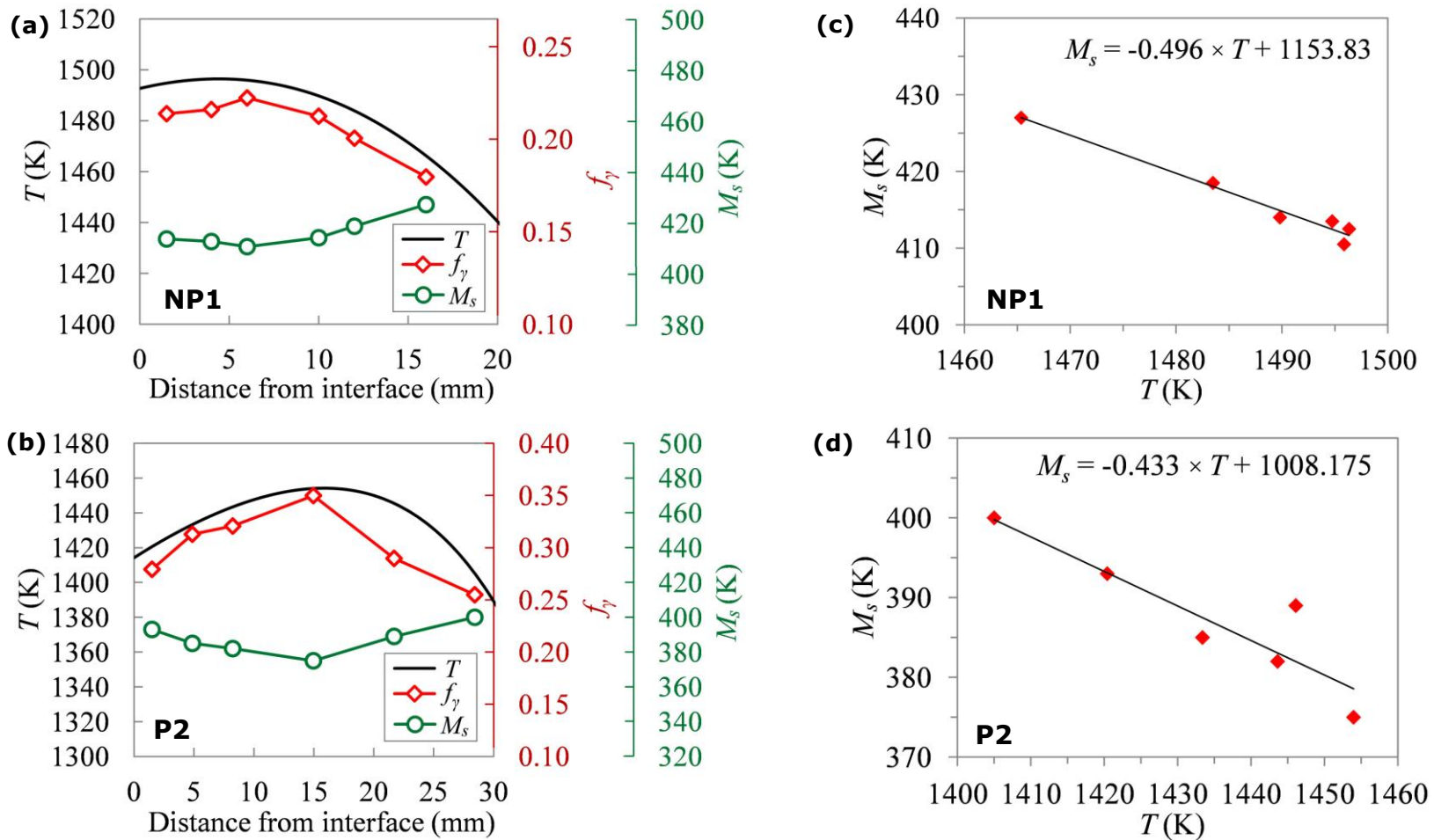
Fig. 4.6. The ND measured f_γ, simulated T and calculated local M_s in preform (a) NP1 and (b) NP2, and (c-d) the corresponding relationship between the local M_s and simulated T.
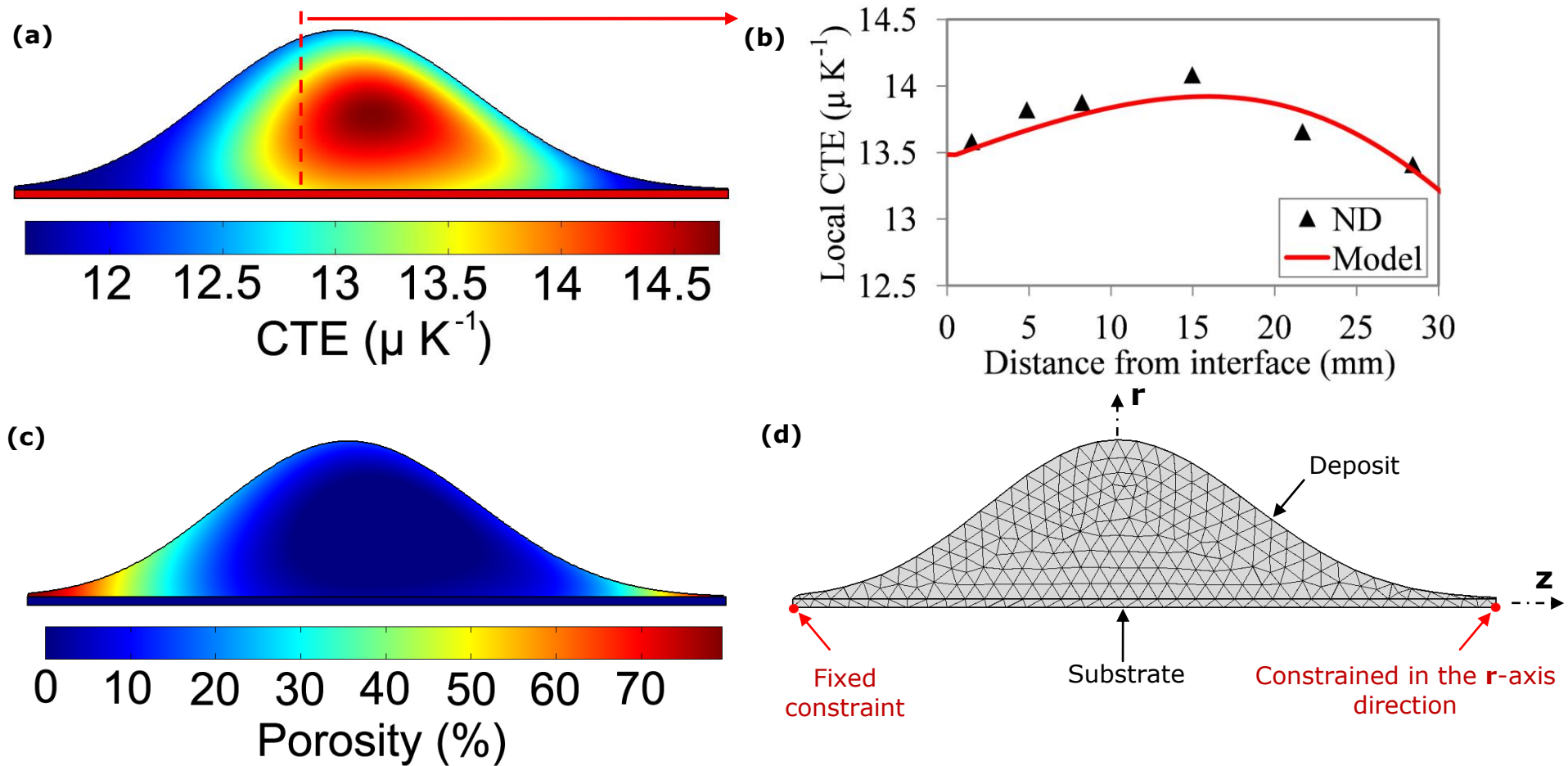
Fig. 4.7. (a) The simulated local CTE distribution in preform P2, (b) the simulated and ND measured local CTE along the preform thickness, (c) simulated porosity distribution and (d) the boundary conditions specified for the residual stress model (larger mesh size was used for clarity).

Coupled with the aforementioned thermal model, the thermal strains in the preform can thus be calculated using [151]:

$$\varepsilon_{TH} = \alpha \, (T - T_{sf}) \qquad (4.29)$$

where α is the material CTE tensor, T is the preform temperature, and $T_{sf} = 1158$ K is the stress-free temperature above which most steels including high strength steels [218] lose their strength.

The preform domain was constrained by defining a fixed constraint at one corner of the substrate inner surface boundary and constraining the movement in the preform radial direction at other corner (Fig. 4.7d). These boundary conditions were specified to prevent rigid body movement and do not affect the stress distributions especially in the central region of the preform. Triangular mesh elements with average mesh quality of 0.98 were employed to simulate the stress distribution in the preform. Isotropic and bilinear kinematic hardening material models were used and phase transformation effects were not considered. The yield strength (σ_{yield}) and kinematic tangent modulus (K_T) used for the HSS and mild steel in the stress simulation were based on based on experimental measurements from [219, 220] and [221], respectively as shown in Fig. 4.8a and their values are given in Table 4.4. The σ_{yield} of the steels were temperature-dependent and their values at elevated temperatures were estimated based on measured yield strength reduction factor measurements (Fig. 4.8b) from [218].

Table 4.4. The room temperature σ_{yield} and K_T used for the HSS [219, 220] and mild steel [221] in the stress simulation.

Steel	M2	ASP30	Mild steel
σ_{yield} (MPa)	2330	2330	401
K_T (GPa)	40	40	0.83
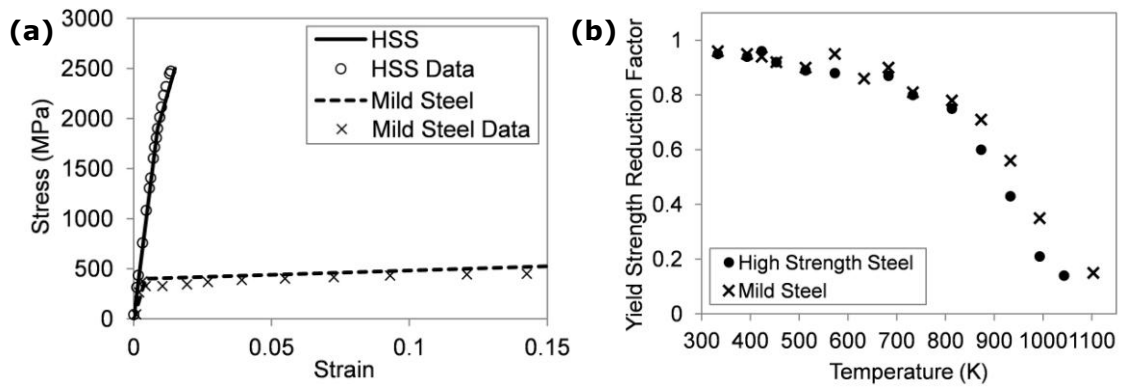
Fig. 4.8. (a) The stress-strain curves of the HSS [219] and mild steel [221] at ambient temperature used in the bilinear kinematic hardening material models and (b) the yield strength reduction factor with respect to temperature [218].

The effects of porosity on the material properties were taken into account in the model by calculating the local porous Young's modulus (E_{Porous}) and Poisson's ratio (ν_{Porous}) using the models developed for sintered steels [222-224]:

$$E_{Porous} = E_D \left[\frac{(1-P)^2}{1+(2-3\nu)P} \right] \tag{4.30}$$

where E_D the Young's modulus of the dense HSS and P is porosity. ν_{Porous} for the deposit layer was determined using [223]:

$$\nu_{Porous} = (\nu + 1)\left(\frac{0.41 - P}{0.41} \right)^{0.0855} - 1 \tag{4.31}$$

where ν is the Poisson's ratio of the dense alloy, P is ≤ 0.22 and regions where $P > 0.22$ were assumed with $\nu_{Porous} = 0.217$ (derived using $P = 0.22$).

4.5   Summary

A numerical model was developed to simulate the preform shape evolution, thermal history and thermal stress development. The model used an efficient mesh deformation method with automated re-meshing algorithm used to model the growing performs and address the coupling of the droplet mass/enthalpy input at the deposition surface. In addition, the model incorporated a substrate preheating model to simulate the complete preform thermal history and mapped the microstructure distributions into the preform domain to take into account their effects on the material properties and the corresponding stress developed.

In the subsequent chapters, the simulated thermal histories and stress distributions were employed as a means of assessing the quality of the interfacial bonding formed in the preforms non-destructively by comparing with the neutron diffraction characterised residual stress distributions.

CHAPTER 5 : MODELLING AND 3D CHARACTERISATION OF SPRAY FORMED DISSIMILAR STEEL

This chapter presents the systematic study of 3D characterisations of the microstructures and residual stress developed in the as-sprayed dissimilar steel tube preforms manufactured with different spray parameters. Numerical modelling of the preform shape evolution, thermal history and stress are presented. The study established for the first time the links between preform thermal history, corresponding microstructure formed and the interfacial bonding developed to provide the key insights to understand the interfacial bonding and residual stress development mechanisms in as-sprayed dissimilar steel preforms.

5.1   Preform shape simulation and validation

Fig. 5.1 shows the simulated and measured shapes of the as-sprayed preforms. The non-preheated preforms (Fig. 5.1a and Fig. 5.1b) were sprayed with higher substrate retraction speeds thereby producing relatively longer tube preforms in comparison to the preheated preforms (Fig. 5.1c and Fig. 5.1d). The effect of the progressively reducing mass flow rate towards the end of the spraying process is more apparent in the longer preforms that showed a tapered shape. The model generally showed good agreements with the measured preform shapes (both the shorter and longer preforms) which verified the mass flow rate reduction factor towards the end of the spraying process assumed in the model. The irregular surface of preform NP1 (Fig. 5.1a inset) caused the differences between the measured and simulated shape especially at ~50 - 110 mm along the tube length and the heat flow simulation described later in this chapter was used to investigate the key factor that contributed to such surface irregularities.
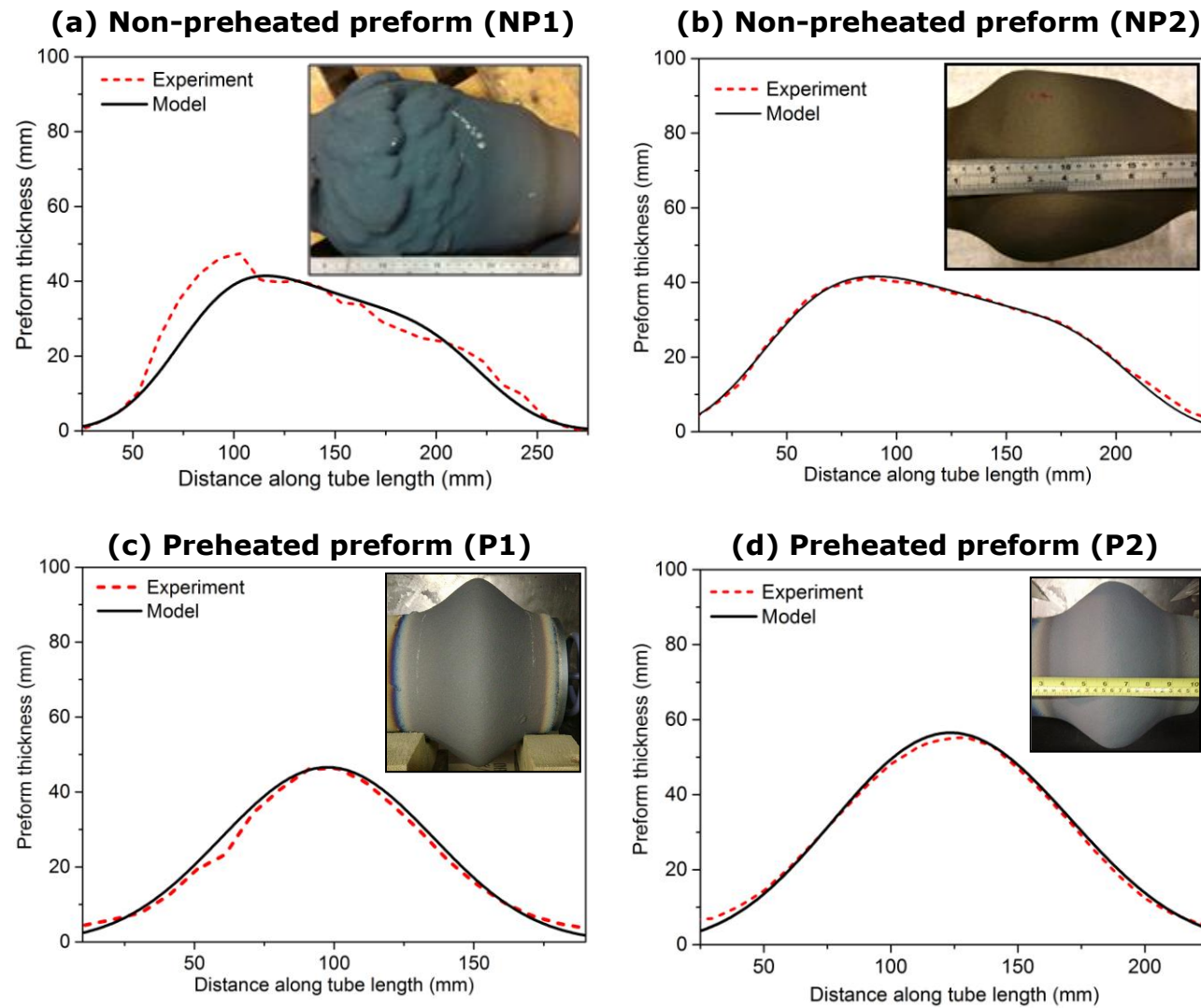
Fig. 5.1. The simulated and measured shapes of the (a-b) non-preheated and (c-d) preheated preforms.

5.2 Thermal model sensitivity studies and validation against experiment

5.2.1 Induction heating of the substrate

The simulation of the substrate induction heating was compared with the measured temperatures (Fig. 5.2a) along the preheated tube length using different induction heating input voltages. In general, the substrate heating rate increases with increasing temperature as shown in Fig. 5.2b and Fig. 5.2c, and the heating rate noticeably decreased at 973 - 1073 K due to tube substrate material (mild steel) transformed into a non-magnetic material when it was heated above the Curie temperature (1033 K). When cooled to ambient temperatures, the tube substrate regained its magnetic properties and can be reheated by induction with similar heating rates or profiles, theoretically. The maximum substrate temperature after being preheated for 150 s using 350 V input voltage is ~1050 K and increased to ~1200 K using 400 V input voltage. In Fig. 5.2c, the starting temperature for the measured temperature profile was relatively higher due to the experiment was carried out in a thermal cycling manner and the initial substrate temperature in the model was updated accordingly.

In addition, the substrate in a typical spray forming set-up can be subjected to atomiser gas cooling before spraying. Thus, temperature profile was measured at d_S = 600 mm whilst under the influence of induction heating. The simulated temperature profile during cooling showed good agreements with the temperature measurements (Fig. 5.2d) which also confirmed the validity of the h used in the thermal model. The differences between the simulated and measured substrate temperatures using the pyrometer may be due to the substrate rotation during measurement. Nevertheless, the model showed good agreements with the thermocouple (TC1) measurements and predicted the heating profile trend reasonably well.
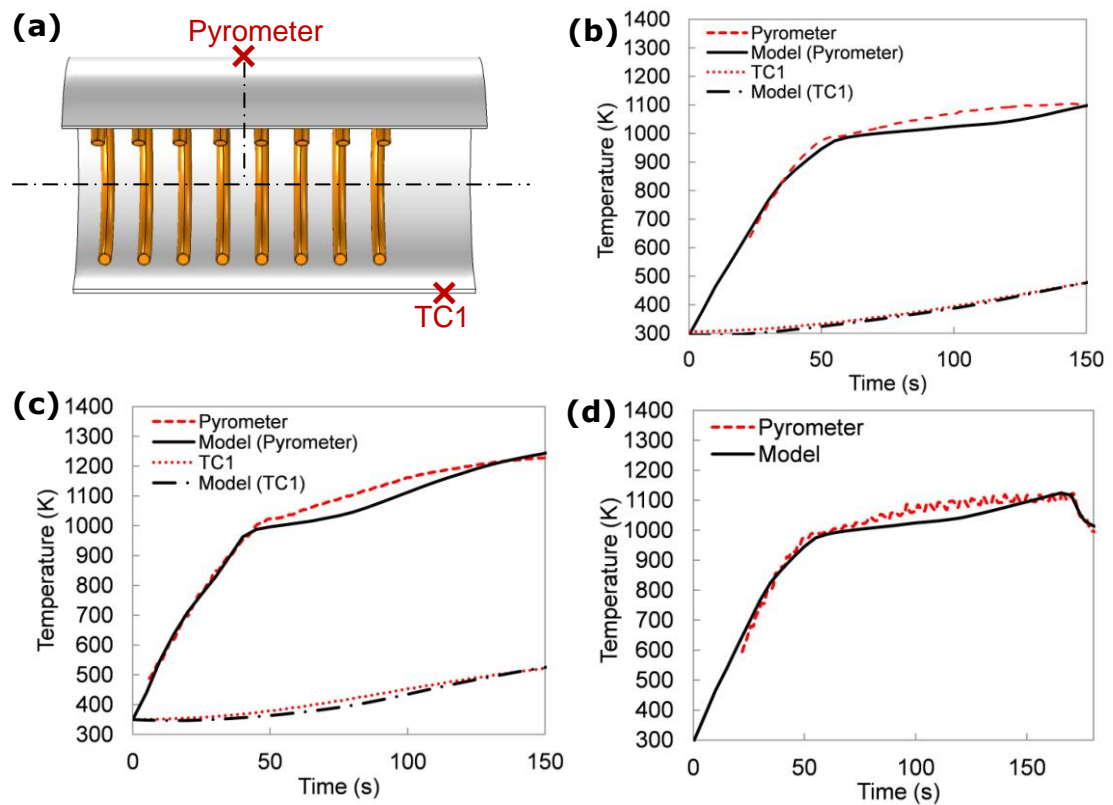
Fig. 5.2. (a) A schematic of the temperature measurement positions marked using red × along the preheated tube substrate length, the comparison between simulated and measured temperatures with induction heating voltage set at (b) 350 V and (c) 400 V, and (d) subjected to atomiser gas cooling at d_S = 600 mm.

5.2.2 Heat transfer coefficients

The convective heat transfer coefficients used have significant effects on the simulated preform heat flow and thermal histories. The difficulty lies in obtaining the sensible heat transfer coefficient values and its distribution along the preform/substrate surface. Therefore, the preform thermal histories at the interface were simulated repeatedly at a fixed d_S (= 600 mm) using different h during spraying but a constant h after spraying (Fig. 5.3a and Fig. 5.3b) to assess the sensitivity of the calculated temperatures due to the assumed heat transfer coefficients and to find the best approximation to the experimental temperature measurements obtained from the thermocouple positioned at the interface. Due to the recirculating droplets/powders in the spray chamber during spraying, the preform surface temperature measurements acquired using the pyrometer were unreliable and similar findings were reported in previous spray forming

studies [7]. Thus, the simulated preform thermal history was validated against the measurements obtained using the thermocouple at the interface. Heat transfer coefficients of 440 W m^{-2} K^{-1} and 125 W m^{-2} K^{-1} defined along the preform surface and substrate inner surface, respectively gave the best agreement between the simulated and measured temperatures, and thus, were used in the simulations.

A similar approach was used to investigate the effects of the different h after atomiser gas flow ended (Fig. 5.3c) and h = 65 W m^{-2} K^{-1} showed good agreements with the measured cooling rates. The interfacial heat transfer coefficient specified in the model was in the range of typically used values in previous models [95, 96] and therefore no further sensitivity study was performed.
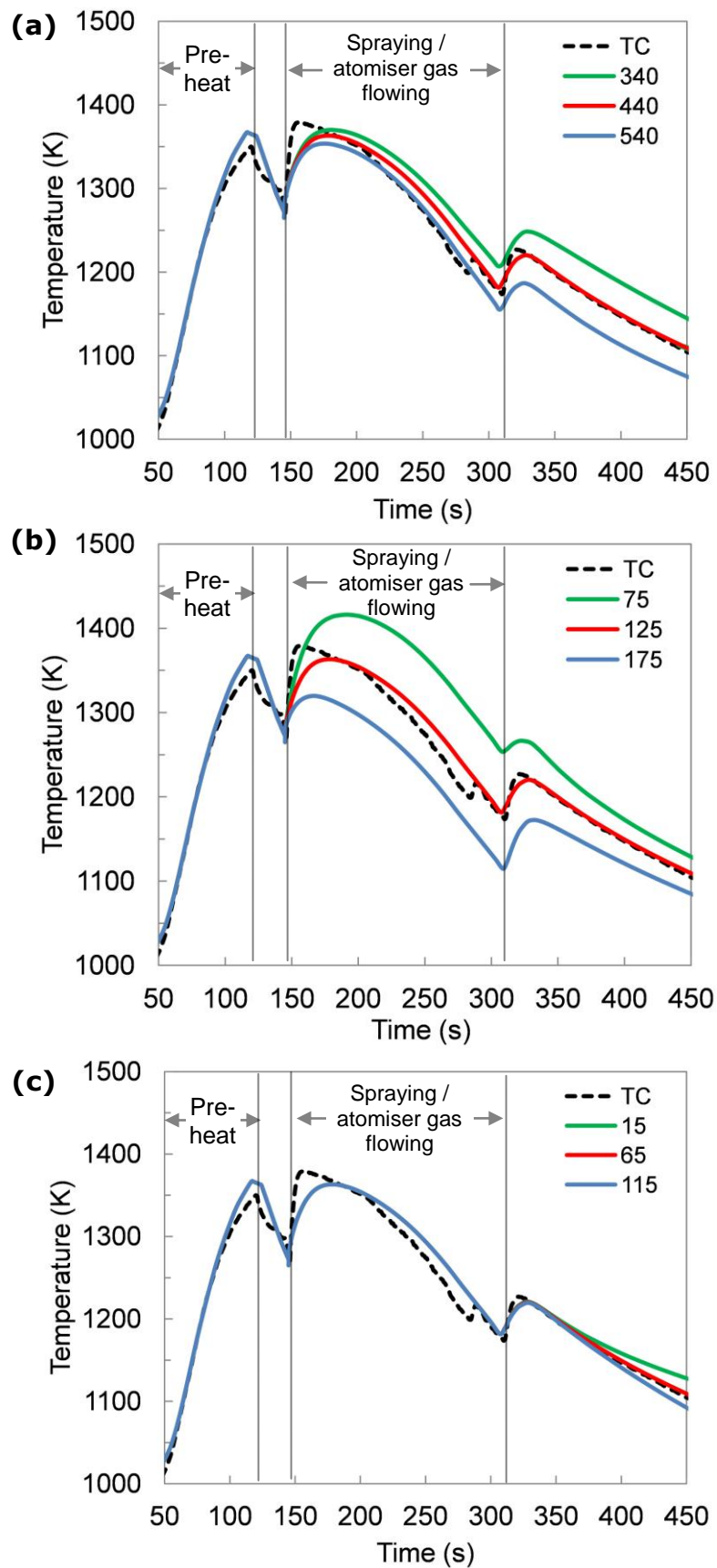
Fig. 5.3. Simulated and measured temperatures from the thermocouple (TC) set at the interface of the preheated preform P2 using different convective heat transfer coefficients (W m^{-2} K^{-1}) defined along (a) preform surface, (b) substrate surface during spraying and (c) after atomiser gas flow ended.

5.3 Preform heat flow simulation

The simulated thermal histories and heat flows in the non-preheated preforms NP1 and NP2 are shown in Fig. 5.4a and Fig. 5.4b, respectively. In general, the preform surface directly under the spray cone was in a mushy state during spraying and the mushy zone was predominantly formed along the central region of the preform thickness as the deposition progressed along the tube length. The tube preform surface is generally colder especially at larger substrate retractions because the preform surface is subjected to deposition of smaller and colder droplets from the spray periphery. After the spray ended, heat flows from the centre of the preform towards the colder preform surface regions.

Due to the shorter spray distance (lower average spray solid fraction) used to spray preform NP1, the maximum temperature and liquid fraction in the preform central region ($\sim$1620 K and $f_L = \sim$0.5) were higher in comparison to preform NP2 ($\sim$1600 K and $f_L = \sim$0.4) especially in the initial phase of spraying at 10 s. The relatively high f_L in preform NP1 can cause droplet splashing and give rise to irregular preform surface especially under the effect of higher atomising gas flow velocities at the shorter spray distance used.

The simulated thermal histories and heat flows in the preheated preform P1 and P2 are shown in Fig. 5.4c and Fig. 5.4d, respectively. In comparison to the non-preheated preforms, the substrate heating rate is higher due to the smaller temperature differences between the depositing droplets and the substrate surface temperature. It is noteworthy that the relatively lower maximum f_L in the preheated preforms during spraying is due to the relatively longer spray distances used as compared to the non-preheated preforms. Nevertheless, the preheated preforms showed similar heat flow trends.

The maximum preheated substrate temperature (at 0 s) was higher in preform P2 ($\sim$ 1300 K in Fig. 5.4d) as compared to preform P1 ($\sim$900 K in Fig. 5.4c) due to the substrate being shielded from the atomiser gas flow before spraying commenced. During spraying, both preheated preforms

maintained a mushy zone directly under the spray cone with a maximum f_L = ~0.30. The mushy zone f_L in preform P1 decreased at a faster rate when the melt flow rate reduced towards the end of the spray process due to the higher GMR used as described in Table 3.3.
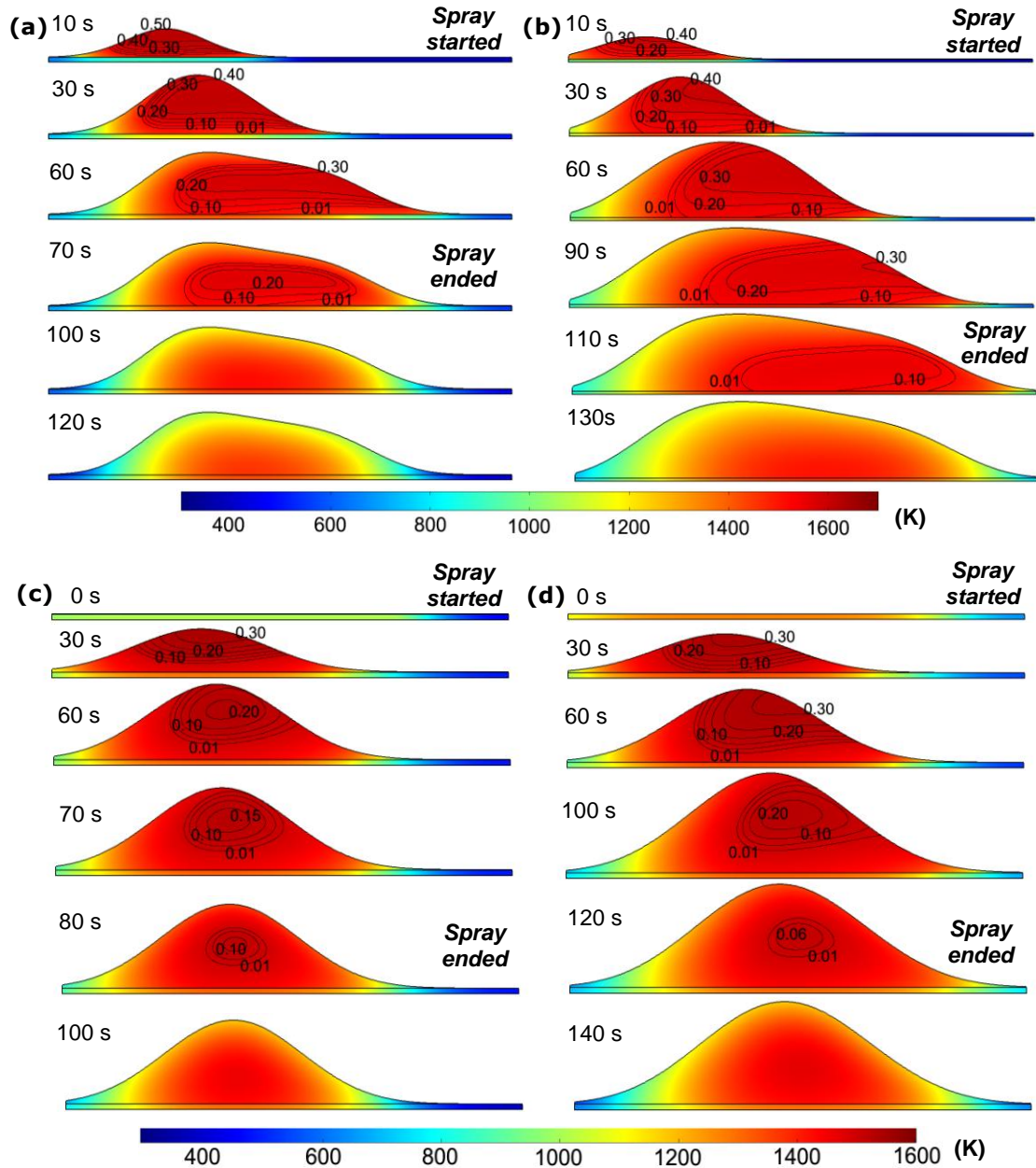
Fig. 5.4. The simulated thermal histories and heat flow contours in the non-preheated preform (a) NP1 and (b) NP2, (c) preheated preform P1, and (d) P2 at the selected spray time for each case.

The relatively colder spray temperature towards the end of the spraying process caused the reduced f_L in the mushy zone directly under the spray cone in the preforms and its effect on the microstructures and the corresponding thermal residual stress will described later in this chapter.

5.4 The correlation between thermal history and the porosity distribution

The X-ray µCT characterised porosity distributions along the non-preheated and preheated preform thickness are shown in Fig. 5.5a and Fig. 5.5b, respectively. Due to geometrical constraints during sectioning, preform NP1 thickness was limited to 20 mm. Nevertheless, the constraint did not affect the porosity characterisation in the interface region. Generally, a layer of porosity was formed in the interface and preform surface regions and a dense (near to zero porosity) material formed predominantly in the central region of the deposit. The formation of porosity in these regions was typical for spray formed materials [60] and the porosity in the interface and surface regions of spray formed alloys such as Ni superalloys, Al alloys and steel are generally higher (up to ~30%) than the preform central region [225, 226]. It is noteworthy that the porosity levels in the interface region were lower in the preheated preforms as compared to the non-preheated preforms.

The simulated temperatures of each deposited layers (T_{Layer}) immediately before the next deposition round were extracted from the thermal model and superimposed in Fig. 5.5. It is compelling to find that when the deposited layers maintained $f_L \geq 0.20$ during spraying, the measured porosity for that layer after spraying is near zero (dense material formed). This is true for all the studied cases in this research, a finding consistent with spray formed steel tubes reported by previous studies [95]. $f_L = 0.20$ is the lower limit for the preforms described herein and Fig. 5.5 also showed that spray formed layers without porosity can be formed when the deposited layer maintained a liquid fraction of up to 0.55 as found in preform NP1.
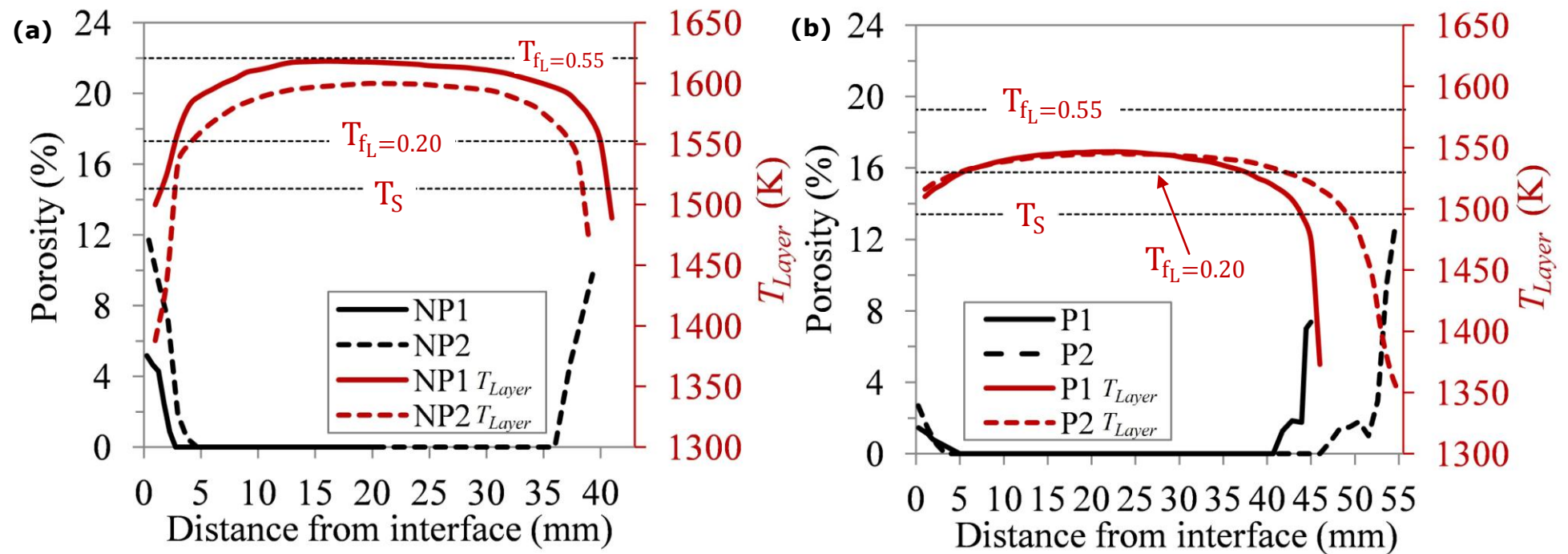
Fig. 5.5. The X-ray μCT characterised porosity distribution along the as-sprayed (a) non-preheated and (b) preheated preform thickness with the respective simulated deposited layer temperatures superimposed.
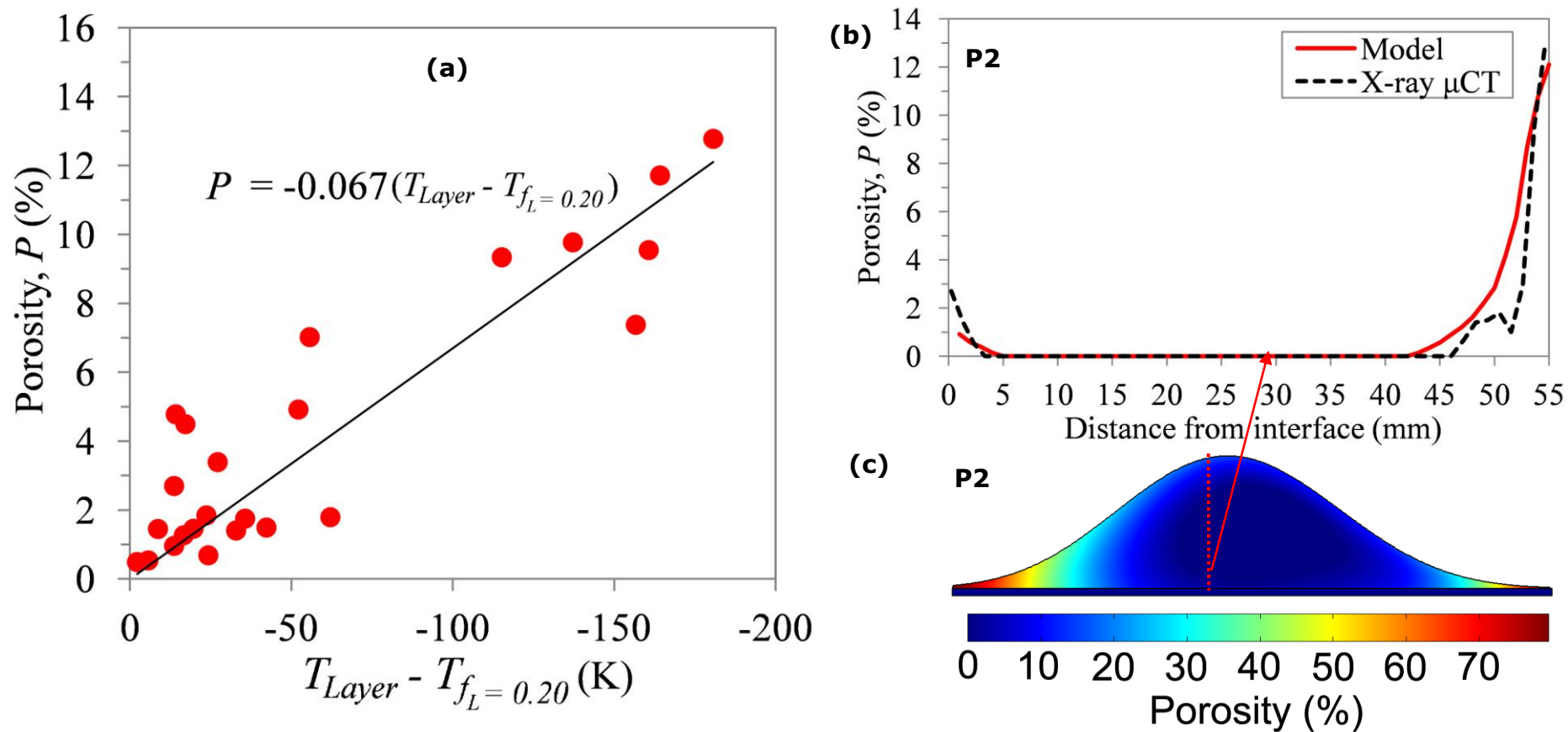
Fig. 5.6. (a) The established correlation between the porosity and the temperature of the deposited layer relative to the alloy temperature at $f_L = 0.20$, (b) the simulated porosity distribution along the thickness of preform P2, and (c) the simulated porosity distribution throughout the preform.

Although porosity in the preform can be reduced by maintaining high liquid fractions in the deposited layers, excessive liquid fractions was shown to give rise to poor and irregular preform surface quality (Fig. 5.1a). Hence, there is a trade-off between porosity and preform surface quality. Nevertheless, the study showed that increased substrate temperature prior to spraying is an effective approach to overcome the trade-off to produce preforms with low porosity and good surface quality. The excessive heat typically required in a non-preheated preform set-up to maintain the optimum liquid fractions in the deposited layers, especially in the first few layers that come in direct contact with the "cold" substrate, can be inhibited by reducing the temperature difference between the substrate surface and the impinging droplets which can be realised by preheating the substrate. The preheated substrate enabled spraying the alloy and maintaining the deposited layers at temperatures near to the lower limit ($T_{f_L=0.20}$) as soon as spraying commenced which suppressed porosity formation especially in the interface region (Fig. 5.5). The reduced temperature difference can also inhibit the stress developed in the interface region as the hot metal droplets do not experience the strong quenching effects as they would in a non-preheated set-up, and combined with the lower porosity directly give rise to a stronger interfacial bond.

Generally, porosity is formed in the preform interface and surface regions where $T_{Layer} < T_{f_L=0.20}$ and the porosity level gradually increased with the decrease in T_{Layer}. The porosity formation in the interface region can therefore be inhibited by preheating the substrate to promote re-melting of the solidified droplets deposited. Fig. 5.5b showed that the preheated substrate led to higher T_{Layer} near to the interface region (~0 – 5 mm from the interface) that gave rise to relatively low porosity in this region as compared to the non-preheated substrate (Fig. 5.5a). The correlation between the porosity (P) formed and T_{Layer} relative to $T_{f_L=0.20}$ was established (Fig. 5.6a) from the X-ray µCT characterised porosity distributions and simulated preform thermal history:

$$P = -0.067\left(T_{Layer} - T_{f_L=0.2}\right) \qquad (5.1)$$

where $P = 0$ at $T_{f_L=0.20} < T_{Layer} < T_{f_L=0.55}$ and $T_{f_L=0.55}$ is the alloy temperature at $f_L = 0.55$. The simulated porosity distribution in preform P2 (Fig. 5.6b) using the correlation established in Eqn. (5.1) showed reasonable agreement with the measured distribution. The simulated porosity distribution throughout the preform (Fig. 5.6c) showed that relatively high porosity was formed in the extreme edges of the preform where solidified/colder droplets were deposited predominantly during spraying. The substrate was assumed to be free from porosity.

5.5   The correlation between thermal history and carbides formed

The carbides typically formed in the dense and porous (interface) region of the as-sprayed HSS are shown in Fig. 5.7a and Fig. 5.7b, respectively. In the dense region of preform NP1, M_2C carbides (lamellar-like and acicular morphology) were formed along the grain boundaries. The carbides formed predominantly along the grain boundaries in the interface region were M_6C carbides with spherical MC carbides uniformly distributed throughout the microstructure as a result of M_2C carbides decomposition [227-229]. The synchrotron X-ray µCT 3D carbide renderings shown in Fig. 5.7c and Fig. 5.7d revealed clearly the 3D morphology of the continuous M_2C carbide network and the finer discontinuous M_6C carbides, respectively.

The final carbide microstructure formed in as-sprayed steels is dependent on the preform cooling rates [230]. Metastable M_2C carbides are generally formed during rapid solidification and they tend to decompose to form M_6C and MC carbides when exposed to high temperatures (>1273 K) [228, 231]. Although the temperatures in the preforms during spraying were generally >1273 K, some M_2C carbides were retained in the dense region of the as-sprayed HSS due to the relatively short dwell times (~100 s) at these temperatures in comparison to the typical time required for M_2C carbide decomposition which is in the range of a few hours [126].

Nevertheless, the finer M_2C carbides formed at higher cooling rates can undergo decomposition easily when exposed to high temperature in a short amount of time [126, 227]. Mesquita *et al.* [232] suggested that finer carbides were formed in the porous regions of spray formed HSS billets due

to the fine microstructures developed in the droplets prior to deposition were not altered significantly as a result of the low liquid fractions in these regions. Hence, the finer carbides in the interface region exposed to typical temperatures of ~1400 K during spraying decomposed to form the discontinuous and fine M_6C carbides (~1 - 2 μm).
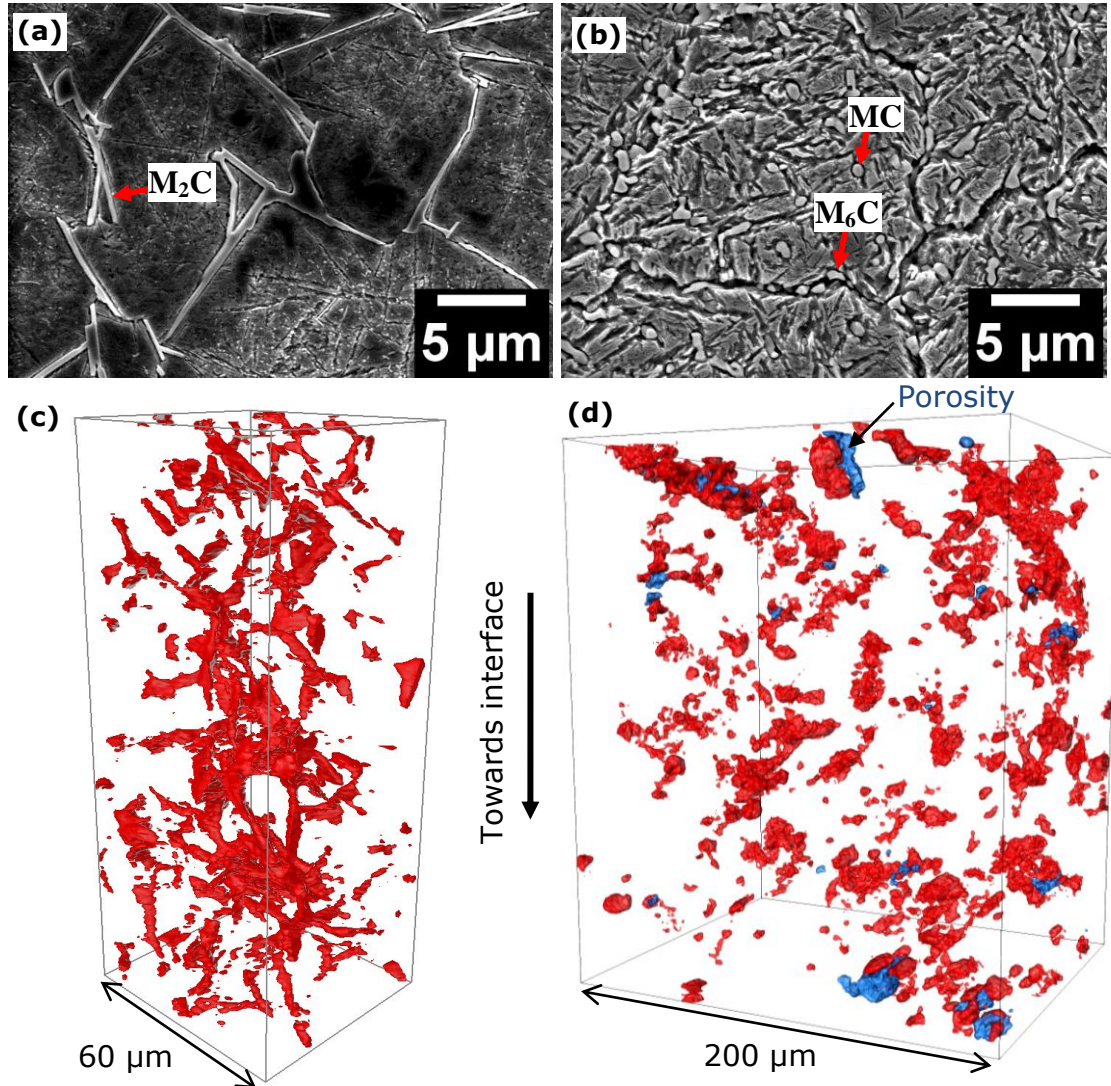
Fig. 5.7. The carbides formed in the (a) dense region of preform NP1 and (b) interface region of preform P2, and the corresponding synchrotron X-ray μCT 3D rendering of the (c) continuous M_2C carbide network (d) discontinuous M_6C carbides with the porosity shown in blue.

5.6   Residual stress distribution and interfacial bonding

Fig. 5.8a and Fig. 5.8b shows the residual stress distributions in the as-sprayed dissimilar steel preform NP1 and P2, respectively. Generally, the simulated stress distributions show tensile stress in the substrate and compressive stress in the deposit due to the underlying mild steel substrate with higher CTE was constrained by the deposited layer during cooling. In the preheated preform (P2), ND measurements showed that tensile stress of up to ~220 MPa was found in the in substrate which is near to the stress predicted by the model (~230 MPa) and a tensile stress of ~130 MPa in the deposit region next to the interface (~1.5 mm from the interface). On the other hand, near to zero stress in the substrate was measured in the non-preheated preform (NP1) and a relatively high tensile stress of up to ~350 MPa was found in the deposit directly next to the interface (~1.5 mm from the interface). The compressive stresses developed in the deposit region of preform P2 were relatively higher (up to ~170 MPa) in comparison to preform NP1.

The simulated stress distributions were based on a perfectly bonded deposit and substrate preform. Hence, the difference between the simulated and measured stress especially in the substrate (Table 5.1), is indicative of how perfectly the interface is bonded together. The near to zero stress in the substrate of the non-preheated preform NP1 (Fig. 5.8a) suggests that although the substrate was seemingly bonded to the deposit from the SEM analysis, there is actually a poor bonding without strength, and the adhesion is most likely due to a mechanical interlock mechanism caused by the substrate surface roughness [233].
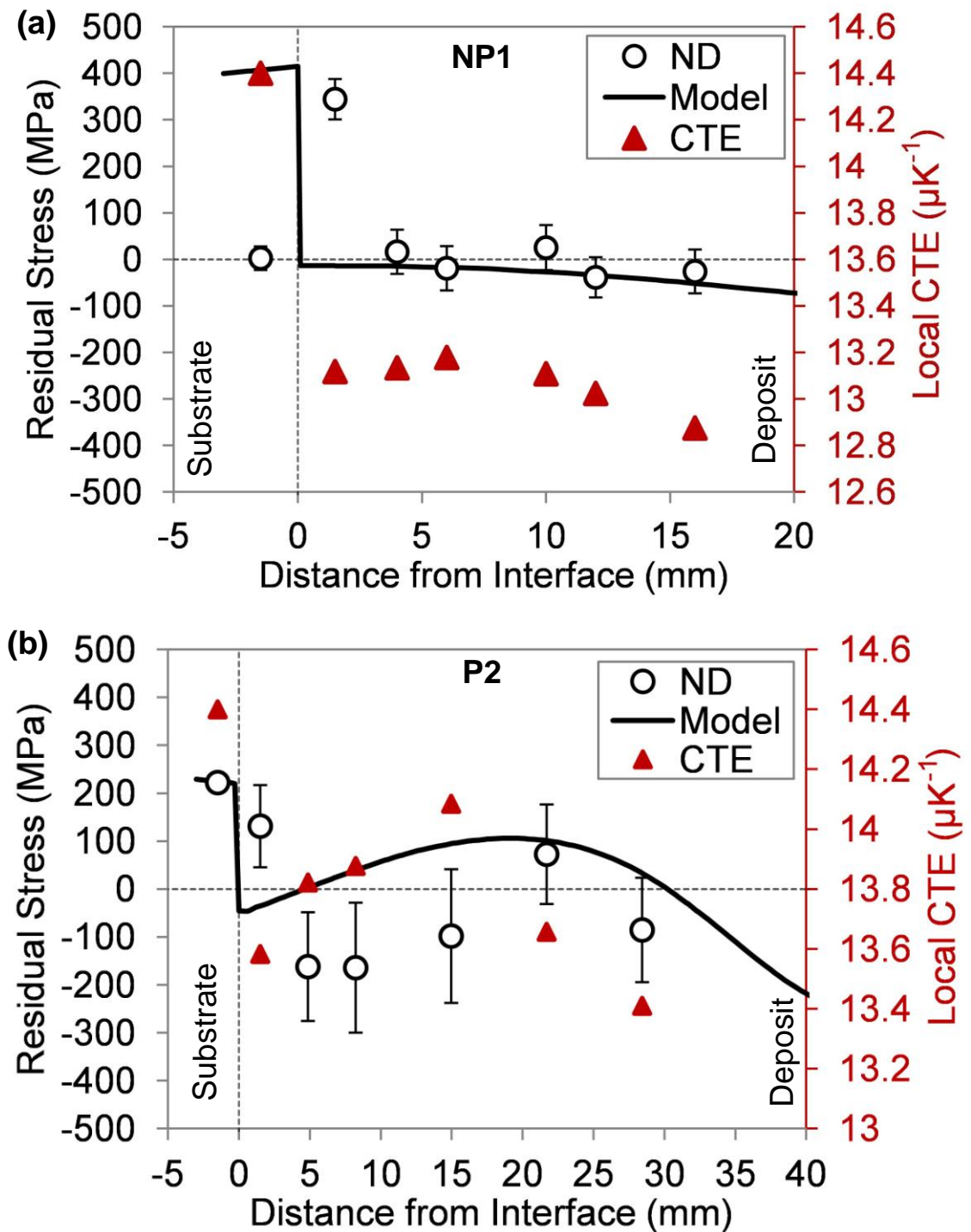
Fig. 5.8. The simulated and ND measured residual stress distributions along the preform thickness of the as-sprayed preform (a) NP1 and (b) P2 with the ND measured local CTE distributions superimposed.

Table 5.1. The ND measured and simulated residual stress in the substrate.

Preform	NP1	P2
ND (MPa)	2.6	222.3
Model (MPa)	404.5	234.4

On the other hand, the ND measurements revealed that a considerable amount of tensile residual stress (222.3 MPa) was developed in the preheated preform P2 (Fig. 5.8b), indicating that a strong bond was formed at the interface. The residual stress simulation showed that a perfect metallurgical bonding would result in a higher tensile stress in the substrate of 234.4 MPa. Therefore, comparing the ND measured stress profile with the simulated profile, the quality of the interfacial bonding can be assessed quantitatively, and linked to the simulated thermal histories which in turn controlled by many spray forming parameters. This combined modelling and experimental approaches successfully linked the quality of interfacial bonding directly with the parameters used in the spray forming processes.

5.7 Effects of substrate temperature on interfacial bonding and residual stress

The ND and SEM analyses of the interface bond showed that a strong bond can be formed when the substrate is preheated. Nevertheless, the deposited layer in the preheated preform P1 was not bonded to the substrate due to the maximum substrate preheat temperature (~1020 K) was lower than that of preform P2 (~1270 K) as shown in Fig. 5.4c and Fig. 5.4d, respectively. This suggests that the interfacial bond is formed under the condition that the substrate preheat temperature above a certain threshold is met and is consistent with previous experimental studies [4]. Therefore, the substrate preheat temperature affects the interfacial bond formation and in return the residual stress distribution in the as-sprayed preform.

The ND measured residual stress distributions (Fig. 5.8) showed that the increased substrate temperature decreased the residual stress developed in the preform especially near to the interface region. In most thermally sprayed materials, the residual stress generated can be contributed by the thermal mismatch between the constituent materials and quenching stress [234, 235]. The relatively high tensile stress measured in the non-preheated preform (Fig. 5.8a) deposit layer next to the interface region (~1.5 mm from the interface) is likely to be due to the quenching stress induced by the large initial temperature difference between the depositing droplets and the substrate (at ambient temperature). The initially "cold"

substrate caused the deposited layer directly next substrate surface to sustain significant tensile stress since its contraction was constrained by the underlying substrate as its temperature rapidly drops [235]. The development of such significant tensile stress can lead to crack formation at the interface which deteriorates the interfacial adhesion and could have caused the poor interfacial bond in preform NP1. The stress in this region (~1.5 mm from the interface) was reduced when the substrate was preheated before spraying (Fig. 5.8b) indicating a lower quenching stress due to the smaller temperature differences.

The effects of different substrate preheat temperatures on the residual stress and microstructures developed are shown Fig. 5.9. The residual stress and local CTE distributions were simulated using preform P2 spraying parameters. The substrate preheat temperature was increased and decreased by 250 K to study the effect of preheating the substrate above and well below the alloy solidus temperature (1495.5 K), respectively while maintaining the same droplet spray temperature. Fig. 5.9a shows that increasing the substrate preheat temperature causes a decrease in the residual stress developed in the preform. The lower residual stress especially in the substrate was due to the corresponding change in local CTE developed in the deposited layer (Fig. 5.9b). Higher substrate preheat temperatures decreases the deposited layer cooling rate especially the layer next to the substrate surface leading to lesser α'-Fe formed in the deposited layer. Consequently, the CTE mismatch between the substrate and deposit decreases leading to smaller residual stress developed in the as-sprayed preform. The change in local CTE is larger near to the substrate surface where the effect of the higher preheat temperature is more significant.
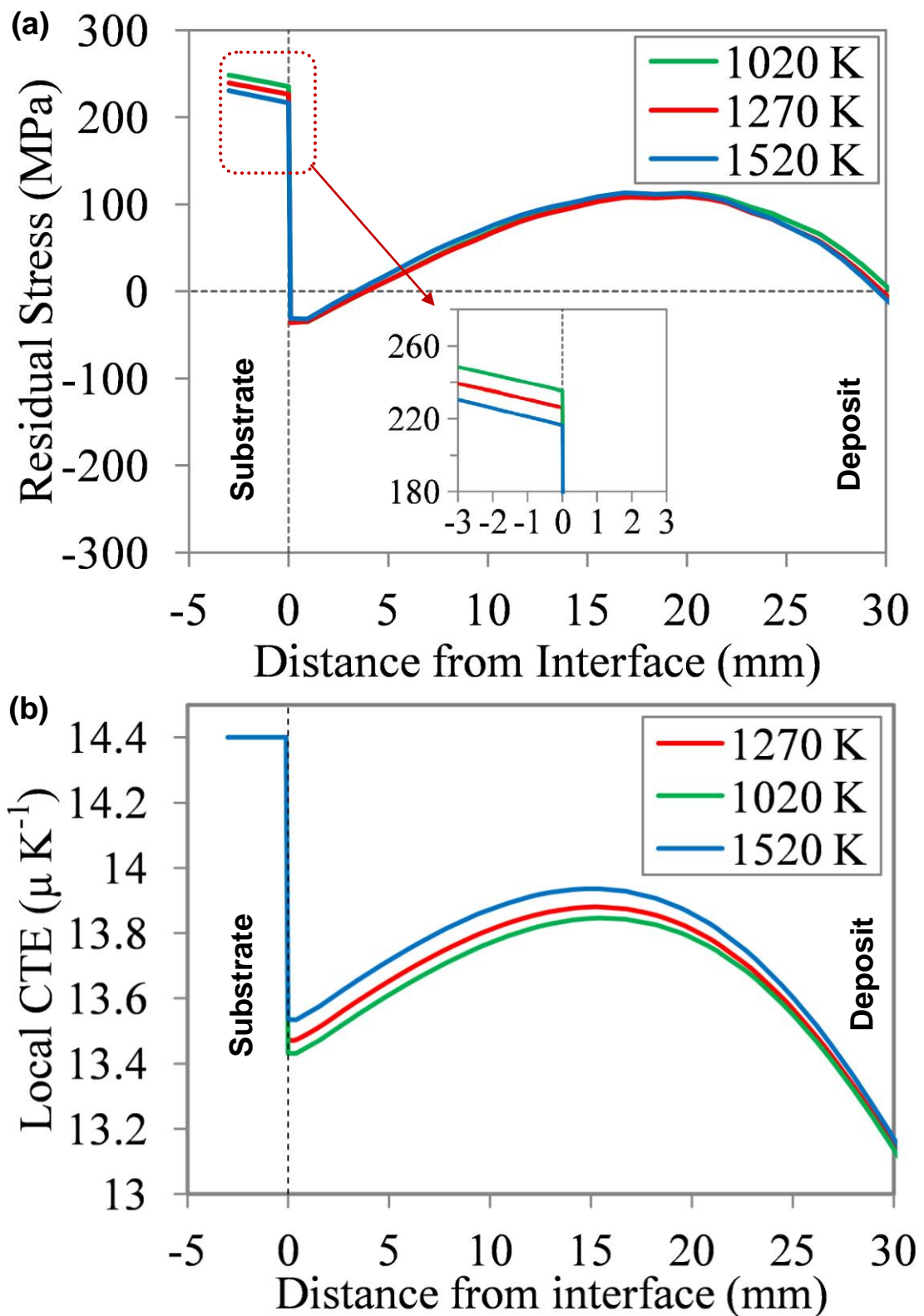
Fig. 5.9. (a) The simulated residual stress distribution in preform P2 using different substrate preheat temperatures while maintaining the same spray temperature and (b) the corresponding simulated local CTE distribution developed.

5.8 Effects of spray temperature on interfacial bonding and residual stress

The spray temperature in a typical spray forming process also has a direct effect on the interfacial bond formation since a colder spray would give rise to significant porosity formation that can weaken the interfacial bond and in more extreme cases, the integrity of the sprayed layer. Preform P1 was sprayed with a higher gas-to-melt flow ratio (GMR = 0.61) as compared to that of preform P2 (GMR = 0.56) and the higher GMR would result in a colder spray. Therefore, the interfacial bond formed in preform P1 would typically be weaker especially with the combined effects of the lower substrate preheat temperature as described previously.

The effects of different GMR on the residual stress and microstructures developed are shown in Fig. 5.10. Similarly, the residual stress and local CTE distributions were simulated using preform P2 spraying parameters. The GMR was increased and decreased by 0.10 while maintaining the substrate preheat temperature at 1270 K. The simulated stress distributions showed that increased GMR/colder spray temperatures would lead to higher residual stress developed in the preform (Fig. 5.10a). The higher stress developed was due to the increased cooling rates which give rise to more α'-Fe formed in the deposited layer and thus, leading to a larger CTE mismatch between the substrate and deposited layer (Fig. 5.10b).
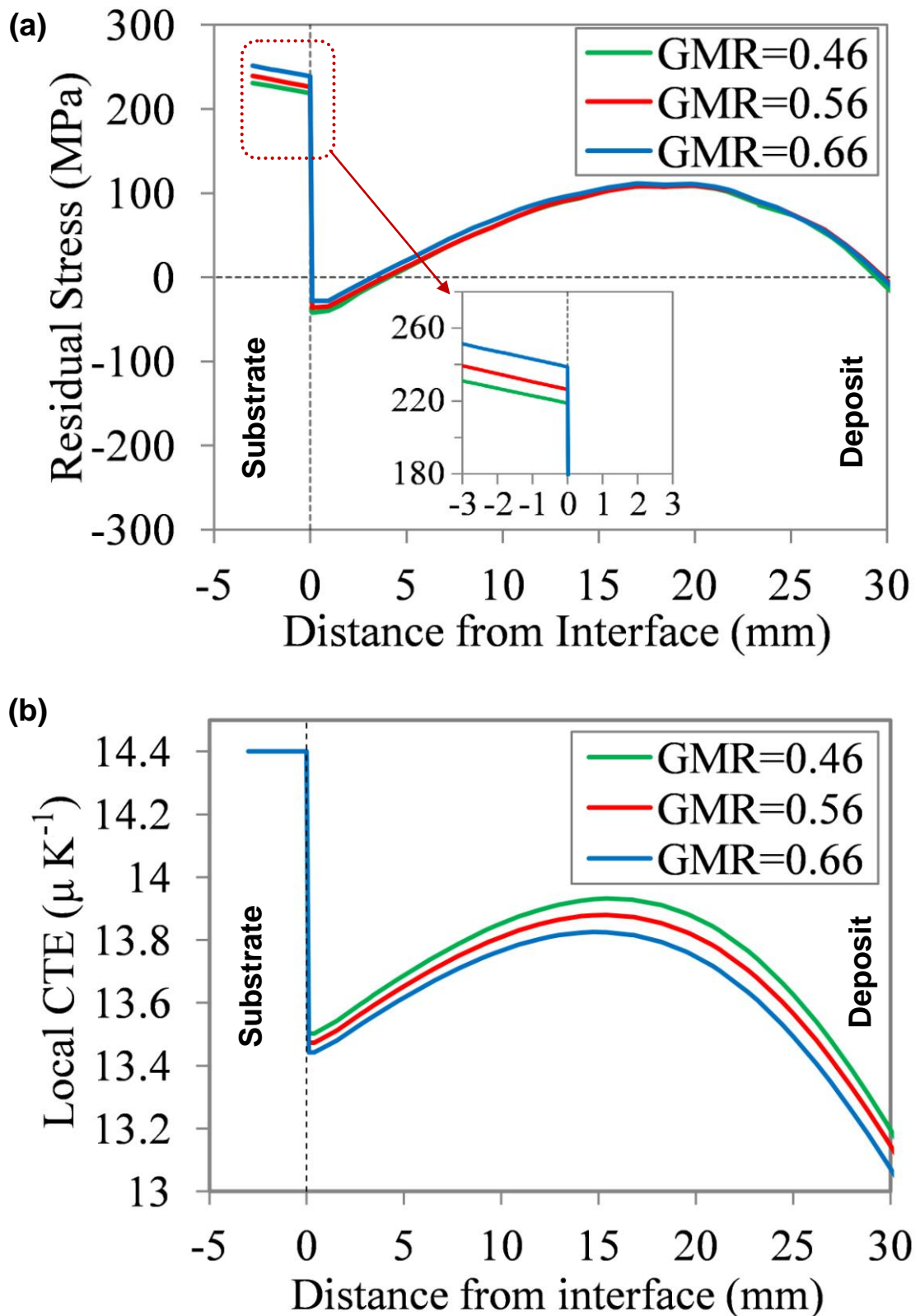
Fig. 5.10. (a) The simulated residual stress distribution in preform P2 using different droplet spray GMR and (b) the corresponding simulated local CTE distribution developed. Substrate preheat temperature was maintained at 1270 K.

5.9   Effects microstructural change on the residual stress development

Fig. 5.11a and Fig. 5.11b shows the relationship between the maximum residual stress developed in the substrate and the substrate preheat temperature and GMR, respectively. The relationships suggest that a hotter substrate and spray directly result in a lower residual stress developed in the preform. The stress change was due to the corresponding difference in preform thermal history and the microstructure formed that affected the CTE mismatch at the interface.

The stress change associated with the microstructure difference is also shown in the simulated and ND measured residual stress distributions along the preform thickness (Fig. 5.8). The lower cooling rate in the central region of the preform led to lesser α'-Fe formed which gave rise to a higher local CTE than the interface and surface regions, and thus, developed more tensile residual stress after cooling. Hence, the systematic study revealed that residual stress distribution in the as-sprayed dissimilar alloy preforms can be controlled via the spray forming parameters, in particular, the spray and substrate preheat temperatures to control the microstructures and the corresponding CTE mismatch between the substrate and sprayed material, in order to manufacture a high integrity preform with strong interfacial bonding.
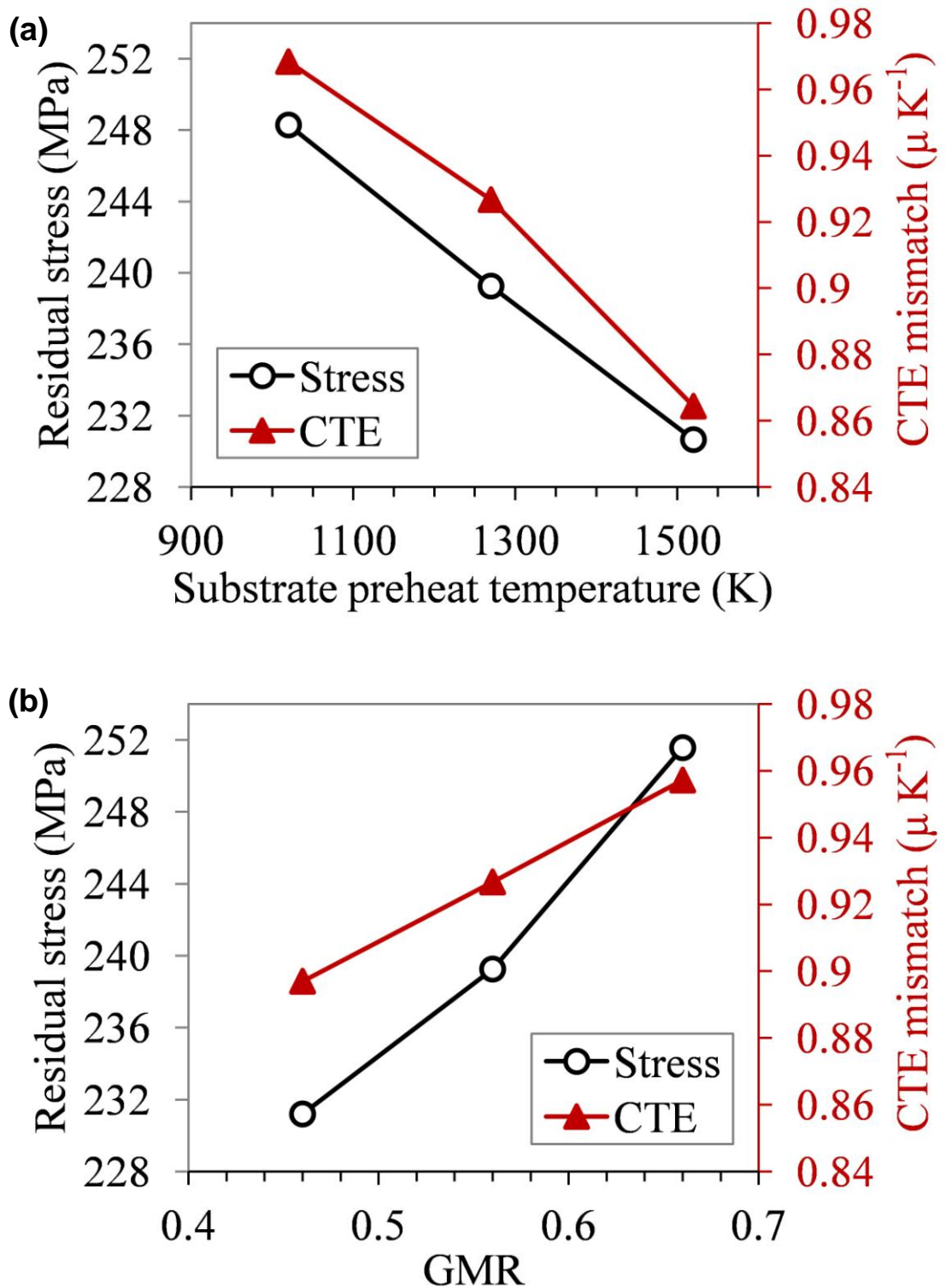
Fig. 5.11.The relationship between maximum residual stress developed in the substrate due to different (a) substrate preheat temperature and (b) GMR, and the corresponding CTE mismatch at the interface.

5.10 Summary

The combined 3D microstructure characterisation and numerical modelling of the preform thermal history established the correlation between the porosity and thermal history of the preform that was used to simulate the porosity distribution throughout the preform. The preform thermal histories revealed that the tube preform interface and surface regions comprised of low liquid fractions during spraying which led to the formation of porosity and finer carbides with a discontinuous network in these regions. A region of dense material with a continuous carbide network can be formed when the liquid fraction of between 0.20 - 0.55 is maintained during spraying. Although porosity in the preform can be reduced by maintaining high liquid fractions in the deposited layers, excessive liquid fractions were shown to give rise to poor and irregular preform surface quality. Preheating the substrate before spraying can overcome the trade-off between porosity and preform surface quality and lead to a strong interfacial bond. The comparison between residual stress distribution across the interface of dissimilar steel preforms characterised using neutron diffraction and simulated stress distribution provided a non-destructive means of assessing the quality of the interfacial bonding formed in the preforms, quantitatively. The systematic study with the use of 3D microstructure characterisation and numerical modelling successfully established the links between preform thermal history, corresponding microstructure formed and the interfacial bonding developed to provide the key insights to understand the interfacial bond and residual stress development mechanisms in thick as-sprayed dissimilar steel preforms. The relationships suggest that a hotter substrate and spray directly result in a lower residual stress developed in the preform. The stress change was due to the corresponding difference in preform thermal history and the microstructure formed that affected the coefficient of thermal expansion mismatch at the interface.

CHAPTER 6 : PHYSICAL AND NUMERICAL SIMULATION OF MICROSTRUCTURAL CHANGE DURING SPRAY DEPOSITION

This chapter describes a systematic study on using rapid heating (thermal shock) of atomised metallic powders to simulate the consolidation conditions during spray forming, and reveals the dominant control mechanism for the formation of the equiaxed microstructure during spray deposition.

Refined and equiaxed grain microstructures are often found in the spray formed materials regardless of the alloys used. Generally, the two competing theories proposed in previous studies on the mechanism that governed the dendritic-to-equiaxed microstructural transformation are:

- During droplet deposition at the preform surface, the solidified smaller droplets in the spray are remelted or at least partially remelted by the relatively hot top surface of the preform, or by the relative large droplets with high liquid fraction deposited together at the preform top surface [83, 236, 237]. The remelted or partially remelted dendritic microstructures in the solidified droplets provided the grain multiplication effect in the consolidating preform [123].

- Some other studies suggested that the mechanical deformation and fragmentation occurred at deposition effectively break up the microstructures in the partially solidified droplets formed prior to deposition and give rise to the increased nuclei during consolidation [131, 132].

Thus, it is generally well perceived that the thermal and/or mechanical shock experienced by the consolidating metallic droplets caused the dendrite fragmentation that increased the nucleation sites to produce a grain multiplication effect. However, between the thermal and mechanical shock, the dominant mechanism to influence the microstructure evolution has not been well elucidated because direct *in situ* experimental measurements and observations are currently impossible due to the highly dynamic conditions. Most of the understanding of the microstructural changes that take place in the droplets/powders has been obtained from

studying materials after processing is complete, which has experienced many cooling/heating cycles or long isothermal hold times [125, 128, 134-137, 238].

The focus of this study is the microstructural change of powders during heating and cooling cycles, with a time period of a few seconds. This is the regime that encompasses many rapid sintering techniques, some types of additive manufacture and spray forming [96, 122, 151]. The dynamics of microstructural change are important because increasingly in these powder-based processes, conditions are manipulated to try and minimise microstructural change or coarsening since the powders often have attractive features (refined grains and secondary phases, metastable phases, low levels of elemental segregation, etc) that are beneficial if retained into the bulk component.

Therefore, the microstructural change in low temperature hot isostatically pressed (HIPed) atomised Ni superalloy powders during a rapid heating and cooling cycle ($\sim$500 K s^{-1}) with a short ($\sim$10 s) high temperature hold time was studied using a Gleeble 3500 thermomechanical simulator. A Ni superalloy was chosen due to its significant industrial applications for manufacturing high temperature resistant components [239] and its widespread use in thermal spraying, spray forming, powder metallurgy and additive manufacturing. In addition, the Ni superalloy is the key research material for the Chinese Ministry of Science and Technology project described in Chapter 3. Although Ni superalloy powders were used, the dynamics of the rapid microstructural change revealed in this study is relevant to other metallic powders in general.

The thermal shock experiment was conducted by the researchers at BIAM and the author was involved in characterising the microstructures of the thermally shocked specimens with the BIAM researchers at OU and HU. A range of isothermal temperatures were investigated in the vicinity of the γ' solvus temperature (γ' is the principal strengthening phase in the alloy, see later) and the alloy solidus temperature. The powder microstructures were investigated by various microscopies, including electron microprobe microanalysis (EPMA) and electron back-scatter diffraction (EBSD) for

elemental segregation and grain morphology changes, respectively. In order to understand the temperature conditions in the powders during the cycle, the author also developed a FE based model of the heat flow in the Gleeble apparatus and the powder compact. Calculated temperatures were calibrated to fit the surface temperature of the can containing the powder compact measured by thermocouples. The model was then used to provide detailed information of the powder compact internal temperatures (which were otherwise unavailable). The rapid microstructural change in the powders was then rationalised in terms of the transient internal temperature conditions.

6.1   Gleeble thermal shock experiment

Gas atomised Ni superalloy powders with the nominal composition (wt%) Ni-12.9Cr-20.2Co-2.0W-3.9Mo-2.3Ta-3.5Al-3.7Ti-0.03B-0.05Zr-0.13Fe-1.0Nb-0.02C were sieved and the powders with 63 - 100 μm diameters (encompassing the typical mass mean diameter of gas atomised Ni superalloys) were canned into cylindrical 304 stainless steel cans of 200 mm length, 10 mm inner diameter and 1 mm (wall thickness). The cans were evacuated to 1.0×10^{-3} Pa, sealed and HIPed at 1188 ± 5 K and 120 MPa for 2 hours. The HIP cycle was an essential step in producing a coherent powder compact suitable for mounting in the Gleeble apparatus and applying rapid Joule heating, but the HIP temperature and time were much lower than typically used for full consolidation (temperatures for fully dense Ni superalloys are typically >1373 K). A low temperature minimised microstructural change and resulted in a porous, coherent Ni superalloy powder compact. Fig. 6.1a shows a backscattered electron image (Zeiss EVO 60) of part of the cross-section of a typical HIPed powder compact with an average porosity of 19.4% ± 4.4% determined by digital analysis of multiple images using public domain software ImageJ.

Fig. 6.1b shows back scattered electron images of cross-sections of the deep-etched as-atomised powder prior to canning, with a typical fine-scale dendritic structure with inter-dendritic contrast provided by distinct micro-segregation of Nb and other elements (see later). Similar cross-sections of the powders after the HIP cycle in Fig. 6.1c show that while the relatively low temperature HIP process conditions had restricted coarsening, there

was nonetheless a morphological change in which the dendrites had became more rounded.
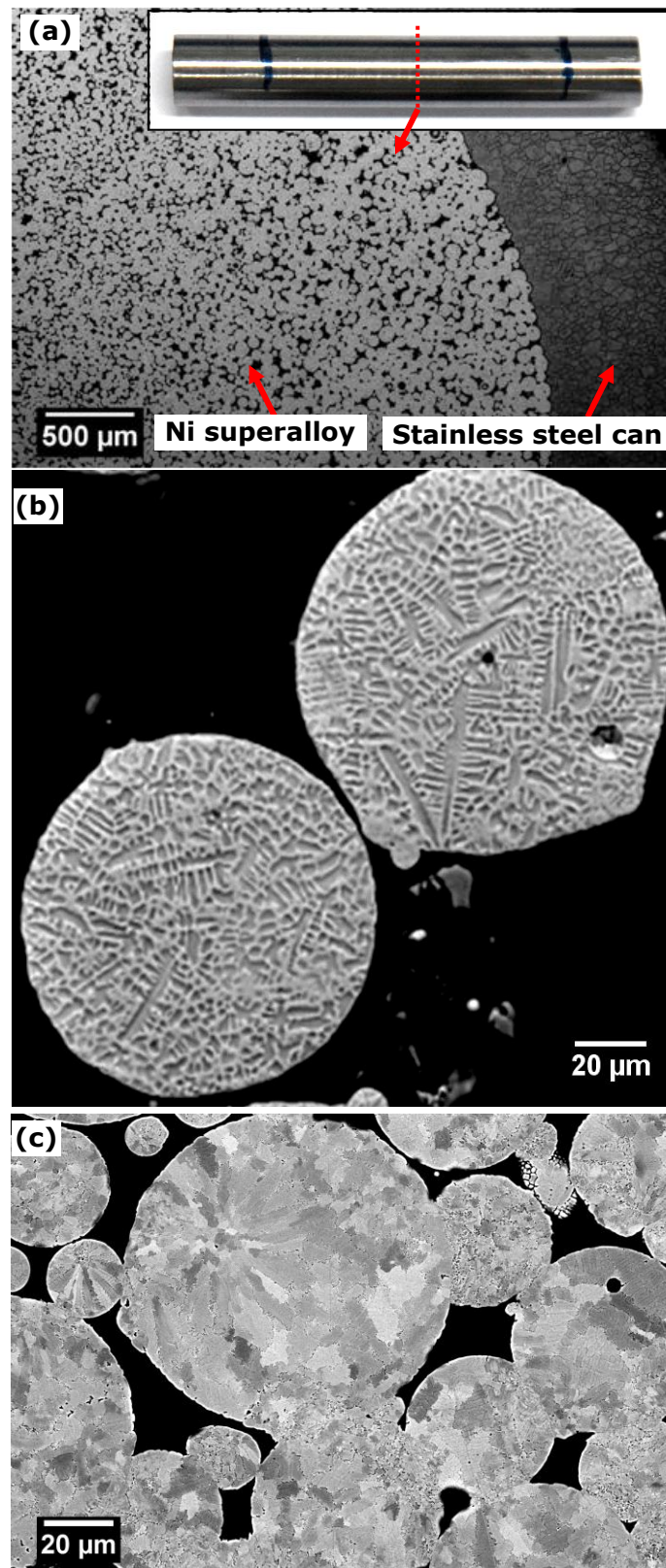
Fig. 6.1. Back-scattered electron image of (a) the HIPed Ni superalloy powders in the stainless steel can (figure inset), (b) the microstructure of the deep-etched as-atomised powders and (c) the microstructure of the powders after HIP.

The HIPed cans were cut into 50 mm sections and clamped into the Cu grips of a Gleeble 3500 thermo-mechanical simulator. Direct current (DC) was discharged into the specimen through the Cu grips causing Joule heating in the powder compact and a rapid increase in temperature to a pre-defined isothermal hold temperature that was controlled by a S-type thermocouple welded to the external surface of the can mid-way along its length (Fig. 6.2a). In order to select isothermal temperatures (Table 6.1) below and above the alloy γ' solvus and solidus temperatures, differential scanning calorimetry (DSC) investigations of the powders were carried out in a Netzsch 409C DSC operating at a heating rate of 10 K min^{-1} under a dynamic Ar atmosphere. From a typical heating cycle shown in Fig. 6.2b, the alloy γ' solvus ($T_{\gamma'}$), incipient melting temperature (T_{IM}) and liquidus temperature (T_L) were determined as 1428 K, 1483 K and 1612 K, respectively. After reaching and holding for 10 s the powders at the upper target temperature, the current flow was terminated and the specimens cooled naturally to room temperature. Fig. 6.3a shows the overall experimental arrangement and Fig. 6.3b shows a schematic of a cross-sectional of the specimen and Cu grip arrangement.

Although the thermocouple data from the can surface was essential for control of the heating and hold cycle, significant temperature differences between the can surface temperature and the temperatures experienced by the powder compact within the can were expected. Therefore as described later, a numerical model of the transient heat flow conditions in the entire grip/can arrangement was developed.

Table 6.1. Isothermal hold temperatures and times for the powder compacts.

Heat treatment designation	Isothermal hold temperature (K): can surface temperature and (calculated temperature at the centre of the powder compact)	Isothermal hold time (s)
T_1	1373 (1383)	10
T_2	1423 (1436)	10
T_3	1473 (1489)	8
T_4	1523 (1542)	10

The HIPed and rapidly heat treated specimens were cut at the mid-length (at the thermocouple position) and subsequently polished and etched using a solution of HCl (50 vol. %) + H_2O_2 (50 vol.%) for microstructure and elemental mapping analyses using SEM, EBSD (Oxford Instruments with JEOL JSM-6480) and EPMA (JEOL JXA-8800). Changes in grain morphology and size were investigated qualitatively in the SEM and quantitatively by EBSD, respectively. Where polygonal grains evolved, the grain size (D_g) was estimated from at least 10 measurements using the mean intercept length method assuming spherical grains [240]:

$$D_g = K_g \; \frac{L_g}{N_g} \qquad\qquad (6.1)$$

where K_g = 1.5 is a proportionality constant for spherical grains [241], L_g is the summation of chord length intercepting the grains and N_g is the number of grain boundary intercepts along the line.
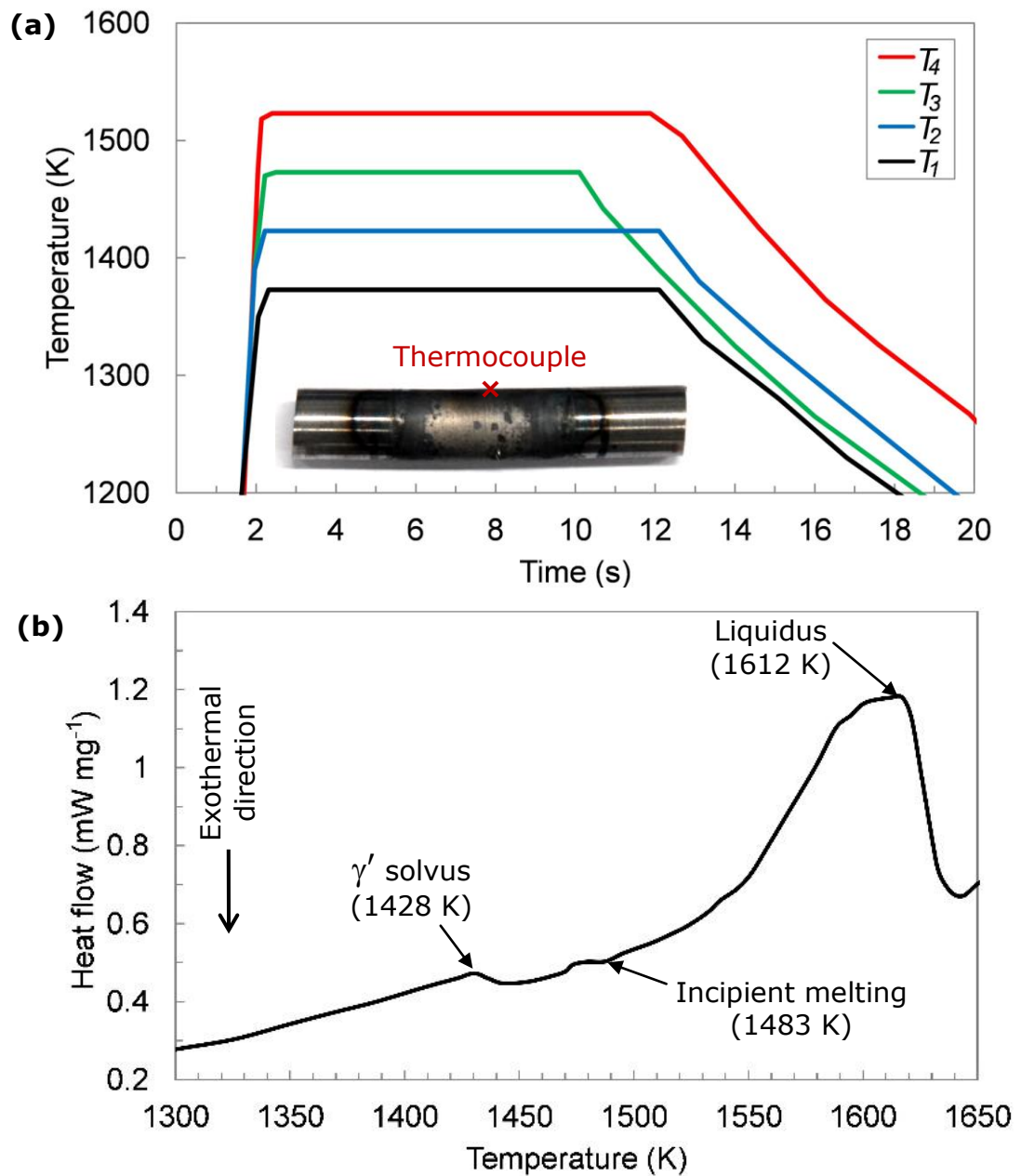
Fig. 6.2. (a) The measured temperature profiles at the can surface, with the temperature measurement position marked by the red cross in the inset figure and (b) the measured γ' solvus, incipient melting and liquidus temperatures of the Ni superalloy powder determined using DSC.

6.2 Finite element modelling of the thermal shock process

A 2D axis-symmetrical model of the heat flow in the grip/can/powder compact arrangement was constructed in the commercial FE solver COMSOL Multiphysics®. The electrical potential field generated by the DC current passing through the specimen is governed by the equations:

$$\nabla \cdot J = -\frac{\partial \rho_v}{\partial t} \qquad (6.2)$$

$$J = -\sigma \nabla E_V \qquad (6.3)$$

where J is the electrical current density vector, ρ_v is the electric charge density, σ is the electrical conductivity and E_V is the electrical potential.

The electrical potential distribution between the Gleeble Cu grips was simulated by prescribing $E_V = 0$ along the surface of the low electrical potential grip and an input current density (J_{in}) along the surface of the high electrical potential grip as indicated in Fig. 6.3b. J_{in} was given by:

$$-J \cdot n_J = J_{in} \qquad (6.4)$$

where n_J is the local outward unit normal vector. J_{in} represents the energy input to the can/powder compact arrangement and thus has a dominant effect on all calculated temperatures, and was unavailable experimentally. Therefore, best-fitting of the simulated surface temperature profiles to the experimental profiles at the can surface was used to estimate the J_{in} at each incremental time step that the model was executed to compute the transient heat flow. Although this approach restricts the broader applicability of the model, because the model could only be applied for conditions for which experimental data existed, it had the significant advantage that it eliminated the need for complex and probably inaccurate assumptions assumptions, for example, of the electrical contact resistance between the Ni superalloy powder compact and the Cu grip. This restriction was acceptable in the context of this study since the key information required was the internal temperature distribution at the four conditions in Table 6.1 only.
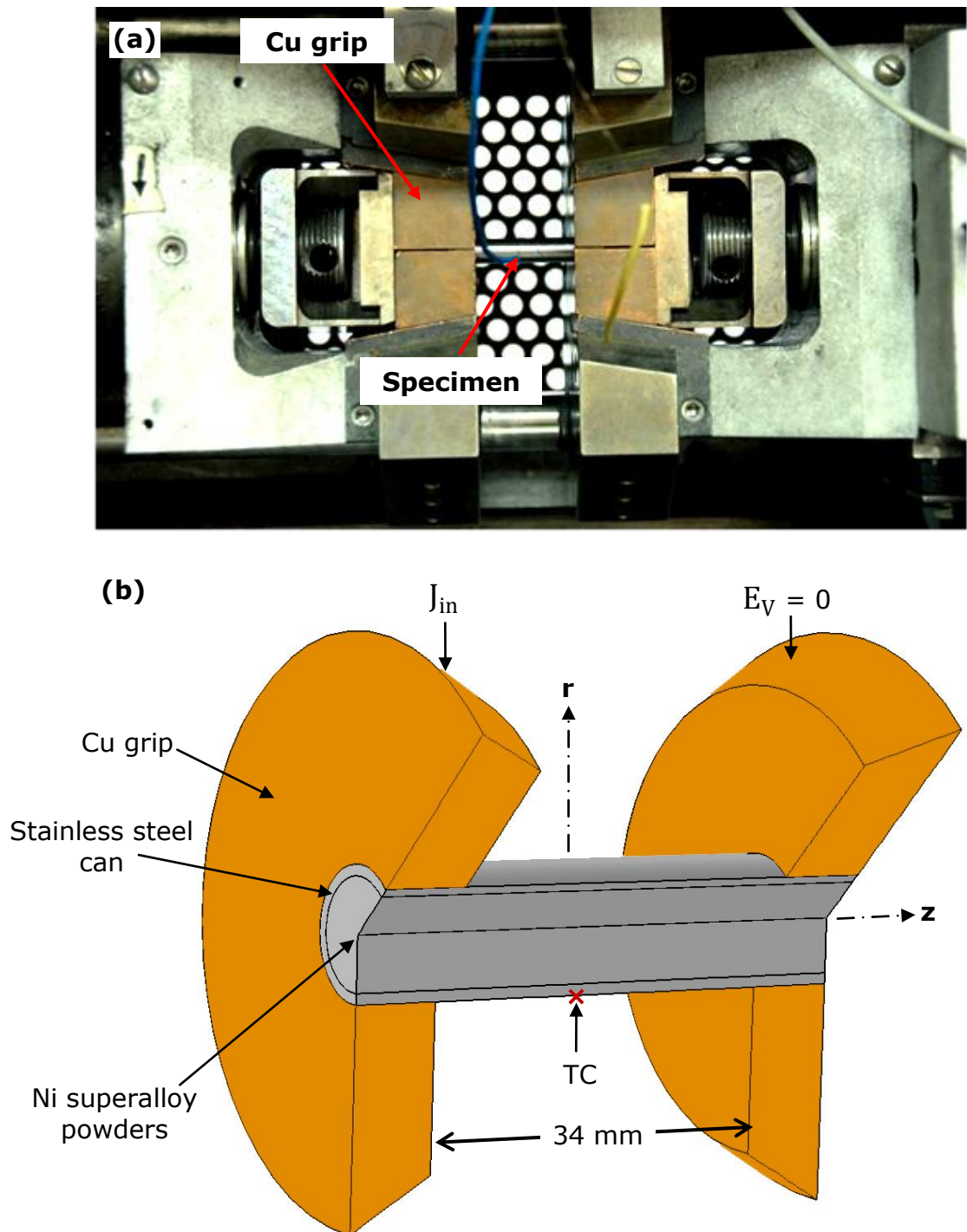
Fig. 6.3. (a) A general overview of the Gleeble rapid heating/cooling experimental arrangement, and (b) a schematic of the cross-section of the experimental arrangement and the key boundary conditions used in the model, and the location of the thermocouple (TC).

Fig. 6.4a shows the electrical conductivity of the Ni superalloy and stainless steel can as a function of temperature used in the model taken from [242] and [243], respectively. Because electrical conductivity was not available for the specific alloy of interest, the temperature-dependent electrical conductivity data up to 1700 K assumed was that for Ni superalloy IN718, which had previously been shown to be similar to that of Ni superalloy Waspaloy [244], which is close in composition to the alloy used.

Because the powder compact within the can was porous, the effect on electrical conductivity of the HIPed powders was taken into account using:

$$\sigma_P = \sigma \cdot f_\sigma \qquad (6.5)$$

where σ_P is the effective electrical conductivity and f_σ (= 0.59 at 19.4% porosity) is the electrical conductivity reduction factor due to porosity (Fig. 6.4b), which is based on the correlation established from experimental σ measurements of powder metallurgy Ni from [245].

The specimen heating in 2D cylindrical polar coordinates (z, r) is governed by,

$$\rho_{ts}C_{ts}\frac{\partial T}{\partial t} = \frac{1}{r}\left[\frac{\partial}{\partial z}\left(K_{ts}\cdot r\frac{\partial T}{\partial z}\right) + \frac{1}{r}\cdot\frac{\partial}{\partial r}\left(K_{ts}\frac{\partial T}{\partial r}\right)\right] + Q_V \qquad (6.6)$$

$$Q_V = \frac{J^2}{\sigma} \qquad (6.7)$$

where the coefficients bear the same meaning as those specified in Eqn. (4.8) but refer to the respective thermal shock specimen material properties using the subscript "ts" and Q_V is the heat source term due to the current flux.
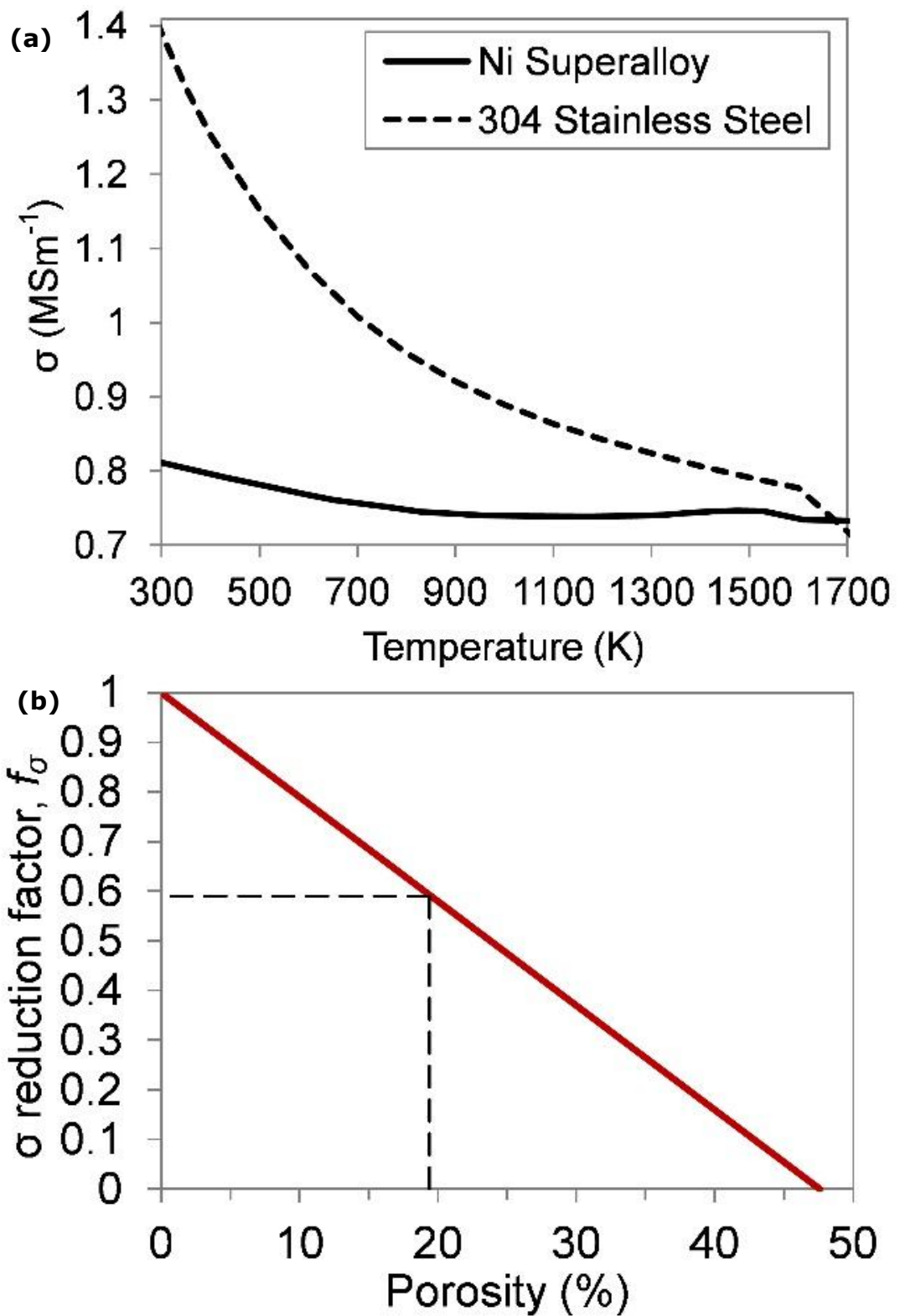
Fig. 6.4. (a) The electrical conductivity of the Ni superalloy and stainless steel as a function of temperature taken from [242] and [243], respectively and (b) the electrical conductivity reduction factor of the Ni superalloy powder compact as a function of porosity taken from [245].

Since grain boundaries are the last regions to freeze during solidification of the atomised powders (and will be relatively enriched in some of the alloying elements that preferentially segregate to the liquid, see Fig. 6.1b), they can be expected to be the first regions to melt (incipient melting) during re-heating and coarsening is typically accelerated in the presence of liquid at the grain boundaries [135]. Sintering rates can also be expected to accelerate. Although sintering will give rise to shrinkage of the powder compact, due to the very short high temperature hold times and the added significant complexity, shrinkage effects were ignored in the model.

To account for any latent heat of melting, an alloy effective heat capacity C_{eff} was defined as:

$$C_{eff} = C_{ts} - L_f \left(\frac{\partial f_S}{\partial T} \right)$$ (6.8)

The volume fractions of the alloy liquid and solid phases during solidification are temperature dependent and can be determined using the Scheil function. Fig. 6.5a shows the calculated Ni superalloy liquid fraction using a best fit value of k_p = 0.38 to the data derived from the DSC experiment (Fig. 6.2b) and Eqn. (4.11) with the incipient melting point assumed from the DSC data as the solidus temperature T_S = 1483 K and T_L = 1612 K, while Fig. 6.5b and Fig. 6.5c show the thermal conductivity and the effective heat capacity over the temperature range of 1100-1700 K using Eqn. (4.12) and (4.14), respectively. The additional thermo-physical and electrical properties used in the model are shown in Table 6.2, based on Waspaloy wherever possible, or IN718 where Waspaloy data was unavailable. Overall, the thermo-physical differences from Ni-based alloy to alloy can be expected to relatively small when compared with larger order effects of changes in current density under investigation.

The effect of porosity in the Ni superalloy powder compact on thermal conductivity of was taken into account using [246]:

$$K_P = (1 - P) \cdot K$$ (6.9)

where K_P is the effective thermal conductivity of the porous powder compact and P is porosity.
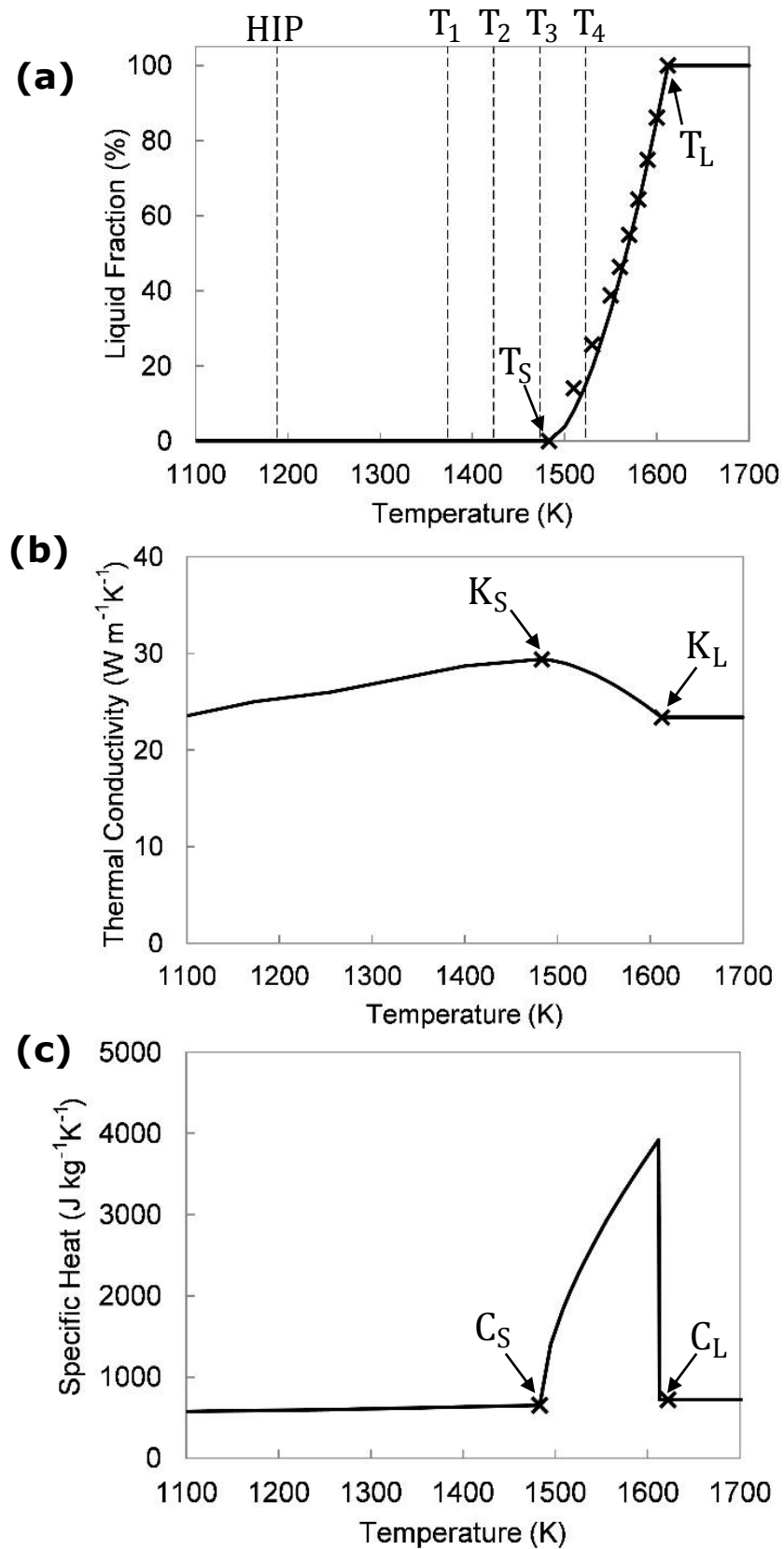
Fig. 6.5. The calculated Ni superalloy (a) liquid fraction, (b) thermal conductivity and (c) effective heat capacity as a function of temperature. The measured data are marked by ×.

Table 6.2. Thermophysical and electrical properties of the Ni superalloy [242, 247-249], stainless steel can [243, 250] and Cu grip [209].

Material		Ni superalloy	Stainless steel can	Cu grip
ρ (kg m^{-3})		$-1.42 \times 10^{-4} \times T^2 - 0.12 \times T + 8336$	$-5.15 \times 10^{-5} \times T^2 - 0.36 \times T + 8020$	8700
C_{eff} (J kg^{-1} K^{-1})	$293\,K < T < T_S$	$0.1522 \times T + 407.82$	$5.77 \times 10^{-7} \times T^3 - 1.38 \times 10^{-3} \times T^2 + 1.21 \times T + 206$	385
	$T = T_S$	652.7	-	-
	$T_S < T < T_L$	$C + L_f \left(\dfrac{\partial f_L}{\partial T} \right)$	-	-
	$T \geq T_L$	720	-	-
K (W m^{-1} K^{-1})	$293\,K < T < T_S$	$-5.48 \times 10^{-9} \times T^3 + 1.74 \times 10^{-5} \times T^2 - 2.68 \times 10^{-5} \times T + 9.67$	$-2.13 \times 10^{-6} \times T^2 + 0.0176 \times T + 9.84$	400
	T_S	29.40	-	-
	$T_S < T < T_L$	$f_S K_S + f_L K_L$		
	$T > T_L$	23.40	-	-
L_f (kJ kg^{-1})		256	-	-
σ (S m^{-1})	$293\,K < T \leq T_S$	$0.11 \times T^2 - 239.12 \times \times T + 0.87 \times 10^6$	$-4.22 \times 10^{-4} \times T^3 + 1.63 \times T^2 - 2260 \times T + 1.93 \times 10^6$	$-9.91 \times 10^{-2} \times T^3 + 289 \times T^2 - 2.96 \times 10^5 \times T + 1.21 \times 10^8$
	$T_S < T < T_L$	$7.06 \times 10^{-2} \times T^2 - 283 \times T + 1.01 \times 10^6$	-	-

A convective heat flux boundary was applied at the surface of the can with the rate of heat loss due to convection per unit area ($\dot{Q}_{con}$) given by:

$$\dot{Q}_{con} = h \, (T - T_{amb}) \tag{6.10}$$

where h = 15 W m^{-2} K^{-1} and T_{amb} = 293 K is ambient temperature. The specimen surfaces were specified with h = 65 W m^{-2} K^{-1} during the heating process. The heat transfer from the Cu grips to the water cooled steel frame was controlled by a similar expression to Eqn. (6.10), with an interfacial heat transfer coefficient of h = 200 W m^{-2} K^{-1}.

The rate of radiative heat loss per unit area ($\dot{Q}_{rad}$) from the heated specimen surface was given by:

$$\dot{Q}_{rad} = \sigma_{SB} \cdot \varepsilon_e \, (T^4 - T_{amb}^4) \tag{6.11}$$

In the absence of available references or experimental data, and in the light of apparent diffusion bonding of the Ni superalloy powders to the stainless steel can (Fig. 6.1a), the powder-can interface was assumed to be perfectly conducting i.e. the thermal contact resistance at the interface was assumed to be zero. A similar assumption was also made for the Cu grip-can interface.

6.2.1 Simulated thermal history and validation

The experimental and simulated specimen surface temperatures at the thermocouple measurement point as a function of time when heated to the different isothermal hold temperatures are shown in Fig. 6.6a. As described earlier, the current flux condition in the model was adjusted to provide this good best-fit agreement, with all other parameters fixed and as described above. The calculated temperature distribution across the powder compact cross-section at T_2 immediately before cooling is shown in Fig. 6.6b. The hottest region was concentrated at the mid-point of the length of the specimen, with temperature gradients along both the axial and radial directions.
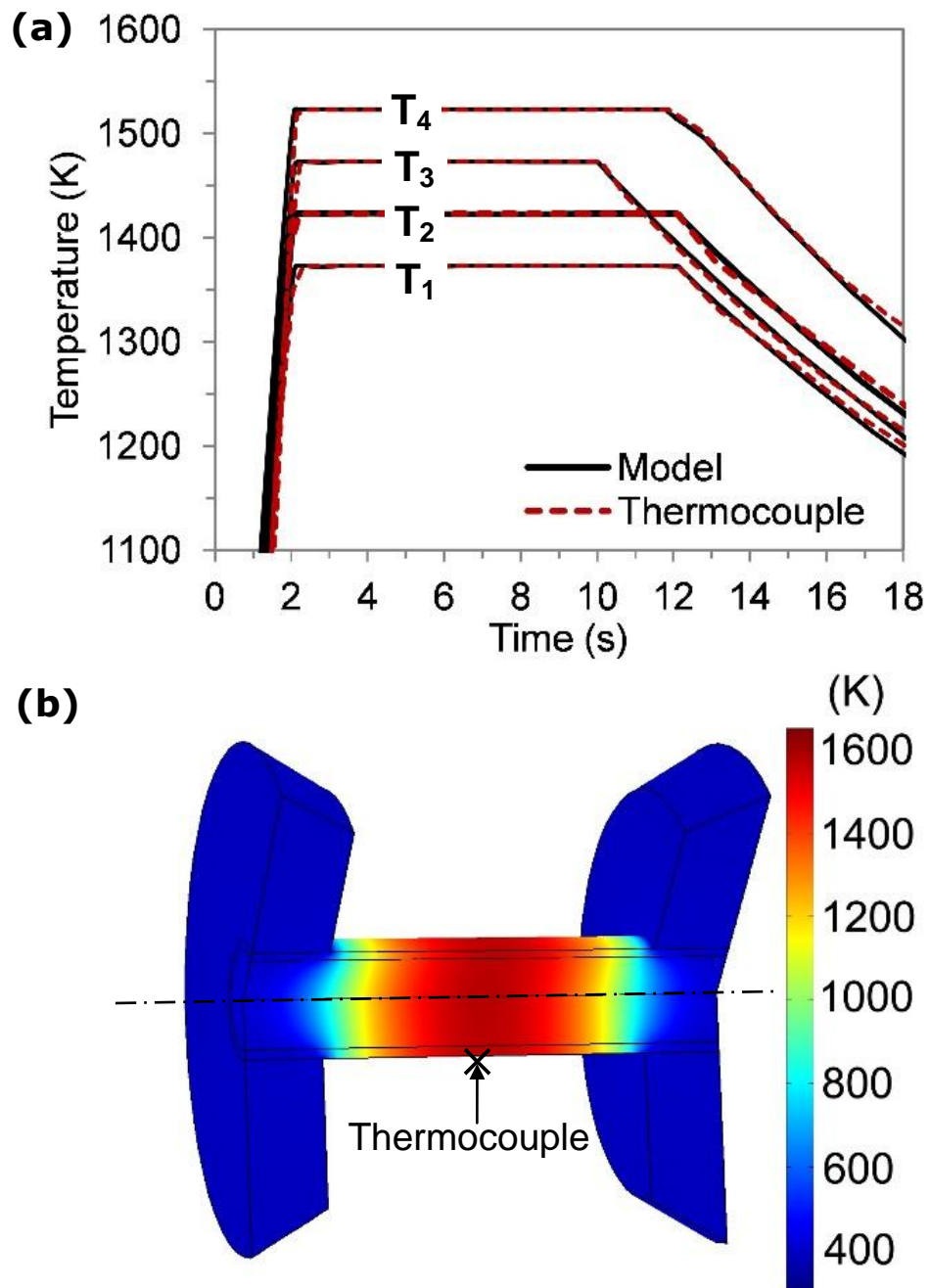
Fig. 6.6. (a) The calculated and measured specimen surface thermal history at the thermocouple measurement point for the four isothermal hold temperatures, and (b) the calculated specimen cross-sectional temperature distribution at T_2 immediately before cooling.

The calculated axial temperature gradient was induced because of the current density distribution in the axial (Fig. 6.7a) direction during heating. The current density was the greatest (up to $\sim$28.7 MA m^{-2}) at the mid-point of the specimen in the axial directions and gave rise to the highest temperature in this region (Fig. 6.7b) under all conditions. A significant radial temperature gradient was induced due to heat loss from the specimen surface (Fig. 6.7c). The difference between the maximum temperature in the central region of the specimen (T_{centre}) and the temperature at the can surface ($T_{surface}$) increased linearly with the isothermal heat treatment temperature, as shown in Fig. 6.7d. The difference was more significant as the heat treatment temperature increased. At T_1, the Ni superalloy powder compact in the central region achieved a maximum temperature of $\sim$1383 K while at T_2, the powders were heated to $\sim$1436 K (8 K above $T_{\gamma'}$). At T_3, the powders were heated up to $\sim$1489 K (3 K above T_{IM}), while the powders achieved a maximum temperature of $\sim$1542 K (f_L = 0.46) at T_4.

The temperature gradients from the specimen mid-point were 1.6 – 3.2 K mm^{-1} and 49 – 56 K mm^{-1} in the radial and axial directions respectively, as shown in Fig. 6.7e and Fig. 6.7f. The radial temperature gradient was calculated from the specimen mid-point to the can surface, while the axial temperature gradient was determined from the specimen mid-point to the temperature plateau region at $\sim$5 mm or $\sim$45 mm along the central axis. The slightly higher axial temperature gradient at T_3 was due to the slightly shorter isothermal heat treatment period.
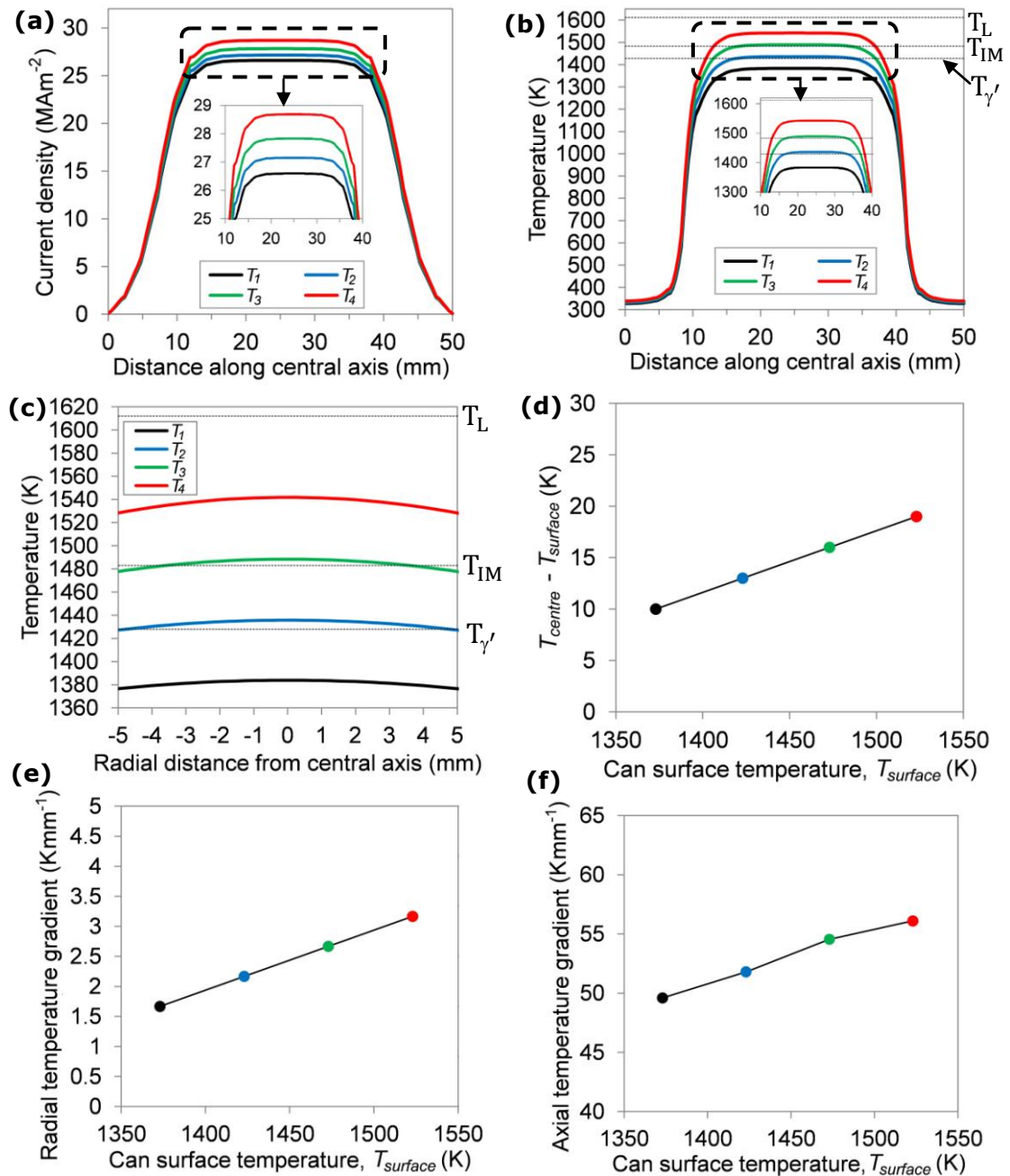
Fig. 6.7. (a) The specimen axial current density distribution, (b) axial temperature distribution, (c) radial temperature distribution, (d) difference between the maximum temperature in the central region of the specimen (T_{centre}) and the temperature at the can surface ($T_{surface}$) for the heat treatment conditions used, (e) radial temperature gradient as a function of heat treatment temperature and (f) axial temperature gradient as a function of heat treatment temperature.

6.3   Microstructural Change

Fig. 6.8a and Fig. 6.8b show the microstructures of the powders after HIP and heat treatment at T_1 = 1383 K. Here the T_1 to T_4 temperatures are now the calculated temperature at the centre of the powder compact rather than surface temperatures from the thermocouple, with the inter-relation between them given in Table 6.1. At T_1, there was no significant change in the as-HIPed microstructure, with the remnants of the dendritic microstructure of the gas atomised powders and after the low temperature HIP retained. When the hold temperature increased to T_2 and the powders in the central region reached 1436 K (just above the $T_{\gamma'}$) in Fig. 6.8c, the relatively fine-scale primary γ-Ni dendrites transformed to polygonal, more equiaxed grains and grain growth occurred, even over a period of 10 s. At T_3 (only 3 K above T_{IM}) in Fig. 6.8d, the transition from the as-solidified fine-scale dendritic structure to equiaxed grains was complete in 8 s or less, and grain growth and coalescence was widespread. At the highest heat treatment temperature T_4 = 1542 K in Fig. 6.8e where melting was expected, the powders formed a significantly more consolidated compact, with a fully equiaxed, coarsened microstructure with residual porosity and only traces of the original powder geometry through prior particle boundaries (PPBs).

The grain size as a function of hold temperature is shown in Fig. 6.8f. There was only slight coarsening (~2 μm) below the alloy γ' solvus temperature, although absolute measurements of grain size in this regime were questionable since the fine-scale dendrites were far from spheroidal. Significant grain coarsening occurred when the powders were heated to just above the alloy γ' solvus temperature, with a near doubling in grain size. In the as-atomised state, precipitation (e.g. γ') in the Ni superalloy powders was likely limited by the rapid cooling, and some alloying elements were retained in solid solution [251]. Although precipitates (including γ') will then start to form during the HIPing process, they will not be fully developed at the relatively low HIP temperature used [252]. The slight grain coarsening

below the γ' solvus in this study suggested that nonetheless there was sufficient precipitation during atomisation and/or HIP to provide some grain morphology/size stabilisation (at least over short timescales). However, once dissolved, significant morphological changes and grain coarsening rapidly took place. As shown Fig. 6.8f, grain sizes increased more dramatically around the incipient melting temperature.
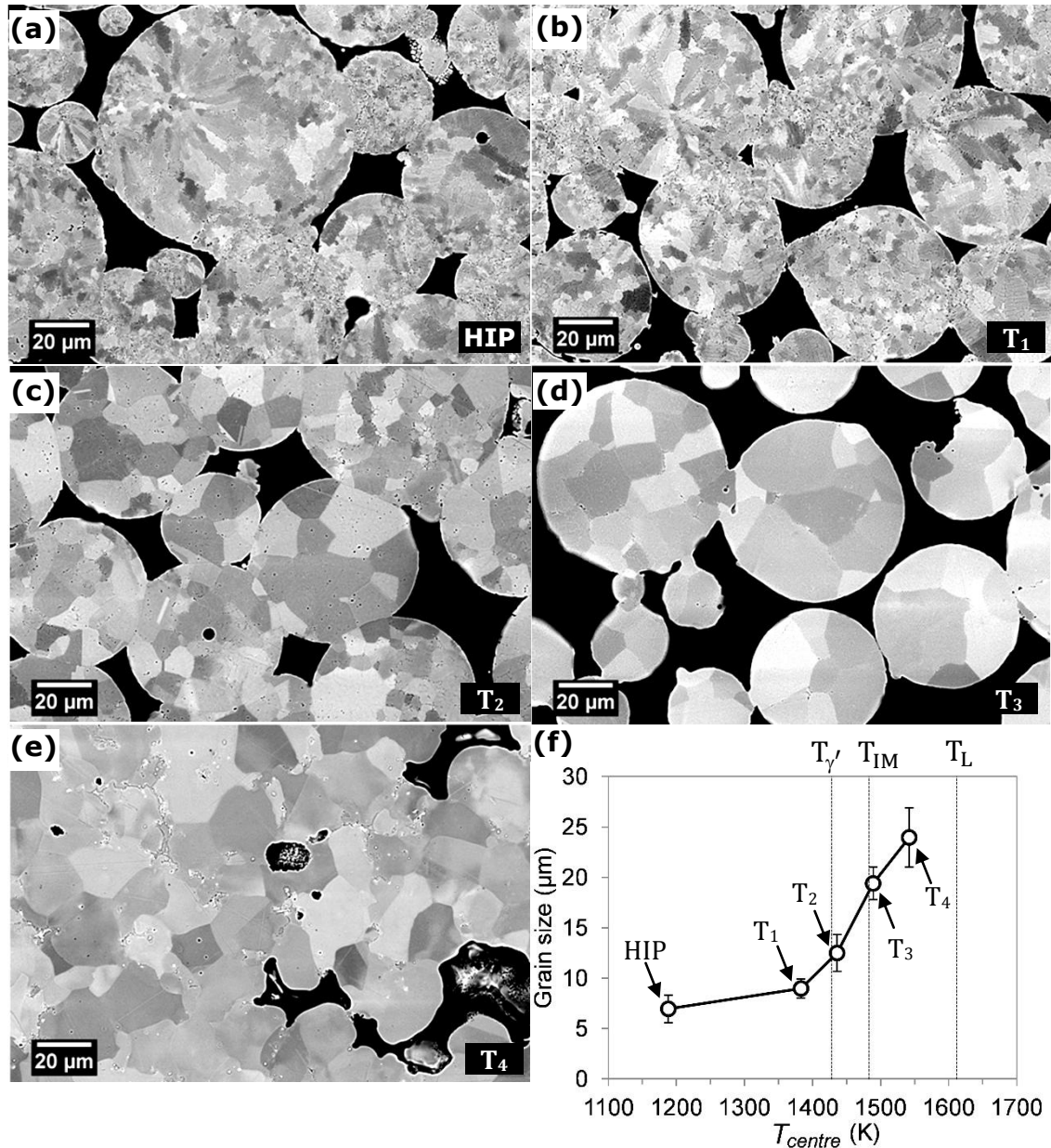
Fig. 6.8. The microstructures of the Ni superalloy powders in the central region of the specimen after (a) HIP, thermally shocked at (b) T_1, (c) T_2, (d) T_3, and (e) T_4. (f) The grain size measured with respect to the calculated temperature in the central region of the specimen for the respective heat treatment temperatures. Uniform specimen temperature distribution during HIP was assumed.

Backscatter electron images in Fig. 6.9a to Fig. 6.9c for as-HIPed, T_2 and T_4 heat treated powders, and the corresponding EBSD orientation maps in Fig. 6.9d to Fig. 6.9f, underline the rapid transition from the as-solidified fine-scale columnar dendritic structure to the coarser polygonal, equiaxed grains. The spheroidisation of the dendritic structure cannot be de-convoluted from coarsening, both of which occurred in a number of seconds once temperatures beyond the alloy γ' solvus and incipient melting point were achieved. Even with EBSD data it was difficult to compare quantitatively the grain sizes of the as-HIPed dendritic grains and the spheroidised grains at T_2 because of the marked change in morphology. Nonetheless, the images gave a strong impression that at T_2 only some grain refinement may have taken place, due to the pinching-off of primary or secondary dendrite arms (fragmentation) corresponding to the sudden appearance of the solute-rich liquid in the inter-dendritic regions. While some of these fragments may fully re-melt, others rapidly spheroidised and started to coarsen, alongside similar behaviour of the dendrites from which they were formed. This destabilisation or fragmentation effect provides an initial refinement, before the rapid coarsening in the presence of a minority liquid fraction dominated the microstructural response.

Support for significant re-melting (a requirement for any fragmentation) was provided in the EPMA maps for Ti, W, Ta and Nb in Fig. 6.9g to Fig. 6.9i for as-HIPed, T_2 and T_4 heat treated powders, taken from the red boxed regions in Fig. 6.9a to Fig. 6.9c. As HIPed, Ti, W, Ta and Nb all showed resolvable micro-segregation into the inter-dendritic regions, over length-scales of a few μm: Ti, Ta and Nb segregated into the inter-dendritic channels (binary partition coefficient with Ni < 1), W segregated to the primary γ-Ni (binary partition coefficient with Ni > 1). Although the extent of this micro-segregation was likely reduced by the HIPing procedure that acted as a homogenisation heat treatment, diffusion rates of these elements were too slow to eradicate micro-segregation even over these short distances in 2 hrs. In contrast, following rapid heat treatment at the higher T_2 temperature, significant homogenisation of the microstructure occurred, due both to faster solid-state diffusion at the elevated temperature but also

due to the effects of partial re-melting that provided a homogenising effect as liquid solute rich regions mix with solvent (Ni) rich regions. At T_4, the extent of re-melting was significantly greater so that any benefits of the fine-scale dendritic structure, the short diffusion distances, and a microstructural scale constrained to the powder diameter was lost. The powder compact re-solidified as a coherent whole and although some solid remained at T_4, and again spheroidised and coarsened, the re-solidification of the integral, relative dense powder mass was comparatively slow so that a relatively coarse cellular/dendritic structure and significant inter-cellular micro-segregation resulted. As shown in the EMPA maps, micro-segregation led to the formation of Ti, Ta and Nb-rich particles, which may be Laves or other generally less-desirable phases [253-255]. The wavy grain boundaries in the EBSD maps suggested that these particles were still small enough to provide a pinning effect [256] to grain coarsening in the solid state, but overall the benefits of the rapidly solidified powder microstructure were largely lost at T_4.
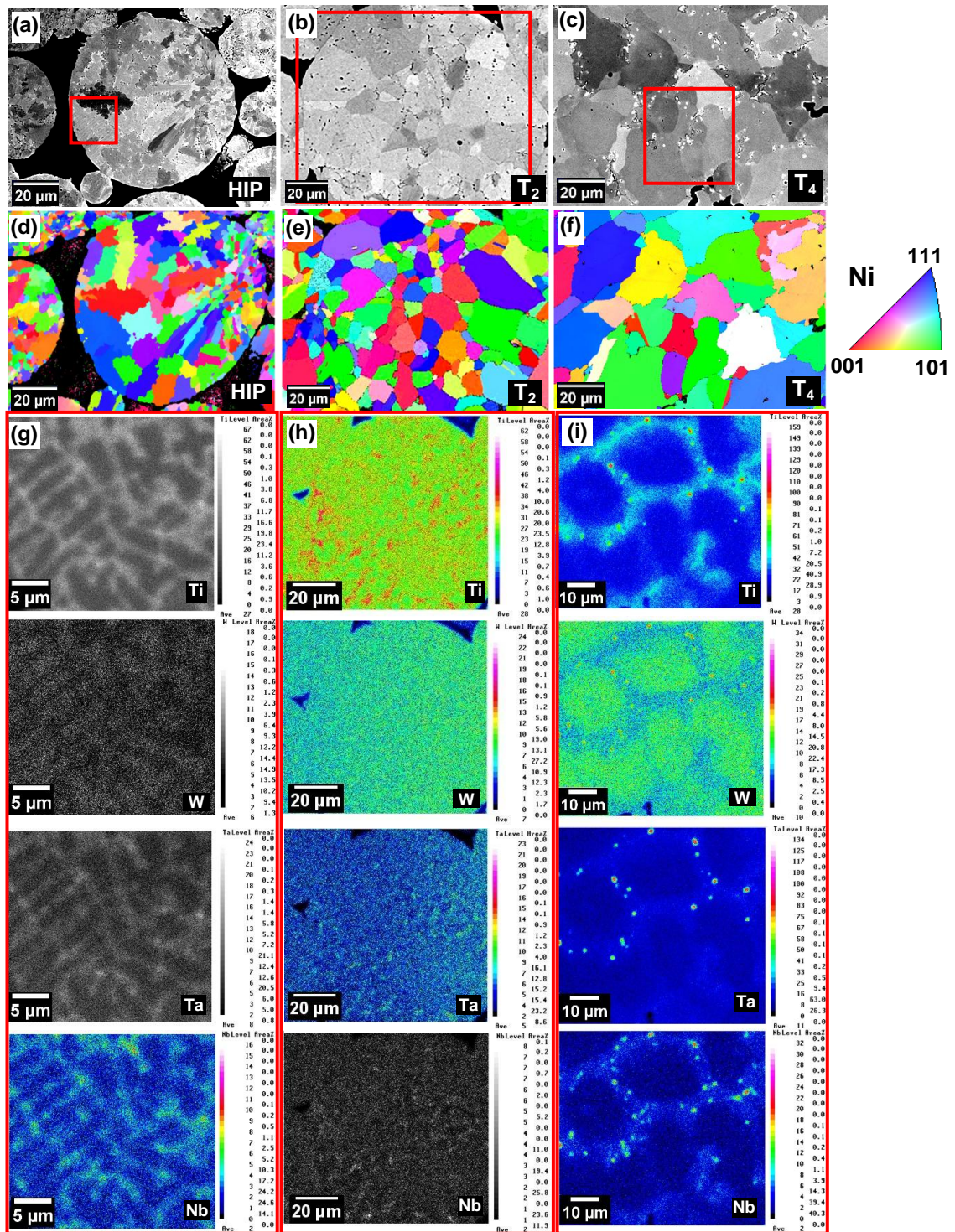
Fig. 6.9. SEM images of the (a) HIPed and (b), (c) rapidly heated Ni superalloy powders to T_2 and T_4 respectively, (d-f) the corresponding EBSD orientation maps, and (g-i) the corresponding EPMA maps for Ti, W, Ta and Nb from the red bounded box regions marked in the SEM images.

6.4   Summary

Ni superalloy gas atomised powders were thermally shocked (a heating rate of ~500 K s^{-1}) to different target temperatures followed by a short period of isothermal holding (~10 s) using a Gleeble 3500 thermomechanical simulator. A 2D axis-symmetrical finite element based numerical model was also constructed to simulate the temperature distributions inside the powder compact, which cannot be measured experimentally. Microstructural characterisations using SEM, EPMA and EBSD methods show that, temperature plays a crucial role in driving the microstructure changes in the thermally shocked powders. At elevated temperatures below the γ' solvus temperature for 10 s, the powders showed relatively small morphological changes only; however above the γ' solvus temperature, spheroidisation and coarsening were rapid, and advanced still more dramatically once the incipient melting temperature of the powder was exceeded. There was some evidence to suggest that the sudden appearance of liquid in inter-dendritic regions led to dendritic fragmentation, although fragments also rapidly coarsened. At higher temperatures, where approximately 0.45 liquid fraction was expected, the powder-processed microstructure with a characteristic length-scale restricted to the powder diameter was completely absent, and the material behaved as a coherent larger volume that consequently re-solidified with a much coarser cellular structure and significant coarser scale micro-segregation including the formation of potentially detrimental phases. In this regime, any microstructural benefits from the rapidly solidified powders were lost. These results can be useful in reconciling thermal histories and microstructures in the as-sprayed preforms, and may guide the optimisation of the spray forming process if desirable microstructural features are to be preserved into the bulk preform.

CHAPTER 7 : IN SITU NEUTRON DIFFRACTION STUDY OF THE DEFORMATION OF DISSIMILAR STEELS

This chapter describes the bending deformation behaviours of the as-sprayed steels, and how neutron diffraction was used to acquire *in situ* the diffraction spectra at different load steps and, then to calculate the strains at the measured gauge volumes. In this way, the strain and stress distribution profiles along the measured path at different load conditions during the three-point bending tests were obtained. These data are essential for understanding the elastic and plastic deformation behaviours of the spray formed steels containing different levels of porosity and the integrity of the bonded interface of the spray formed dissimilar steels.

7.1 Calculation of the specimen second moment of inertia and neutral axis

Porosity in the specimen was taken into account using the composite beam theory when calculating the local applied stress. In the three-point bend test shown in Fig. 7.1a, the moment (M_B) generated due to the applied force (F_B) from the crosshead is maximum at the centre of the specimen,

$$M_B = \frac{F_B \, L_{Span}}{4} \qquad (7.1)$$

and the flexural stress (σ_B) applied on the specimen along the applied force direction can be determined using,

$$\sigma_B = - \frac{M_B \, y_B}{I_B} \qquad (7.2)$$

where y_B is the distance in the specimen from the neutral axis (NA) and I_B is the second moment of area. The position of NA in the specimen can be derived using,

$$NA = \frac{\sum y_n \, A_n}{\sum A_n} \qquad (7.3)$$

where the subscript "n" refers to the respective layer in the beam, y_n is the distance between the centroid of the respective layer to a reference datum, and A_n is the cross-sectional area of the layer. The typical three-point bend test specimen is subjected to maximum compressive and tensile stress at

the extreme ends of the specimens along the loading axis, and zero stress at the NA during the bend test as indicated in Fig. 7.1b.

However, the NA and I_B can change if the specimen is made up of different material (composite beam) and can be determined by transforming the composite beam into an equivalent beam made of a single material using the modular ratio (n_m) of the materials' Young's modulus [257]. For the specimen that is made up of a porous upper layer and a dense lower layer as illustrated in Fig. 7.1c, n_m can be expressed as,

$$n_m = \frac{E_D}{E_{Porous}} \qquad (7.4)$$

and the corresponding NA and I_B can be determined from the transformed equivalent beam using Eqn. (7.3) and parallel axis theorem [257], respectively.

A similar approach was used to determine the corresponding NA and I_B for the specimen comprising of different steels and porosity, and the modular ratio was calculated using the Young's modulus of mild steel at room temperature (201 GPa [194]).

The corresponding flexural strengths of the specimens after fracture were determined using,

$$\sigma_F = \frac{3L_{Span}F_F}{2w_S t_S{}^2} \qquad (7.5)$$

where F_F is the load at fracture, w_S and t_S are the specimen width and thickness, respectively.
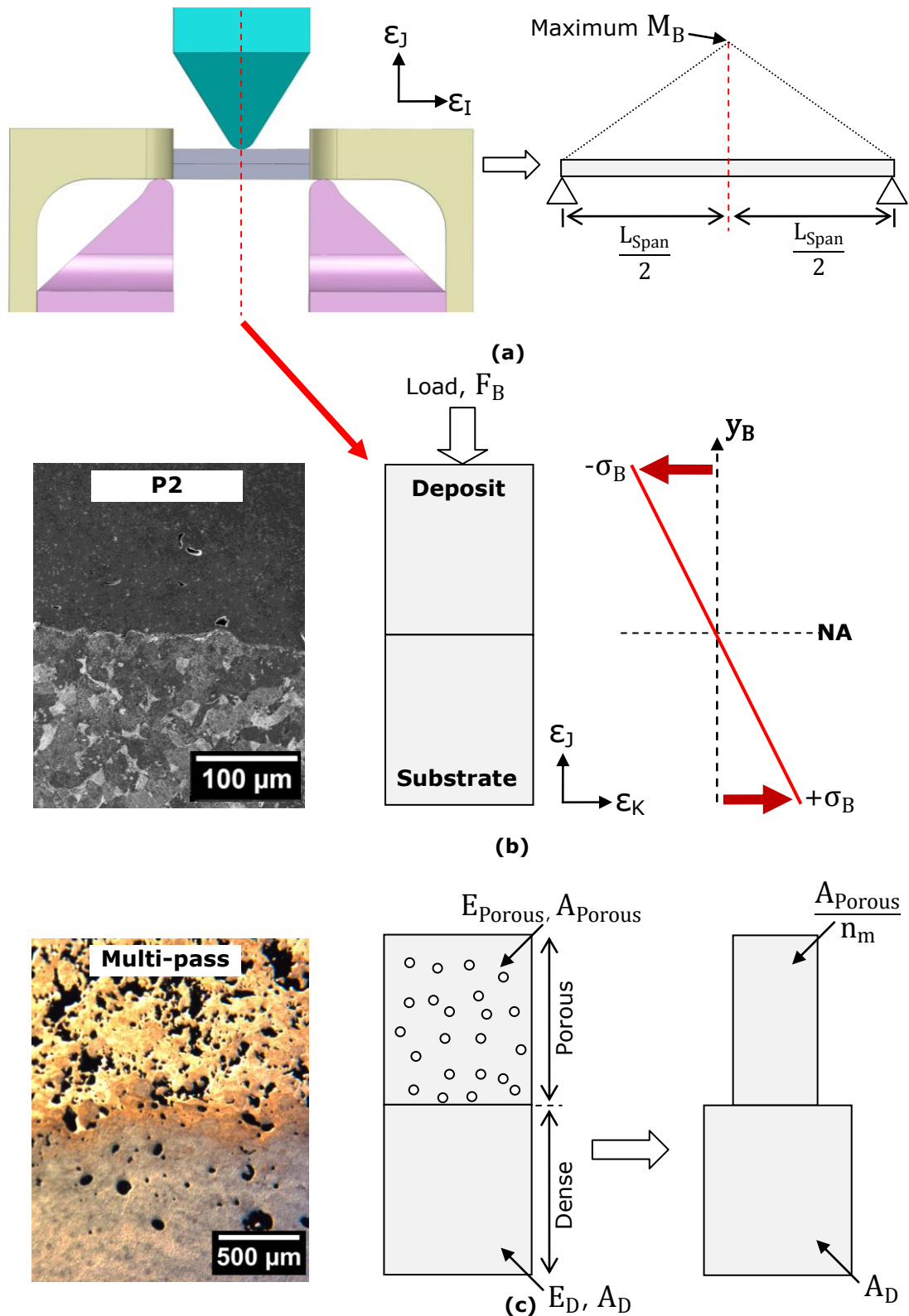
Fig. 7.1. Schematic diagrams showing (a) the maximum moment applied at the centre of the three-point bend test specimen, (b) the stress applied on the dissimilar alloy specimen along the applied force direction and (c) the transformation of the composite beam that is made up of a porous upper layer and a dense lower into an equivalent beam made of a single material using modular ratio.

7.2   The strength and hardness of the as-sprayed steels

The measured load-deflection curves from bend tests are shown in Fig. 7.2a and Fig. 7.2b. The creep effects when the load was held constant for the ND measurement were more apparent at higher loads. The ε_I and ε_K measurements from the as-sprayed HSS specimen at the final preset load (10.40 kN) were not available as the specimen fractured during the load increment from 9.24 kN and thus, the stress distributions at the final preset load were not derived. Fig. 7.2c showed that the effective flexural strength of the as-sprayed HSS decreased from ~1200 MPa to ~800 MPa when sprayed and bonded to the mild steel substrate.

The hardness across the bonded interface in preform P2 was measured using Vickers hardness tester and showed that the as-sprayed ASP30 HSS had an average hardness of ~589 HV across the interface (Fig. 7.3). The hardness of the as-sprayed HSS deposit can be estimated using the weighted average hardness of the individual phases [258]:

$$H_{avg} = f_{\alpha'} H_{\alpha'} + (1 - f_{\alpha'}) H_{\gamma} \qquad (7.6)$$

where $H_{\alpha'}$ and H_{γ} are the hardness of martensite and austenite phase, respectively. $H_{\alpha'}$ and H_{γ} were assumed to be 660 and 260 HV, respectively based on data from [259] while $f_{\alpha'}$ near to the interface region was taken as 0.71 based on the PWF distribution measurements from ND (Fig. 3.12c). The hardness of the as-sprayed ASP30 HSS was calculated as 544.2 HV which is relatively consistent with the Vickers hardness test results.
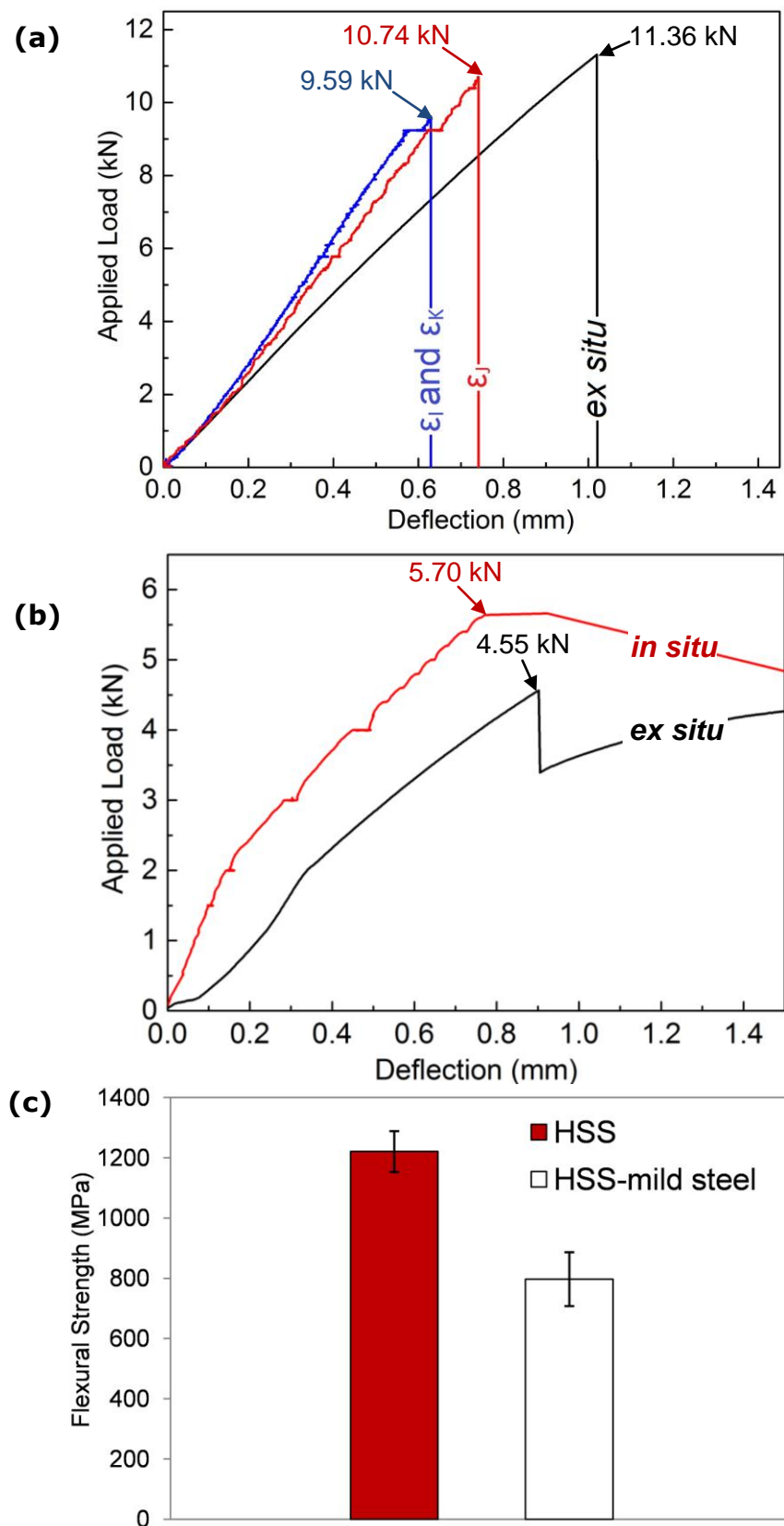
Fig. 7.2. The load-deflection curves measured from the *in situ* ND bending tests for the specimen containing (a) porosity and (b) the bonded interface and the *ex situ* bending test (without ND measurement) results are also superimposed, and (c) the corresponding flexural strengths.

(a)

(b)
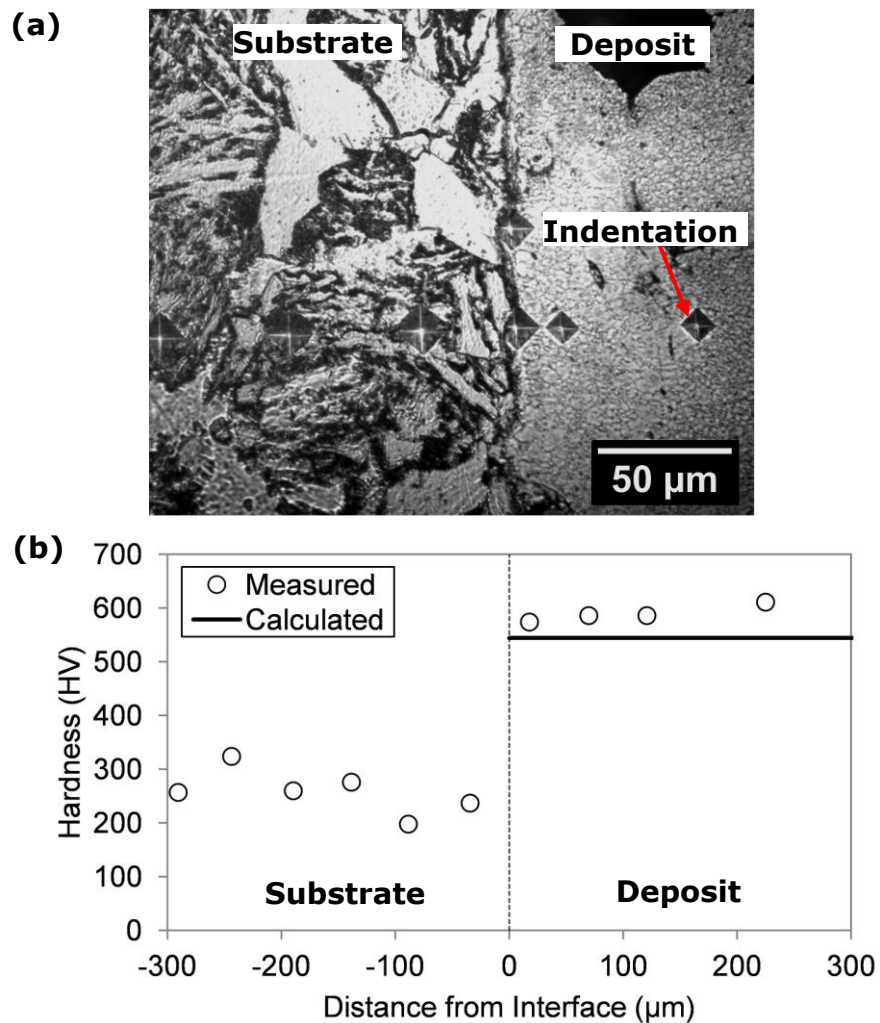
Fig. 7.3. (a) The indentations made across the bonded interface of preform P2 and (b) the corresponding Vickers hardness.

7.3 The fracture modes of the as-sprayed steels and interface

The fractographs of the as-sprayed HSS (Fig. 7.4) shows the crack initiation point (CIP) at the base of the specimen (furthest from the crosshead) and the fracture surfaces in the dense-to-porous transition region. The CIP can be observed from the crack propagations (steps between cleavage or parallel planes indicated as dotted arrows in Fig. 7.4a). The surface of the fracture (Fig. 7.4b and Fig. 7.4c) shows cleavage facets which are indicative of a brittle fracture mode for the as-sprayed HSS [260]. The circular indents on the fracture surface are likely due to the solidified droplets (relatively small diameters of <20 µm) that detached during fracture.
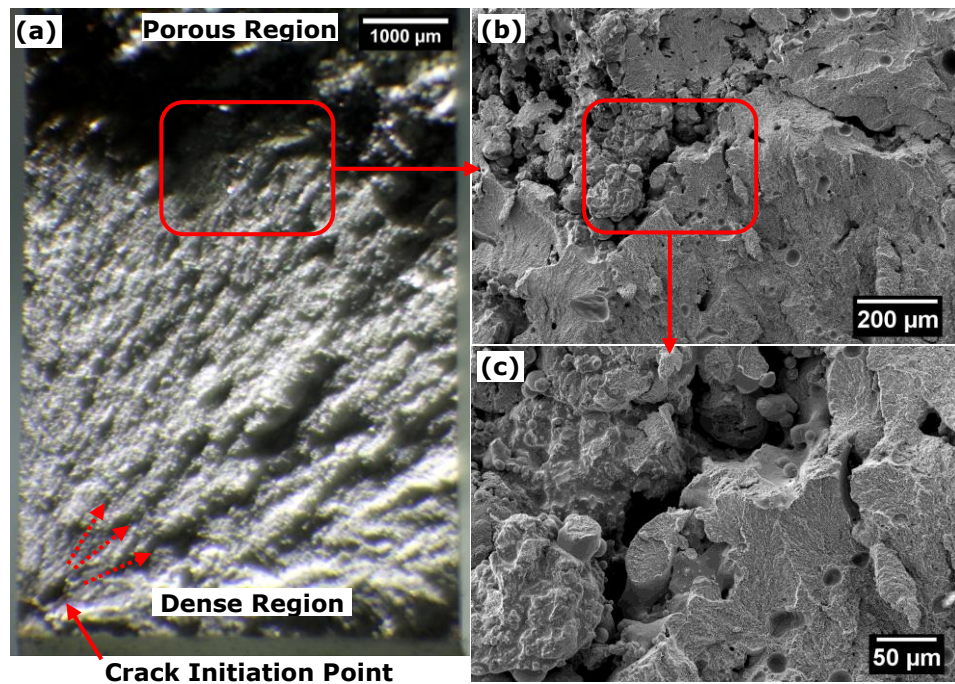
Fig. 7.4. Fractographs of the as-sprayed HSS showing the (a) crack initiation point with the crack propagations marked as dotted arrows and (b-c) cleavage facets in the dense-to-porous transition region.
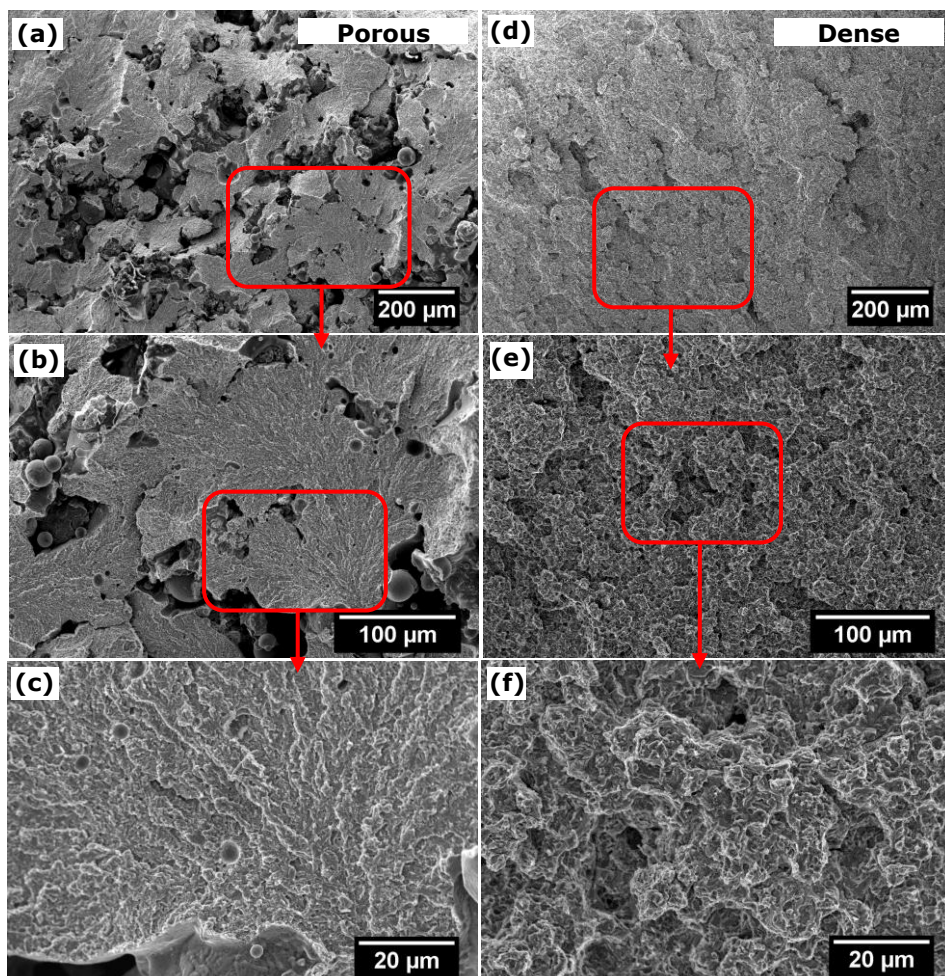
Fig. 7.5. Fractographs of the as-sprayed HSS (a-c) porous and (d-f) dense region.

The fractographs from the porous and dense regions are shown in Fig. 7.5. Similarly, cleavage facets can be observed from both regions. A noticeable difference between the two regions is that the circular indents (due to the detached solidified droplets) were only found in the porous region and is typically due to the lower spray temperatures and alloy liquid fraction in this region as revealed by the correlation established from the preform heat flow simulations and microstructure characterisations described in Chapter 5.

The fractograph (Fig. 7.6) acquired from the bonded interface region showed that the as-sprayed HSS did not delaminate from the substrate after fracture. The specimen failure was most likely due to the porosity and inclusion in the deposit near to the interface based on the crack propagations (marked as dotted red arrows). The inclusion in the CIP can be seen to appear brighter under SEM observations (Fig. 7.7a and Fig. 7.7b). In addition, Fig. 7.7c and Fig. 7.7d showed that the some of the crack propagations ended at the interface. In spite of that, there was no apparent crack or fracture along the interface where the crack propagation ended. This indicates the relatively strong bonding formed along the interface and is in agreement with the non-destructive interfacial assessment described in Chapter 5.

The different fracture modes in the dissimilar steel specimen are shown in Fig. 7.8. The deposit region (Fig. 7.8a and Fig. 7.8b) showed cleavage facets which are indicative of a brittle fracture mode while the dimple structure on the substrate fracture surface (Fig. 7.8e and Fig. 7.8f) indicated a ductile fracture mode. The interface region (Fig. 7.8c and Fig. 7.8d) exhibits the intersection point between the brittle deposit and ductile substrate fracture modes.
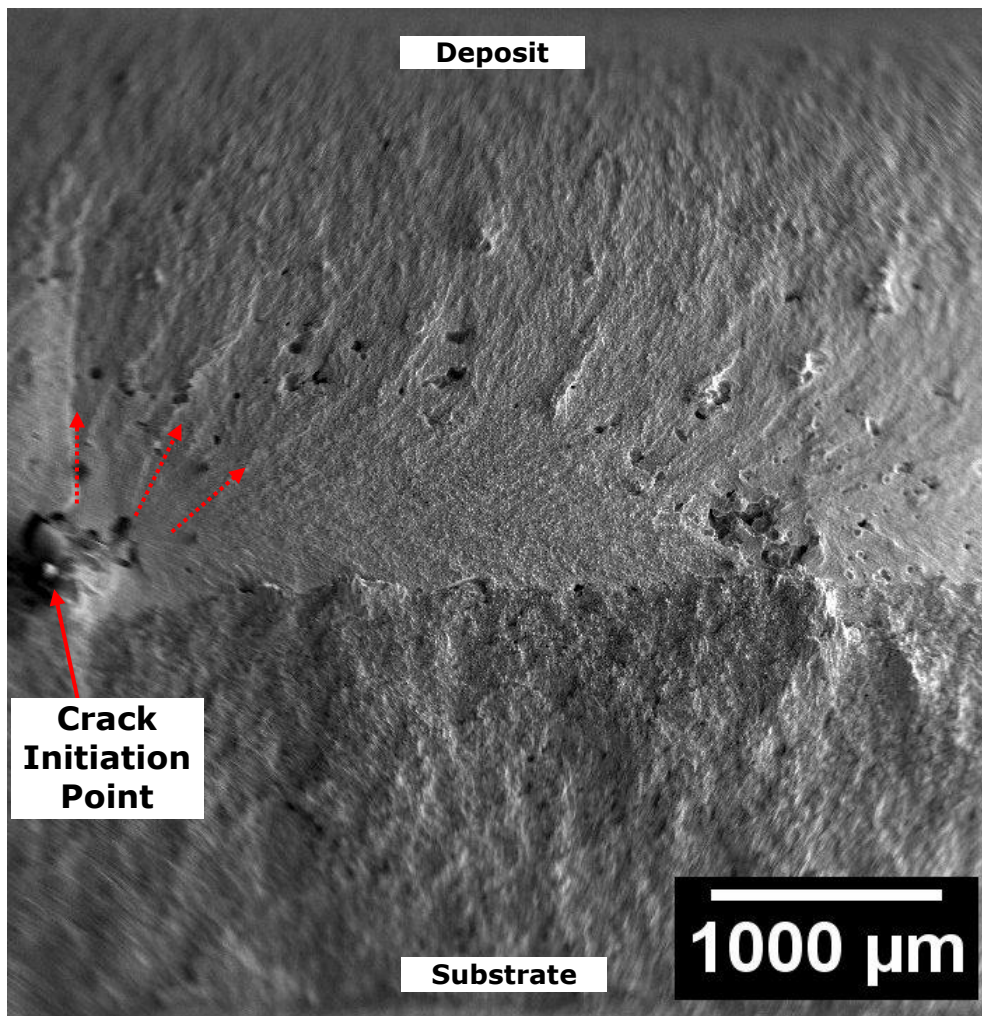
Fig. 7.6. Fractograph acquired from the bonded interface region showing the overall interface condition after fracture and the crack propagations (marked as dotted red arrows) from the crack initiation point.
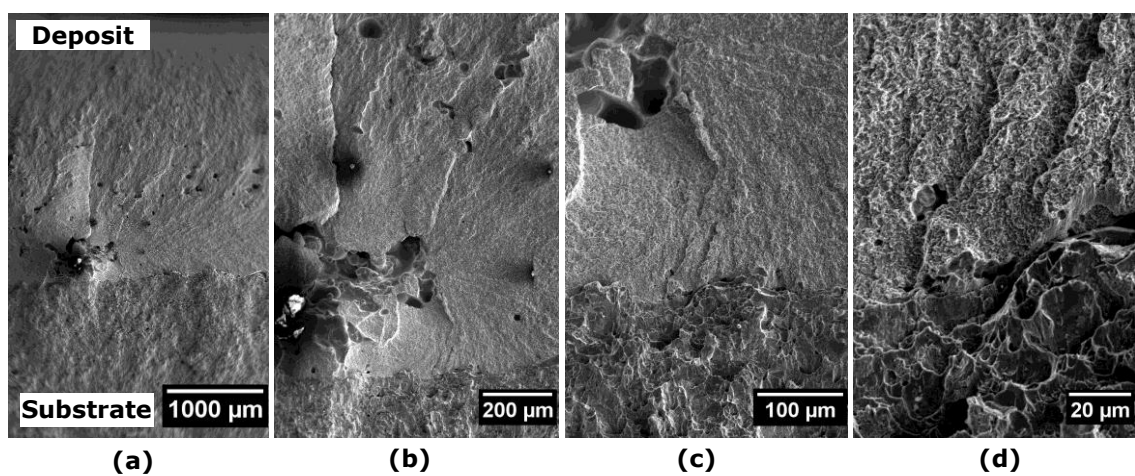
Fig. 7.7. Fractographs acquired from the bonded interface region showing the (a-b) inclusion in the crack initiation point and (c-d) the crack propagations that ended at the interface.
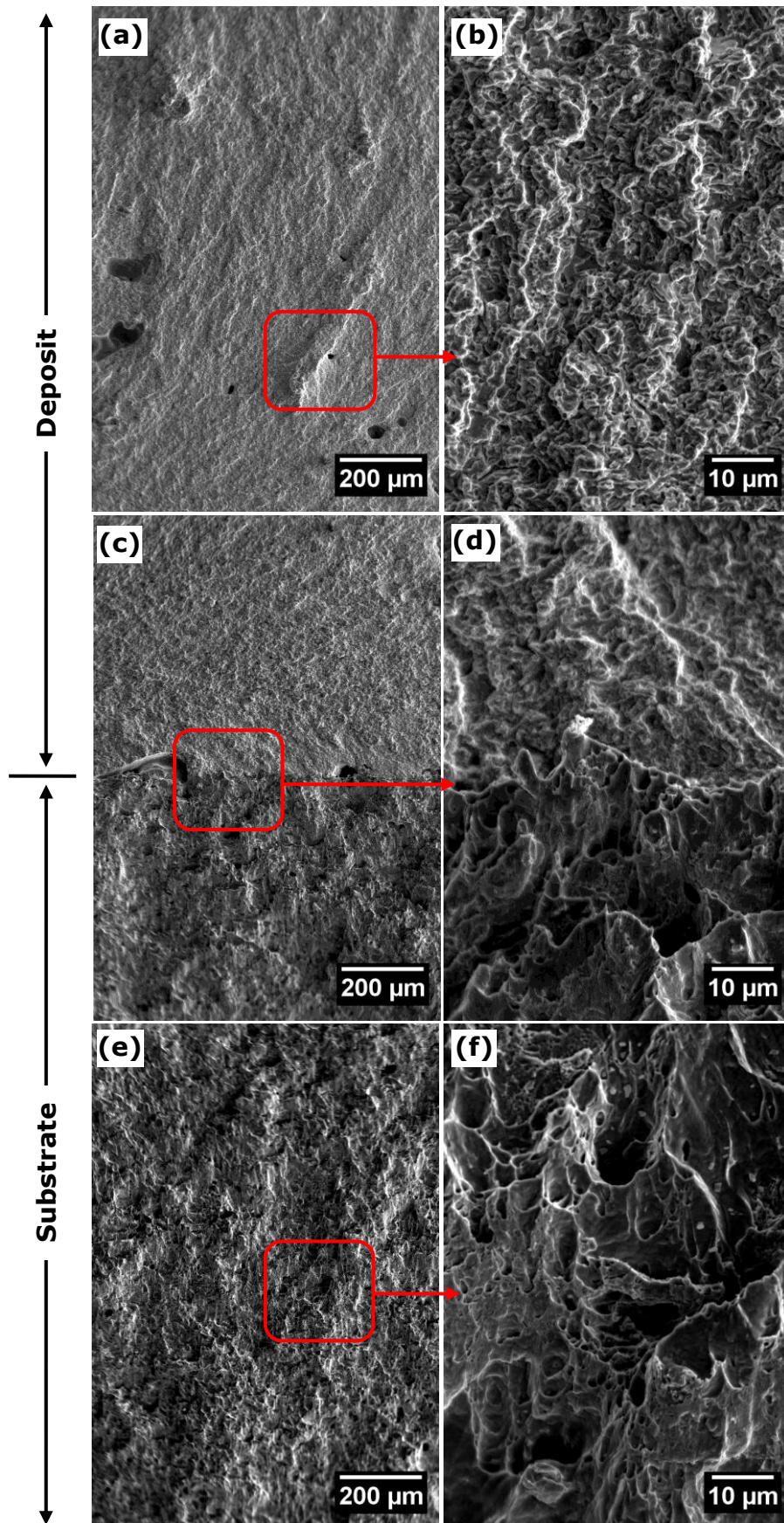
Fig. 7.8. The fractographs acquired from the (a-b) deposit, (c-d) interface and (e-f) substrate region of the as-sprayed dissimilar steels specimen.

7.4 Macro-stress and inter-phase stress evolution

Fig. 7.9 shows the phase-specific and bulk stress distributions along the HSS specimen thickness at the different applied load levels. In general, compressive stresses were found in the region near to the crosshead (0 - 5 mm) refered to as the top region hereafter, while tensile stresses were present at the base of the specimen (-5 - 0 mm). The σ_I showed the highest magnitude with up to ~830 MPa in the base region and ~ -640 MPa near to the crosshead. Compressive σ_J of ~ -330 MPa was measured near to the crosshead due to the compression in this region during loading and the stress diminished to near to zero further from the crosshead towards the base of the specimen. Near to zero σ_K was measured along the thickness of the specimen. Therefore, the stress distributions measured showed that the specimen would most likely fail due to σ_I along the thickness of the specimen.
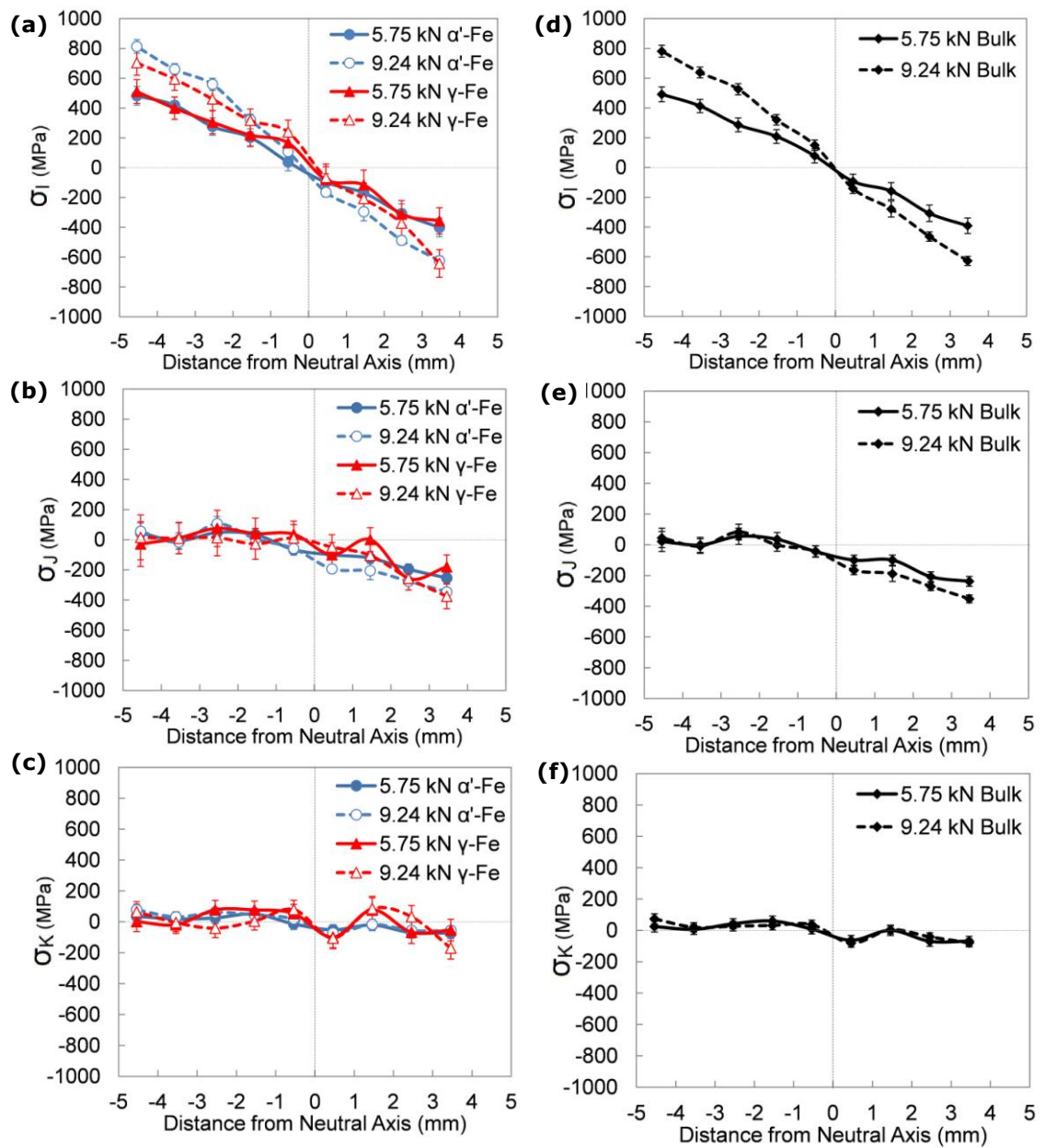
Fig. 7.9. The (a-c) phase and (d-f) bulk stress distributions along the as-sprayed HSS specimen thickness at increasing applied bending loads.

7.5   Inter-phase strain evolution

The nonlinearity in strain distribution is indicative of plastic deformation [261] and the elastic phase strain distributions (Fig. 7.10) showed nonlinear strains towards the base and top edges of the HSS specimen especially for ε_I. At 5.75 kN, the nonlinearity started at ~3.5 mm from the NA which indicates the onset of the elastic-plastic behaviour of the material in this region. The nonlinearity creeps progressively into the core section of the specimen with respect to an increase in the applied bending load. When the load applied was increased to the plastic regime (9.24 kN), the nonlinearity progressed further into the specimen and occurred at ~1.5 mm from the NA. The measurement point at the top extreme edge (~4.5 mm) for ε_J was disregarded due to the GV incorporated the crosshead material at the measurement point in the horizontal load frame scan orientation.

It is evident that the ε_I and σ_I were significantly higher than the other strain or stress components from the *in situ* ND bend test of the as-sprayed HSS (Fig. 7.9 and Fig. 7.10). Therefore, the ε_I distributions along the dissimilar steels specimen thickness were measured *in situ* using ND during the bend test. The strains from the dominant phases in the HSS deposit (α'-Fe and γ-Fe) and mild steel substrate (α-Fe) are shown in Fig. 7.11. It is noteworthy that the deposit-substrate interface of the specimen was not the neutral axis of the bend test specimen and its position is indicated in the strain distributions using a vertical line at -0.46 mm from the NA.

Generally, compressive strains were found in the deposit region and tensile strains were measured from the substrate region. When the load applied was increased to plastic regime (>2 kN), α'-Fe exhibited relatively smaller strains up to ~ -0.1% at 4 kN (Fig. 7.11a) as compared to the γ-Fe phase which showed strains of up to ~ -0.32% (Fig. 7.11b). Nonlinearity in the strain distributions occurred in the deposit region at ~0.2 - 0.8 mm from the NA when the load applied was increased to the plastic regime (>2 kN) implying the onset of plastic deformation in this region while the substrate showed no apparent nonlinearity.
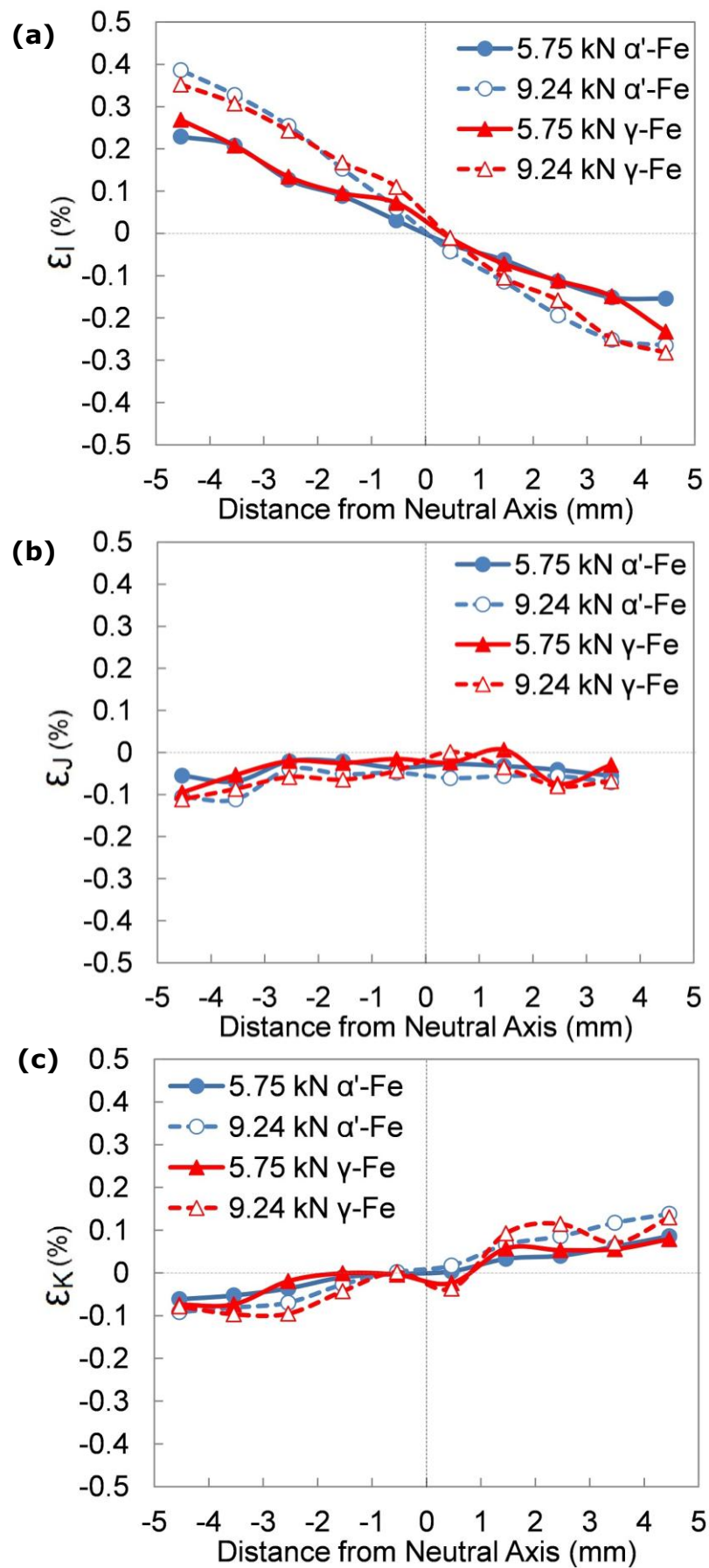
Fig. 7.10. The (a) ε_I, (b) ε_J and (c) ε_K phase strain distributions along the as-sprayed HSS specimen thickness at increasing applied bending loads.
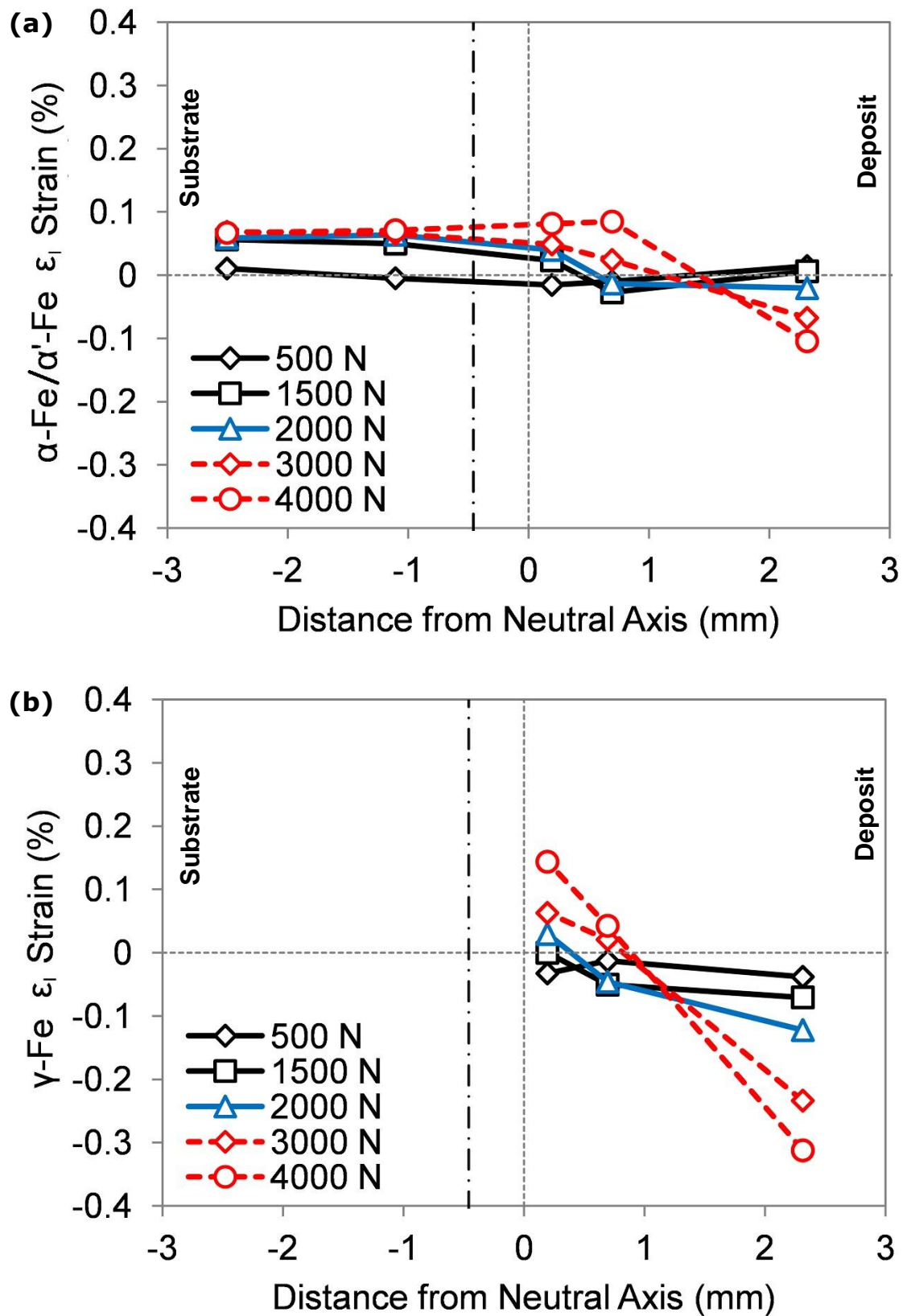
Fig. 7.11. The (a) α′-Fe or α-Fe, and (b) γ-Fe phase ε_I distributions along the dissimilar steels specimen thickness. Deposit-substrate interface position was at -0.46 mm from the NA of the specimen.

7.6 Inter-granular strain evolution

Inter-granular stress-strain curves show the elastic and plastic deformation behaviours of the respective *hkl* planes and their interactions with each other in the material. The stress-strain curve of the respective *hkl* planes that undergoes plastic deformation will deflect upwards (reduced elastic strain), and the load will be transferred to the other phases or planes that remain elastic which would show a downwards deflection from linearity (increased elastic strain) [262].

The α'(200), α'(211), γ(200), γ(220) and γ(311) planes in the as-sprayed HSS were selected for the inter-granular strain analysis. The γ(311) and α'(211) planes are considered as the most representative of the bulk material behaviour [263, 264] and the other planes that have different elastic moduli were included to reveal the load-redistributions between the planes or phases at the onset of plasticity. In addition, the peaks were not overlapped as shown in the typical diffractograms acquired from the porous and dense regions of the specimen (Fig. 7.12).
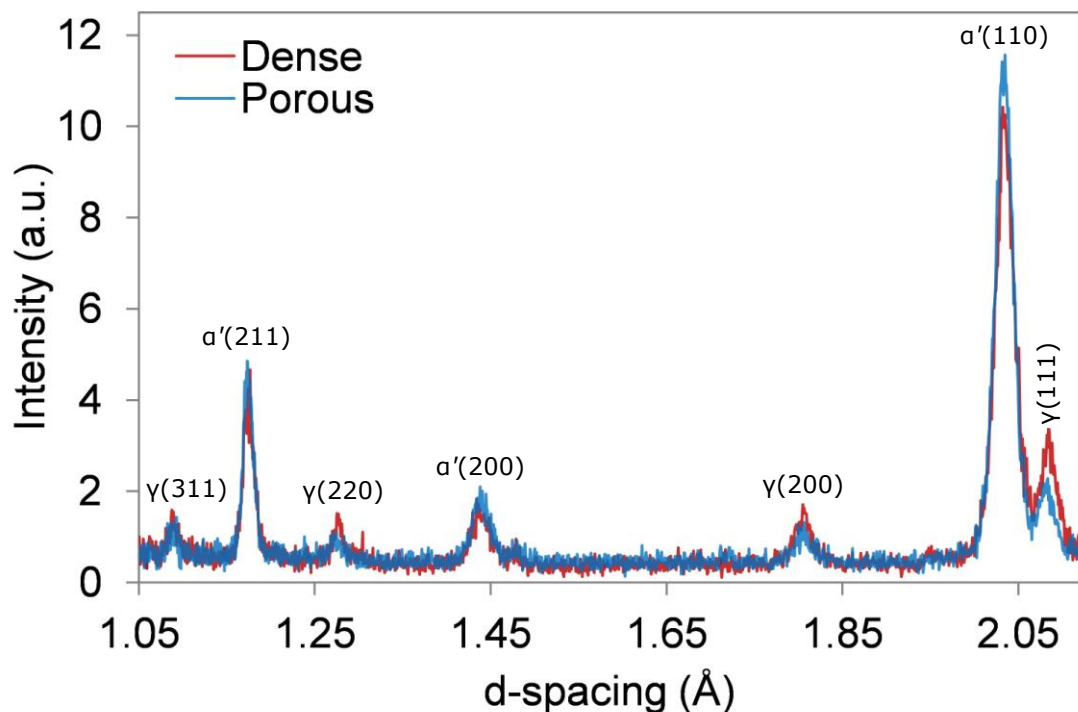
Fig. 7.12. The typical TOF diffractograms acquired from the porous and dense regions of the as-sprayed HSS specimen.
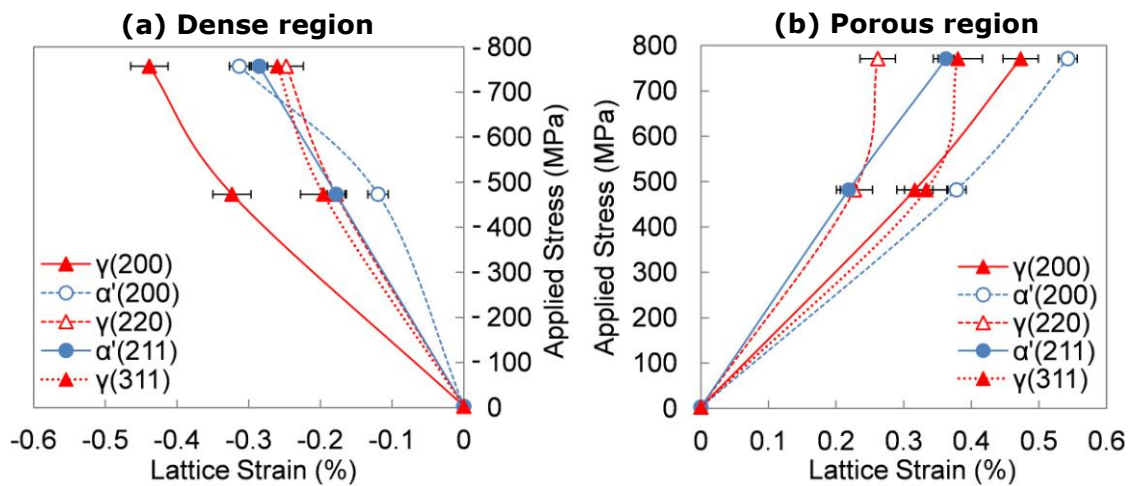
Fig. 7.13. *hkl* plane elastic lattice ε_I with respect to local stress applied in (a) the porous (4.5 mm from NA) and (b) the dense (-4.5 mm from NA) regions of the as-sprayed HSS.
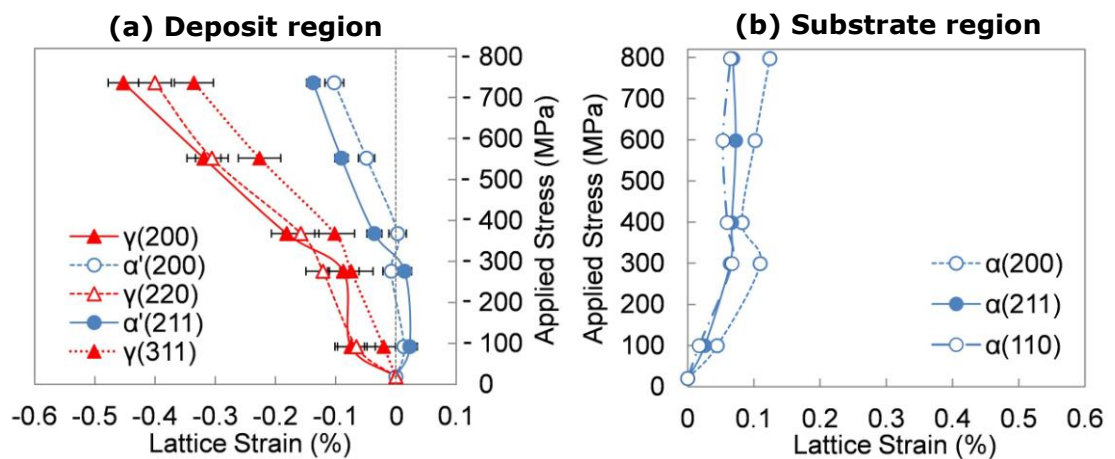
Fig. 7.14. *hkl* plane elastic lattice ε_I with respect to local stress applied in the (a) deposit (2.3 mm from NA) and (b) substrate (-2.5 mm from NA) regions of the as-sprayed dissimilar steels.

Fig. 7.13a and Fig. 7.13b show the selected *hkl* plane lattice strains of porous and dense region in the as-sprayed HSS with respect to the applied compressive and tensile stress, respectively. The local stress applied in along the specimen thickness was derived using Eqn. (7.2) and the GV measurement positions at the extreme top and base regions of the specimen were 4.5 mm and -4.5 mm from the NA, respectively.

Under compressive applied stress, the respective *hkl* planes were expected to generally show a linear response up to the elastic limit (~ -480 MPa). The different slopes in the elastic region were due to the elastic moduli pertaining to the respective planes. As reported in previous studies on austenitic stainless steel, the γ(200) plane is the most compliant γ-Fe plane which showed the highest lattice strain [265, 266]. In addition, the α'-Fe planes showed lower lattice strains as compared to the γ-Fe and this indicated the relatively higher stiffness of the α'-Fe phase.

When the applied load was increased above the elastic limit, the nonlinear response in the respective planes was observed. The γ-Fe planes showed smaller increments in lattice strains which implied the onset of plastic deformations and the plastic flow in this phase [267]. This trend indicates that slip initiates preferentially in the γ-Fe planes of the as-sprayed HSS in the elastoplastic regime. Load-redistribution from the γ-Fe planes to the α'-Fe planes may have occurred since the α'(200) plane showed relatively higher lattice strain increments above the elastic limit. In the plastic regime, the α'(211) plane showed a more linear response in comparison to the γ-Fe planes. Therefore, the α'-Fe planes generally remained elastic above the elastic limit which indicated that the α'-Fe phase acts as an elastic reinforcing phase to the γ-Fe phase under compressive loading.

When subjected to tensile stress, the α'(211) plane which is most representative of the bulk material also showed the highest stiffness in comparison to the γ(311) plane. The (200) planes that showed the highest lattice strain indicated their higher compliance in comparison to the other planes when subjected to tensile deformation. Beyond the elastoplastic regime (>480 MPa), the nonlinear response from in the γ-Fe planes with smaller increments in lattice strains indicated that the load was transferred

from the plastically deformed γ(311) and γ(220) planes to the α'-Fe phase. This trend is consistent with the response under compressive stress. The elastic response of the α'(211) plane in the plastic regime (up to ~790 MPa) also revealed the role of α'-Fe to act as a reinforcing phase when the as-sprayed HSS is subjected to tensile deformation.

The ε_I strain distributions along the specimen thickness of the α'(211) and γ(311) planes with respect to the increasing applied bending loads (Fig. 7.15) also showed the more elastic response of the α'-Fe phase at different applied stress directions and magnitudes. The deformation behaviours of the dominant phases when subjected to compressive and tensile stresses in the as-sprayed HSS revealed is consistent with other *in situ* ND uniaxial deformation studies of conventionally produced alloy steels [264, 268].

The inter-granular strains in the deposit and substrate of the as-sprayed dissimilar steels with respect to local stress applied are shown in Fig. 7.14a and Fig. 7.14b, respectively. The α(200), α(211) and α(110) planes from the mild steel substrate were selected for the inter-granular strain analysis. In the deposit region (Fig. 7.14a), the *hkl* planes generally showed linear strain increments up to the elastic limit (~ -370 MPa) and the difference in the slopes were due to the different elastic moduli of the respective *hkl* planes. The smaller strain increment in the elastically softer γ(200) plane near to the elastic limit (~ -290 MPa) indicate the onset of plastic flow in the γ-Fe phase. This deformation behaviour trend showed that slip was initiated preferentially in some of the γ-Fe planes near to the elastic limit.

In the elastoplastic regime (~ -300 to -400 MPa), the γ-Fe planes exhibit relatively significant nonlinear response and the larger lattice strain increments especially in the γ(220) and γ(311) planes implied that a load-redistribution occurred from the plastically deformed γ(200) plane. In addition, the α'-Fe planes showed that load was transferred from the softer α'(200) to the α'(211) plane. Further stress increments up to ~ -730 MPa caused the plastic flow in the γ(220) and γ(311) planes and the larger strain increments in the γ(200) plane indicate the strain-hardening in this regime. The α'-Fe planes generally showed a more linear response in

comparison to the γ-Fe planes which further confirmed their role as a strengthening phase in the as-sprayed HSS.

In the substrate region (Fig. 7.14b), the α-Fe planes generally showed a linear response up to the elastic limit and the most compliant plane, α(200) showed relatively larger strain increments in comparison to the other α-Fe planes. In the elastoplastic regime (~300 - 400 MPa), the α-Fe planes exhibited nonlinear responses. The α(200) and α(110) planes showed smaller strain increments which suggested that plastic flow started in the α-Fe phase and that slip was initiated at relatively low applied stress which is in agreement with previous uniaxial deformation studies [267]. Further tensile stress increments led to an increase in work-hardening of the α-Fe planes especially for the α(200) and α(110) plane.

Therefore, the inter-granular strain analysis revealed that slip was initiated preferentially in some of the γ-Fe and α-Fe planes near to the elastic limit and predominantly in the more compliant (200) planes.
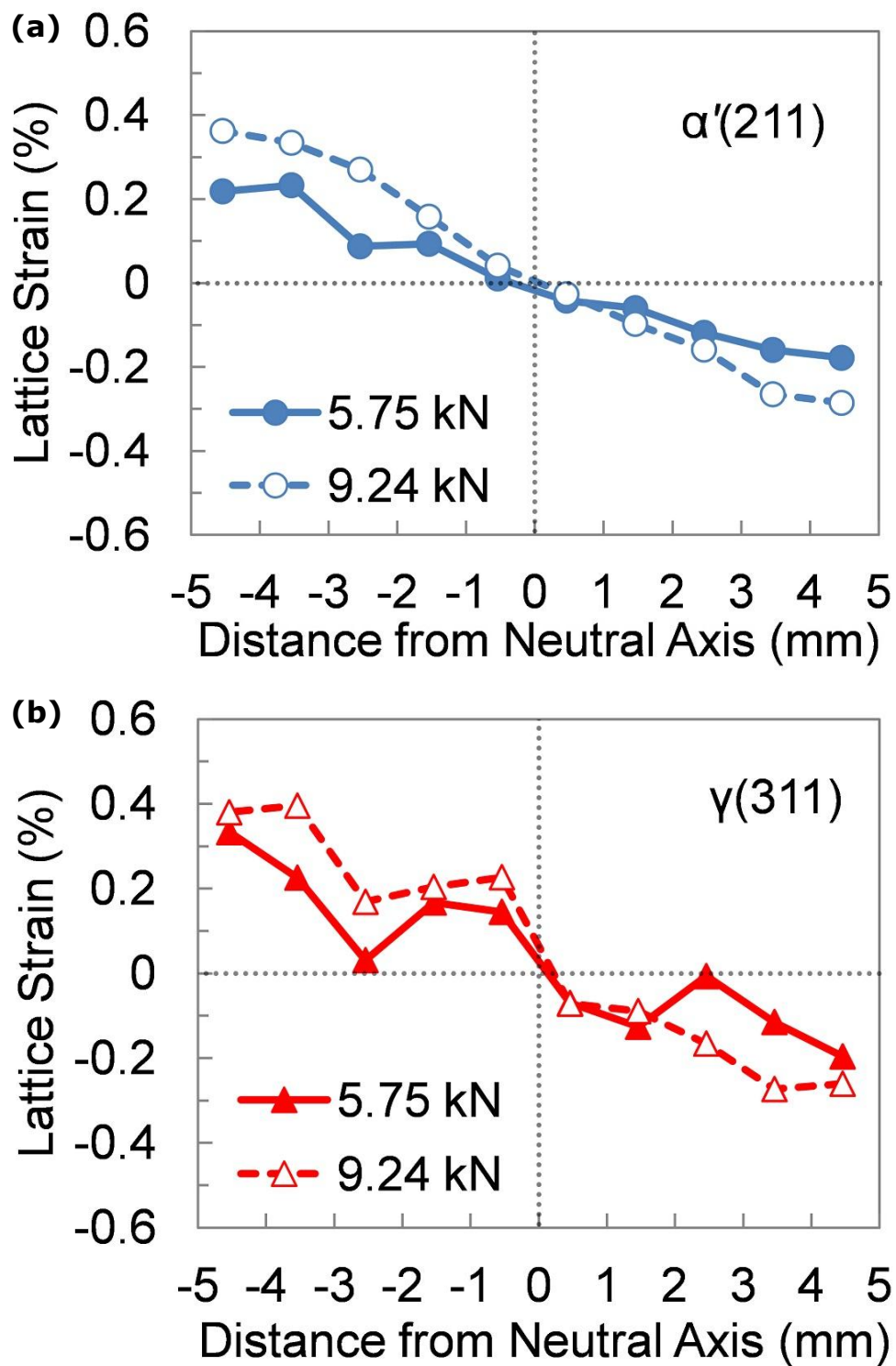
Fig. 7.15. The ε_I strain distributions along the as-sprayed HSS specimen thickness of the (a) α'(211) and (b) γ(311) planes with respect to the increasing applied bending loads.

7.7   Summary

The elastic and plastic deformation behaviours of the spray formed steels containing different levels of porosity and the integrity of the bonded interface of the spray formed dissimilar steels were studied *in situ* using three-point bend tests with neutron diffraction. The inter-granular lattice strains showed that the stiffer α'-Fe phase in the as-sprayed high speed steel generally acts as a reinforcing phase to the γ-Fe phase when subjected to compressive or tensile stresses above the elastic limit. The bend tests also revealed that the as-sprayed high speed steel layer did not delaminate from the substrate after fracture which indicates the relatively strong bonding formed along the interface and is in agreement with the non-destructive interfacial assessment described in Chapter 5.

CHAPTER 8 : SUMMARY AND FUTURE WORK

8.1   Summary

Systematic experimental and numerical modelling studies were carried out to reveal the underlying mechanisms that governed the interfacial bonding, microstructure formation and mechanical deformation characteristics in the as-sprayed dissimilar metallic alloy preforms. The key findings from this research are:

- The combined 3D microstructure characterisation and numerical modelling of the preform thermal history established the correlation between the microstructures formed and thermal history of the preform. The preform thermal histories revealed that the tube preform interface and surface regions comprised of low liquid fractions during spraying which led to the formation of porosity and finer carbides with a discontinuous network in these regions. A region of dense material with a continuous carbide network can be formed when the liquid fraction of between 0.20 - 0.55 is maintained during spraying. Although porosity in the preform can be reduced by maintaining high liquid fractions in the deposited layers, excessive liquid fractions were shown to give rise to poor and irregular preform surface quality. Preheating the substrate before spraying can overcome the trade-off between porosity and preform surface quality effectively and led to a strong interfacial bond.

- The comparison between residual stress distribution across the interface of dissimilar steel preforms characterised using neutron diffraction and simulated stress distribution provided a non-destructive means of assessing the quality of the interfacial bonding formed in the preforms, quantitatively. The combined experimental and numerical modelling approach employed successfully established the links between preform thermal history, corresponding microstructure formed and the interfacial bonding developed to provide the key insights to understand the interfacial bond and residual stress development mechanisms in as-sprayed dissimilar steel preforms. The relationships suggest that a hotter substrate and

spray directly result in a lower residual stress developed in the preform. The stress change was due to the corresponding difference in preform thermal history and the microstructure formed that affected the material coefficient of thermal expansion mismatch at the interface.

- The dynamics of the rapid microstructural change of atomised droplets during deposition was revealed by rapidly heating and cooling atomised Ni superalloy powders with a time period of a few seconds to a range of isothermal temperatures in the vicinity of the γ'solvus and alloy solidus temperatures. At elevated temperature for 10 s, the powders showed relatively small morphological changes only; however above the γ'solvus temperature, spheroidisation and coarsening were rapid, and advanced still more dramatically once the incipient melting temperature of the powder was exceeded. There was some evidence to suggest that the sudden appearance of liquid in inter-dendritic regions led to dendritic fragmentation, although fragments then rapidly coarsened. At higher temperatures, where approximately 0.45 liquid fraction was expected, the powder-processed microstructure with a characteristic length-scale restricted to the powder diameter was completely absent, and the material behaved as a coherent larger volume that consequently re-solidified with a much coarser cellular structure and more significant coarser scale micro-segregration including the formation of potentially detrimental phases. In this regime, any microstructural benefits from the rapidly solidified powders were lost.

- *In situ* neutron diffraction bend test experiments revealed that the stiffer martensite phase in the as-sprayed high speed steel generally acts as a reinforcing phase to the retained austenite phase when subjected to compressive or tensile stresses above the elastic limit.

- The three-point bend tests of the as-sprayed dissimilar steels revealed that the high speed steel layer sprayed onto the preheated substrate did not delaminate from the substrate after fracture. This indicated that a relatively strong bonding was formed along the

interface and is in agreement with the non-destructive assessment carried out using neutron diffraction measurement and numerical modelling of the residual stress distribution.

8.2 Future work

In order to improve the accuracy of the numerical model developed in this research, phase transformation effects such as volumetric strain change should be taken into account. In this research, the austenite to martensite transformation would generally lead to more compressive stresses developed in the preform especially in the preform central/interface regions. Nevertheless, the phase transformation effects were not expected to cause significant changes in the trend of the stress distribution simulated using the thermal stress model described in this research. A systematic temperature measurement of the preform temperature distribution throughout the spraying process should be carried out. The preform thermal stress model developed can be used to study the interfacial bond formed in preforms sprayed with dissimilar metallic alloys that have relatively larger differences in material properties to investigate the limitations of the model. It would be interesting to apply the approach used in this research to establish the correlations between the preform thermal history and the microstructures formed in other dissimilar metallic alloys and compare their effects on the interfacial bond formed.

References

[1]   A. Singer. Principles of Spray Rolling of Metals, Metals Materials 4 (1970) 246-250.

[2]   P.S. Grant. Spray forming, Progress in Materials Science 39 (1995) 497-545.

[3]   Y. Ikawa, T. Itami, K. Kumagai, Y. Kawashima, A. Leatham, J. Coombs, R. Brooks. Spray deposition method and its application to the production of mill rolls, ISIJ International 30 (1990) 756-763.

[4]   J. Wahlroos, T. Liimatainen. Interface adherence of spray formed compound tube. Second International Conference on Spray Forming, 1993. p.225-234.

[5]   U. Forsberg, A. Wilson, L. Nylof, M. Yaman. Sandvik Sanicro 65 composite tube for municipal waste incinerators. Proceedings of the 3rd Int. Conf. on Spray Forming, 1999.

[6]   J. Forrest, R. Price, D. Hanlon. Manufacturing clad products by spray forming, International journal of powder metallurgy 33 (1997) 21-29.

[7]   D. Hanlon, W. Rainforth, C. Sellars, R. Price, H. Gisborne, J. Forrest. The structure and properties of spray formed cold rolling mill work roll steels, Journal of Materials Science 33 (1998) 3233-3244.

[8]   P. Chesney, J. Mascolino. Market, Economics and Opportunities for Tubular and Bimetallic Spray Formed Products. In: Wood J, (Ed.). Proceedings of ICSF 3. Cardiff, UK: Paul Ellerington Printers (Keysoe, Beds), 1996. p.115-122.

[9]   A. Leatham. Spray Forming: Alloys, products, and markets, J. Metals 51 (1999).

[10]   P. Chesney. A new spray coating process for manufacture of stainless steel clad construction steel with resistance to corrosion by de-icing salts & seawater, proceedings of SDMA 2003 and ICSF V (2003) 3-9.

[11]   A. Leatham, R. Brooks, J. Coombs, G. Ogilvy. Paper 1. In: Wood J, (Ed.). 1st international Conference on Spray Forming. Osprey Metals Ltd, Neath, 1991.

[12]   A.G. Leatham, A. Lawley. The osprey process: principles and applications, International journal of powder metallurgy 29 (1993) 321-329.

[13]   P. Grant, B. Cantor, L. Katgerman. Modelling of droplet dynamic and thermal histories during spray forming—I. Individual droplet behaviour, Acta Metallurgica et Materialia 41 (1993) 3097-3108.

[14]   P.S. Grant. Schematic of the spray forming process. vol. 2015: University of Oxford.

[15]   W. Carter Jr, M. Benz, A. Basu, R. Zabala, B. Knudsen, R.F. Jones, H. Lippard, R. Kennedy. The CMSF Process: The Spray Forming of Clean Metal, JOM-e 51 (1999) 7.

[16]   S. Markus, C. Cui, U. Fritsching. Analysis of deposit growth in spray forming with multiple atomizers, Materials Science and Engineering: A 383 (2004) 166-174.

[17]   Y. Zhang, G. Zhang, L. Zhou, Z. Li, Y. Hua, W. Xu, L. Na, S. Tian. Analysis of Twin-nozzle-scanning spray forming process and spray formed high speed steel (HSS), Journal of Iron and Steel Research, International 14 (2007) 7-10.

[18]   G. Zhang, Z. Li, Y. Zhang, J. Mi, P. Grant. Modeling the deposition dynamics of a twin-atomizer spray forming system, Metallurgical and Materials Transactions B 41 (2010) 303-307.

[19]   G.A. Roberts, R. Kennedy, G. Krauss. Tool Steels, 5th Edition, ASM International, 1998.

[20]   A. Leatham. Commercial spray forming: exploiting the metallurgical benefits, Materials world 4 (1996) 317-320.

[21]   H. Fiedler, T. Sawyer, R. Kopp, A. Leatham. The spray forming of superalloys, JOM 39 (1987) 28-33.

[22]   R.D. Cava, L. Aliaga, C.T. Rios, V. Uhlenwinkel, N. Ellendt, C. Kiminami, C. Bolfarini. Microstructure Characterization and Kinetics of Crystallization Behavior of Tubular Spray Formed Fe43. 2Co28. 8B19. 2Si4. 8Nb4 Bulk Metallic Glass*, HTM Journal of Heat Treatment and Materials 69 (2014) 312-321.

[23]   J. Lee, J. Jung, E.-S. Lee, W. Park, S. Ahn, N.J. Kim. Microstructure and properties of titanium boride dispersed Cu alloys fabricated by spray forming, Materials Science and Engineering: A 277 (2000) 274-283.

[24]   V. Srivastava, R. Mandal, S.N. Ojha. Microstructure and mechanical properties of Al–Si alloys produced by spray forming process, Materials Science and Engineering: A 304 (2001) 555-558.

[25]   V. Srivastava, R. Mandal, S. Ojha. Evolution of microstructure in spray formed Al–18% Si alloy, Materials Science and Engineering: A 383 (2004) 14-20.

[26]   M. Amateau. Properties of Spray Metal Formed Ultra-High Temperature Aluminium Alloys. 4th Int. Conf. on Spray Forming.

[27]   S. Hogg, I. Palmer, L. Thomas, P. Grant. Processing, microstructure and property aspects of a spraycast Al–Mg–Li–Zr alloy, Acta Materialia 55 (2007) 1885-1894.

[28]   S. Hogg, J. Mi, K. Nilsen, E. Liotti, P. Grant. Microstructure and property development in spray formed and extruded Al-Mg-Li-Zr alloys for aerospace and autosport applications. Entwicklung von Gefüge und Eigenschaften sprühkompaktierter und extrudierter Al-Mg-Li-Zr-Legierungen für Luftfahrt-und Autosportanwendungen, Materialwissenschaft und Werkstofftechnik 41 (2010) 562-567.

[29]   L. Shaw, C. Spiegelhauer. Spray forming large diameter special steel billets, International journal of powder metallurgy 33 (1997) 31-36.

[30]   C. Spiegelhauer. Properties of spray formed tool and high speed steels. 3rd Pacific Rim Int. Conf. on Advanced Materials and Processing, 1998. p.1653-1659.

[31]   A. Singer. Metal matrix composites made by spray forming, Mater. Sci. Eng. A 135 (1991) 13-17.

[32]   C. Spiegelhauer. Industrial production of tool steels using the spray forming technology, The use of tool steels: Experience and research 2 (2002) 1101-1109.

[33]   D. Hanlon, W. Rainforth. The rolling sliding wear response of conventionally processed and spray formed high speed steel at ambient and elevated temperature, Wear 255 (2003) 956-966.

[34]   G. Hoyle. High speed steels, Butterworths, 1988.

[35]   H.A. Garner, G. Del Corso. Powder metallurgy tool steels, Advanced materials & processes 149 (1996) 25-26.

[36]   P. Ray, P. Pal. High Speed Steel Semis--Alternate Production Routes. PM'90. PM Into the 1990's. International Conference on Powder Metallurgy., vol. 2, 1990. p.159-169.

[37]   A. Kasak, E. Dulis. Powder-metallurgy tool steels, Powder Metallurgy 21 (1978) 114-121.

[38]   D. Davies, A. Singer. Spray Forming by Centrifugal Spray Deposition, Advances in Powder Metallurgy & Particulate Materials--1992. 1 (1992) 301-317.

[39]   T. Itami, Y. Kawashima. The Production of Rolling Mill Rolls and High Speed Cutting Tools at Sumitomo Heavy Industries, *Spray Forming: Science, Technlogy, and Application*, Metal Powder Industries Federation (1992) 77-91.

[40]   W. Cai, E. Lavernia. Modeling of porosity during spray forming, Materials Science and Engineering: A 226 (1997) 8-12.

[41]   R.D. Payne, A.L. Moran, R.C. Cammarata. Relating porosity and mechanical properties in spray formed tubulars, Scripta Metallurgica et Materialia 29 (1993) 907-912.

[42]   C. Meyer, N. Ellendt, L. Mädler, H. Müller, F. Reimer, V. Uhlenwinkel. Spray forming of high density sheets, Materialwissenschaft und Werkstofftechnik 45 (2014) 642-651.

[43]   Spray forming bypasses PM for tool steels, Metal Powder Report 59 (2004) 20.

[44]   K. Hummert, B. Commandeur, A. Leatham, A. Ogilvy, W. Hunt Jr. High performance, low cost aluminium alloys manufactured by spray forming. Metal Powder Industries Federation, Proceedings of the Powder Metallurgy Aluminum & Light Alloys for Automotive Applications Conference(USA), 1998. p.107-114.

[45]   C. Cui, A. Schulz, J. Epp, H. Zoch. Deformation behavior of spray-formed hypereutectic Al–Si alloys, Journal of Materials Science 45 (2010) 2798-2807.

[46]   N. Ashgriz. Handbook of Atomization and Sprays: Theory and Applications, Springer, 2011.

[47]   U. Fritsching. Spray Simulation: Modeling and Numerical Simulation of Sprayforming metals, Cambridge University Press, 2004.

[48]   E.J. Lavernia, Y. Wu. Spray atomization and deposition, John Wiley, 1996.

[49]   U. Fritsching. Spray Simulation: Modeling and Numerical Simulation of Sprayforming Metals, Cambridge University Press, 2007.

[50]   B. Bewlay, B. Cantor. Modeling of spray deposition: measurements of particle size, gas velocity, particle velocity, and spray temperature in gas-atomized sprays, MTB 21 (1990) 899-912.

[51]   P. Grant, B. Cantor. Modelling of spray forming, Cast Metals 4 (1991) 140-151.

[52]   S. Connelly, J. Coombs, J. Medwell. Flow Characteristics of Metal Particles in Atomised Sprays, Met. Powder Rep. 41 (1986) 653.

[53]   E. Lavernia, E. Gutierrez, J. Szekely, N. Grant. A MATHEMATICAL-MODEL OF THE LIQUID DYNAMIC COMPACTION PROCESS. 1. HEAT-FLOW IN GAS ATOMIZATION, International Journal of Rapid Solidification 4 (1988) 89-124.

[54]   P. Mathur, D. Apelian, A. Lawley. Analysis of the spray deposition process, Acta Metallurgica 37 (1989) 429-443.

[55]   Fritsching, U., K. Bauckhage. Investigations on the atomization of molten metals: the coaxial jet and the gas flow in the nozzle near field, PHOENICS J. Comput. Fluid Dyn. 5 (1992) 81-98.

[56]   N. Dombrowski, W.R. Johns. The aerodynamic instability and disintegration of viscous liquid sheets, Chemical Engineering Science 18 (1963) 203-214.

[57]   Y. Wang, K.-S. Im, K. Fezzaa. Similarity between the Primary and Secondary Air-Assisted Liquid Jet Breakup Mechanisms, Physical Review Letters 100 (2008) 154502.

[58] P.S. Grant, B. Cantor, L. Katgerman. Modelling of droplet dynamic and thermal histories during spray forming—I. individual droplet behaviour, Acta Metallurgica et Materialia 41 (1993) 3097-3108.

[59] H. Lubanska. Correlation of spray ring data for gas atomization of liquid metals., Journal of Metals 22 (1970) 45-49.

[60] B.P. Bewlay, B. Cantor. The relationship between thermal history and microstructure in spray-deposited tin-lead alloys, Journal of Materials Research 6 (1991) 1433-1454.

[61] S. Annavarapu, D. Apelian, A. Lawley. Spray casting of steel strip: process analysis, MTA 21 (1990) 3237-3256.

[62] P. Grant, B. Cantor, L. Katgerman. Modelling of droplet dynamic and thermal histories during spray forming—II. Effect of process parameters, Acta Metallurgica et Materialia 41 (1993) 3109-3118.

[63] N.H. Pryds, J.H. Hattel, T.B. Pedersen, J. Thorborg. An integrated numerical model of the spray forming process, Acta Materialia 50 (2002) 4075-4091.

[64] J.H. Hattel, N.H. Pryds, J. Thorborg, P. Ottosen. A quasi-stationary numerical model of atomized metal droplets. I: Model formulation, Modelling and Simulation in Materials Science and Engineering 7 (1999) 413.

[65] N.H. Pryds, J.H. Hattel, J. Thorborg. A quasi-stationary numerical model of atomized metal droplets. II: Prediction and assessment, Modelling and Simulation in Materials Science and Engineering 7 (1999) 431.

[66] W.-D. Chen, Y.-H. Lin, C.-P. Chang, Y. Sung, Y.-M. Liu, M.-D. Ger. Fabrication of high-resolution conductive line via inkjet printing of nano-palladium catalyst onto PET substrate, Surface and Coatings Technology 205 (2011) 4750-4756.

[67] G.H. Geiger, D.R. Poirier. Transport phenomena in metallurgy, Addison-Wesley Pub. Co., 1973.

[68] R. Clift, J.R. Grace, M.E. Weber. Bubbles, Drops, and Particles, Dover Publications, 2013.

[69] D. Bergmann, U. Fritsching, K. Bauckhage. A mathematical model for cooling and rapid solidification of molten metal droplets, International Journal of Thermal Sciences 39 (2000) 53-62.

[70] H.-K. Seok, K.H. Oh, H.Y. Ra, D.-H. Yeo, H.-I. Lee. A three-dimensional model of the spray forming method, Metallurgical and Materials Transactions B 29 (1998) 699-708.

[71] R. Ristau, A. Becker, V. Uhlenwinkel, R. Kienzler. Simulations of Temperatures, Residual Stresses, and Porosity Measurements in Spray Formed Super Alloys Tubes. Superalloy 718 and Derivatives. John Wiley & Sons, Inc., 2010. pp. 470-485.

[72] C. Cui, U. Fritsching, A. Schulz, Q. Li. Mathematical modeling of spray forming process of tubular preforms: Part 1. Shape evolution, Acta Materialia 53 (2005) 2765-2774.

[73] Y. Lin, E. Lavernia, J. Bobrow, D. White. Modeling of spray-formed materials: Geometrical considerations, Metallurgical and Materials Transactions A 31 (2000) 2917-2929.

[74] S. Kang, D.-H. Chang. Modelling of billet shapes in spray forming using a scanning atomizer, Materials Science and Engineering: A 260 (1999) 161-169.

[75] F.S. Hill, S.M. Kelley. Computer Graphics: Using OpenGL, Pearson Prentice Hall, 2007.

[76] J.F. Hughes, A. Van Dam, J.D. Foley, S.K. Feiner. Computer Graphics: Principles and Practice, Addison-Wesley, 2013.

[77]   D. Ginsburg, B. Purnomo, D. Shreiner, A. Munshi. OpenGL ES 3.0 Programming Guide, Pearson Education, 2014.

[78]   S. Annavarapu, R. Doherty, D. Apelian, A. Lawley, P. Mathur. Fundamental aspects of consolidation and microstructure development during spray casting. The First International Conference on Spray Forming, 1990.

[79]   J. Tillwick, V. Uhlenwinkel, K. Bauckhage. Analysis of the spray forming process using backscattering phase-Doppler anemometry, International journal of heat and fluid flow 20 (1999) 530-537.

[80]   Z. Djuric, P. Grant. Two-dimensional simulation of liquid metal spray deposition onto a complex surface: II. Splashing and redeposition, Modelling and Simulation in Materials Science and Engineering 9 (2001) 111.

[81]   Z. Djuric, P. Newbery, P. Grant. Two-dimensional simulation of liquid metal spray deposition onto a complex surface, Modelling and Simulation in Materials Science and Engineering 7 (1999) 553.

[82]   J. Mi, P.S. Grant. Modelling the shape and thermal dynamics of Ni superalloy rings during spray forming Part 1: Shape modelling - Droplet deposition, splashing and redeposition, Acta Materialia 56 (2008) 1588-1596.

[83]   P. Mathur, S. Annavarapu, D. Apelian, A. Lawley. Spray casting: an integral model for process understanding and control, Materials Science and Engineering: A 142 (1991) 261-276.

[84]   C. Kramer, V. Uhlenwinkel, K. Bauckhage. The sticking efficiency at the spray forming of metals. In: Wood J, (Ed.). The Third International Conference on Spray Forming. Cardiff, 1996. p.273.

[85]   D. Spencer, R. Mehrabian, M.C. Flemings. Rheological behavior of Sn-15 pct Pb in the crystallization range, MT 3 (1972) 1925-1932.

[86]   W. Cai, E.J. Lavernia. Modeling of porosity during spray forming: Part I. Effects of processing parameters, Metallurgical and Materials Transactions B 29 (1998) 1085-1096.

[87]   W. Cai, E.J. Lavernia. Modeling of porosity during spray forming: Part II. Effects of atomization gas chemistry and alloy compositions, Metallurgical and Materials Transactions B 29 (1998) 1097-1106.

[88]   X. Liang, J. Earthman, E. Lavernia. On the mechanism of grain formation during spray atomization and deposition, Acta Metallurgica et Materialia 40 (1992) 3003-3016.

[89]   O. Meyer, U. Fritsching, K. Bauckhage. Numerical investigation of alternative process conditions for influencing the thermal history of spray deposited billets, International Journal of Thermal Sciences 42 (2003) 153-168.

[90]   M. Buchholz, V. Uhlenwinkel, N. Ellendt. The Effect of Deposit Temperature on the Sticking Efficiency During Spray Forming. Proc. Int. Conf. on Spray Forming, Baltimore, USA, 1999.

[91]   K. Mingard, P. Alexander, S. Langridge, G. Tomlinson, B. Cantor. Direct measurement of sprayform temperatures and the effect of liquid fraction on microstructure, Acta Materialia 46 (1998) 3511-3521.

[92]   O. Meyer, A. Schneider, V. Uhlenwinkel, U. Fritsching. Convective heat transfer from a billet due to an oblique impinging circular jet within the spray forming process, International Journal of Thermal Sciences 42 (2003) 561-569.

[93]   C. Cui, U. Fritsching, A. Schulz, K. Bauckhage, P. Mayr. Control of cooling during spray forming of bearing steel billets, Materials Science and Engineering: A 383 (2004) 158-165.

[94] C. Cui, U. Fritsching, A. Schulz, R. Tinscher, K. Bauckhage, P. Mayr. Spray forming of homogeneous 100Cr6 bearing steel billets, Journal of Materials Processing Technology 168 (2005) 496-504.

[95] C. Cui, U. Fritsching, A. Schulz, Q. Li. Mathematical modeling of spray forming process of tubular preforms: Part 2. Heat transfer, Acta Materialia 53 (2005) 2775-2784.

[96] J. Mi, P.S. Grant. Modelling the shape and thermal dynamics of Ni superalloy rings during spray forming. Part 2: Thermal modelling - Heat flow and solidification, Acta Materialia 56 (2008) 1597-1608.

[97] Y. Lin, K.M. McHugh, Y. Zhou, E.J. Lavernia. Modeling the spray forming of H13 steel tooling, Metallurgical and Materials Transactions A 38 (2007) 1632-1637.

[98] M.J. Baines. Moving finite elements, Oxford University Press, Inc., 1994.

[99] M. Baines, M. Hubbard, P. Jimack. A moving mesh finite element algorithm for the adaptive solution of time-dependent partial differential equations with moving boundaries, Applied Numerical Mathematics 54 (2005) 450-469.

[100] B.N. Azarenok, T. Tang. Second-order Godunov-type scheme for reactive flow calculations on moving meshes, Journal of Computational Physics 206 (2005) 48-80.

[101] M. Baines, M. Hubbard, P. Jimack. A moving mesh finite element algorithm for fluid flow problems with moving boundaries, International journal for numerical methods in fluids 47 (2005) 1077-1083.

[102] G. Beckett, J.A. Mackenzie, M. Robertson. A moving mesh finite element method for the solution of two-dimensional Stefan problems, Journal of Computational Physics 168 (2001) 500-518.

[103] W. Cao, W. Huang, R.D. Russell. Anr-adaptive finite element method based upon moving mesh PDEs, Journal of Computational Physics 149 (1999) 221-244.

[104] COMSOL. Sloshing Tank. vol. 2015, 2015.

[105] W. Cao, W. Huang, R.D. Russell. A moving mesh method based on the geometric conservation law, SIAM Journal on Scientific Computing 24 (2002) 118-142.

[106] M. Baines, M. Hubbard, P. Jimack, R. Mahmood. A moving-mesh finite element method and its application to the numerical solution of phase-change problems, Communications in Computational Physics 6 (2009) 595-624.

[107] E. Sparrow, C. Altemani, A. Chaboki. Jet-impingement heat transfer for a circular jet impinging in crossflow on a cylinder, Journal of Heat Transfer 106 (1984) 570-577.

[108] A. Tawfek. Heat transfer due to a round jet impinging normal to a circular cylinder, Heat and mass transfer 35 (1999) 327-333.

[109] C. Cui, A. Schulz, K. Schimanski, H.-W. Zoch. Spray forming of hypereutectic Al–Si alloys, Journal of Materials Processing Technology 209 (2009) 5220-5228.

[110] P. Grant, W. Kim, B. Cantor. Spray forming of aluminium-copper alloys, Materials Science and Engineering: A 134 (1991) 1111-1114.

[111] M. Gupta, F. Mohamed, E. Lavernia. The Effect of ceramic reinforcements during spray atomization and codeposition of metal matrix composites: part i. heat transfer, MTA 23 (1992) 831-843.

[112] S. Annavarapu, R. Doherty. Evolution of microstructure in spray casting, International journal of powder metallurgy 29 (1993) 331-343.

[113] H. Hu, E.J. Lavernia, Z.H. Lee, D.R. White. On the evolution of porosity in spray-deposited tool steels, Metallurgical and Materials Transactions A 31 (2000) 725-735.

[114] K.Y. Sastry, L. Froyen, J. Vleugels, E.H. Bentefour, C. Glorieux. Effect of porosity on thermal conductivity of Al–Si–Fe–X alloy powder compacts, International journal of thermophysics 25 (2004) 1611-1622.

[115] P. Liu, T. Li, C. Fu. Relationship between electrical resistivity and porosity for porous metals, Materials Science and Engineering: A 268 (1999) 208-215.

[116] N. Ellendt, O. Stelling, V. Uhlenwinkel, A. von Hehl, P. Krug. Influence of spray forming process parameters on the microstructure and porosity of Mg2Si rich aluminum alloys. Einfluss der Prozessparameter auf Mikrostruktur und Porosität beim Sprühkompaktieren von Aluminium-Legierungen mit hohen Mg2Si–Gehalten, Materialwissenschaft und Werkstofftechnik 41 (2010) 532-540.

[117] N. Ellendt, V. Uhlenwinkel, L. Mädler. High yield spray forming of small diameter tubes using pressure-gas-atomization, Materialwissenschaft und Werkstofftechnik 45 (2014) 699-707.

[118] G. Watson. Thermal and microstructural characterization of spray cast copper alloy strip. Proceedings of the First International Conference on Spray Forming, 17th% 19th September, 1990.

[119] L. Achelis, V. Uhlenwinkel, R. Ristau, P. Krug. Transient temperatures and microstructure of spray formed aluminium alloy Al-Si sheets. Transiente Temperaturen und Mikrostruktur von sprühkompaktierten Al-Si-Flachprodukten, Materialwissenschaft und Werkstofftechnik 41 (2010) 498-503.

[120] L. Warner, C. Cai, S. Annavarapu, R. Doherty. Modelling Microstructural Development in Spray Forming: Experimental Verification, Powder Metallurgy 40 (1997) 121-125.

[121] M. Walter, M. Stockinger, J. Tockner, N. Ellendt, V. Uhlenwinkel. Spray forming and post processing of superalloy rings, Superalloys 718, 625, 706 and Derivatives (2006) 429-440.

[122] A. Simchi. Direct laser sintering of metal powders: Mechanism, kinetics and microstructural features, Materials Science and Engineering: A 428 (2006) 148-158.

[123] P. Grant. Solidification in spray forming, Metallurgical and Materials Transactions A 38 (2007) 1520-1529.

[124] S. Das, J.J. Beama, M. Wohlert, D.L. Bourell. Direct laser freeform fabrication of high performance metal components, Rapid Prototyping Journal 4 (1998) 112-117.

[125] X. Liang, E.J. Lavernia. On the dendrite-equiaxed grain transition in atomized Ni3Al powders, Scripta Metallurgica et Materialia 25 (1991) 1199-1204.

[126] E.-S. Lee, W.-J. Park, J.Y. Jung, S. Ahn. Solidification microstructure and M2C carbide decomposition in a spray-formed high-speed steel, Metallurgical and Materials Transactions A 29 (1998) 1395-1404.

[127] X. Liang, E.J. Lavernia. Evolution of interaction domain microstructure during spray deposition, Metallurgical and Materials Transactions A 25 (1994) 2341-2355.

[128] A. Simchi, H. Pohl. Effects of laser sintering processing parameters on the microstructure and densification of iron powder, Materials Science and Engineering: A 359 (2003) 119-128.

[129] L.E. Murr, E. Martinez, X.M. Pan, S.M. Gaytan, J.A. Castro, C.A. Terrazas, F. Medina, R.B. Wicker, D.H. Abbott. Microstructures of Rene 142

nickel-based superalloy fabricated by electron beam melting, Acta Materialia 61 (2013) 4289-4296.

[130] K. Amato, S. Gaytan, L. Murr, E. Martinez, P. Shindo, J. Hernandez, S. Collins, F. Medina. Microstructures and mechanical behavior of Inconel 718 fabricated by selective laser melting, Acta Materialia 60 (2012) 2229-2239.

[131] Y. Wu, W.A. Cassada, E.J. Lavernia. Microstructure and mechanical properties of spray-deposited Al-17Si-4.5 Cu-0.6 Mg wrought alloy, Metallurgical and Materials Transactions A 26 (1995) 1235-1247.

[132] X. Liang, E. Lavernia. Evolution of interaction domain microstructure during spray deposition, Metallurgical and Materials Transactions A 25 (1994) 2341-2355.

[133] Y. Zhang, Z. Guo, G. Zhang, J. Mi, P.S. Grant. Modelling and experiments concerning dendrite re-melting and its role in microstructural evolution in spray formed Ni superalloys. Materials Science Forum, vol. 654-656, 2010. p.1363-1366.

[134] X. Liang, J.C. Earthman, E.J. Lavernia. On the mechanism of grain formation during spray atomization and deposition, Acta Metallurgica et Materialia 40 (1992) 3003-3016.

[135] E.D. Manson-Whitton, I.C. Stone, J.R. Jones, P.S. Grant, B. Cantor. Isothermal grain coarsening of spray formed alloys in the semi-solid state, Acta Materialia 50 (2002) 2517-2535.

[136] E. Tzimas, A. Zavaliangos. Evolution of near-equiaxed microstructure in the semisolid state, Materials Science and Engineering: A 289 (2000) 228-240.

[137] N.E. Glover, C.L. Davis. Thermal cycle simulation of a Ni-base superalloy, Scripta Materialia 34 (1996) 675-684.

[138] Y. Zhang, N. Liu, Z. Li, G. Zhang, H. Yuan, W. Xu, Z. Gao, J. Mi. Gleeble experiments concerning dendrite re-melting and its role in microstructural evolution in spray formed high-alloy metals, Rare Metals 30 (2011) 401-404.

[139] S. Annavarapu, R. Doherty. Inhibited coarsening of solid-liquid microstructures in spray casting at high volume fractions of solid, Acta Metallurgica et Materialia 43 (1995) 3207-3230.

[140] E. Manson-Whitton, I. Stone, J. Jones, P. Grant, B. Cantor. Isothermal grain coarsening of spray formed alloys in the semi-solid state, Acta Materialia 50 (2002) 2517-2535.

[141] P. Kjeldsteen, C. Spiegelhauer, O. Sandberg. Investigation of the homogeneity of a spray formed tool steel billet. In: Bauckhage K, (Ed.). 2nd International Conference on Spray Deposition and Melt Atomization, vol. 1. Bremen, Germany, 2003.

[142] R.A. Mesquita, C.A. Barbosa. Spray forming high speed steel—properties and processing, Materials Science and Engineering: A 383 (2004) 87-95.

[143] Y. Tsui, S. Howard, T. Clyne. The effect of residual stresses on the debonding of coatings—II. An experimental study of a thermally sprayed system, Acta Metallurgica et Materialia 42 (1994) 2837-2844.

[144] S. Howard, Y. Tsui, T. Clyne. The effect of residual stresses on the debonding of coatings—I. A model for delamination at a bimaterial interface, Acta Metallurgica et Materialia 42 (1994) 2823-2836.

[145] R.T.R. McGrann, D.J. Greving, J.R. Shadley, E.F. Rybicki, T.L. Kruecke, B.E. Bodger. The effect of coating residual stress on the fatigue life of thermal spray-coated steel and aluminum, Surface and Coatings Technology 108–109 (1998) 59-64.

[146] S. Ho, E. Lavernia. The effect of ceramic reinforcement on residual stresses during spray atomization and co-deposition of metal matrix composites, Scripta Materialia 34 (1996) 1911-1918.

[147] S. Ho, E. Lavernia. Thermal residual stresses in functionally graded and layered 6061 Al/SiC materials, Metallurgical and Materials Transactions A 27 (1996) 3241-3249.

[148] S. Ho, E.J. Lavernia. Thermal residual stresses in spray atomized and deposited Ni3Al, Scripta Materialia 34 (1996) 527-536.

[149] H.M. Hu, E.J. Lavernia, Z.H. Lee, D.R. White. Residual stresses in spray-formed A2 tool steel, Journal of Materials Research 14 (1999) 4521-4530.

[150] P. Grant, B. Cantor. Modelling of droplet dynamic and thermal histories during spray forming—III. Analysis of spray solid fraction, Acta Metallurgica et Materialia 43 (1995) 913-921.

[151] T.L. Lee, J. Mi, S.L. Zhao, J.F. Fan, S.Y. Zhang, S. Kabra, P.S. Grant. Characterization of the residual stresses in spray-formed steels using neutron diffraction, Scripta Materialia 100 (2015) 82-85.

[152] D.S. Kupperman, S. Majumdar, J.P. Singh, A. Saigal. Application of Neutron Diffraction Time-of-Flight Measurements to the Study of Strain in Composites. in: Hutchings M, Krawitz A, (Eds.). Measurement of Residual and Applied Stress Using Neutron Diffraction, vol. 216. Springer Netherlands, 1992. pp. 439-450.

[153] J.R. Santisteban, M.R. Daymond, J.A. James, L. Edwards. ENGIN-X: A third-generation neutron strain scanner, Journal of Applied Crystallography 39 (2006) 812-825.

[154] P. Withers, H. Bhadeshia. Residual stress. Part 1–measurement techniques, Materials Science and Technology 17 (2001) 355-365.

[155] W. Reimers, A.R. Pyzalla, A.K. Schreyer, H. Clemens. Neutrons and Synchrotron Radiation in Engineering Materials Science: From Fundamentals to Material and Component Characterization, John Wiley & Sons, 2008.

[156] P.J. Withers. Residual stresses: measurement by diffraction. In: Buschow KHJ, (Ed.). Encyclopedia of materials: science and technology. Oxford: Elsevier, 2001. p.8158-8170.

[157] T. Clyne, S. Gill. Residual Stresses in Thermal Spray Coatings and Their Effect on Interfacial Adhesion: A Review of Recent Work, Journal of Thermal Spray Technology 5 (1996) 401-418.

[158] S. Kuroda, T. Fukushima, S. Kitahara. Insitu measurement of coating thickness during thermal spraying using an optical displacement meter, Journal of Vacuum Science & Technology A 5 (1987) 82-87.

[159] G.G. Stoney. The tension of metallic films deposited by electrolysis, Proceedings of the Royal Society of London. Series A, Containing Papers of a Mathematical and Physical Character 82 (1909) 172-175.

[160] G.C.A.M. Janssen, M.M. Abdalla, F. van Keulen, B.R. Pujada, B. van Venrooy. Celebrating the 100th anniversary of the Stoney equation for film stress: Developments from polycrystalline steel strips to single crystal silicon wafers, Thin Solid Films 517 (2009) 1858-1867.

[161] K. Sasaki, M. Kishida, T. Itoh. The accuracy of residual stress measurement by the hole-drilling method, Experimental Mechanics 37 (1997) 250-257.

[162] G.S. Schajer, M. Tootoonian. A new rosette design for more reliable hole-drilling residual stress measurements, Experimental Mechanics 37 (1997) 299-306.

[163] P.J. Withers. Neutron strain measurement of internal strain in metal and ceramic matrix composites. Key Engineering Materials, vol. 108: Trans Tech Publ, 1995. p.291-314.

[164] R. Pynn. Neutron scattering: a primer, Los Alamos Science 19 (1990) 1-31.

[165] B.D. Cullity. Elements of X-ray Diffraction, Addison-Wesley Publishing Company, 1978.

[166] P. Withers, P. Webster. Neutron and synchrotron x-ray strain scanning, Strain 37 (2001) 19-33.

[167] M.R. Daymond, P.J. Withers. A synchrotron radiation study of transient internal strain changes during the early stages of thermal cycling in an Al / SiCw MMC, Scripta Materialia 35 (1996) 1229-1234.

[168] T.L. Lee, J.C. Khong, K. Fezzaa, J.W. Mi. Ultrafast X-ray imaging and modelling of ultrasonic cavitations in liquid metal. Materials Science Forum, vol. 765: Trans Tech Publ, 2013. p.190-194.

[169] D.Y. Tan, J.W. Mi. High Speed Imaging Study of the Dynamics of Ultrasonic Bubbles at a Liquid-Solid Interface. Materials Science Forum, vol. 765: Trans Tech Publ, 2013. p.230-234.

[170] J. Mi, D. Tan, T.L. Lee. In Situ Synchrotron X-ray Study of Ultrasound Cavitation and Its Effect on Solidification Microstructures, Metallurgical and Materials Transactions B (2014) 1-5.

[171] D. Tan, T.L. Lee, J.C. Khong, T. Connolley, K. Fezzaa, J. Mi. High-Speed Synchrotron X-ray Imaging Studies of the Ultrasound Shockwave and Enhanced Flow during Metal Solidification Processes, Metallurgical and Materials Transactions A (2015) 1-11.

[172] P.J. Withers. Depth capabilities of neutron and synchrotron diffraction strain measurement instruments. I. The maximum feasible path length, Journal of Applied Crystallography 37 (2004) 596-606.

[173] R. Pynn. LECTURE 1: Introduction & Neutron Scattering "Theory", Los Alamos Neutron Science Center, Los Alamos Science (1989).

[174] L. Van Hove. Correlations in space and time and Born approximation scattering in systems of interacting particles, Physical Review 95 (1954) 249.

[175] W.L. Bragg. The diffraction of short electromagnetic waves by a crystal. Proceedings of the Cambridge Philosophical Society, vol. 17, 1913. p.4.

[176] K. Andersen. Reactor & Spallation Neutron Sources. Oxford School of Neutron Scattering, 2013.

[177] J. Hsieh. Computed tomography: principles, design, artifacts, and recent advances. SPIE Bellingham, WA, 2009.

[178] G.T. Herman. Fundamentals of Computerized Tomography: Image Reconstruction from Projections, Springer, 2009.

[179] E.N. Landis, D.T. Keane. X-ray microtomography, Materials Characterization 61 (2010) 1305-1316.

[180] J.H. Kinney, M.C. Nichols. X-Ray Tomographic Microscopy (XTM) Using Synchrotron Radiation, Annual Review of Materials Science 22 (1992) 121-152.

[181] J. Radon. On the determination of functions from their integral values along certain manifolds, Medical Imaging, IEEE Transactions on 5 (1986) 170-176.

[182] J. Cockcroft, S. Jacques. Production of Spallation Neutrons.

[183] R. Williamson. Introduction to the ISIS Accelerator and Targets.

[184] ASTM. E290-09, "Standard Test Methods for Bend Testing of Material for Ductility" ASTM International, West Conshohocken, PA.

[185] P.J. Withers, M. Preuss, A. Steuwer, J.W.L. Pang. Methods for obtaining the strain-free lattice parameter when using diffraction to determine residual stress, Journal of Applied Crystallography 40 (2007) 891-904.

[186] H. Rietveld. A profile refinement method for nuclear and magnetic structures, Journal of Applied Crystallography 2 (1969) 65-71.

[187] M.R. Daymond, M.A.M. Bourke, R.B. Von Dreele, B. Clausen, T. Lorentzen. Use of Rietveld refinement for elastic macrostrain determination and for evaluation of plastic strain history from diffraction spectra, Journal of Applied Physics 82 (1997) 1554-1562.

[188] A.C. Larson, R.B.V. Dreele. General Structure Analysis System (GSAS). Los Alamos National Laboratory Report LAUR 86-748, 2004.

[189] R.J. Hill, C.J. Howard. Quantitative phase analysis from neutron powder diffraction data using the Rietveld method, Journal of Applied Crystallography 20 (1987) 467-474.

[190] M.T. Hutchings, A.D. Krawitz. Measurement of Residual and Applied Stress Using Neutron Diffraction, Kluwer Academic, 1992.

[191] J. Lu. Handbook of Measurement of Residual Stresses, Fairmont Press, 1996.

[192] F. Yan, Z. Xu, H. Shi, J. Fan. Microstructure of the spray formed Vanadis 4 steel and its ultrafine structure, Materials Characterization 59 (2008) 592-597.

[193] D. Yu, K. An, Y. Chen, X. Chen. Revealing the cyclic hardening mechanism of an austenitic stainless steel by real-time in situ neutron diffraction, Scripta Materialia 89 (2014) 45-48.

[194] http://www.matweb.com/.

[195] P.J. Withers, M.W. Johnson, J.S. Wright. Neutron strain scanning using a radially collimated diffracted beam, Physica B: Condensed Matter 292 (2000) 273-285.

[196] S. Spooner, X.-L. Wang. Diffraction peak displacement in residual stress samples due to partial burial of the sampling volume, Journal of Applied Crystallography 30 (1997) 449-455.

[197] L. Lutterotti, M. Bortolotti, G. Ischia, I. Lonardelli, H.-R. Wenk. Rietveld texture analysis from diffraction images, Zeitschrift für Kristallographie Supplements (2007).

[198] I. Lonardelli, H.-R. Wenk, L. Lutterotti, M. Goodwin. Texture analysis from synchrotron diffraction images with the Rietveld method: dinosaur tendon and salmon scale, Journal of synchrotron radiation 12 (2005) 354-360.

[199] L. Lutterotti, D. Chateigner, S. Ferrari, J. Ricote. Texture, residual stress and structural analysis of thin films using a combined X-ray analysis, Thin Solid Films 450 (2004) 34-41.

[200] S. Matthies, H.-R. Wenk, G. Vinel. Some basic concepts of texture analysis and comparison of three methods to calculate orientation distributions from pole figures, Journal of Applied Crystallography 21 (1988) 285-304.

[201] S. Matthies, G. Vinel. On the reproduction of the orientation distribution function of texturized samples from reduced pole figures using the conception of a conditional ghost correction, physica status solidi (b) 112 (1982) K111-K114.

[202] G. Zhang, H. Yuan, D. Jiao, Z. Li, Y. Zhang, Z. Liu. Microstructure evolution and mechanical properties of T15 high speed steel prepared by twin-atomiser spray forming and thermo-mechanical processing, Materials Science and Engineering A 558 (2012) 566-571.

[203] S. Middleman. An Introduction to Fluid Dynamics: Principles of Analysis and Design, Wiley, 1998.

[204] J. Mi, P.S. Grant, U. Fritsching, O. Belkessam, I. Garmendia, A. Landaberea. Multiphysics modelling of the spray forming process, Materials Science and Engineering: A 477 (2008) 2-8.

[205] G. Gu, R. Pesci, L. Langlois, E. Becker, R. Bigot. Microstructure investigation and flow behavior during thixoextrusion of M2 steel grade, Journal of Materials Processing Technology 216 (2015) 178-187.

[206] W.J. Park, E.S. Lee, S.H. Ahn. High speed tool steel, and manufacturing method therefor. US Patent 5976277 A, 1999.

[207] T. Fujii, D.R. Poirier, M.C. Flemings. Macrosegregation in a multicomponent low alloy steel, MTB 10 (1979) 331-339.

[208] J. Bird. Electrical and Electronic Principles and Technology, Taylor & Francis, 2010.

[209] V. Rudnev, D. Loveless, R.L. Cook, M. Black. Handbook of Induction Heating, CRC Press, 2002.

[210] T. Lennon. Designers' Guide to EN 1991-1-2, EN 1993-1-2 and EN 1994-1-2: Handbook for the Fire Design of Steel, Composite and Concrete Structures to the Eurocodes, Thomas Telford, 2007.

[211] E.A. Brandes, G.B. Brook, C.J. Smithells. Smithells metals reference book, Butterworth-Heinemann, 1998.

[212] D. Bergmann, U. Fritsching, C. Crowe. Multiphase Flows in the Spray Forming Process. Proc. 2nd Int. Conf Multiphase Flow, Kyoto, Japan, 1995. p.3-7.

[213] F. Bay, V. Labbé, Y. Favennec, J.-L. Chenot. A numerical model for induction heating processes coupling electromagnetism and thermomechanics, International journal for numerical methods in engineering 58 (2003) 839-867.

[214] COMSOL. Inductive Heating of Copper Cylinder. vol. 2015, 2015.

[215] COMSOL. Comsol Multiphysics Reference Manual. Version, 2014.

[216] D. Koistinen, R. Marburger. A general equation prescribing the extent of the austenite-martensite transformation in pure iron-carbon alloys and plain carbon steels, Acta Metallurgica 7 (1959) 59-60.

[217] H.G. Nanesa, M. Jahazi, R. Naraghi. Martensitic transformation in AISI D2 tool steel during continuous cooling to 173 K, Journal of Materials Science (2015) 1-11.

[218] J. Chen, B. Young, B. Uy. Behavior of high strength structural steel at elevated temperatures, Journal of Structural Engineering 132 (2006) 1948-1954.

[219] P. Brøndsted, P. Skov-Hansen. Fatigue properties of high-strength materials used in cold-forging tools, International journal of fatigue 20 (1998) 373-381.

[220] A.H. Grobe, G.A. Roberts. The Bend Test for Hardened High Speed Steel, Transactions ASM 40 (1948) 435-490.

[221] T. Nicholas. Dynamic tensile testing of structural materials using a split Hopkinson bar apparatus. DTIC Document, 1980.

[222] N. Chawla, X. Deng. Microstructure and mechanical behavior of porous sintered steels, Materials Science and Engineering A 390 (2005) 98-112.

[223] J. Kováčik. Correlation between Poisson's ratio and porosity in porous materials, Journal of Materials Science 41 (2006) 1247-1249.

[224] N. Ramakrishnan, V.S. Arunachalam. Effective elastic moduli of porous ceramic materials, Journal of the American Ceramic Society 76 (1993) 2745-2752.

[225] H.C. Fiedler, T.F. Sawyer, R.W. Kopp, A.G. Leatham. The Spray Forming of Superalloys, JOM 39 (1987) 28-33.

[226] S. Annavarapu, D. Apelian, A. Lawley. Processing effects in spray casting of steel strip, MTA 19 (1988) 3077-3086.

[227] H.F. Fischmeister, R. Riedl, S. Karagöz. Solidification of high-speed tool steels, MTA 20 (1989) 2133-2148.

[228] R.H. Barkalow, R.W. Kraft, J.I. Goldstein. Solidification of M2 high speed steel, MT 3 (1972) 919-926.

[229] M. Boccalini, H. Goldenstein. Solidification of high speed steels, International Materials Reviews 46 (2001) 92-115.

[230] E.S. Lee, W.J. Park, K.H. Baik, S. Ahn. Different carbide types and their effect on bend properties of a spray-formed high speed steel, Scripta Materialia 39 (1998) 1133-1138.

[231] S. Karagöz, I. Liem, E. Bischoff, H.F. Fischmeister. Determination of carbide and matrix compositions in high-speed steels by analytical electron microscopy, Metallurgical and Materials Transactions A 20 (1989) 2695-2701.

[232] R.A. Mesquita, C.A. Barbosa. High-speed steels produced by conventional casting, spray forming and powder metallurgy. Materials science forum, vol. 498: Trans Tech Publ, 2005. p.244-250.

[233] X. Jiang, J. Matejicek, S. Sampath. Substrate temperature effects on the splat formation, microstructure development and properties of plasma sprayed coatings: Part II: case study for molybdenum, Materials Science and Engineering: A 272 (1999) 189-198.

[234] J. Matejicek, S. Sampath, D. Gilmore, R. Neiser. In situ measurement of residual stresses and elastic moduli in thermal sprayed coatings: Part 2: processing effects on properties of Mo coatings, Acta Materialia 51 (2003) 873-885.

[235] J. Matejicek, S. Sampath, P. Brand, H. Prask. Quenching, thermal and residual stress in plasma sprayed deposits: NiCrAlY and YSZ coatings, Acta Materialia 47 (1999) 607-617.

[236] J.-P. Delplanque, R. Rangel. A comparison of models, numerical simulation, and experimental results in droplet deposition processes, Acta Materialia 46 (1998) 4925-4933.

[237] A. Newbery, P. Grant. Droplet splashing during arc spraying of steel and the effect on deposit microstructure, Journal of Thermal Spray Technology 9 (2000) 250-258.

[238] A. Simchi, D. Godlinski. Effect of SiC particles on the laser sintering of Al–7Si–0.3 Mg alloy, Scripta Materialia 59 (2008) 199-202.

[239] R.C. Reed. The Superalloys: Fundamentals and Applications, Cambridge University Press, 2006.

[240] J.-H. Han, D.-Y. Kim. Analysis of the proportionality constant correlating the mean intercept length to the average grain size, Acta Metallurgica et Materialia 43 (1995) 3185-3188.

[241] R.L. Fullman. Measurement of particle sizes in opaque bodies, J. Metals 5 (1953) 447-452.

[242] D. Basak, R. Overfelt, D. Wang. Measurement of specific heat capacity and electrical resistivity of industrial alloys using pulse heating techniques, International journal of thermophysics 24 (2003) 1721-1733.

[243] C.Y. Ho, T. Chu. Electrical resistivity and thermal conductivity of nine selected AISI stainless steels. DTIC Document, 1977.

[244] http://www.goodfellow.com/.

[245] P. Grootenhuis, R.W. Powell, R.P. Tye. Thermal and Electrical Conductivity of Porous Metals made by Powder Metallurgy Methods, Proceedings of the Physical Society. Section B 65 (1952) 502.

[246] J. Francl, W. Kingery. Thermal conductivity: IX, Experimental investigation of effect of porosity on thermal conductivity, Journal of the American Ceramic Society 37 (1954) 99-107.

[247] P. Quested, K. Mills, R. Brooks, A. Day, R. Taylor, H. Szelagowski. Physical property measurement for simulation modelling of heat and fluid flow during solidification. In: Mitchell A, Auburtin P, (Eds.). Proceedings of the 1997 international symposium on liquid metal processing and casting. Sante Fe, 1997. p.1-17.

[248] H. Ding, Y.C. Shin. Improvement of machinability of Waspaloy via laser-assisted machining, The International Journal of Advanced Manufacturing Technology 64 (2013) 475-486.

[249] C. Jeanfils, J. Chen, H. Klein. Modeling of Macrosegregation in Electroslag Remelting of Superalloys, Superalloys 1980   119.

[250] D. Peckner, I.M. Bernstein. Handbook of stainless steels, McGraw-Hill New York, NY, 1977.

[251] A.M. Ritter, M.F. Henry. Precipitation in an as-atomized nickel-based superalloy powder, Journal of Materials Science 17 (1982) 73-80.

[252] X. Pierron, A. Banik, G. Maurer, J. Lemsky, D. Furrer, S. Jain. Sub-solidus HIP process for P/M superalloy conventional billet conversion, Pollock TM, Kissinger RD, Bowman, et al. Superalloys (2000) 425-433.

[253] J. Radavich. The physical metallurgy of cast and wrought alloy 718. In: Loria E, (Ed.). Superalloys 718—Metallurgy and Applications. Warrendale, PA: TMS, 1989. p.229-240.

[254] L.L. Parimi, R.G. A, D. Clark, M.M. Attallah. Microstructural and texture development in direct laser fabricated IN718, Materials Characterization 89 (2014) 102-111.

[255] L. Zheng, G. Zhang, T.L. Lee, M.J. Gorley, Y. Wang, C. Xiao, Z. Li. The effects of Ta on the stress rupture properties and microstructural stability of a novel Ni-base superalloy for land-based high temperature applications, Materials & Design 61 (2014) 61-69.

[256] H. Qi, M. Azer, A. Ritter. Studies of Standard Heat Treatment Effects on Microstructure and Mechanical Properties of Laser Net Shape Manufactured INCONEL 718, Metallurgical and Materials Transactions A 40 (2009) 2410-2422.

[257] J. Gere, B. Goodno. Mechanics of Materials, SI Edition, Cengage Learning, 2012.

[258] L. Costa, R. Vilar, T. Reti, A. Deus. Rapid tooling by laser powder deposition: Process simulation using finite element analysis, Acta Materialia 53 (2005) 3987-3999.

[259] R. Colaco, R. Vilar. Effect of laser surface melting on the tempering behaviour of DIN X42Cr13 stainless tool steel, Scripta Materialia 38 (1997) 107-113.

[260] L. Engel, H. Klingele. An atlas of metal damage, Wolfe Publishing Ltd. (1981) 271.

[261] M. Croft, V. Shukla, E. Akdoğan, N. Jisrawi, Z. Zhong, R. Sadangi, A. Ignatov, L. Balarinni, K. Horvath, T. Tsakalakos. In situ strain profiling of elastoplastic bending in Ti–6Al–4V alloy by synchrotron energy dispersive x-ray diffraction, Journal of Applied Physics 105 (2009) 093505.

[262] H. Van Swygenhoven, S. Van Petegem. In-situ mechanical testing during X-ray diffraction, Materials Characterization 78 (2013) 47-59.

[263] B. Clausen, T. Lorentzen, T. Leffers. Self-consistent modelling of the plastic deformation of fcc polycrystals and its implications for diffraction measurements of internal stresses, Acta Materialia 46 (1998) 3087-3098.

[264] K. Spencer, J.D. Embury, K.T. Conlon, M. Véron, Y. Bréchet. Strengthening via the formation of strain-induced martensite in stainless steels, Materials Science and Engineering: A 387–389 (2004) 873-881.

[265] M. Daymond, C. Tomé, M. Bourke. Measured and predicted intergranular strains in textured austenitic steel, Acta Materialia 48 (2000) 553-564.

[266] J. Pang, T. Holden, J. Wright, T. Mason. The generation of intergranular strains in 309H stainless steel under uniaxial loading, Acta Materialia 48 (2000) 1131-1140.

[267] N. Jia, Z.H. Cong, X. Sun, S. Cheng, Z.H. Nie, Y. Ren, P.K. Liaw, Y.D. Wang. An in situ high-energy X-ray diffraction study of micromechanical behavior of multiple phases in advanced high-strength steels, Acta Materialia 57 (2009) 3965-3977.

[268] I. Ahmed. The Influence of Material Factors, Including Cold Work on the Susceptibility of Stainless Steels to Stress Corrosion Cracking. PhD Thesis: University of Manchester, 2011.

Appendix 1 : Bend test rig design

Bend test rig assembly view

ITEM NO.	PART NUMBER	QTY.
1	Base	1
2	Adapter	1
3	Support	2
4	Positioner	2
5	Crosshead Adapter	1
6	Crosshead	1
7	Pin 15mm	1

Rig_Assembly

Bend test rig base

Ø51 Ø50 Ø22 4 x R6.50

120
112
99
72.50
60
47.50
21
8

40
120
200
240

Ø51
10
50
25
5
Ø50

ALL DIMENSIONS ARE IN MILLIMETRES

Bend test rig base adapter

R25

84

50

35

23

M20 x 2.5

M20 x 2.5
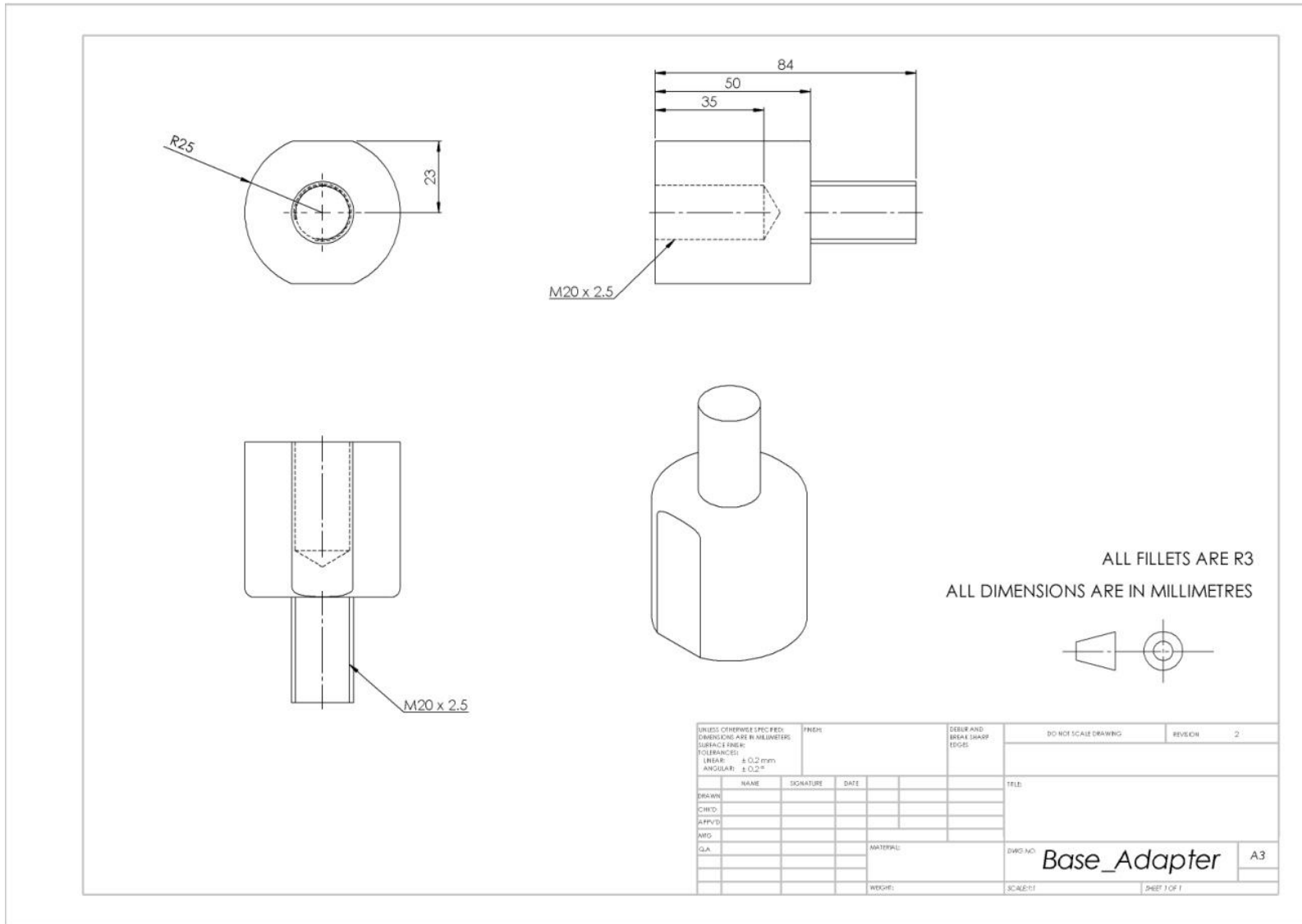
ALL FILLETS ARE R3

ALL DIMENSIONS ARE IN MILLIMETRES

Bend test rig support

R15
R5
45°

60 ± 0.05
30
15
5
10 ± 0.05

R15
2 x M6 x 1.0

14.50
47.50
54.50 ± 0.05
65.50 ± 0.05
72.50
105.50
120

50
40
15
10

4 x M12 x 1.75

ALL DIMENSIONS ARE IN MILLIMETRES

Specimen positioning guides

ALL DIMENSIONS ARE IN MILLIMETRES

Positioner

Crosshead adapter

R25

23

Ø50

Ø24.80

Ø13 THRU

100±0.1

70±0.1

50

35

M20 x 2.5

ALL DIMENSIONS ARE IN MILLIMETRES

	NAME	SIGNATURE	DATE			TITLE:		
DRAWN								
CHK'D								
APPV'D								
MFG								
Q.A			MATERIAL:					

UNLESS OTHERWISE SPECIFIED:
DIMENSIONS ARE IN MILLIMETERS
SURFACE FINISH:
TOLERANCES:
LINEAR: ± 0.2 mm
ANGULAR: ± 0.2 °

FINISH:

DEBUR AND
BREAK SHARP
EDGES

DO NOT SCALE DRAWING

REVISION   2

DWG NO.

Crosshead Adapter

A3

WEIGHT:

SCALE:1:2

SHEET 1 OF 1

Crosshead

∅ 12.70 ± 0.1 THRU

60° 60°

R5

∅ 12.70 ± 0.1 THRU

20 ± 0.1

50

88.30

21
25
29
50

∅ 25 ⊽ 50 ± 0.1

50

50

ALL DIMENSIONS ARE IN MILLIMETRES

Crosshead locking pin

R5

$\varnothing 12.60 \pm 0.1$

R5

$\varnothing 20$

140

120

ALL DIMENSIONS ARE IN MILLIMETRES

	NAME	SIGNATURE	DATE			TITLE:		
DRAWN								
CHK'D								
APPV'D								
MFG								
QA				MATERIAL:		DWG.NO.		
						Pin 15mm		A3
				WEIGHT:		SCALE:1:2	SHEET 1 OF 1	

230

Appendix 2 : MATLAB code used for time-averaged deposition profile

```matlab
clear all

%Substrate tube parameters
Sub_Surface=0;    %Substrate surface position (mm)
L_Start=-300;     %Starting point of the substrate (mm)
L_End=300;        %End point of the substrate (mm)
L_Mesh_Size=3;    %The mesh size along the length of the substrate (mm)
L_Sub=(L_Start:L_Mesh_Size:L_End);  %Substrate length array
R_Sub(1:length(L_Sub))=Sub_Surface; %Substrate radius array

%Atomiser scanning parameters
Frequency=16.6;          %Hz
Scan_angle=2.5;          %Degrees
Period=1/Frequency;
dt=0.25*Period;          %Time step
d_s=600;                 %Spray distance (mm)

%Experiment measurement from the preform sprayed with a non-retracting
%but rotating substrate and the atomiser scanning parameters described
%above.
Preform_Thickness=44.7; %Maximum preform thickness (mm)
Spray_Time=60;           %(s)
Measured_Deposition_Rate=Preform_Thickness/Spray_Time; %(mm/s)
b_spray=0.0006;      %Experiment radial spray distribution coefficient

%The deposition rate measured from the preform shape produced by the
%scanning atomiser was used to determine the actual deposition rate
%from the spray without scanning

for time=(0:dt:1);

%Atomiser scanning algorithm
Angle=Scan_angle.*sin(2.*22/7.*Frequency.*time);
Spray_start_position=0;
Spray_axis=d_s.*tand(Angle);
Spray_centre=Spray_start_position+Spray_axis;

%Deposition profile
a_spray=Measured_Deposition_Rate*dt;
Depo_height = a_spray.*exp(-b_spray.*abs(L_Sub-Spray_centre).^2);

if time == 0;
    height=R_Sub+Depo_height;
end

if time >0;
    height=height+Depo_height;
end

Actual_deposition_rate=Measured_Deposition_Rate*(Measured_Deposition_R
ate/max(height));

end
```

```matlab
%The time averaged deposition profile in 1 s using the scanning
%atomiser

for t=(0:dt:1)

%Atomiser scanning algorithm
Angle=Scan_angle.*sin(2.*22/7.*Frequency.*t);
Spray_start_position=0;
Spray_axis=d_s.*tand(Angle);
Spray_centre=Spray_start_position+Spray_axis;

%Deposition profile using actual deposition rate
a_scan_spray=Actual_deposition_rate*dt;
Depo_height_scan = a_scan_spray.*exp(-b_spray.*abs(L_Sub-
Spray_centre).^2);

if t == 0;
    height_scan=R_Sub+Depo_height_scan;
end

if t >0;
    height_scan=height_scan+Depo_height_scan;
end

plot(L_Sub, height_scan);
axis([-300 300 0 0.8]);
        xlabel('Length, mm')
        ylabel('Radius, mm')
        grid on
end
```